

Biomimetic Synthesis of Metal Oxide Nanoparticles

By

Sarah Lynn Sewell

Dissertation

Submitted to the Faculty of the
Graduate School of Vanderbilt University
in partial fulfillment of the requirements
for the degree of

DOCTOR OF PHILOSOPHY

in

Chemistry

May, 2007

Nashville, Tennessee

Approved:

Professor David W. Wright

Professor Timothy P. Hanusa

Professor David E. Cliffel

Professor John P. Wikswo

Professor Charles M. Lukehart

ACKNOWLEDGEMENTS

There have been so many encouraging people on the road to graduate school. First and foremost, I would like to thank God for allowing me to come to Vanderbilt and study chemistry. Also, I would like to thank Him for letting several reactions work and several not work (like controls). Many days were spent praying about reactions, pictures, instruments, and results.

My entire family has been incredibly supportive in this marathon. Mom and Dad, thanks for everything. Mom, thanks for boiling cabbage and sparking my interest in chemistry. Dad, thanks for all your morning pep-talks and raising your girls to be confident. Katie, thanks for your optimistic fun view of life and helping me decorate my apartment. I would like to thank my grandparents, John and Nina Reese and Bertie Sewell, for all their encouraging words of wisdom. Cary, thanks for “understanding” all my science from a banking perspective. There were so many dates that started with running by the lab so that I could check a reaction or put a sample in the XRD. Thank you for keeping me company and helping with everything. I don’t know how we’ll begin our dates now!

I would like to thank my boss, David Wright, for the education I received. I could not have had a better mentor to teach scientific thinking and writing. Thank you for all the grand events that were hosted by your family. The trips to Florida, brunches, and cookouts are among my most fond grad school memories. Additionally, I would like to thank Dr. Lukehart, Dr. Hanusa, Dr. Cliffel, and Dr. Wikswo for the constructive discussions at my committee meetings.

I would like to thank the members of the Wright Lab throughout the years, in no particular order: Dr. Clare Kenny Carney, Dr. Crystal Miller, Dr. Scott Miller, Dr. Joe Slocik, Dr. Marc Knecht, Elizabeth Bentzen, Goska Broncel, Reese Harry, Kristin Halfpenny, Alex Rutledge, Ryan Rutledge, Melissa Carter, Leila Deravi, and Jonas Perez. Ryan, it has been fantastic sharing a desk with you. Thanks for proofreading this document and for all your outstanding sports advice. Elizabeth, thanks for being a fantastic host for so many social events. Clare, you have been so encouraging throughout my whole graduate school career. I truly cannot thank you enough for all that you have done. Kristin, thanks for all your fashion advice and walks around campus. Reese, thanks for all your help throughout graduate school and undergraduate. I don't think I could have made it through all those labs had you not been my lab partner! Alex, thanks for your help with planning microarrays and mass spectrometry experiments. Melissa, thanks for being a fantastic friend. I have enjoyed all our lunches. Leila, thanks for having an upbeat, positive attitude and being patient with me while I tried to explain techniques.

There are several people outside the Wright lab that I would like to thank as well! Tripp, you have been a fantastic friend. Thanks for all the insightful discussions about nanomaterials and techniques. I would also like to thank Jane Brown, Denise Zannino, and Kristin Kalie for all their encouragement.

TABLE OF CONTENTS

	Page
ACKNOWLEDGEMENTS.....	ii
LIST OF TABLES.....	vi
LIST OF FIGURES.....	vii
LIST OF ABBREVIATIONS.....	xiv
Chapter	
I. GENERAL INTRODUCTION.....	1
Introduction.....	1
Constrained Synthesis of Metal Oxide Nanocomposites.....	3
Biosynthesis of Iron Oxide by Ferritin.....	4
Synthesis of Metal Oxide Nanocomposites Using Ferritin.....	6
Applications of Ferritin Metal Oxide Nanocomposites.....	10
Mineralization by Bacteria, Enzymes and Viruses.....	21
Template Directed Synthesis of Metal Oxide Nanocomposites.....	29
Peptide and Protein Templates.....	30
Proteins from <i>Fusarium oxysporum</i>	30
Peptide Display Libraries.....	33
Silicatein.....	36
Diatoms.....	42
Research Aims and Goals.....	48
References.....	49
II. BIOMIMETIC SYNTHESIS OF TITANIUM DIOXIDE UTILIZING BIO-POLYMERS.....	59
Introduction.....	59
The R5 Peptide.....	64
Polymers.....	68
Synthesis of Metal Oxides.....	69
Experimental.....	74
Results and Discussions.....	77
R5 Peptide Mediated Formation of TiO ₂	77
PLL Mediated Formation of TiO ₂	81
Nanoparticle Characterization.....	82
X-Ray Diffraction Analysis.....	86

	Conclusion	88
	References.....	89
III.	SIZE CONTROL OF DENDRIMER TEMPLATED SILICA.....	94
	Introduction.....	94
	Dendrimers.....	97
	Experimental.....	102
	Results and Discussions.....	103
	Effect of Phosphate Concentration	103
	Effect of Various Salt Concentrations	107
	Conclusions.....	110
	References.....	111
IV.	AMINE TERMINATED DENDRIMERS: VERSATILE BIOMIMETIC TEMPLATES FOR ALTERNATE SUBSTRATES	113
	Introduction.....	113
	Dendrimer Mediated Synthesis of Multi-component Nanoparticles	114
	Carboxyl Terminated Dendrimer Metal Oxide Synthesis	117
	Experimental.....	118
	Results and Discussions.....	120
	Dendrimer Mediated Metal Oxide Formation	120
	Nanoparticle Characterization	124
	XRD Analysis	127
	Conclusions.....	132
	References.....	133

Appendix

A.	CHARACTERIZATION OF THE R5 PEPTIDE AND PLL TEMPLATE AND THE RESULTING TITANIUM DIOXIDE NANOPARTICLES	137
B.	CHARACTERIZATION OF DENDRIMER PRECIPITATED SILICA NANOPARTICLES.....	145
C.	CHARACTERIZATION OF DENDRIMER PRECIPITATED TITANIUM DIOXIDE AND GERMANIUM DIOXIDE NANOPARTICLES.....	191
D.	CURRICULUM VITAE.....	227

LIST OF TABLES

Table	Page
1. Interior and exterior diameter of protein cages commonly used in metal oxide synthesis.....	3
2. Biologically derived iron catalyst for nanotube formation	25
3. Silica precipitating ability of the R5 peptide and truncates	65
4. Characterization of TiO ₂ precipitating peptides and the resulting nanoparticles	79
5. Scherrer's analysis of R5 peptide and PLL templated TiO ₂	87
6. Dendrimer Activity	122

LIST OF FIGURES

Figure	Page
1. A) TEM image of <i>Cylindrotheca fusiformis</i> B) TEM image of <i>Magnetospirillum magnetotacticum</i>	2
2. The ferroxidase center of human H-chain ferritin	5
3. Alternate pathways for ferritin mediated metal oxide formation	7
4. SEM of spatially arrayed ferritin iron oxide nanoparticles A) as deposited B) with heat treatment at 300°C C) with heat treatments at 500°C D) with heat treatments at 700°C.....	13
5. A) AFM topography image of SWNT synthesized with ferritin iron oxide nanoparticles as a template B) TEM image of SWNT synthesized from ferritin iron oxide nanoparticles, arrow pointing to iron oxide nanoparticle	18
6. Schematic of SWNT growth utilizing a ferritin deposited iron oxide nanoparticle	19
7. Photograph of <i>Tethya aurantia</i>	37
8. A) Unreacted silicatein filament B) Silicatein filament reacted with TEOS C) Silicatein filament reacted with TBALDH D) Silicatein filament reacted with gallium nitrate.....	38
9. Mechanism of silicatein catalyzed TEOS hydrolysis	39
10. A) SEM of <i>Thalassiosira oestruppi</i> B) SEM of a valve from <i>Porodiscus hirsutus</i> C) SEM of a valve from <i>Kittonia elaborata</i>	42
11. Diatom cell division.....	45
12. A) SEM image of the interior of <i>C. granii</i> . B) SEM image of the exterior of <i>C. granii</i>	46
13. AFM image of the outer surface of <i>C. granii</i>	47
14. A) Comparison of the SDS/PAGE gel of ammonium fluoride and HF extracted silaffins B) Amino acid sequence of Sil1p	61
15. Structure of natSil-1A	62

16.	A) SEM of arch-like silica structures formed from flowing nitrogen through the reaction. B) SEM of silica fibrous structures formed when shear is applied.....	66
17.	Silica nanoparticles formed from polyamines isolated from <i>N. angularis</i> diatom	68
18.	A) Silica nanoparticles formed from poly(L-cysteine ₃₀ -L-lysine ₂₀₀) under nitrogen. B) Silica columns formed from poly(L-cysteine ₃₀ -L-lysine ₂₀₀) in air	70
19.	TiO ₂ production as a function of R5 concentration	78
20.	Titanium dioxide production as a function of pH.....	80
21.	TiO ₂ produced as a function of PLL concentration	81
22.	A) SEM micrograph of R5 templated TiO ₂ nanoparticles B) SEM micrograph of PLL templated TiO ₂ nanoparticles	82
23.	A) Variable temperature XRD of R5 templated TiO ₂ synthesized in water. B) Variable temperature XRD of R5 templated TiO ₂ synthesized in 100 mM phosphate buffer.....	84
24.	A) Variable temperature XRD of PLL templated TiO ₂ in the presence of water. B) Variable temperature XRD of PLL templated TiO ₂ synthesized in 100 mM phosphate buffer	85
25.	Silica nanoparticle diameter as a function of phosphate buffer concentration using polyamines from <i>S. turris</i> as the biomimetic template.....	94
26.	Amount of silica produced as a function of phosphate concentration using PAA as a biomimetic template	95
27.	Aggregation of PAA at various phosphate concentration.....	96
28.	The structure of the silaffin from <i>C. fusiformis</i> , the R5 peptide, PAMAM dendrimer and PPI dendrimer	98
29.	A) The nmols of silica produced as a function of PAMAM primary amine concentration B) The nmols of silica produced as a function of PPI primary amine concentration	99
30.	IR of dendrimer templated nanoparticles.....	100
31.	Dendrimer templated silica production as a function of phosphate buffer concentration.....	104

32.	A) Nanoparticle size as a function of phosphate buffer concentration for G3 PAMAM templated silica B) Size distributions for silica nanoparticles produced from G0-G6 PAMAM templates	105
33.	Silica production as a function of salt concentration	107
34.	A) Nanoparticle size as a function of NaCl concentration B) Size distributions for silica nanoparticles produced from various salts.....	108
35.	A) A schematic of dendrimer mediated silica encapsulation of quantum dots B) A SEM image of the silica/quantum dot nanocomposite C) A confocal image of silica/quantum dot nanocomposite.....	114
36.	A schematic of dendrimer mediated gold nanoparticle encapsulation in silica nanoparticles	115
37.	A) G0, G2, G4, and G6 PAMAM templated TiO ₂ production as a function of primary amine concentration in phosphate buffer and water. B) G4 and G5 PPI templated TiO ₂ production as a function of primary amine concentration in phosphate buffer and water.....	121
38.	A) G4 and G6 PAMAM templated GeO ₂ production as a function of primary amine concentration in phosphate buffer and water. B) G4 and G5 PPI templated GeO ₂ production as a function of primary amine concentration in phosphate buffer and water	123
39.	Reseeding experiment for A) TiO ₂ and B) GeO ₂	124
40.	A) SEM of G4 PAMAM templated TiO ₂ formed in water B) SEM of G4 PAMAM templated GeO ₂ formed in water C) SEM of G4 PAMAM templated TiO ₂ formed in phosphate buffer D) SEM of G4 PAMAM templated GeO ₂ formed in phosphate buffer	125
41.	A) Variable temperature XRD of G4 PAMAM templated TiO ₂ in water. B) Variable temperature XRD of G4 PAMAM templated TiO ₂ in phosphate buffer.....	128
42.	A) XRD of G4 PAMAM templated GeO ₂ in water. B) XRD of G4 PAMAM templated GeO ₂ in phosphate buffer	129
43.	A) Photoluminescence spectrum for G4 PAMAM templated germanium dioxide in phosphate buffer. B) Photoluminescence spectrum for G4 PAMAM templated germanium dioxide in water	132
44.	CD of PLL in phosphate buffer	138

45.	CD of PLL in the presence of phosphate buffer and TBALDH	138
46.	CD of PLL in water	139
47.	CD of PLL in water and TBALDH.....	139
48.	EDS of R5 templated TiO ₂ synthesized in the presence of water.....	140
49.	EDS of R5 templated TiO ₂ synthesized in the presence of phosphate buffer	140
50.	EDS of poly-L-lysine templated TiO ₂ synthesized in the presence of water ..	141
51.	EDS of poly-L-lysine templated TiO ₂ synthesized in the presence of phosphate buffer	141
52.	IR of R5 peptide.....	142
53.	IR of R5 templated TiO ₂ synthesized in the presence of water	142
54.	IR of R5 templated TiO ₂ synthesized in the presence of phosphate buffer	143
55.	IR of PLL	143
56.	IR of PLL templated TiO ₂ synthesized in the presence of water.....	144
57.	IR of PLL templated TiO ₂ synthesized in the presence of phosphate buffer ...	144
58.	A representative sample of SEMs that were analyzed for each histogram (from G6 PAMAM 60 mM phosphate buffer).....	146
59.	SEM micrographs and histograms of silica nanoparticles produced from the G0 PAMAM template in concentrations of phosphate buffer of a) 0.5 mM, b) 5 mM, c) 10 mM, d) 20 mM, e) 40 mM, f) 60 mM, g) 80 mM and h) 100 mM .	147
60.	SEM micrographs and histograms of silica nanoparticles produced from the G1 PAMAM template in concentrations of phosphate buffer of a) 0.5 mM, b) 5 mM, c) 10 mM, d) 20 mM, e) 40 mM, f) 60 mM, g) 80 mM and h) 100 mM .	149
61.	SEM micrographs and histograms of silica nanoparticles produced from the G2 PAMAM template in concentrations of phosphate buffer of a) 0.5 mM, b) 5 mM, c) 10 mM, d) 20 mM, e) 40 mM, f) 60 mM, g) 80 mM and h) 100 mM .	151
62.	SEM micrographs and histograms of silica nanoparticles produced from the G3 PAMAM template in concentrations of phosphate buffer of a) 0.5 mM, b) 5 mM, c) 10 mM, d) 20 mM, e) 40 mM, f) 60 mM, g) 80 mM and h) 100 mM .	153

63. SEM micrographs and histograms of silica nanoparticles produced from the G4 PAMAM template in concentrations of phosphate buffer of a) 0.5 mM, b) 5 mM, c) 10 mM, d) 20 mM, e) 40 mM, f) 60 mM, g) 80 mM and h) 100 mM .155
64. SEM micrographs and histograms of silica nanoparticles produced from the G5 PAMAM template in concentrations of phosphate buffer of a) 0.5 mM, b) 5 mM, c) 10 mM, d) 20 mM, e) 40 mM, f) 60 mM, g) 80 mM and h) 100 mM .157
65. SEM micrographs and histograms of silica nanoparticles produced from the G6 PAMAM template in concentrations of phosphate buffer of a) 0.5 mM, b) 5 mM, c) 10 mM, d) 20 mM, e) 40 mM, f) 60 mM, g) 80 mM and h) 100 mM .159
66. SEM micrographs and histograms of silica nanoparticles produced from the G1 PPI template in concentrations of phosphate buffer of a) 0.5 mM, b) 5 mM, c) 10 mM, d) 20 mM, e) 40 mM, f) 60 mM, g) 80 mM and h) 100 mM.....161
67. SEM micrographs and histograms of silica nanoparticles produced from the G2 PPI template in concentrations of phosphate buffer of a) 0.5 mM, b) 5 mM, c) 10 mM, d) 20 mM, e) 40 mM, f) 60 mM, g) 80 mM and h) 100 mM.....163
68. SEM micrographs and histograms of silica nanoparticles produced from the G3 PPI template in concentrations of phosphate buffer of a) 0.5 mM, b) 5 mM, c) 10 mM, d) 20 mM, e) 40 mM, f) 60 mM, g) 80 mM and h) 100 mM.....165
69. SEM micrographs and histograms of silica nanoparticles produced from the G4 PPI template in concentrations of phosphate buffer of a) 0.5 mM, b) 5 mM, c) 10 mM, d) 20 mM, e) 40 mM, f) 60 mM, g) 80 mM and h) 100 mM.....167
70. SEM micrographs and histograms of silica nanoparticles produced from the G5 PPI template in concentrations of phosphate buffer of a) 0.5 mM, b) 5 mM, c) 10 mM, d) 20 mM, e) 40 mM, f) 60 mM, g) 80 mM and h) 100 mM.....169
71. SEM micrographs and histograms of silica nanoparticles produced from the G4 PAMAM template in a LiCl solution with concentrations of a) 0.5 mM, b) 5 mM, c) 10 mM, d) 20 mM, e) 40 mM, f) 60 mM, g) 80 mM, h) 100 mM, i) 200 mM, j) 300 mM and k) 400 mM.....171
72. SEM micrographs and histograms of silica nanoparticles produced from the G4 PAMAM template in a NaCl solution with concentrations of a) 0.5 mM, b) 5 mM, c) 10 mM, d) 20 mM, e) 40 mM, f) 60 mM, g) 80 mM, h) 100 mM, i) 200 mM, j) 300 mM and k) 400 mM.....174
73. SEM micrographs and histograms of silica nanoparticles produced from the G4 PAMAM template in a KCl solution with concentrations of a) 0.5 mM, b) 5

	mM, c) 10 mM, d) 20 mM, e) 40 mM, f) 60 mM, g) 80 mM, h) 100 mM, i) 200 mM, j) 300 mM and k) 400 mM.....	177
74.	SEM micrograph and histogram of silica nanoparticles produced from the G4 PAMAM template in a RbCl solution with concentrations of a) 0.5 mM, b) 5 mM, c) 10 mM, d) 20 mM, e) 40 mM, f) 60 mM, g) 80 mM, h) 100 mM, i) 200 mM, j) 300 mM and k) 400 mM.....	180
75.	SEM micrographs and histograms of silica nanoparticles produced from the G4 PAMAM template in a CsCl solution with concentrations of a) 0.5 mM, b) 5 mM, c) 10 mM, d) 20 mM, e) 40 mM, f) 60 mM, g) 80 mM, h) 100 mM, i) 200 mM, j) 300 mM and k) 400 mM.....	183
76.	SEM micrographs and histograms of silica nanoparticles produced from the G4 PAMAM template in a MgCl ₂ solution with concentrations of a) 0.5 mM, b) 5 mM, c) 10 mM, d) 20 mM, e) 40 mM, f) 60 mM, g) 80 mM, h) 100 mM.....	186
77.	MgCl ₂ concentration effects on a) silica production activity of 20 mM primary amine concentration of G4 PAMAM dendrimers and b) particle size distribution.....	188
78.	Silica production as a function of the primary amine concentration of the G4 PAMAM template in a 100 mM NaCl solution	189
79.	Effects of phosphate buffer concentration on the silica formation activity of PPI dendrimers a) silica production activity and b) size distributions for nanospheres produced from PPI dendrimers.	190
80.	Titanium dioxide production as a function of G0 PAMAM primary amine concentration.....	192
81.	Titanium dioxide production as a function of pH.....	192
82.	Germanium dioxide production as a function of pH	193
83.	SEM micrographs and histograms of titanium dioxide nanoparticles precipitated in phosphate buffer from: a) G0 PAMAM, b) G-2 PAMAM, c) G-4 PAMAM, d) G-6 PAMAM, e) G4-PPI f) G-5 PPI	194
84.	SEM micrographs of titanium dioxide nanoparticles precipitated in water from: a) G-0 PAMAM, b) G-2 PAMAM, c) G-4 PAMAM, d) G-6 PAMAM, e) G4-PPI f) G-5 PPI	196
85.	Infra-red spectra of titanium dioxide precipitated in phosphate buffer from: a) G-0 PAMAM, b) G-2 PAMAM, c) G-4 PAMAM, d) G-6 PAMAM, e) G4-PPI f) G-5 PPI.....	198

86.	Infra-red spectra of titanium dioxide precipitated in water from: a) G-0 PAMAM, b) G2 PAMAM, c) G-4 PAMAM, d) G-6 PAMAM, e) G4-PPI f) G-5 PPI	200
87.	Variable temperature X-ray diffraction spectra of titanium dioxide precipitated in phosphate buffer from a) G-2 PAMAM, b) G-4 PAMAM, c) G-6 PAMAM, d) G4-PPI e) G-5 PPI	202
88.	Variable temperature X-ray diffraction spectra of titanium dioxide precipitated in water from a) G-2 PAMAM, b) G-4 PAMAM, c) G-6 PAMAM, d) G4-PPI e) G-5 PPI.....	205
89.	SEM micrographs and histograms of germanium dioxide nanoparticles precipitated in phosphate buffer from: a) G-0 PAMAM, b) G-2 PAMAM, c) G-4 PAMAM, d) G-6 PAMAM, e) G4-PPI f) G-5 PPI.....	208
90.	SEM micrographs of germanium dioxide nanoparticles precipitated in water from: a) G-0 PAMAM, b) G-2 PAMAM, c) G-4 PAMAM, d) G-6 PAMAM, e) G4-PPI f) G-5 PPI.....	210
91.	Infra-red spectra of germanium dioxide precipitated in phosphate buffer from: a) G-0 PAMAM, b) G-2 PAMAM, c) G-4 PAMAM, d) G-6 PAMAM, e) G4-PPI f) G-5 PPI	212
92.	Infra-red spectra of germanium dioxide precipitated in water from: a) G-0 PAMAM, b) G-2 PAMAM, c) G-4 PAMAM, d) G-6 PAMAM, e) G4-PPI f) G-5 PPI.....	214
93.	Variable temperature X-ray diffraction spectra of germanium dioxide precipitated in phosphate buffer from a) G-0 PAMAM, b) G-2 PAMAM, c) G-4 PAMAM, f) G-6 PAMAM, e) G4-PPI f) G-5 PPI.....	216
94.	Variable temperature X-ray diffraction spectra of germanium dioxide precipitated in water from a) G-0 PAMAM, b) G-2 PAMAM, c) G-4 PAMAM, f) G-6 PAMAM, e) G4-PPI f) G-5 PPI.....	219
95.	Variable temperature X-ray diffraction spectra of G4 PAMAM templated germanium dioxide in phosphate buffer	222
96.	Variable temperature X-ray diffraction spectra of G4 PAMAM templated germanium dioxide in water	222
97.	A) Light scattering profile of G4 dendrimer templated GeO ₂ reaction in water. B) Light scattering profile of G4 dendrimer templated TiO ₂ reaction in water. (absorbance at 480).....	223

98.	A) XRD of G4 PAMAM templated GeO ₂ in water using TMOG as the precursor. B) XRD of G4 PAMAM templated GeO ₂ in phosphate buffer, 100 mM, pH 7.5, using TMOG as the precursor (♦ α -phase).....	223
99.	XRD of G4 PAMAM templated GeO ₂ using TIPG as the precursor and phosphate buffer (100 mM, pH 7.5) as the solvent.....	224
100.	XRD of G4 PAMAM templated GeO ₂ using TIPG as the precursor and water as the solvent.....	224
101.	XRD of PLL templated GeO ₂ using TMOG as the precursor and phosphate buffer (100 mM, pH 7.5) as the solvent (♦ α -phase)	225
102.	XRD of PLL templated GeO ₂ using TEOG as the precursor and phosphate buffer (100 mM, pH 7.5) as the solvent (♦ α -phase)	225
103.	XRD of PLL templated GeO ₂ using TIPG as the precursor and phosphate buffer (100 mM, pH 7.5) as the solvent.....	226

LIST OF ABBREVIATIONS

AFM:	atomic force microscope
AMP dots:	amphiphilic quantum dots
CVD:	chemical vapor deposition
DCM:	dichloromethane
DIEA:	diisopropylamine
DLS:	dynamic light scattering
DMF:	N,N-dimethylformamide
EDS:	energy dispersion spectrometry
Fmoc:	fluorenylmethoxycarbonyl
FTIR:	fourier transform infra-red spectroscopy
HBTU:	2-(1H-benzotriazole-1-yl)-1,1,3,3-tetramethyluronium hexafluorophosphate
HOBt:	N-hydroxybenzotriazole
HPLC:	high performance liquid chromatography
HRTEM:	high resolution transmission electron microscopy
MALDI-TOF:	matrix assisted laser desorption ionization – time of flight mass spectrometry
MWNT	multi-walled nanotube
NMR:	nuclear magnetic resonance
PAA:	poly(allyl)amine
PAGE:	polyacrylamide gel electrophoresis

PAMAM:	polyamidoamine
PCR:	polymerase chain reaction
PLL:	poly-L-lysine
PPI:	polypropylenimine
Qdot:	quantum dot
SADP:	selected area diffraction pattern
SEM:	scanning electron microscopy
SWNT:	single-walled nanotube
TBALDH:	titanium bis(ammonia lactato) dihydroxide
TEM:	transmission electron microscopy
TEOS:	tetraethylorthosilicate
TFA:	trifluoroacetic acid
TMOS:	tetramethylorthosilicate
XRD:	x-ray diffraction

CHAPTER I

GENERAL INTRODUCTION

Introduction

There are many potential applications of metal oxide nanoparticles including chemical sensors, field effect transistors, catalysts, drug delivery agents, electronics, optics, and magnetic storage devices.¹⁻⁶ Many of the common synthetic methods for metal oxide nanocomposites, which include electron beam lithography, laser vaporization, ball milling, microwave irradiation, and emulsification of molten salts and metals, use high temperatures, pressures, and caustic chemicals.⁷⁻¹³ These extreme conditions can be limiting when designing and constructing delicate nanodevices or biologically relevant materials. Biomimetic synthesis is an alternative to the harsh conditions of conventional synthetic methods. Because of this, biomimetic synthesis, defined for the purposes of this paper as methods that mimic natural biomineralization processes, has become an attractive research field. Additionally, biomimetically synthesized nanoparticles can be used as unique templates for controlled synthesis and catalysis. Biomimetic synthesis offers a plethora of routes to metal oxide nanocomposites which occur at ambient conditions and temperatures for use in various applications.¹⁴

Through precisely tuned processes, nature is able to synthesize a variety of metal oxide nanocomposites under ambient conditions that function as storage units, structural supports and magnetic navigation devices. A few examples include ferritin, silica, iron

titanium oxide, and iron oxide. Ferritin, a highly conserved protein, stores iron as iron oxyhydroxide until it is ready for use by the body.¹⁵⁻¹⁷ In an aqueous environment, diatoms mineralize silica which function as an exoskeleton (**Figure 1A**).¹⁸ Also, the Oriental hornet, *Vespa orientalis*, incorporates crystalline iron titanium oxide into the cell walls of their nests for a gravity reference point.^{19,20} Magnetotactic bacteria crystallize iron oxide nanoparticles, which helps align them with the earth's magnetic field (**Figure 1B**).^{21,22} Salmon have iron oxide located in their head for magnetic navigation.²³ These examples suggest that through the mimicry of nature, metal oxide nanocomposites can be synthesized at lower temperatures and pressures than previous synthetic methods. These nanocomposites can then be used for nanodevices, catalysis, and synthetic templates.

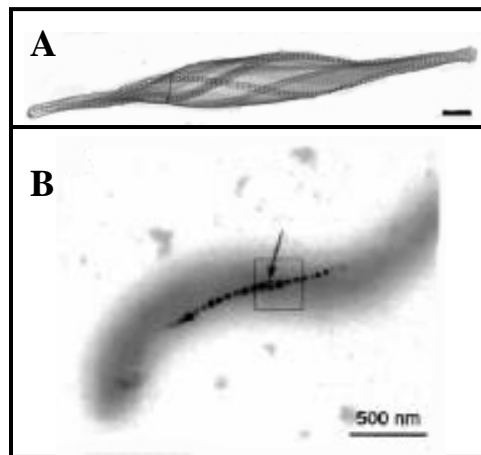


Figure 1: A) TEM image of *Cylandretheca fusiformis*²⁴, scale bar 5 μ m. B) TEM image of *Magnetospirillum magnetotacticum*²², scale bar 500 nm.

Constrained Synthesis of Metal Oxide Nanocomposites

Size often determines the magnetic, electronic, and chemical properties of nanoparticles. For example, nanoparticles of titanium dioxide have an enhanced redox potential and many bulk metals contain a conduction band while nanoparticles do not.^{25,26} The magnetic properties of cobalt and cobalt oxide nanoparticles vary as a function of size.²⁷⁻²⁹ Additionally, the chemical reactivity of several metal oxides is enhanced due to the large area of the nanoparticle as compared to the bulk metal oxide.^{30,31} Therefore, novel methods of creating metal oxide nanoparticles with a defined size are necessary for achieving desired electronic, magnetic, and chemical properties. Many proteins found in nature have contained environments that are ideal for controlling the size nanoparticles. Ferritins, cage-like enzymes, and virus capsids represent constrained environments for the synthesis of relatively monodisperse metal oxide nanocomposites (**Table 1**).

Table 1. Interior and Exterior Diameter of Protein Cages Commonly Used in Metal Oxide Synthesis³²

Protein Cage	Interior Diameter (nm)	Exterior Diameter (nm)
Horse Spleen Ferritin	8	12
Dps from <i>L. innocua</i>	6	9
Lumazine Synthase from <i>B. Subtilis</i>	8	15
Cowpea Chlorotic Mottle Virus from <i>B. Subtilis</i>	24	28

Biosynthesis of Iron Oxide by Ferritin

Ferritin is a conserved 450 kD iron storage protein found widely throughout nature.^{15,16} Even though there are subtle differences in prokaryotic, eukaryotic, and archeal ferritin, the overall structure is similar. Generally, the protein consists of 24 subunits assembled into a cage-like structure that mineralizes iron oxide from Fe^{2+} . Mammalian ferritin consists of two subunits, H and L (Heavy and Light, respectively) that vary in percentages from organism to organism.³³ The two subunits are structurally analogous, consisting of a four helix bundle with a fifth helical domain that caps the protein.^{15,34} The outer diameter of the assembled protein is 12 nm, with an interior of 8 nm.³⁵ The way the subunits interact leads to the formation of threefold and fourfold channels approximately 3 Å in diameter. The threefold channels consist of hydrophilic aspartate and glutamate amino acid residues, while the fourfold channels are hydrophobic.¹⁷ Ion probe studies conducted by Arosio and coworkers show that the uptake of iron, a charge dependant process, occurs through the threefold hydrophilic channels.³⁶ Two-thirds of the iron oxide cores formed by ferritin exist as ferrihydrite (FeOOH). Other iron oxide species that are present in the core are hematite ($\alpha\text{-Fe}_2\text{O}_3$), magnetite (Fe_3O_4), maghemite ($\gamma\text{-Fe}_2\text{O}_3$), as well as amorphous iron oxide structures.³⁷ The shape and size of the protein keeps the iron from condensing into insoluble aggregates and allows for the storage of approximately 4500 iron atoms.¹⁶

The process of *in vitro* iron uptake and storage has been extensively investigated by Zhao and coworkers using human recombinant H-and L-chain ferritin.³⁸ Ferritin sequesters iron(II) and oxidizes it to a mineral form through a combination of processes. Three mechanisms have been proposed for the *in vitro* oxidation of iron(II)³⁸:



Mechanism (1) is believed to occur in the H chain of ferritin at the ferroxidase center. The ferroxidase center has two binding sites that contain coordinating histidine and glutamic acid residues with a glutamic acid bridging the two sites (**Figure 2**).

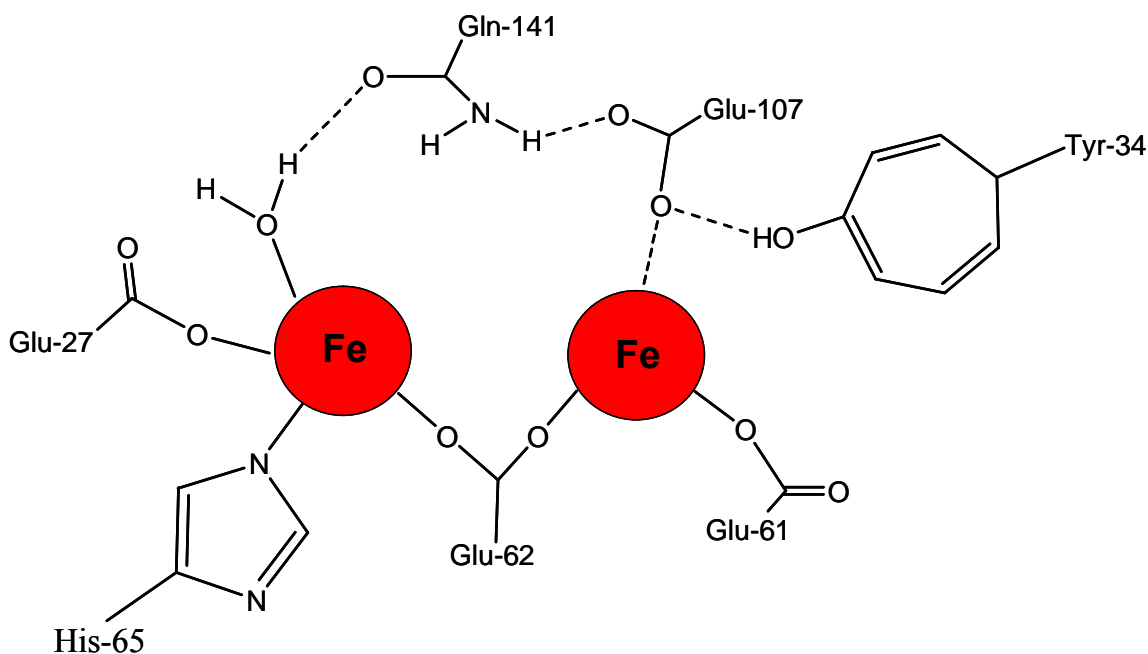


Figure 2: The ferroxidase center of human H-chain ferritin.³⁸

This mechanism is a protein mediated reaction that is present at all iron loadings studied (48-800 Fe(II) per protein), but decreases as iron concentration increases. Iron is oxidized by dioxygen forming a μ -1,2-peroxodiiron(III) intermediate that decays to an μ -

oxodiiron(III) intermediate, ultimately forming the ferritin iron oxyhydroxide core.³⁹⁻⁴⁵ Identical to the auto oxidation of iron⁴⁶, mechanism (2) is dominant at levels of high iron concentration (800 Fe(II) per protein). At higher concentration levels according to crystal growth models, iron is thought to be directly deposited on the mineralized core.^{47,48} Mechanism (3) occurs at intermediate Fe(II) levels (100-500 Fe(II) per protein), detoxifying the hydrogen peroxide produced from mechanism (1).³⁸ To date, the *in vivo* mechanism of iron mineralization by ferritin is unknown, however, an oxidative process is thought to be responsible since cores cannot be reconstituted without the presence of an oxidizing agent.^{15,16,38}

Synthesis of Metal Oxide Nanocomposites Using Ferritin

The natural ferrihydrite core of ferritin can be removed using thioglycolic acid, resulting in apoferritin.⁴⁹ The iron oxyhydroxide core can subsequently be reconstituted by introducing an iron anion in the presence of an oxidant, usually oxygen in air.⁵⁰ Under controlled conditions (slow addition of Fe(II) ions at 55°C) ferrimagnetic iron oxide magnetite is formed in the ferritin shell.⁵¹ Additionally, nanoparticles of metal hydroxides and metal oxides that are not found in the natural environment of ferritin have been crystallized in the interior (**Figure 3**). For example, Mn(II) ions are air oxidized to form a manganese oxyhydroxide and manganese oxide core at a pH of 8.9.⁵²⁻⁵⁴ The majority of the substrates used for the crystallization normally form bulk precipitates in solutions when ferritin is not present. However, when ferritin is introduced, the materials are formed exclusively in the interior of ferritin, indicating that ferritin mechanistically controls the uptake and formation of the metal oxide nanocomposites.

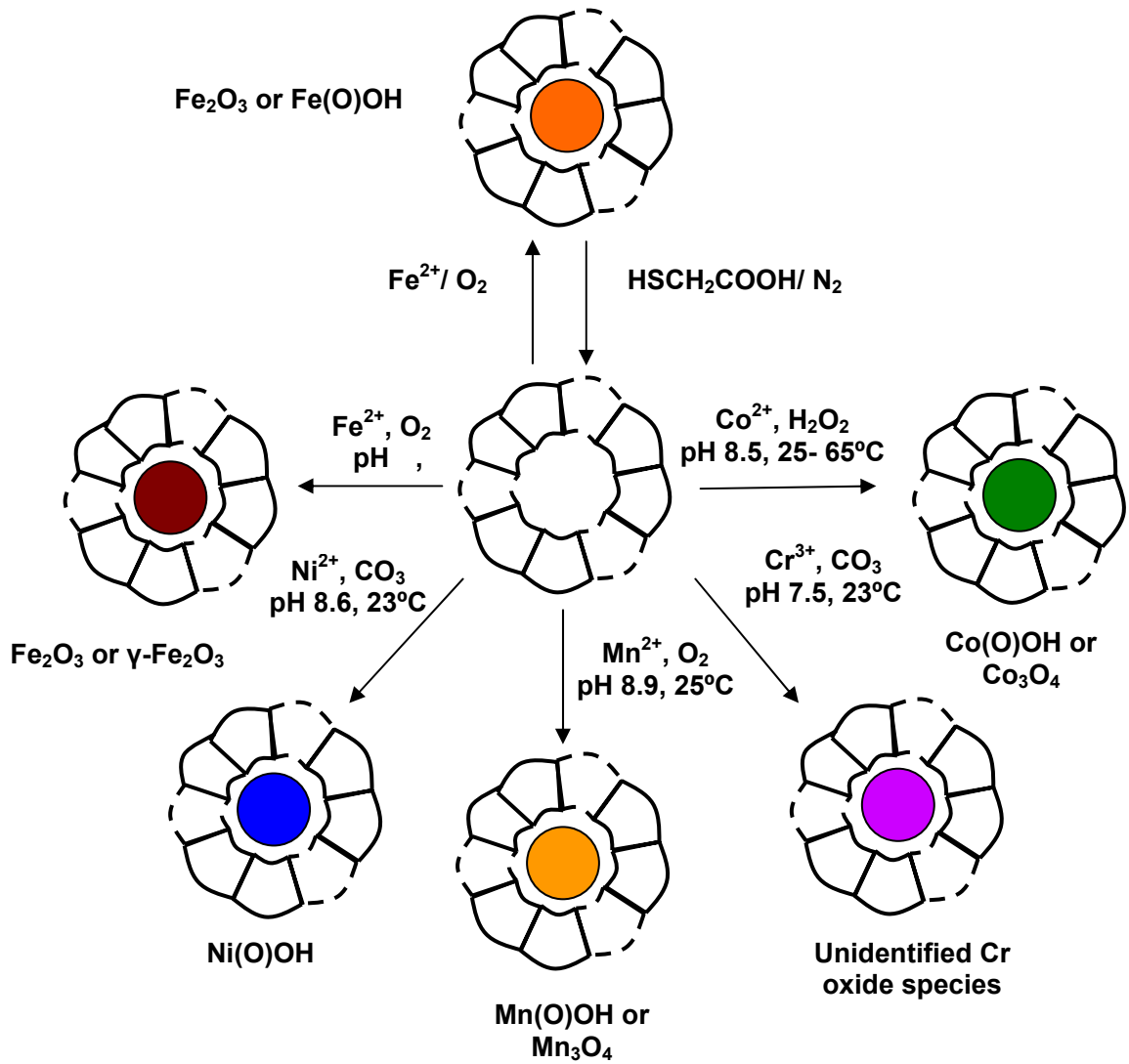
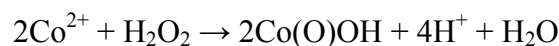


Figure 3: Alternate pathways for ferritin mediated metal oxide formation

Recently, oxyhydroxides of cobalt, nickel, and chromium have been synthesized in the interior of apoferritin. When apoferritin is exposed to Co(II) ions at a pH of 8.5 in the presence of hydrogen peroxide, a cobalt oxyhydroxide core is formed.⁵⁵ A pH of 8.5 was necessary, as the cobalt oxyhydroxide mineral is partially soluble at a neutral or acidic pH. In control reactions where O₂ was used as the reducing agent, no mineralization occurred. Therefore, hydrogen peroxide is responsible for the oxidation of Co(II) to Co(III). Additionally, control reactions lacking the protein resulted in bulk precipitation of cobalt oxyhydroxide aggregates, indicating that ferritin is acting as a constrained, controlled environment for the oxidation and hydrolysis reaction of Co(II).⁵⁵ The stoichiometry of the overall reaction, as determined by pH titration data, is as follows:



The protein content of the cobalt loaded ferritin was measured by the Biuret method, and the cobalt concentration was determined spectrophotometrically using the nitroso-R salt method.^{56,57} The combined data from these methods indicates there are 2000 atoms of Co per ferritin protein. When the concentrations of Co to protein were adjusted in an attempt to achieve higher loadings, bulk precipitation of the oxyhydroxide mineral occurred, indicating that the maximum amount of Co that the protein can oxidize is 2000 atoms.⁵⁵ The reduced amount of metal ions that can be oxidized, as compared to reconstituted iron oxide, is probably due to the formation of hollow nanoparticles.⁵⁸ Further studies of ferritin mediated cobalt oxide mineralization have shown that when the substrate is added in a controlled fashion, Co₃O₄ nanoparticles are formed.⁵⁸

When nickel and chromium ions are exposed to apoferritin in the presence of carbonate, the respective metal oxyhydroxides are formed, and no core formation is observed in the presence of degassed solvents.⁵⁹ The carbonate ions in the solution are proposed to expedite the formation of the metal oxyhydroxide cores. In the case of nickel, the carbonate ions are thought to act as ligands, decomposing into CO₂ and OH⁻ in the ferritin cavity. The presence of OH⁻ would raise the pH, promoting biomineralization. Optimal reaction conditions for nickel core formation were studied extensively. Initially, bulk precipitation was observed in the presence of the protein; however, the addition of ammonia ions to the nickel ferritin reaction reduced the bulk precipitation. The authors propose that the ammonia ions coordinate with the excess nickel, preventing the precipitation of nickel oxyhydroxide in solution. Loadings of 3,300, 5,000, 8,300, and 16,000 nickel atoms per ferritin were studied, as well as pHs of 8.48, 8.58, and 8.73. Nickel oxyhydroxide cores were identified using transmission electron microscopy (TEM) and energy dispersion spectrometry (EDS). The most effective nickel core formation occurred at a pH of 8.58 with 5000 iron atoms per ferritin. However, when the nickel loaded ferritin is exposed to water, the nickel core resolubilizes. Different nickel anions (sulfate, chloride, and nitrate) were evaluated to determine if anions affected the core formation or solubility; however, no significant difference was observed. Unlike nickel, bulk precipitation did not occur with chromium in the presence of ferritin, indicating an increase in solubility due to the ammonia ions. However, the chromium oxyhydroxide synthesis did require carbonate ions in the solution. While the chromium core formed at a pH of 7.38, variable concentrations were

not investigated, as a chromium oxyhydroxide core was formed within ferritin at ambient conditions.⁵⁹

Applications of Ferritin Metal Oxide Nanocomposites

The controlled sizes of ferritin nanoparticles are advantageous for many applications such as carbon nanotube synthesis or a variety of catalytic functions. The ferrihydrite core of ferritin has been shown to catalytically reduce Cr(VI) as well as Cu(II).^{60,61} Spatially arrayed conductive iron oxide is being studied for electronic nanodevices.⁶²⁻⁶⁵ The defined size of the metal oxyhydroxide core of ferritin is advantageous for studying the physical and electronic properties of carbon nanotubes. Ferritin nanoparticles can be used as catalysts, semiconductors, or templating agents.

Chromium Reduction

Cr(VI), an environmental hazard, is highly toxic while Cr(III) is relatively harmless.⁶⁶ The ferrihydrite core of ferritin reduced Cr(VI) to Cr(III) in the presence of light, while apoferritin was ineffective.⁶⁰ Ferritin was shown to reduce 20 times more Cr(VI) than Fe located in the protein, indicating that the reduction is catalytic, not stoichiometric. Douglas and coworkers propose that the ferric oxyhydroxide in the protein shell functions as a band-gap semiconductor. An electron-hole pair, formed by exciting valence band electrons into the conduction band, participates in the redox reaction of Cr(VI). There are two potential mechanisms that have been proposed for the Cr(VI) reduction. The first mechanism is a photo-induced electron transfer from the ferrihydrite core through the protein shell to the Cr(VI) acceptor. The second is electron

transfer via direct contact of Cr(VI) with the iron oxyhydroxide core. XPS analysis of the protein after exposure to chromium indicates that Fe(O)OH is still intact in the protein shell and Cr(III) is present in the protein cage. To test for Cr(III) uptake, ferritin was suspended in a Cr(III) solution. XPS analysis shows that there is no Cr(III) present in the protein shell, indicating that Cr(III) from the reduction reaction is produced in the interior of the protein supporting the direct contact mechanism. Even though there is evidence of Cr(III) in the protein shell, the majority of Cr(III) is found in solution, supporting the first mechanism. However, from the present experiments it cannot be determined if the Cr(VI) reduction primarily occurs in the solution. The photoreduction rate of Cr(VI) varies with the loading factor of the ferritin. With higher loadings (3000 iron atoms), the rate of chromium reduction increases by 25 and 55% as compared to the loading of 500 and 100, respectively. Douglas and coworkers propose that electron transfer through the protein shell only occurs at interfaces where the iron oxide core is in contact with the protein. Ferritin loaded with 1000 and 3000 iron atoms may have similar protein coverage, resulting in similar rates. With loadings of 500 and 100 atoms, less protein area is covered, resulting in a decrease in the rate of Cr(VI) reduction. Therefore, both mechanisms are thought to participate in the reduction of Cr(VI).⁶⁰

Copper Reduction

The ferrihydrite core of ferritin not only reduces Cr(VI), but also photocatalytically reduces aqueous Cu(II) in the presence of a reductant such as citrate or tartrate, to form copper metal colloids.⁶¹ As expected, the control reactions of Cu(II) with unmineralized ferritin, aqueous Fe(II) with Cu(II), and ferritin mediated reactions in

the dark did not yield copper metal colloids. The copper metal was identified by selected area diffraction patterns (SADP), which showed characteristic face-centered cubic copper metal d-spacings. The ratio of Cu to the mineralized iron core determines the size of the Cu nanoparticles produced. As the concentration of the soluble copper increases, the particle size of copper metal also increases. The size of the metal nanoparticles as determined from TEM images are 4.5 ± 0.8 nm, 9.7 ± 4.2 nm, 12.7 ± 3.6 nm, and 31.4 ± 10.1 nm for Cu(II) loadings of 250, 500, 1000, and 2500, respectively. Unlike the Cr(VI) reduction rates, the reduction rate of Cu(II) increases at smaller iron loadings. Reactions of 2 mg/mL ferritin with an iron loading of 500 and 1 mg/mL ferritin with an iron loading of 1000 atoms were studied. The increase in catalytic activity for the lower loading is attributed to an increased amount of ferritin molecules present, leading to a greater iron surface area for reductions to take place. Since the size and charge of Cu(II) is similar to Fe(II), uptake into the protein is hypothesized to occur by the same hydrophilic channels as iron. Additionally, the kinetic plot of copper formation is sigmoidal, similar to kinetic plots for iron oxyhydroxide formation. In the case of iron oxidation, mineral nucleation is followed by the rapid autocatalysis on the growing mineral surface. In Cu nanoparticle formation, the sigmoidal curve implies a slow nucleation step and fast particle growth.⁶¹ However, since some Cu metal nanoparticles produced are larger than the interior of ferritin either the growth of the copper colloids expands the protein or there is nucleation on the exterior of the protein. Unlike the Cr(VI) reduction, TEM images negatively stained with uranyl acid show that the larger nanoparticles are surrounded by a protein membrane, indicating the Cu colloids are formed in the interior of the protein.⁶¹ The fact that ferritin encapsulated iron oxide

acts as a catalyst while the bulk precipitate does not is quite interesting and as such the catalytic properties of other metal oxide ferritin cores are currently being investigated.

Iron Oxide Nanodot Arrays

Ferritin has been used to construct nanodot arrays of iron oxide for potential use in quantum electronic devices.⁶²⁻⁶⁴ Previously it has been shown that thin films of ferritin nanoparticles are formed at an air-water interface in the presence of poly-1-benzyl-L histidine.⁶⁷ Iron-loaded ferritin at the air-water surface interface was attached to a silicon wafer utilizing hydrophobic interactions (**Figure 4 A**).⁶² The protein shell

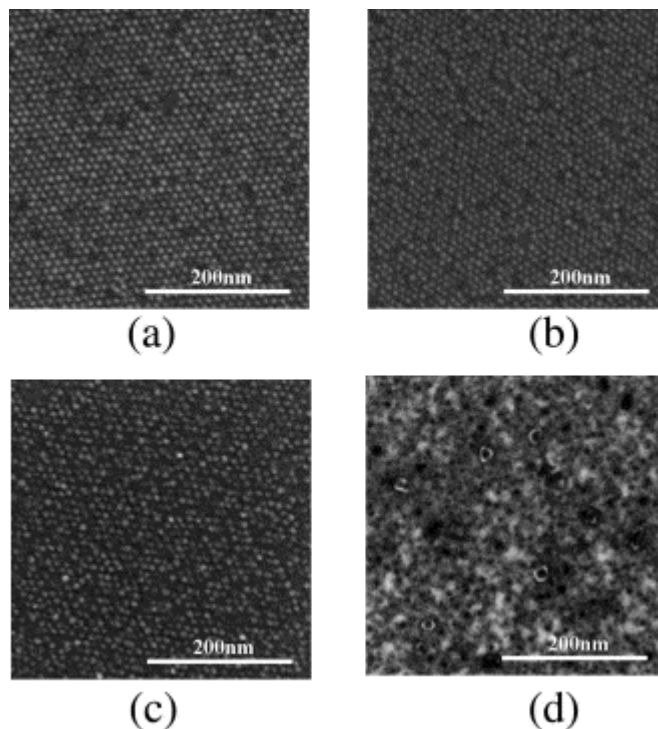


Figure 4: SEM of spatially arrayed ferritin iron oxide nanoparticles A) as deposited B) with heat treatment at 300°C C) with heat treatments at 500°C D) with heat treatments at 700°C. ⁶²

was removed under nitrogen at variable temperatures, depositing spatially arrayed iron oxide cores that were roughly 6 nm in diameter according to AFM images. Fourier transform infrared (FTIR) spectrophotometry confirmed the removal of the protein shell by monitoring the disappearance of the amide peptide bond signal that is associated with the protein structure. The protein shell was partially removed at 300°C (**Figure 4 B**), and at 500°C, the protein shell was completely removed while the iron oxide nanoparticle arrangement was not disturbed (**Figure 4 C**). At 700°C, the protein shell was removed, but the discrete iron cores were disrupted. This led to some iron oxide aggregates up to 20 nm in diameter (**Figure 4 D**). This data suggested an optimum temperature of 500°C for protein removal. XRD analysis of the iron oxide cores deposited after protein removal show that the crystal structure of iron oxide is wustite (FeO). Current-voltage curves of the FeO deposits indicate conductivity; therefore, the array of nanoparticles obtained from ferritin could be used to construct electronic nanodevices.⁶²

Size Control of Arrayed Iron Oxide Core

Size control of the iron oxyhydroxide precipitate can be controlled after the deposition of the ferritin core onto a silicon substrate. This control is typically achieved through variation of the Fe (II) loading or via the usage of an iron chelator.^{63,65} Douglas and coworkers studied protein loadings of 100 and 2500 atoms of iron per ferritin molecule.⁶⁵ The mineralized ferritin nanoparticles with the different loadings were deposited on a silica substrate. The protein shell was removed by heating the mineralized ferritin to 388 K, leaving discrete nanoparticles of ferrihydrite spatially deposited on the silica substrate. The removal of the protein shell was confirmed by

monitoring the disappearance of the N 1s and C 1s XPS peaks. The ferritin loaded with 100 atoms of iron deposited iron oxyhydroxide nanoparticles with an average diameter of 2.5 ± 0.7 nm, as shown by atomic force microscopy (AFM). However, when 2500 atoms of iron were loaded into ferritin, the average particle size deposited was 6.0 ± 1.5 nm.⁶⁵ The size difference is attributed to less iron available to accumulate in the protein, forming the core.

The size of ferritin nanoparticles can also be controlled by employing iron chelators.⁶³ Ferritin was deposited on a silicon substrate utilizing the electrostatic interaction between negatively charged ferritin and positively charged 3-aminopropyltrimethoxysilane coated silicon surfaces. Nitrolotriacetic acid (NTA), an iron chelator, was applied to the array for variable times. NTA is a small molecule that passes through iron channels, reacting with Fe(III) to form NTA-Fe(III) or bis(NTA-Fe(III)) complexes.⁶⁸ As the immersion time increases, the core size decreases.⁶³ Untreated ferritin cores were 4.8 ± 1.0 nm in diameter, while cores exposed to NTA for 20 minutes were 1.3 ± 0.5 nm in diameter, according to AFM measurements. After 30 minutes, almost all ferritin cores were dissolved or below the 0.25 nm detection limit.⁶³ The ability to control the size of the nanoparticles deposited is very advantageous for SWNT synthesis, as a relationship between the size of the template and the diameter of the nanotube can be determined.

Ferritin Deposited Cobalt Oxide Nanodot Arrays

Arrays of ferritin deposited cobalt oxide nanoparticles have been used as a floating nanodot array for a metal-oxide-semiconductor (MOS) field effect transistor.⁶⁴

Co₃O₄ filled ferritin was deposited on a silicon substrate using the electrostatic interactions of the negative ferritin and positive coated silica substrate. The protein shell was removed by a UV/ozone treatment for 60 minutes at 115°C. SEM images show spatially arranged Co cores approximately 7 nm in diameter. The cores were buried in 17 nm of control oxide and aluminum was deposited as the gate electrode. The MOS device was annealed to 450°C for one hour. TEM images of the device cross-section show intact Co-cores, indicating the particles are strong enough to undergo the device fabrication process. When an electric field is applied to the Co core MOS, a C-V hysteresis curve is evident and current-drain voltage curves also show a hysteresis shift. The authors attribute these shifts to electron-hole confinement in the ferritin deposited cores. Additionally, the shifts indicate that the core functions as the storage node of a floating nanodot gate MOS device.⁶⁴

Carbon Nanotube Synthesis

The biomimetically synthesized iron oxide and cobalt oxide cores of ferritin have been used as a synthetic template for the synthesis of multiwall carbon nanotubes (MWNT) and single wall carbon nanotubes (SWNT).⁶⁹⁻⁷¹ To obtain nanotubes with monodisperse diameters, monodisperse nanoparticles need to be distributed on a substrate. Previous methods for synthesizing MWNT or SWNT precursors such as impregnation methods and liquid phase methods form templates where the size of the nanoparticles are difficult to determine because the nanoparticles are intermingled with a powdery support material.⁷²⁻⁷⁸ These synthetic methods result in a broad distribution of diameter size for the nanotubes, making an investigation of the electronic properties of

the nanotubes difficult as the electronic properties are a result of the chirality and diameter of the tube. In contrast, using ferritin nanoparticles as a template for MWNT or SWNT synthesis is advantageous because the size of the template is discrete and known *a priori*. Therefore, a relationship between the size of the template and the size of the nanotube produced can be determined.

By using ferritin deposited iron oxide as a template for SWNT synthesis, Li and coworkers have shown that the diameter of SWNT is directly related to the size of the nanoparticle template.⁷⁰ By varying the iron loading of ferritin, two sizes of iron oxide nanoparticles were synthesized. Ferritin was deposited on a silica substrate and the protein was removed by heating to 800°C, leaving spatially arrayed iron oxide particles. Ferritin loaded with 200 and 1000 atoms of iron deposited iron oxide cores that were 1.9 ± 0.3 nm and 3.7 ± 1.1 nm, respectively. SWNT were synthesized by chemical vapor deposition (CVD) where the substrate is heated to 900°C in the presence of methane for 5 minutes. The SWNTs grown from the iron oxide nanoparticles, as shown by TEM images, range in length from 0.5 μ m to 20 μ m. The iron oxide cores with diameters of 1.9 nm and 3.7 nm formed SWNTs with diameters of 1.5 ± 0.4 nm and 3.0 ± 0.9 nm, respectively. The majority of the SWNTs formed appear to be straight; however, a few are curved due to the flexibility of the nanotubes. It is also worth mentioning that a few circular SWNTs known as “crop circles” with a diameter of approximately 200 nm were seen (**Figure 5 A**). Crop circles are not a completely new phenomenon as they have been previously witnessed in laser ablation SWNT synthesis and when SWNT are sonicated.^{79,80} Kinks were seen in a few nanotubes, which can either be attributed to the mechanical forces on the nanotube as it grows along the substrate or a defect in the

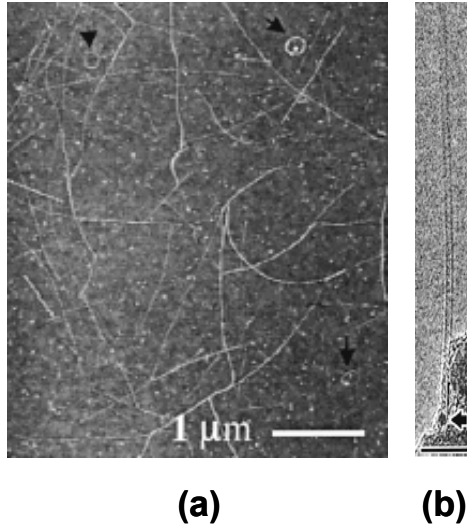


Figure 5: A) AFM topography image of SWNT synthesized with ferritin iron oxide nanoparticles as a template B) TEM image of SWNT synthesized from ferritin iron oxide nanoparticles, arrow pointing to iron oxide nanoparticle, scale bar 10 nm.⁷⁰

nanotube structure. TEM images show that most SWNT have an iron oxide nanoparticle attached to one end (**Figure 5 B**) with the other end being closed.⁷⁰ The ability to see the discrete iron oxide template particles has allowed for conclusions to be drawn about SWNT formation. The fact that single nanotubes have nanoparticles attached supports the base-growth models, in which the nanotube grows out from a nanoparticle with a closed end (**Figure 6**).^{75,76,81} Unfortunately, only a small portion of the nanoparticles grew SWNT. In both size cases, smaller nanoparticles were more likely to grow SWNT. Larger particles, 7 nm in diameter, did not display any SWNT growth. It has been proposed that the size dependence of SWNT growth due to the ability of smaller nanoparticles to be supersaturated with carbon, allowing for growth.⁷⁰

In addition to iron oxide, cobalt oxide was explored as a catalyst for SWNT.⁶⁹ Cobalt oxide nanoparticles were deposited on silica pillar substrates by spin coating. AFM revealed that the average diameter of the cobalt oxyhydroxide encapsulated in ferritin was 6.4 ± 1.0 nm. After calcination to remove the protein shell, the average size of the cobalt oxyhydroxide core was 4.7 ± 0.7 nm. Thermal chemical vapor deposition in the presence of methane under a pressure of 500 Torr at variable temperatures was used to grow the SWNTs. At 900°C, the size of the SWNTs was 1.17 ± 0.27 nm, while at 1000°C the size of the SWNTs was 1.53 ± 0.37 nm. At higher temperatures the cobalt

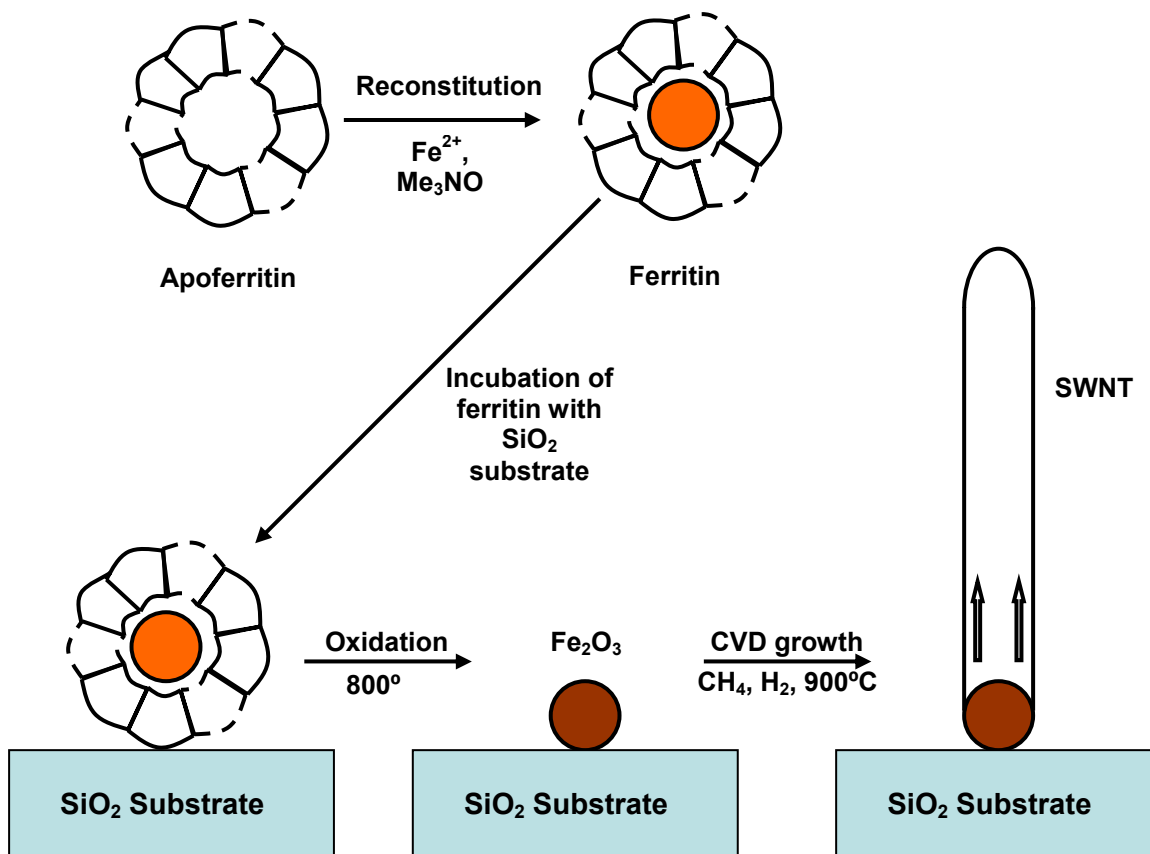


Figure 6: Schematic of SWNT growth utilizing a ferritin deposited iron oxide nanoparticle.

particles aggregate, leading to a larger diameter SWNT. Under the same conditions, iron oxide nanoparticles severely aggregated.⁶⁹ Interestingly, the size of the cobalt oxide templated SWNTs are much smaller than the size of the nanoparticle, while the iron oxide templated SWNT size is very similar to the nanoparticle template. Preliminary data suggests that the directionality of SWNT growth could be due to the site on the substrate where the cobalt oxide nanoparticles are located.⁶⁹ Nanotubes formed from cobalt oxide nanoparticles located on the side or edge of a pillar grew parallel to the substrate. Nanoparticles located on the top of the pillars grew SWNTs with an upward direction until they fell on the substrate, resulting in curved SWNTs.⁶⁹ The use of biomimetically synthesized iron oxide and cobalt oxide has allowed a relationship between the size of the nanoparticle template and the size of the SWNT to be examined.

Control of the direction of nanotube growth has been explored using ferritin deposited iron oxide as a template.⁸² The control of the direction of nanotube growth is necessary for applications such as nanotube sensor arrays and integrated circuits. Ferritin was deposited on a-plane, m-plane, r-plane, and c-plane sapphire substrates. SWNT were grown using CVD at 900°C for 10 minutes in the presence of methane, ethane, and hydrogen. A-plane and r-plane sapphire substrates appeared to direct the direction of SWNT growth, with m-plane and c-plane yielding randomly oriented nanotubes. Additionally, nanotubes did not grow in the direction of gas flow and AFM studies of the sapphire substrates show that the surface morphology of the substrate did not affect the directionality of growth. SWNTs, approximately 10 μm with an average diameter of 1.34 ± 0.30 nm, grew with the [001] direction of the a-plane sapphire with an average spacing of 200 nm. Interestingly, when Fe films are deposited on a-plane

sapphire substrates, the SWNTs produced have a random orientation. Therefore, the discrete iron oxide nanoparticles are believed to participate in the control of directionality.⁸²

Mineralization by bacteria, enzymes and viruses

Dps protein from *Listeria innocua* and *Bacillus subtilis*

A 250 kD ferritin-like protein with a 3:2 tetrahedral symmetry has been isolated from the bacteria *Listeria innocua*. The protein contains twelve polypeptides that assemble into a four helix bundle.^{83,84} The protein from *L. innocua* has several structural similarities to the iron storage protein ferritin. The interior is electrostatically negative due to an abundance of Glu and Asp residues, analogous to the L chain of ferritin. Also, there are three-fold hydrophilic pores that are lined with negatively charged amino acid residues, which incorporate the iron into the protein cage.⁸⁵ Recently, Su and coworkers have shown that *L. innocua* ferritin also has several structural and functional similarities to Dps (DNA protection during starvation) proteins.⁸⁶ The amino acid sequence of the protein resembles the amino acids sequence of the Dps protein from *Escherichia coli*, which also produces an iron oxyhydroxide core.^{84,87} The *L. innocua* Dps protein protects the DNA of the organism by using excess hydrogen peroxide to oxidize Fe(II), forming the iron oxyhydroxide core.⁸⁸ The iron core nucleation site residues are composed of two symmetry related protein subunits, one that provides His-31, His-43, and Asp-47. The other subunit provides Asp-58 and Glu-62.⁸⁵ *L. innocua* Dps protein can oxidize and store up to 500 atoms of iron.⁸³ To date, the composition of the iron oxyhydroxide

core has not been identified. Similar to mammalian ferritin, the shape and size of the iron oxide particles produced are dictated by the interior of the protein cage. In contrast to mammalian ferritin, *L. innocua* ferritin has an interior diameter of 6 nm and an exterior diameter of 9 nm.^{83,85} Under physiological conditions, a ferric oxyhydroxide core is formed in the interior of the apoferritin when an iron precursor is introduced.⁸⁹

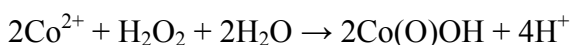
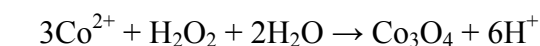
When non-physiological conditions are employed, superparamagnetic maghemite, $\gamma\text{-Fe}_2\text{O}_3$, nanoparticles are produced with a diameter of 4.1 ± 1.1 nm as shown by TEM images.⁶⁵ With a pH of 8.5 at 65°C, Fe^{2+} ions were introduced into a solution containing *L. innocua* protein in the presence of hydrogen peroxide, which acts as an oxidant. The final loading was 400 atoms of iron per protein. As expected, control reactions lead to bulk precipitation. The H^+ produced from the ensuing reaction was monitored, indicating that the stoichiometry for the overall reaction is as follows:



TEM images stained with uranyl acetate show that the protein shell encapsulates the nanoparticle, demonstrating that the reaction occurs in the interior of the protein. The mineral isolated from the protein was identified by powder diffraction as either the cubic iron oxide phase $\gamma\text{-Fe}_2\text{O}_3$ or Fe_3O_4 . Peak overlap in the spectra made it impossible to distinguish between the iron oxide species. Both the mineralized protein and unmineralized protein eluted at the same time in size exclusion chromatography studies signifying that the protein is unchanged and intact after the reaction. Also, dynamic light scattering (DLS) indicates that the size of the protein shell remains unchanged after addition of the iron atoms. The hydrodynamic diameter of the protein before the addition of iron atoms is 9.2 ± 0.4 nm, and after the addition of iron oxide, the particle

size is 9.3 ± 0.2 nm.⁶⁵ Douglas and coworkers have successfully synthesized magnetic iron oxide in the core of *L. innocua*, which, similar to ferritin iron oxide cores, could potentially lead to conductive spatial arrays of nanoparticles for use in electronic nanodevices.

In addition to iron oxide, alternate cobalt substrates have been introduced into the Dps protein from *L. innocua*, forming cobalt oxide and cobalt oxyhydroxide nanoparticles.⁹⁰ At pH 8.5 in the presence of H₂O₂, the Co(II) precursor is oxidized forming cobalt oxyhydroxide at low temperatures (23°C), while higher temperatures (65°C) result in Co₃O₄. DLS data indicates that the hydrodynamic radius of the protein is 9.2 ± 0.4 nm and there is no change in the size at 65°C. No bulk precipitation was observed in the mineralization reactions, indicating the cobalt oxide nucleation occurred in the protein shell. Titration of the H⁺ generated in the reactions lead to the determination of the overall stoichiometry of the two reactions at 65°C and 25°C, respectively, which are as follows:



In concurrence with the titration data, UV-Vis spectroscopy indicated that the rate of the reaction was limited by the amount of Co(II) added. Uranyl acetate stained TEM images show that the protein cage is intact around the metal oxide cores at both temperatures. As expected, the SADP indicates that the nanoparticles synthesized at the higher temperature are more crystalline. Additionally, the d-spacings from SADP indicate that Co₃O₄ is in the spinel phase. SADP from the cobalt oxyhydroxide nanoparticles were not observed, indicating that the nanoparticles were mostly amorphous. The average




diameter of the Co_3O_4 nanoparticles was determined from TEM images to be 4.34 ± 0.55 nm, however the size of the cobalt oxyhydroxide nanoparticles was unable to be determined. Similar to the iron oxide nanoparticle synthesis, DLS shows that the protein size remains unchanged after exposure to the cobalt ions. Co-migration of mineralized and unmineralized protein in gel electrophoresis determined that the electrostatic character of the protein shell remained unchanged after mineralization, supporting the hypothesis that mineralization occurs in the interior of the protein shell.⁹⁰

Not only has cobalt oxide been synthesized in the interior of *L. innocua*, it has also been deposited on a silica substrate similar to ferritin nanoparticles.⁶⁵ By using the previously discussed high temperature synthesis, *L. innocua* loaded with cobalt oxide was distributed on a silica substrate.⁹⁰ The protein shell was removed with heat, leaving spatially arranged nanoparticles.⁹⁰ Additionally, Co_3O_4 mineralized from *L. innocua* has been shown to display lower Néel temperature (15 ± 2 K), as compared to the bulk oxide (40 K).^{91,92} *L. innocua*, like ferritin, has the ability to mineralize non-natural metal oxides of a discrete size having the potential for electronic and magnetic applications.

The constrained environment of the Dps protein from *Bacillus subtilis* produces nanoparticles that have been used as a catalyst in SWNT synthesis.⁹³ DLS of the protein shows that the protein cage is 9.0 ± 1.1 nm in diameter. Additionally, TEM images reveal that the protein has an outer diameter of 9 nm and an inner diameter of approximately 4 nm. Each Dps protein was loaded with approximately 180 iron atoms, and deposited on a silica substrate. The protein shell was removed by heating at 900°C for 30 minutes, resulting in nanoparticles approximately 1.05 ± 0.11 nm in diameter. Nanotube growth was achieved using CVD with a 1:1 mixture of methane and hydrogen

gas at 900°C for 10 minutes. Approximately 20% of the iron oxide nanoparticles resulted in nanotubes ranging in size from 20 nm to 1 μm, according to SEM images.

Table 2: Biologically Derived Iron Catalyst for Nanotube Formation

			
Protein	Loaded Dps ⁹³	Partially Loaded Ferritin ⁷⁰	Loaded Ferritin ⁷¹
Fe ²⁺ per protein	182	200 or 1000	3000
Nanotube type	SWNT	SWNT	MWNT
Nanotube Diameter (nm)	1.0 ± 0.1	1.5 ± 0.4 or 3.0 ± 0.9	5.2 ± 0.6

Crop circles and curved morphologies were observed, probably due to the flexibility of the nanotubes. In contrast to ferritin templated nanotubes, the diameters of the nanotubes were quite monodisperse with an average diameter of 1.0 ± 0.1 nm (**Table 2**).

The monodispersity of the SWNTs is attributed to the iron saturation of the protein, resulting in monodisperse nanoparticles.

Lumazine Synthase

Lumazine synthase, an enzyme present in bacteria and fungi involved in the biosynthetic pathway of riboflavin, has also been known to form iron oxide nanoparticles.⁹⁴ Crystal structure studies confirm that lumazine synthase is a 1 MD enzyme with an outer diameter of 15 nm and an interior diameter of 8 nm.^{95,96} Sixty β subunits form a hollow icosahedral (T=1) enzyme capsid with an α trimer located in the core.⁹⁵ The trimer contains a region of three glutamic acids similar to the active site for iron oxidation in ferritin.⁹⁶ In certain buffers such as Tris-HCl, a 30 nm form of the enzyme is present.⁹⁷ The 30 nm form is an icosahedral arrangement of 180 to 240 β subunits that lack alpha subunits.

In vivo, lumazine synthase does not produce iron oxide. However, when aqueous Fe(II) is added to the enzyme solution, iron oxide is produced in the interior.⁹⁸ Iron uptake is hypothesized to occur through hydrophilic channels containing glutamic acid located along the ten threefold axes and the six fivefold pentamer axis of the enzyme.⁹⁶ Shenton and coworkers have studied a variety of iron loadings in lumazine synthase capsids.⁹⁸ The lumazine synthase capsids were prepared in 4-morpholine-ethanesulfonic acid (MES) buffer at pH 6.5. A TEM image stained with uranyl acetate shows that the enzyme was stable and only 5% of the protein was in the 30 nm form. Loadings of 300, 1000, 1500, and 2000 Fe(II) atoms per enzyme were examined. As expected, bulk precipitation of iron oxide occurred in the control experiments, while none was observed in the experiments with lumazine synthase. At 300 ions of atoms per capsid, the SAPD indicates that the iron(III) oxide mineral lepidocrocite (γ -FeOOH) is present, however it is not very crystalline. As the loadings increase, the lepidocrocite

appears to be more crystalline.⁹⁸ The average diameter of the particles produced from the lumazine synthase loaded with 1000 atoms of iron was 13.4 ± 2.0 nm. Uranyl acetate stained TEM images of the capsids after mineralization showed that 30% of the capsids were 15 nm in diameter and 70% of the capsids were 30 nm in diameter, indicating that the larger diameter capsids are more stable in the presence of Fe(III).⁹⁸ To date, alternate substrates or arrays have not been investigated.

Cowpea Chlorotic Mottle Virus

Virus capsids such as the cowpea chlorotic mottle virus (CCMV) have also been utilized for metal oxide nanoparticle formation. CCMV has a protein shell with an exterior diameter of 28 nm and an interior diameter ranging from 18-24 nm.⁹⁹ There are 180 coat protein subunits that assemble into an icosahedral symmetry. In vitro, these purified coat protein subunits can self assemble into the same arrangement as the native virus.¹⁰⁰ Each coat protein contains 9 basic amino acids, lysine and arginine, which provide the interior of the virion with a positive charge.¹⁰¹ In the native environment, the positive charge is used to assemble negatively charged RNA; however, when anionic metal oxides are introduced, the positively charged area becomes a site for nucleation and crystallization.¹⁰² CCMV has a pH dependant gating mechanism which has been utilized to crystallize nanoparticles.¹⁰³ When the pH is greater than 6.5, the viral capsid size increases by 10% allowing negative ions to enter the interior through 60 pores located at the subunit interface. When the pH is below 6.5, the viral capsid retracts and there is no uptake of ions. The polyoxometalate species of molybdate³², paratungstate¹⁰³, and decavandate¹⁰³ have been formed in the interior of CCMV.

The viral cage of CCMV has been engineered by Douglas and coworkers to produce iron oxide.¹⁰² Genetic analysis of CCMV determined that the N-termini of the coat proteins are not required for self assembly, therefore, they may be modified to change the electrostatics of the interior of the virion cage without altering the overall cage structure. The electrostatic character of the cage was changed from positive to negative by changing the basic residues located at the N termini to glutamic acid. At pH 6.5 Fe(II) ions were added to the engineered virion cages, mineralizing iron oxide nanoparticles in the interior of the virion. In contrast, reactions lacking the virion, as well as reactions containing the unmodified virion, resulted in bulk precipitation.¹⁰²

Uranyl acetate TEM images revealed that the virion protein surrounded the nanoparticles and appeared intact.¹⁰² To determine the spatial location of the mineral core in relation to the protein, electron energy loss spectra identified the locations of O, C, N, and Fe. Overlays of the Fe and N spectra confirmed that the protein shell surrounds the metal oxide core. The primary mineralization (2000 atoms per virion) produced 8.2 ± 1.6 nm lepidocrocite, (γ -FeOOH) particles. High resolution TEM, as well as powder X-ray diffraction (XRD) spectra, confirmed the identity of the iron oxide mineral. High resolution TEM images indicate that the nanoparticles in the virion are single crystals. When a second mineralization was performed (6000 total atoms of iron per virion), the lepidocrocite particles increased in size to 24.0 ± 3.5 nm. The crystals from the first mineralization are proposed to act as a nucleation site for autocatalytic iron oxide mineralization. The structure of the protein cage after mineralization was investigated by gel filtration chromatography and gel electrophoresis. The native CCMV, the engineered CCMV, and the mineralized engineered CCMV co-eluted,

indicating the mineral is formed in the interior of the protein. In the gel electrophoresis, all three co-migrated, indicating the electrostatic character of the exterior protein shell was not changed with mineralization.¹⁰²

Template Directed Synthesis of Metal Oxide Nanocomposites

In addition to constrained environments for metal oxide synthesis, Nature frequently uses organic templates to form inorganic materials. For example, collagen, a macromolecule with a high percentage of glycine, contains spaced notches where hydroxyapatite crystallization occurs.¹⁴ Also, amelogenins, proteins that facilitate hydroxyapatite nucleation, form tooth enamel.¹⁰⁴ Proteins in diatoms, radiolarian, and sponges produce silica that serves as an exoskeleton.¹⁸ By mimicking the chemistry of the macromolecules that cause nucleation, metal oxides can be synthesized from organic templates. Proteins, peptides, polymers, and dendrimers are effective biomimetic templates for metal oxide mineralization. The mild conditions of peptide and dendrimer mediated silica synthesis allows for the encapsulation of biologically relevant enzymes as well as quantum dots and gold nanoparticles.¹⁰⁵ The secondary structure of poly-L-lysine (PLL) have been shown to control the pore size of silica.¹⁰⁶ As the properties of nanoparticles vary based upon size, polymer templates have been used to control the size, as well as the morphology of silica nanoparticles.¹⁰⁷⁻¹⁰⁹ Many of the templates can be patterned or printed, leading to 2D and 3D metal oxide architectures.¹¹⁰

Peptide and Protein Templates

Peptides and proteins are templates that have been extensively used throughout biology for the precise synthesis of inorganic solids. Additionally, proteins and peptides that do not form metal oxides naturally have been utilized as biomineralization templates. For example, proteins from the fungus *Fusarium oxysporum* have been identified as nucleation templates for a variety of metal oxides.¹¹¹⁻¹¹³ Moreover, peptide display libraries have been used to identify peptides not naturally found in biology that facilitate the template directed synthesis of metal oxides.¹¹⁴ The versatility of several proteins and peptides that synthesize metal oxides in nature have also been studied. Certain sponge spicules proteins, termed silicateins, from sponge spicules have successfully mineralized many metal oxides.¹¹⁵⁻¹¹⁸ Additionally, diatoms form reproducible silica nanostructures at low temperatures using a combination of proteins and polymers as a template.^{24,119} Peptides derived from the gene of the *C. fusiformis* diatom have been used in the synthesis of metal oxide nanoparticles such as silica and titanium dioxide.^{120,121} Peptides have not only been used to synthesize metal oxides, they have been used to construct nanopatterns of silica and to encapsulate enzymes.¹²²⁻¹²⁴

Proteins from *Fusarium oxysporum*

The fungus *Fusarium oxysporum* causes vascular wilt on several plant species by clogging the vessels with microconidia, resulting in severe water stress.¹²⁵ Sastry and coworkers have extensively studied the ability of the proteins secreted by the fungus to form metal oxides such as zirconia, silica, titanium dioxide and magnetite.¹¹¹⁻¹¹³ When exposed to the precursor K_2ZrF_6 , nanoparticles of zirconia (ZrO_2) form extracellularly

within 24 hours. Nanoparticles of ZrO_2 are being investigated for piezoelectric and dielectric materials because of their enhanced optical and electronic properties as compared to bulk zirconia.¹²⁶ Other fungi such as *Trichothecium* sp., *Curvularia lunata*, *Collectotrichum gloeosporioides*, *Phomopsis* sp., and *Apergillus niger* did not form zirconia nanoparticles when exposed to K_2ZrF_6 , indicating that sugars or proteins common to fungi do not promiscuously mineralize the substrate.¹¹¹ SADP analysis of the zirconia revealed d-spacings of 3.69, 3.63, 3.16, 2.61, 2.32, and 1.34 Å indicative of the monoclinic phase. TEM images were used to determine an average nanoparticle size of 7.3 ± 2.0 nm. In concurrence with the SADP, XRD patterns of the as-synthesized zirconia indicate the monoclinic phase is present. When the sample is calcined at $600^\circ C$, the crystalline nature of the monoclinic phase improves and the tetragonal phase is present. *F. oxysporum* protein secretion was studied in the presence and absence of K_2ZrF_6 . Gel electrophoresis of the proteins revealed that two extra proteins, with molecular weights of 24 and 28 kDa, were secreted in the presence of K_2ZrF_6 .¹¹¹ The extra proteins present when K_2ZrF_6 is introduced are cationic, as identified by ion exchange chromatography. The proteins are proposed to concentrate the negative precursor, leading to biomineralization. To date, the amino acid sequence and structure of the two peptides have not been determined.

In addition to ZrO_2 , silica and titanium dioxide (TiO_2) were also formed when either K_2SiF_6 or K_2TiF_6 were introduced into a solution containing *F. oxysporum*.¹¹² Within 24 hours, spherical nanoparticles formed with a diameter of 9.8 ± 0.2 nm and 10.2 ± 0.1 nm for silica and TiO_2 , respectively. As a control, several other genera of fungus such as *Curvularia lunata*, *Collectotrichum gloeosporioides*, *Phomopsis* sp., and

Aspergillus niger were exposed to the precursors, but none formed nanoparticles. SADP of the silica nanoparticles show characteristic d-spacings of 3.24, 3.00, 2.50, and 2.09 Å indicating the tridynite polymorph of silica. SADP of the TiO₂ nanoparticles reveal d-spacings of 3.53, 2.90, 2.47, and 2.34 Å, consistent with the brookite phase of TiO₂. In addition to the SADPs, XRD analysis confirmed the identity of the respective metal oxides. FTIR spectra for both metal oxides revealed characteristic amide I and II bands, indicating that proteins from the fungus are associated with the nanoparticles. The proteins produced by the fungus in the presence and absence of the metal oxide substrates were studied using SDS-PAGE gels. Similar to ZrO₂ formation, two proteins with molecular weights of 21 and 24 kD are secreted by the fungus when exposed to the metal oxide precursors. Since the amino acids sequence of the proteins responsible for SiO₂ and TiO₂ nanoparticle formation are similar to the proteins secreted when ZrO₂ nanoparticles form, Sastry and coworker propose that comparable mechanisms are responsible for the biomineralization. The slight difference in the molecular weights between the proteins secreted in response to ZrO₂ precursor and the proteins secreted in response to K₂SiF₆ or K₂TiF₆ could be due to different levels of post-translational modifications of the proteins.¹¹²

The proteins of *F. oxysporum* have been shown to reduce potassium iron thiocyanate salts in approximately 24 hours, forming nanoparticles ranging in size from 20 to 50 nm.¹¹³ SADP analysis indicates the particles are crystalline in nature and XRD confirms that the crystalline phases are predominately Fe₃O₄ and a small percentage of γ-Fe₂O₃. Amide I and II bands are seen in the IR spectra indicating proteins are associated with the nanoparticles, either by incorporation into the nanoparticulate structure or

absorption on the surface. Gel electrophoresis of the fungus extract exposed to the iron precursor and unexposed fungus indicates that an extra 55 kD protein is excreted by the iron exposed fungus. This protein may be responsible for the formation of the nanoparticles as it exhibits hydrolytic activity when exposed to the precursor.¹¹³ Further studies need to be conducted to isolate the protein structure and determine the active amino acids. Since the molecular weight of the proteins that reduce K_2ZrF_6 are vastly different, there is a good possibility that a different mechanism of reduction occurs with each substrate.

Peptide Display Libraries

Combinatorial peptide libraries offer a selective approach to identifying peptides that can bind or mineralize inorganic materials.¹²⁷ One feature of a combinatorial peptide library is that the amino acid sequence is not known *a priori*, rather the focus is on identifying metal binding or hydrolysis. In peptide display libraries, the ability of the identified peptides to precipitate metal oxide nanocomposites is tested. Combinatorial libraries have successfully discovered a number of peptides that form germanium oxide (GeO_2) and silica.

Germanium oxide-silica glasses have enhanced transmission at IR wavelengths, higher refractive indices, and lower viscosities than silica glasses, which makes them interesting materials for optical devices.¹²⁸ Currently, no biological systems are known to produce GeO_2 . Dickerson and coworkers have identified GeO_2 precipitating peptides using a combinatorial phage display peptide library.¹²⁹ Of the twenty one germania binding peptides sequences identified, two sequences TGHQSPGAYAAH (Ge34) and

SLKMPHWPHLLP (Ge8) precipitated GeO₂ nanoparticles when exposed to the alkoxide tetramethoxygermanium. As expected, no GeO₂ was produced when the peptides were omitted from the reaction or when nonspecific peptides were exposed to the alkoxide. GeO₂ production was quantified using an adapted version of the β -silicomolybdate assay.¹³⁰ Both peptides have basic isoelectric points and possess hydroxyl and imidazole amino acid residues. Controls conducted with non specific peptides with basic isoelectric points did not yield GeO₂, indicating that the precipitation is not a pH-dependent process but is mediated by the sequences isolated from the library. Scanning electron microscopy (SEM), TEM, and SADP were used to characterize the nanoparticles produced from both peptides. SEM images show interconnected nanoparticles, ranging in diameter from 50 to 100 nm. Electron diffraction data from several areas revealed that the nanoparticles were amorphous. TEM images show areas of low density which are attributed to pores in the material or entrapped organic material such as the peptide.¹²⁹

In addition to germania precipitating peptides, silica precipitating peptides have also been identified. Naik and coworkers examined a 12 amino acid phage peptide display library to identify Si binding peptides.¹³¹ Silica production was quantified using the β -silicomolybdate assay.¹³⁰ The most reactive silica binding peptide was MSPHPHPRHHHT, producing 680 nmols of silica in 5 minutes. Other peptide precipitating sequences that were identified are LPHHHHLHTKLP (500 nmols), KPShHHHHTGAN (420 nmols), APHHHHPHHLR (334 nmols), MSPHHMHSHGH (240 nmols), and MSASSYASFSWS (187 nmols). As expected, no silica was produced when the peptide was omitted or when nonspecific peptides were used in the synthesis. Similar to the germania precipitating peptides, the most active silica precipitating

peptides contained both hydroxyl and imidazole amino acid residues as well as a large cationic charge. Peptides that did not contain one of these three traits exhibited reduced silica production. The role these amino acid groups play in silica formation in this case is not well understood. However, hydroxyl groups have been proposed to function as an organizational unit for the monosilicic acid precursor by hydrogen or covalent bonding.¹³² Additionally, amine groups have been present in many silica precipitating templates such as silaffins, silicateins, and dendrimers.^{115,133-135} In each case the cationic charge is proposed to stabilize the negatively charge silicic acid. The silica nanoparticles were characterized by SEM, EDS, and SADP. SEM images reveal that the diameters of the nanoparticles range from 250 to 500 nm, and depending on the peptide sequence, the surface morphology of the silica was slightly different. SADP show that the material was mostly amorphous.¹³¹

Sano and coworkers have investigated the ability of the peptide termed TBP-1 (RKLPDAPGMHTW) to mineralize silica.¹³⁶ TBP-1 has shown an affinity for many metals including Ti, Ag, and Si.¹³⁷ To explore the reactivity of the peptide, alanine replaced key amino acid constituents.¹³⁶ Since the alanine side chain is an uncharged methyl group, the metal binding would be reduced. From this study, it was determined that the arginine in the first position, proline in the fourth position, and aspartic acid in the fifth position were all critical for Ti binding. Sano and coworkers propose that the proline produces a kink in the peptide which decreases the distance between the arginine and aspartic acid, resulting in a Lewis acid/base reactivity.¹³⁶ Similar reactivity results were observed with Si; however, when the lysines were replaced, surprisingly, no effect was observed. Lysine has been implicated as a key amino acid in biosilification

reactions where the positive side chain interacts with the negative precursor.¹³⁸ In this case, the positive side chain is interacting with a positive metal, so binding should not be affected.¹³⁶ Silification reactions were carried out by exposing TBP-1 to silicic acid in a buffered solution. Nanospheres approximately 500 nm in diameter rapidly formed. Point mutation of the TBP-1 peptide indicated that the proline in the fourth position is required for silica formation.¹³⁶ To date, TiO₂ mineralization has not been investigated. Silica, as well as germania precipitating peptides, are excellent examples of peptide display libraries identifying non-biological peptides that form metal oxides species rapidly under conditions similar to biologically derived peptides.

Silicatein

Several marine sponges produce silica spicules which help support and protect the sponge from predators (**Figure 7**). The spicules are made in vesicles in specialized cells, sclerocytes.¹³⁹ Generally, the spicules contain a protein filament with a repeating structure as shown by XRD studies.¹⁴⁰ Morse and coworkers have studied the structure and metal oxide precipitating abilities of the protein filaments from the spicules of the marine sponge *Tethya aurantai*.

Amino acid analysis of the spicule filaments (**Figure 8 A**) showed that they are composed of 91% amino acids.¹⁴⁰ The filaments are comprised of three highly homologous proteins, silicatein α , β , and γ , with the molecular weights of 29, 28, and 27 kDa, respectively. Sequence analysis revealed that silicatein α , the most abundant of the

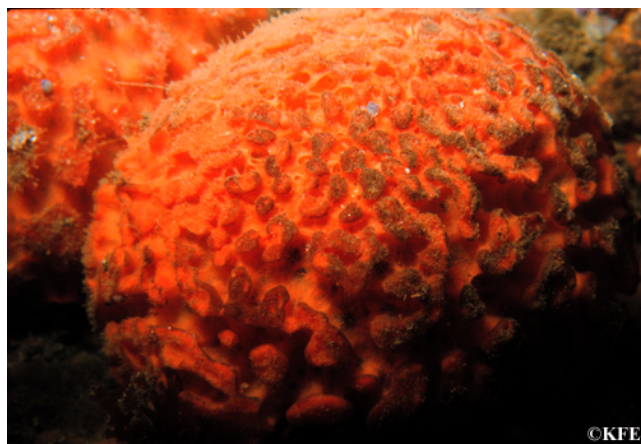


Figure 7: Photograph of *Tethya aurantia*.

three proteins, is a member of the cathepsin L subfamily of papain-like cysteine proteases.¹⁴⁰ These proteases catalyze the hydrolysis of peptide bonds, specifically at cysteine amino acids.¹⁴¹ Even though 75% of the amino acids in human cathepsin L are similar (45% are identical) to silicatein α , there are some distinct differences in the amino acid sequences. For example, serine replaces the catalytic cysteine found in cathepsin L.¹⁴⁰ Similar to metal oxide precipitating peptides isolated from peptide display libraries, silicatein α has a high concentration of hydroxy amino acids. Further mechanistic investigation has shown that Ser-26 and His-165 are required for silica catalysis.¹³³ When these residues are replaced with alanine, the amount of silica produced decreases dramatically. The serine and histidine amino acids are proposed to bridge the substrate binding site, causing the acid/base catalysis of the silicon alkoxide precursor (**Figure 9**). *In vitro*, silicatein filaments and the individual proteins cause the

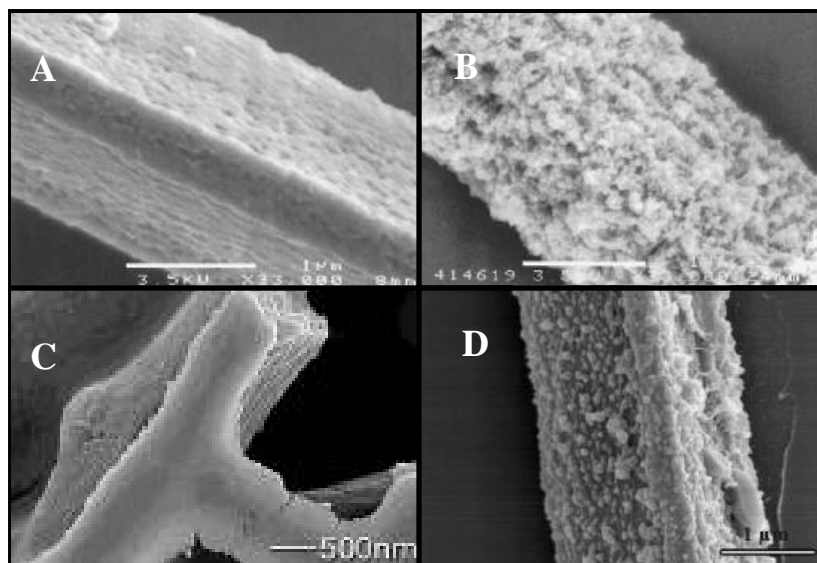


Figure 8: A) Unreacted silicatein filament.¹¹⁵ B) Silicatein filament reacted with TEOS,¹¹⁵ scale bar 1 μ m. C) Silicatein filament reacted with TBALDH.¹¹⁶ D) Silicatein filament reacted with gallium nitrate.¹¹⁷

condensation and polymerization of tetraethyl orthosilicate (TEOS) to form silica at neutral pH and low temperatures (**Figure 8 B**).¹¹⁵ In the absence of the silicatein filaments, no silica nanoparticles form. Furthermore, silicateins do not show any silica precipitation activity when they have been thermally denatured, indicating that the three-dimensional structure of the proteins is vital for silica precipitation.

The biosilification pathway of silicatein can use several alternate substrates to form non-natural metal oxides. When the silicatein filament is exposed to titanium bis(ammonia lactato) dihydroxide (TBALDH, $[\text{CH}_3\text{CH}(\text{O}^-)\text{CO}_2\text{NH}_4]_2\text{Ti}(\text{OH})_2$), TiO_2 nanoparticles form over the course of 24 hours (**Figure 8 C**).^{116,117} As expected, when silicatein has been thermally denatured and reacted with the precursor, no metal oxide formed, implying that, as in silica formation, the three dimensional structure is crucial for the formation of the metal oxides.¹¹⁵ For comparison purposes, base catalyzed TiO_2

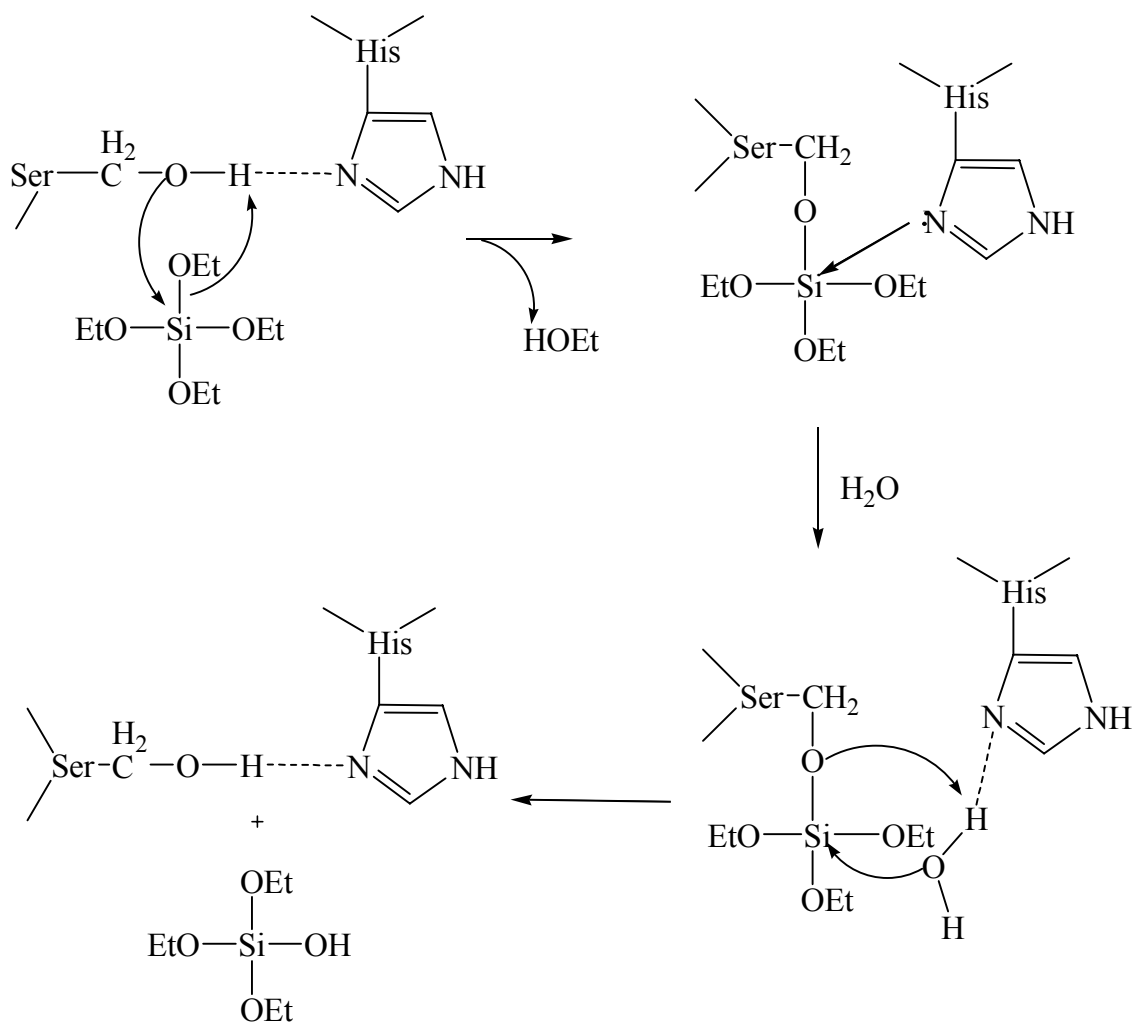


Figure 9: Mechanism of silicatein catalyzed TEOS hydrolysis.¹¹⁵

nanoparticles were also studied. After examination of the SEM images, the surface of the silicatein TiO₂ appeared to be smoother than the surface of base-catalyzed TiO₂.¹¹⁶ There are several nucleation sites located along the silicatein filament, as opposed to homogenous catalysis, where the TiO₂ can condense. The templating effect of silicatein

is proposed to stabilize smaller nuclei resulting in a smoother morphology. SADP patterns on the surface of the nanocomposite were crystalline, while the SADP conducted on the area between the filament and mineral were amorphous. The d-spacings of 3.5, 2.4, and 1.9 Å obtained from SADP on the surface indicate that TiO₂ is in the anatase phase. Controls were conducted to ensure the electron beam did not cause the crystallization of titanium dioxide to the anatase phase by placing amorphous TiO₂ in the beam for 1, 5, 15, and 30 minutes, with no anatase formation observed. Weak interactions such as hydrogen bonding and van der Waals forces between the template and precursor are proposed to stabilize the anatase phase, which is usually formed at higher temperatures. XRD measurements show that the anatase-to-rutile transition is delayed when silicatein is used as the catalyst, as compared to base catalyzed titanium dioxide. The delayed temperature transition is thought to be caused by the presence of organic material from the silicatein.¹¹⁶ Previously, the presence of impurities has been shown to slow the phase transitions of titanium by delaying the rearrangement of ions and retarding crystallization.¹⁴²⁻¹⁴⁴

In addition to TiO₂, gallium oxyhydroxide (GaOOH) and gallium oxide (Ga₂O₃) are formed in the presence of silicatein from gallium (III) nitride under ambient conditions (**Figure 8 D**).¹¹⁷ When lower concentrations of the precursors are combined with silicatein filaments, SADP d-spacings of 2.91, 2.48, 2.08, 1.44, and 1.20 Å indicate that nanocrystals of cubic γ -Ga₂O₃ are formed. The γ -Ga₂O₃ nanoparticles have a diameter of 75 to 200 nm, as shown by SEM images. Interesting attempts by Morse and coworkers to synthesize γ -Ga₂O₃ under basic or acidic conditions resulted in crystalline GaOOH and only with heating did γ -Ga₂O₃ form. High resolution TEM images show

that silicatein directs the orientation of the γ -Ga₂O₃ nanocrystals. Analysis of several different crystals show that the (311) plane was oriented perpendicular to the filament. The authors propose that hydroxyl groups on the surface of the filament direct the crystal growth through hydrogen bonding. Additionally, a similar morphology for GaOOH and γ -Ga₂O₃ nanoparticles was observed, indicating that either a topotactic mechanism or the crystallization and dissolution of the nanoparticle on the silicatein surface is responsible for the formation of the different polymorphs.¹¹⁷

The above work used silicatein filaments as the nucleating template, which can be limiting factors for use in nanodevices and other materials applications due to their rigid structure. Recently Cornow and coworkers expressed outer membrane protein A-silicatein- α (OmpA-Sil) on the surface of *E. coli* cells.¹¹⁸ Similar to other recombinant systems, densitometric measurements indicate that 5×10^4 copies (20-25% of the OM protein) are expressed on each cell.^{145,146} The expression of OmpA-Sil did not effect the viability of the cell line.¹¹⁸ When the cells were exposed to TBALDH, a white precipitate formed that is amorphous at room temperature, according to the XRD analysis of lyophilized cells. However, the SADP of the cell surface shows that the white precipitate is crystalline. Upon heating to 600°C, XRD shows that rhombohedral sodium titanium phosphate (NaTi₂(PO₄)₃) forms and heating to 800°C resulted in formation of cubic titanium phosphate, TiP₂O₇. Previously this form has been synthesized after reacting anatase TiO₂ with 85% phosphoric acid and heating for several hours at 1000°C for several hours or heating titanium phosphate to approximately 900°C.¹⁴⁷ Unfortunately, inductive coupled plasma atomic emission spectroscopy shows that control cells uptake titanium ions similar to the cells expressing OmpA-Sil. The authors

propose that periplasmic enzymes located between the cell wall and cell membrane are responsible for the nonspecific hydrolysis of TBALDH, resulting in the high background.¹¹⁸ While expressing silicatein- α on the surface of cells is progression towards using silicatein in materials applications, several nuances of the system such as periplasmic enzymes need to be investigated.

Diatoms

Another natural source of silica in Nature is diatoms. Diatoms are unicellular, eukaryotic algae, classified under the genera *Nitzschia* or *Hantzschia*, that form intricate silica cell walls, also known as frustule. (Figure 10).¹⁴⁸ Diatoms generally exist as

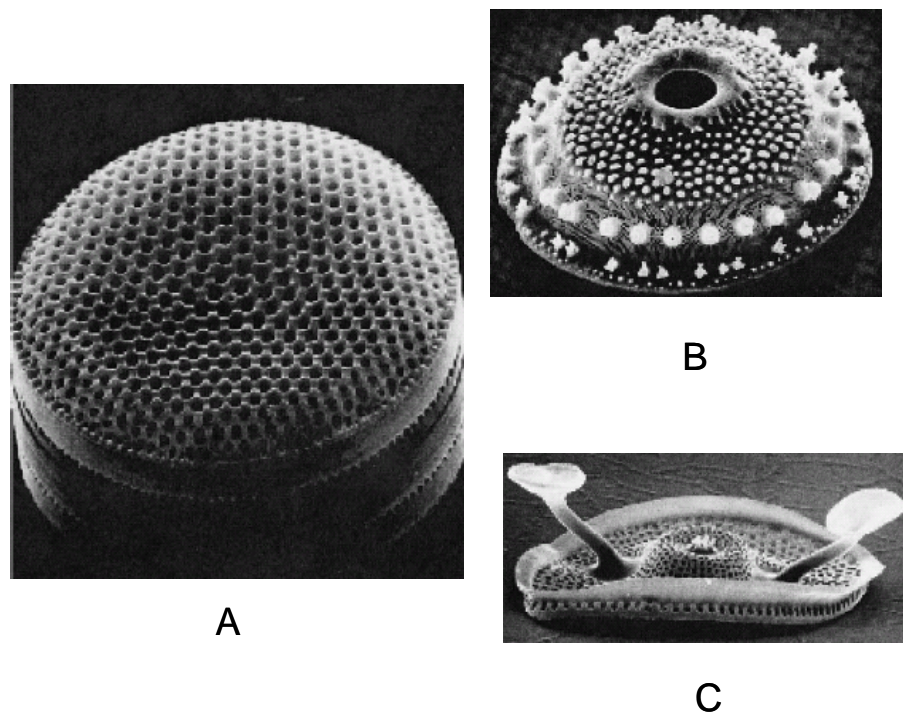


Figure 10: A) SEM of *Thalassiosira oestruppi* diatom B) SEM of a valve from *Porodiscus hirsutus* diatom C) SEM of a valve from *Kittonia elaborata* diatom¹⁴⁹

single cells ranging in size from 5 μm to 5 mm, however some species can form colonies or chains.¹⁵⁰ The patterns produced by the diatoms are species specific and replicated from generation to generation, indicating that silica formation is an incredibly controlled process.¹⁵¹ There are two major diatom groups that are classified by their cell shapes: the centric and pinnate diatoms. Centric diatoms have a radial symmetry with a lengthwise axis penetrating the center of the cell. Pinnate diatoms, on the other hand, have a narrow morphology with an axis that passes through the length of the diatom.¹⁵² By understanding how diatoms form reproducible nanostructures of silica under ambient, aqueous conditions, scientists can begin to mimic the biomineralization process in the hopes of constructing intricate nanopatterns of metal oxides.

Silicic Acid Uptake

Since the availability of precursor is crucial in the biomineralization process, diatoms have developed a specific silicic acid uptake mechanism. The concentration of silicic acid in the ocean is approximately 70 μM ; however, the concentration of silicic acid in diatoms range from 19 to 340 mM.¹⁵³ Silicic acid is transported from the environment through a lipid bilayer cell membrane via Na^+ dependant silica transport proteins (SITs) into the diatom.^{149,154,155} Five different types of SIT genes responsible for silicic acid transport have been identified from the cell walls of *Cylindrotheca fusiformis* by Hildebrand and coworkers.¹⁵⁵ Several factors in the cell control silicic acid uptake including the concentration and type of SIT upregulated. The levels of SITs expressed by the cell have been linked with the amount of silicic acid uptake. Additionally, the different types of SIT are thought to have different transport

capabilities, allowing the cell to regulate the concentration of silicic acid.¹⁵⁵ The variety and regulation of the SIT genes has shown that the uptake of silicic acid is not dependent upon amounts in the environment, but is a controlled, regulated process that is based more precisely upon the need of the cell.

Once inside the cell, not much is known about the transport of silicic acid. Originally Schmid and Schultz proposed that vesicles transport silicic acid to the silica deposition vesicle (SDV).¹⁵⁶ Vesicles were identified fusing to the SDV leading investigators to conclude they were the transportation vehicle of silicic acid. Unfortunately, silicic acid hasn't been found in the vesicles and Li and coworkers suggested that the vesicles were too small and too few to transport the amount of silicic acid needed to form the exoskeleton.¹⁵⁷ Additionally, silicic acid is found throughout the cytoplasm of the cell indicating a cytoplasmic transport mechanism. A SIT-like protein might be responsible for intracellular transport or Hildebrand cautiously suggests that an ionophore or electrophoretic mechanism could be responsible.¹⁴⁹

Once silicic acid is transported into the SDV, polymerization occurs. Iler has extensively investigated the process of silica formation.¹³⁰ Silicic acid polymerization is an energetically favorable process that can occur either by raising the concentration of silicic acid in solution or by decreasing the pH. Silicic acid polymerizes into dimers, trimers, and oligomers eventually forming spherical particles. The sizes of the particles are dictated by pH and ions present in solution. There is a negative charge on the surface of the forming particles from the presence of silonal groups. When no salt is present, at neutral pH the charges repel each other resulting in a gel. However, when

salts or present or at a lower pH, the charge is neutralized, resulting in the formation of particles.¹³⁰

Diatom Cell Division

The SDV performs two functions in the diatom. It provides a controlled environment for silica formation and acts as a mold during cell division to form the intricate silica nanostructures.¹⁴⁹ The diatom cell consists of two halves, the epitheca (top) and hypotheca (bottom) that slightly overlap, similar to a Petri dish (**Figure 11**).¹¹⁹ During mitosis, the nucleus of each daughter cell, as well as the microtubule center (MC) moves to the center of the cell where the hypotheca will be formed. Each daughter cell

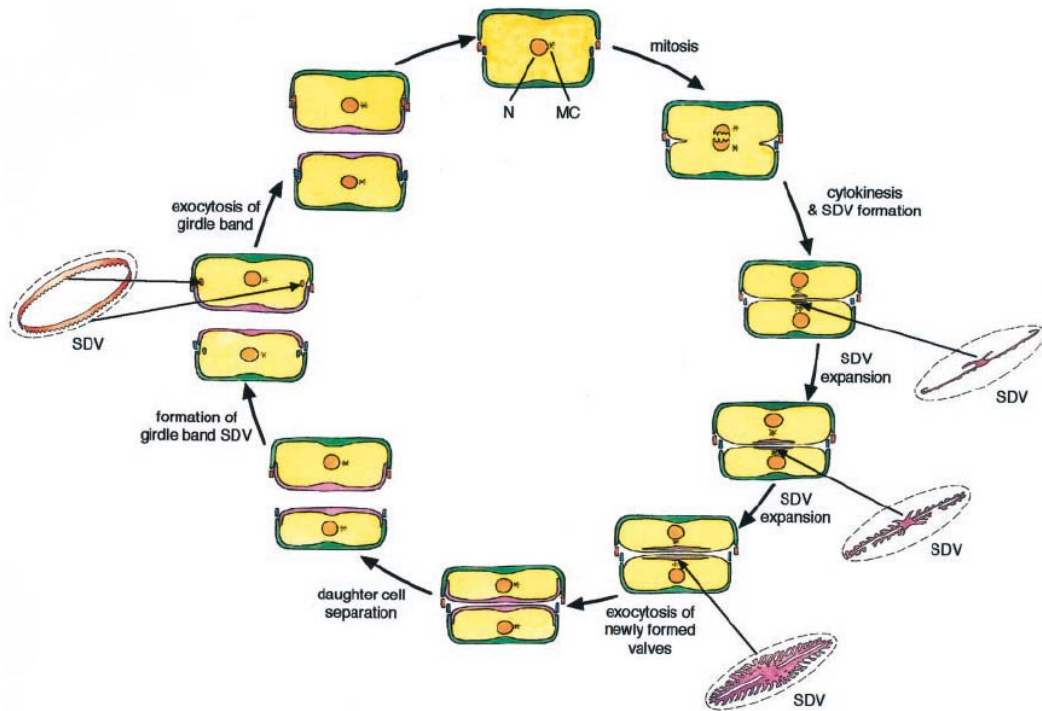


Figure 11: Diatom cell division.¹⁵⁸

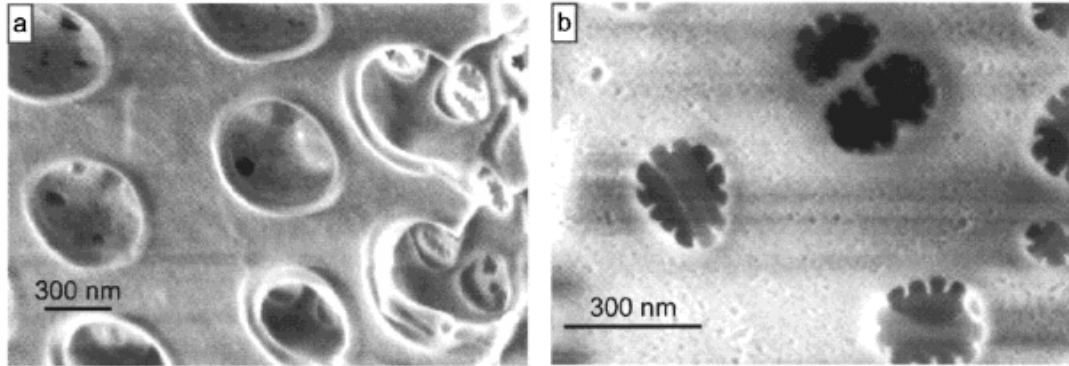


Figure 12: A) SEM image of the interior of *C. granii*. B) SEM image of the exterior of *C. granii*.¹⁵⁹

produces a valve SDV that continually grows in an elongated fashion as silica is deposited. Once valve expansion is complete, the SDV merges with the cell membrane. Since the cell wall is rigid, the only way for the cells to divide is by increasing the distance between the epitheca and hypotheca. Another SDV forms girdle bands that are released, gradually increasing the space between the two cells and preventing gaps in the cell wall. When the new cells reach a predetermined size, cell division will begin again.¹¹⁹ Each division results in a smaller daughter cell. As cell division progress, the size of the cells continues to be reduced. When the cells are approximately 30% of their original size, the diatoms participate in sexual reproduction, which restores the cells.^{150,160}

The Frustule of Diatoms

Atomic force microscopy (AFM) analysis, as well as SEM analysis, of the *Coscinodiscus granii* diatom cell wall have shown a granular nanostructured surface.¹⁵⁹ SEM images reveal that the interior surface of the valve is smooth with 400 nm craters

located spatially throughout (**Figure 12 A**). The morphology of the exterior surface is quite different with teeth-like holes approximately 200-300 nm in diameter and a more porous surface (**Figure 12 B**). AFM images of the interior surface also showed the crater structures, but the “smooth” surface consisted of small granular particles ranging in size from 100 to 200 nm (**Figure 13**). Similar nanoparticles were seen on the exterior surface of the valve.¹⁵⁹ These nanoparticles are very similar to silica formed from proteins and polymers isolated from the cell walls of diatoms. Three different types proteins (frustulins, pleuralins, and silaffins) have been isolated from the cell wall of *C. fusiformis* by Kroger and coworkers.^{24,161,162} Additionally, long chain polyamines with

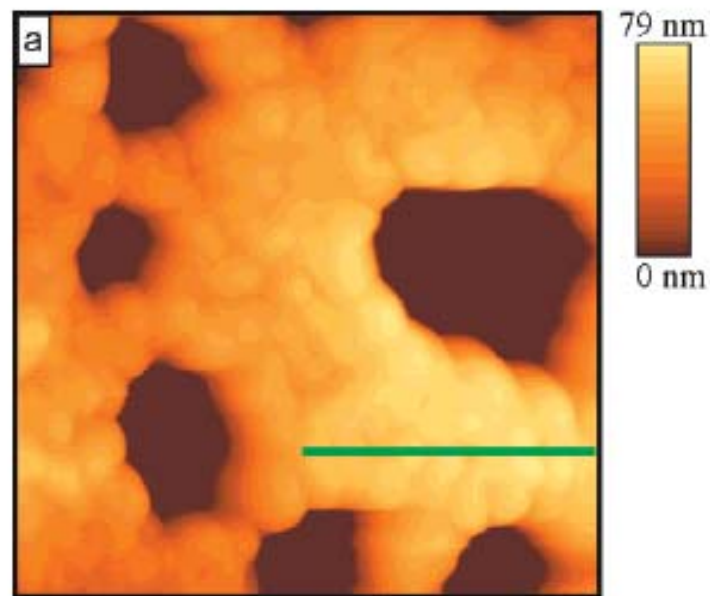


Figure 13: AFM image of the outer surface of *C. granii*.¹⁵⁹

species specific post-translational modifications have been isolated from the cell walls.¹⁶³

A more detailed discussion of the silica forming proteins and polymers is given in Chapter II.

Research Aims and Goals

The goal of this project is to explore the versatility of template based biomimetic molecules that form metal oxides. The ability of amine rich (bio)polymers to condense a wide range of metal oxides from alkoxy precursors under ambient conditions was studied.

- **Biomimetic Synthesis of Titanium Dioxide Utilizing Bio-polymers:** The ability of the R5 peptide, a bioinspired analogue derived from the NatSil protein in *C. fusiformis*, to form TiO₂ from the non-natural substrate, titanium bis(ammonium lactato) dihydroxide (TBALDH) was investigated. Additionally, the polypeptide poly-L-lysine (PLL) acts as a template for the biomimetic synthesis of TiO₂. This research will be presented in Chapter II.
- **Size Control of Dendrimer Templated Silica Nanoparticles:** One of the most significant challenges facing the biomimetic synthesis of materials is controlling the size of nanoparticles. Previously, it has been shown that amine terminated PAMAM and PPI dendrimer are effective biomimetic templates for the synthesis of silica. In Chapter III, various reaction conditions of PAMAM and PPI dendrimer mediated silica synthesis were studied, achieving size control of the resulting silica nanoparticles.
- **Dendrimers as Templates for the Formation of Alternate Metal Oxides:** PAMAM and PPI amine terminated dendrimers were investigated as biomimetic templates for the formation of alternate metal oxides. Through this research, the scope

of dendrimer mediated metal oxide synthesis has been expanded to include TiO₂ and germanium dioxide, a blue photoluminescent material, as discussed in Chapter IV.

References

1. Rao, C. N. R.; Raveau, B., Eds. *Transition Metal Oxides: Structure, Properties, and Synthesis of Ceramic Oxides*; 2nd ed.; Wiley: New York, 1998.
2. Koch, C. C. *Nanostructured Materials*; William Andrew: Norwich, 2002.
3. Wilson, M.; Kannangara, K.; Smith, G.; Simmons, M.; Raguse, B. *Nanotechnology: Basic Science and Emerging Technologies*; CRC: Boca Raton, 2002.
4. Schmid, G., Ed. *Nanoparticles*; Wiley-VCH: Weinheim, 2004.
5. Wang, L. W., *Advanced Materials* **2003**, *15*, 432-436.
6. Barbe, C.; Bartlett, J.; Kong, L.; Finnie, K.; Lin, H. Q.; Larkin, M.; Calleja, S.; Bush, A.; Calleja, G., *Advanced Materials* **2004**, *16*, 1959-1966.
7. Eppler, A. S.; Zhu, J.; Anderson, E. A.; Somorjai, G. A., *Topics in Catalysis* **2000**, *13*, 33-41.
8. Glaspell, G. P.; Jagodzinski, P. W.; Manivannann, A., *J. Phys. Chem. B* **2004**, *108*, 9604-9607.
9. Tan, O. K.; Cao, W.; Hu, Y.; Zhu, W., *Solid State Ionics* **2004**, *172*, 309-316.
10. Ganesh, I.; Johnson, R.; Mahajan, Y. R.; Khan, A.; Madnavendra, S. S.; Reddy, B. M., *J. Mater. Res.* **2004**, *19*, 1015-1023.
11. Wang, H.; Meng, Y.; Yan, H., *Inorg. Chem. Comm.* **2004**, *7*, 553-555.
12. Watanabe, T.; Fujiwara, K., *Chem. Engin. Comm.* **2004**, *191*, 1343-1361.
13. Willert, M.; Roth, R.; Landfester, K.; Antonietti, M., *Chem. Mater.* **2001**, *13*, 4681-4685.
14. Mann, S. *Biomineralization: Principles and Concepts in Bioinorganic Materials Chemistry*; Oxford University Press: Oxford, 2001.
15. Harrison, P. M.; Arosio, P., *Biochem. et Biophys. Acta* **1996**, *1275*.

16. Chasteen, N. D.; Harrison, P. M., *J. Struct. Biol.* **1999**, *126*, 182-194.
17. Harrison, P. M.; Treffry, A.; Lilley, T. H., *J. Inorg. Biochem.* **1986**, *27*, 287-293.
18. Muller, W. E. G., Ed. *Silicon Biomineralization*; Springer: Berlin, 2003; Vol. 33.
19. Ishay, J. S.; Riabinin, K.; Kozhevnikov, M.; van der Want, H.; Stokroos, I., *Biomacromolecules* **2003**, *4*, 469-456.
20. Stokroos, I.; Litinetsky, L.; van der Want, J. J. L.; Ishay, J. S., *Nature* **2001**, *411*, 654.
21. Blackmore, R., *Science* **1975**, *190*, 377-379.
22. Dunin-Borkowski, R. E.; McCartney, M. R.; Frankel, R. B.; Bazylinski, D. A.; Posfai, M.; Buseck, P. R., *Science* **1998**, *282*, 1868-1870.
23. Mann, S.; Sparks, N. H.; Walker, M. M.; Kirschvink, J. L., *J. Exper. Biol.* **1988**, *140*, 35-49.
24. Kroger, N.; Deutzmann, R.; Sumper, M., *Science* **1999**, *286*, 1129-1132.
25. Hoffmann, M. R.; Martin, S. T.; Choi, W.; Bahnemann, D. W., *Chem. Rev.* **1995**, *95*, 69-95.
26. Halperin, W. P., *Rev. of Mod. Physics* **1986**, *58*, 533-609.
27. Puentes, V. F.; Krishnan, K. M.; Alivisatos, A. P., *Science* **2001**, *291*, 2115-2117.
28. Ichiyangi, Y.; Kimishima, Y.; Yamada, S., *J. Mag. Magnetic Mater.* **2004**, *272-276*, e1245-e1246.
29. Soriano, L.; Abbate, M.; Fernandez, A.; Gonzalez-Eliphe, A. R.; Sirotti, F.; Sanz, J. M., *J. Phys. Chem. B* **1999**, *103*, 6676-6679.
30. Wang, C.-B.; Zhang, W.-X., *Environmental Science & Technology* **1997**, *31*, 2154-2156.
31. Zhang, W.-X.; Wang, C.-B.; Lien, H.-L., *Catalysis Today* **1998**, *40*, 387-395.
32. Douglas, T.; Young, M., *Adv. Mater.* **1999**, *11*, 679-681.
33. Jones, T.; Spencer, R.; Walsh, C., *Biochemistry* **1978**, *17*, 4011-4017.
34. Arosio, P.; Adelman, T. G.; Drysdale, J. W., *J. Biol. Chem.* **1978**, *253*, 4451-4458.

35. Lawson, D. M.; Artymuik, P. J.; Yewdall, S. J.; Smith, J. M. A.; Livingstone, C. J.; Treffry, A.; Luzzago, A.; Levi, S.; Arosio, P.; Cesareni, G.; Thomas, C. D.; Shaw, W. V.; Harrison, P. M., *Nature* **1991**, *349*, 541-544.
36. Yang, X.; Arosio, P.; Chasteen, D. N., *Biophys. J.* **2000**, *78*, 2049-2059.
37. Cowley, J. M.; Janney, D. E.; Gerkin, R. C.; Buseck, P. R., *J. Struct. Biol.* **2000**, *131*, 210-216.
38. Zhao, G.; Bou-Abdallah, F.; Arosio, P.; Levi, S.; Janus-Chandler, C.; Chasteen, D. N., *Biochemistry* **2003**, *42*, 3142-3150.
39. Bou-Abdallah, F.; Papaefthymiou, G. C.; Scheswohl, D. M.; Stanga, S. D.; Arosio, P.; Chasteen, D. N., *Biochem. J.* **2003**, *364*, 57-63.
40. Zhao, G.; Bou-Abdallah, F.; Yang, X.; Arosio, P.; Chasteen, D. N., *Biochemistry* **2001**, *40*.
41. Hwang, J.; Krebs, C.; Huynh, B. H.; Edmondson, D. E.; Theil, E. C.; Penner-Hahn, J. E., *Science* **2000**, *287*, 122-125.
42. Jameson, G. N. L.; Jin, W.; Krebs, C.; Perriera, A. S.; Tavares, P.; Liu, X.; Theil, E. C.; Huynh, B. H., *Biochemistry* **2002**, *41*, 13435-13443.
43. Treffry, A.; Zhao, Z.; Quail, M. A.; Guest, J. R.; Harrison, P. M., *Biochemistry* **1995**, *34*, 15204-15213.
44. Pereira, A. S.; Small, W.; Krebs, C.; Tavares, P.; Edmondson, D. E.; Theil, E. C.; Huynh, B. H., *Biochemistry* **1998**, *37*, 9871-9876.
45. Loccoz-Moenne, P.; Krebs, C.; Herlihy, K.; Edmondson, D. E.; Theil, E. C.; Huynh, B. H.; Loehr, T. M., *Biochemistry* **1999**, *38*, 5290-5295.
46. Yang, X.; Chen-Barrett, Y.; Arosio, P.; Chasteen, D. N., *Biochemistry* **1998**, *37*, 9743-9750.
47. Macara, I. G.; Hoy, T. G.; Harrison, P. M., *Biochem. J.* **1973**, *135*.
48. Macara, I. G.; Hoy, T. G.; Harrison, P. M., *Biochem. J.* **1972**, *126*, 151-162.
49. Treffry, A.; Harrison, P. M., *Biochem. J.* **1978**, *171*, 313-320.
50. Mann, S.; Williams, J. M.; Amyra, T.; Harrison, P. M., *J. Molecular Biol.* **1987**, *198*, 405-416.

51. Meldrum, F. C.; Heywood, B. R.; Mann, S., *Science* **1992**, *257*, 522-523.
52. Meldrum, F. C.; Douglas, T.; Levi, S.; Arosio, P.; Mann, S., *J. Inorg. Biochem.* **1995**, *58*, 59-68.
53. Meldrum, F. C.; Wade, V. J.; Nimmo, D. L.; Heywood, B. R.; Mann, S., *Nature* **1991**, *349*, 684-687.
54. Mann, S.; Meldrum, F. C., *Adv. Mater.* **1991**, *3*, 316-318.
55. Douglas, T.; Stark, V. T., *Inorg. Chem* **2000**, *39*, 1828-1830.
56. Dewey, D. W.; Marston, H. R., *Anal. Chim. Acta* **1971**, *57*, 45-49.
57. Wunsch, G., *Talanta* **1978**, *26*, 177-179.
58. Kim, J.-W.; Choi, S. H.; Lillehei, P. T.; Chu, S.-H.; King, G. C.; Watt, G. D., *Chem. Comm.* **2005**.
59. Okuda, M.; Iwahori, K.; Yamashita, I.; Yoshimura, H., *Biotechnology and Bioengineering* **2003**, *84*, 187-194.
60. Kim, I.; Hosein, H.-A.; Strongin, D. R.; Douglas, T., *Chem. Mater.* **2002**, *14*, 4874-4879.
61. Ensign, D.; Young, M.; Douglas, T., *Inorg. Chem* **2004**, *43*, 3441-3446.
62. Yamashita, I., *Thin Solid Films* **2001**, *393*, 12-18.
63. Tominaga, M.; Matsumoto, M.; Soejima, K.; Taniguchi, I., *J. of Colloid and Inter. Science* **2006**, *299*, 761-765.
64. Miura, A.; Hikono, T.; Matsumura, T.; Yano, H.; Hatayama, T.; Uraoka, Y.; Fuyuki, T.; Yoshii, S.; Yamashita, I., *Japan. J. of Appl. Phys.* **2006**, *45*, L1-L3.
65. Hosein, H.-A.; Strongin, D. R.; Allen, M.; Douglas, T., *Langmuir* **2004**, *20*, 10283-10287.
66. Klein, C. B. In *Toxicology of Metals*; Chang, L. W., Ed.; Lewis: Boca Raton, 1996, pp 205-219.
67. Furuno, T.; Sasabe, H.; Ulmer, K. M., *Thin Solid Films* **1989**, *180*, 23-30.
68. Yang, X.; Chasteen, D. N., *Biophys. J.* **1996**, *71*, 1587-1595.

69. Jeong, G.-H.; Yamazaki, A.; Suzuki, S.; Yoshimura, H.; Kobayashi, Y.; Homma, Y., *J. Am. Chem. Soc.* **2005**, *127*.
70. Li, Y.; Kim, W.; Zhang, Y.; Rolandi, M.; Wang, D.; Dai, H., *J. Phys. Chem. B* **2001**, *105*, 11424-11431.
71. Bonard, J.-M.; Chauvin, P.; Klinke, C., *Nano Letters* **2002**, *2*, 665-667.
72. Hafner, J. H.; Bronikowski, M. J.; Azamian, B. R.; Nikolaev, P.; Rinzler, A. G.; Colbert, D. T.; Smith, K. A.; Smalley, R. E., *Chem. Phys. Lett.* **1998**, *296*, 195-202.
73. Hafner, J. H.; Cheung, C. L.; Lieber, C. M., *J. Am. Chem. Soc.* **1999**, *121*, 9750-9751.
74. Cassell, A. M.; Raymakers, J. A.; Kong, J.; Dai, H., *J. Phys. Chem. B* **1999**, *103*, 6484-6492.
75. Kong, J.; Cassell, A. M.; Dai, H., *Chem. Phys. Lett.* **1998**, *292*, 567-574.
76. Kong, J.; Soh, H. T.; Cassell, A. M.; Quate, C. F.; Dai, H., *Nature* **1998**, *395*, 878-881.
77. Cassell, A. M.; Franklin, N. R.; Tomblor, T. W.; Chan, E. M.; Han, J.; Dai, H., *J. Am. Chem. Soc.* **1999**, *121*.
78. Franklin, N. R.; Dai, H., *Adv. Mater.* **2000**, *12*, 890-894.
79. Lui, J.; Dai, H.; Hafner, J. H.; Colbert, D. T.; Smalley, R. E.; Sander, T. J.; Dekker, C., *Nature* **1997**, *385*, 780-781.
80. Martel, R.; Shea, H. R.; Avouris, P., *Nature* **1999**, *398*, 299.
81. Amelinckx, S.; Bernaerts, D.; Zhang, X. B.; Van Teng, G.; Landuyt, J. V., *Science* **1995**, *267*, 1334-1338.
82. Han, S.; Liu, X.; Zhou, C., *J. Am. Chem. Soc.* **2005**, *127*, 5294-5295.
83. Bozzi, M.; Mignogna, G.; Stefanini, S.; Barra, D.; Longhi, C.; Valenti, P.; Chiancone, E., *J. of Biol. Chem.* **1997**, *272*, 3259-3265.
84. Ilari, A.; Savino, C.; Stefanini, S.; Chiancone, E.; Tsernoglou, D., *Acta Cryst. D.* **1999**, *55*, 552-553.
85. Ilari, A.; Stefanini, S.; Chiancone, E.; Tsernoglou, D., *Nature Struct. Biol.* **2000**, *7*, 38-43.

86. Su, M.; Cavallo, S.; Stefanini, S.; Chiancone, E.; Chasteen, N. D., *Biochemistry* **2005**, *44*, 5572-5578.
87. Ilari, A.; Ceci, P.; Ferrari, D.; Rossi, G. L.; Chiancone, E., *J. Biol. Chem.* **2002**, *277*, 37619-37623.
88. Ilari, A.; Latella, M. C.; Ceci, P.; Ribachi, F.; Su, M.; Giangiacomo, L.; Stefanini, S.; Chasteen, N. D.; Chiancone, E., *Biochemistry* **2005**, *44*, 5579-5587.
89. Stefanini, S.; Cavallo, S.; Montagnini, B.; Chiancone, E., *Biochem. J.* **1999**, *338*, 71-75.
90. Allen, M.; Willits, D.; Young, M.; Douglas, T., *Inorg. Chem* **2003**, *42*, 6300-6305.
91. Resnick, D. A.; Gilmore, K.; Idzerda, Y. U.; Klem, M. T.; Allen, M.; Douglas, T.; Arenholz, E.; Young, M., *J. of Appl. Phys.* **2006**, *99*, 08Q501-501 - 508Q501-503.
92. Kilcoyne, S. H.; Cywinski, R., *J. Magn. Magn. Mater.* **1995**, *140*, 1466-1468.
93. Kramer, R. M.; Sowards, L. A.; Pender, M. J.; Stone, M. O.; Naik, R. R., *Langmuir* **2005**, *21*, 8466-8470.
94. Bacher, A.; Fischer, M.; Kis, K.; Krugelbrey, K.; Moerti, S.; Scheuring, J.; Weinkauff, S.; Ederhardt, S.; Schmidt-Base, K., *Biochem. Soc. Trans.* **1996**, *24*, 89-94.
95. Ladenstein, R.; Schneider, M.; Huber, R.; Bartunik, H. D.; Wilson, K.; Schott, K.; Bacher, A., *J. Molecular Biol.* **1988**, *203*, 1045-1070.
96. Ritsert, K.; Huber, R.; Turk, D.; Ladenstein, R.; Schmidt-Base, K.; Bacher, A., *J. Mol. Biol.* **1995**, *253*, 151-167.
97. Schott, K.; Ladenstein, R.; Konig, A.; Bacher, A., *J. Biol. Chem.* **1990**, *265*, 12686-12689.
98. Shenton, W.; Mann, S.; Colfen, H.; Bacher, A.; Fischer, M., *Angew. Chem. Int. Ed.* **2001**, *40*, 442-445.
99. Speir, J. A.; Munshi, S.; Wang, G.; Baker, T. S.; Johnson, J. E., *Structure* **1995**, *3*, 63-78.
100. Zhao, X.; Fox, J. M.; Olson, N. H.; Baker, T. S.; Young, M., *Virology* **1995**, *207*, 486-494.
101. van der Graaf, M.; van Mierlo, C. P. M.; Hemminga, M. A., *Biochemistry* **1991**, *30*, 5722-5727.

102. Douglas, T.; Strable, E.; Willits, D.; Aitouchen, A.; Libera, M.; Young, M., *Adv. Mater.* **2002**, *14*, 415-418.
103. Douglas, T.; Young, M., *Nature* **1998**, *393*, 152-155.
104. Moradian-Oldak, J.; Goldberg, M., *Cells Tissues Organs* **2005**, *181*, 202-218.
105. Knecht, M. R.; Wright, D. W., *Chem. Mater.* **2004**, *16*, 4890-4895.
106. Hawkins, K. M.; Wang, S. S.-S.; Ford, D. M.; Shantz, D. F., *J. Am. Chem. Soc.* **2004**, *126*, 9112-9119.
107. Knecht, M. R.; Sewell, S. L.; Wright, D. W., *Langmuir* **2005**, *21*, 2058-2061.
108. Patwardhan, S. V.; Maheshwari, R.; Mukherjee, N.; Kiick, K. L.; Clarson, S. J., *Biomacromolecules* **2006**, *7*, 491-497.
109. Tomczak, M. M.; Glawe, D. D.; Drummy, L. F.; Lawrence, C. G.; Stone, M. O.; Perry, C. C.; Pochan, D. J.; Deming, T. J.; Naik, R. R., *J. Am. Chem. Soc.* **2005**, *127*, 12577-12582.
110. Xu, M.; Gratson, G. M.; Duoss, E. B.; Sheperd, R. F.; Lewis, J. A., *Soft Matter* **2006**, *2*, 205-209.
111. Bansal, V.; Rautaray, D.; Ahmad, A.; Sastry, M., *J. Mater. Chem.* **2004**, *14*.
112. Bansal, V.; Rautaray, D.; Bharde, A.; Ahire, K.; Sanyal, A.; Ahmad, A.; Sastry, M., *J. Mater. Chem.* **2005**, *15*, 2583-2589.
113. Bharde, A.; Rautaray, D.; Bansal, V.; Ahmad, A.; Sarkar, I.; Yusuf, S. M.; Sanyal, M.; Sastry, M., *Small* **2006**, *2*, 135-141.
114. Sarikaya, M.; Tamerler, C.; Jen, A. K. Y.; Baneyx, F., *Nature Materials* **2003**, *2*, 577-585.
115. Cha, J. N.; Shimizu, K.; Zhou, Y.; Christiansen, S. C.; Chemelka, B. F.; Stucky, G. D.; Morse, D. E., *Proc. Natl. Acad. Sci.* **1999**, *96*, 361-365.
116. Sumerel, J. L.; Yang, W.; Kisailus, D.; Weaver, J. C.; Choi, J. H.; Morse, D. E., *Chem. Mater.* **2003**, *12*, 4804-4809.
117. Kisailus, D.; Choi, J. H.; Weaver, J. C.; Yang, W.; Morse, D. E., *Adv. Mater.* **2005**, *17*, 314-318.

118. Curnow, P.; Bessette, P. H.; Kisailus, D.; Murr, M. M.; Daugherty, P., S.; Morse, D. E., *J. Am. Chem. Soc.* **2005**, *127*, 15749-15755.
119. Sumper, M.; Kroger, N., *J. Mater. Chem.* **2004**, *14*, 2059-2065.
120. Knecht, M. R.; Wright, D. W., *Chem. Comm.* **2003**, *24*, 3038-3039.
121. Sewell, S. L.; Wright, D. W., *Chem. Mater.* **2006**, *18*, 3108-3113.
122. Brott, L. L.; Naik, R. R.; Pikas, D. J.; Kirkpatrick, S. M.; Tomlin, D. W.; Whitlock, P. W.; Clarson, S. J.; Stone, M. O., *Nature* **2001**, *413*, 291-293.
123. Naik, R. R.; Tomczak, M. M.; Luckarift, H. R.; Spain, J. C.; Stone, M. O., *Chem. Comm.* **2004**, 1684-1685.
124. Luckarift, H. R.; Spain, J. C.; Naik, R. R.; Stone, M. O., *Nat. Biotech.* **2004**, *22*, 211-213.
125. Pietro, A. D.; Madrid, M. P.; Caracuel, Z.; Delgado-jarana, J.; Roncero, M. I. G., *Molecular Plat Pathology* **2003**, *4*, 315-325.
126. Somiya, S.; Yamamoto, N.; Yanagina, H., Eds. *Science and Technology of Zirconia III*; American Ceramic Society: Westerville, 1988; Vol. 24.
127. Brown, S., *Nature Biotech.* **1997**, *15*, 269-272.
128. Kato, T.; Suetsugu, Y.; Nishimura, M., *Optics Letters* **1995**, *20*, 2279-2281.
129. Dickerson, M. B.; Naik, R. R.; Stone, M. O.; Cai, Y.; Sandhage, K. H., *Chem. Comm.* **2004**, 1776-1777.
130. Iler, R. K. *The Chemistry of Silica*; Wiley: New York, 1979.
131. Naik, R. R.; Brott, L. L.; Clarson, S. J.; Stone, M. O., *Journal of Nanoscience and Nanotechnology* **2002**, *2*, 95-100.
132. Hecky, R. E.; Mopper, K.; Kilham, P.; Degens, E. T., *Marine Biology* **1973**, *19*, 323-331.
133. Zhou, Y.; Shimizu, K.; Cha, J. N.; Stucky, G. D.; Morse, D. E., *Angew. Chem. Int. Ed.* **1999**, *38*, 779-782.
134. Kroger, N.; Deutzmann, R.; Sumper, M., *J. Biol. Chem.* **2001**, *276*, 26066-26070.
135. Knecht, M. R.; Wright, D. W., *Langmuir* **2004**, *20*, 4728-4732.

136. Sano, K.-I.; Sasaki, H.; Shiba, K., *Langmuir* **2005**, *21*, 3090-3095.
137. Sano, K.-I.; Shiba, K., *J. Am. Chem. Soc.* **2003**, *125*, 14234-14235.
138. Patwardhan, S. V.; Clarson, S. J., *Silicon Chemistry* **2002**, *1*, 207-214.
139. Imsiecke, G.; Steffen, R.; Curstodio, M.; Borojevic, R.; Muller, W. E. G., *In Virto Cell. Dev. Biol.-Animal* **1994**, *31*, 528-535.
140. Shimizu, K.; Cha, J. N.; Stucky, G. D.; Morse, D. E., *Proc. Natl. Acad. Sci.* **1998**, *95*, 6234-6238.
141. Turk, V., Ed. *Proteases: New Perspectives*; Birkhauser Verlag: Boston, 1999.
142. Gruy, F.; Pijolat, M., *J. Am. Cer. Soc.* **1992**, *75*, 663-666.
143. Hahn, H.; Logas, J.; Averbach, R. S., *J. Mater. Res.* **1990**, *5*, 609-614.
144. Yu, J. C.; Zhang, L.; Zheng, Z.; Zhao, J., *Chem. Mater.* **2003**, *15*, 2280-2286.
145. Schweizer, M.; Schwarz, H.; Sonntag, I.; Henning, U., *Biochem. Biophys. Acta* **1976**, *448*, 474-491.
146. Daugherty, P., S.; Olsen, M. J.; Iverson, B.; Georgiou, G., *Protein Engineering* **1999**, *12*, 613-621.
147. Constantino, U.; La Ginestra, A., *Thermochim. Acta.* **1982**, *58*, 179-189.
148. Gordon, R.; Drum, R. W., *Inter. Rev. of Cytology* **1994**, *150*, 243-372.
149. Hildebrand, M., *Progress in Org. Coatings* **2003**, *47*, 256-266.
150. Van Den Hoak, C.; Mann, D. G.; Jahns, H. M. *Algae: An Introduction to Phycology*; Cambridge University Press: New York, 1997.
151. Round, F. E.; Crawford, R. M.; Mann, D. G. *Diatoms: Biology and Morphology of the Genera*; Cambridge University Press: Cambridge, 1990.
152. Kroger, N.; Sumper, M.; Baeuerlein, E., Ed.; John Wiley and Sones: Weinheim, 2000, pp 151-170.
153. V., M.-J.; Hildebrand, M.; Brzenzinski, M. A., *J. Phycol.* **2000**, *36*, 821-840.
154. Hildebrand, M.; Volcani, B. E.; Gassmann, W.; Schroeder, J. I., *Nature* **1997**, *385*, 1997.

155. Hildebrand, M.; Dahlin, K.; Volcani, B. E., *Mol. Gen. Genet.* **1998**, *260*, 480-486.
156. Schmid, A. M. M.; Schulz, D., *Protoplasma* **1979**, *100*, 267-288.
157. Li, C. W.; Volcani, B. E., *Protoplasma* **1985**, *124*, 30-41.
158. Zurzolo, C.; Bowler, C., *Plant Physiology* **2001**, *127*, 1339-1345.
159. Noll, F.; Sumper, M.; Hampp, N., *Nano Letters* **2002**, *2*, 91-95.
160. Mann, D. G., *Hydrobio* **1993**, *270*, 11.
161. Kroger, N.; Lehmann, G.; Rachel, R.; Sumper, M., *Eur. J. Biochem.* **1997**, *250*, 99-105.
162. Kroger, N.; Deutzmann, R.; Bergsdorf, C.; Sumper, M., *EMBO J.* **1994**, *13*, 4676-4683.
163. Kroger, N.; Deutzmann, R.; Bergsdorf, C.; Sumper, M., *Proc. Natl. Acad. Sci.* **2000**, *97*, 14133-14138.

CHAPTER II

BIOMIMETIC SYNTHESIS OF TITANIUM DIOXIDE UTILIZING BIO-POLYMERS

Introduction

Kroger and coworkers have extensively researched the organic molecules responsible for initiating the polymerization of silica in the pennate diatom *C. fusiformis*. Generally two types of peptide based biomimetic templates, proteins and polymers, have been derived from the components of the cell wall. Three different types of proteins, frustulins, pleuralins and silaffins, have been isolated from the cell wall of *C. fusiformis* by Kroger and coworkers.¹⁻³ Additionally, long chain polyamines with species specific post-translational modifications have also been isolated.⁴ The ability peptides and polymers derived from the natural templates to form metal oxides has been extensively studied by several researchers.⁵⁻¹⁰

Frustulins

Ethylenediaminetetraacetic acid (EDTA) extraction of the *C. fusiformis* cell wall revealed a family of proteins called frustulins.³ Four frustulins were extracted with molecular weights of 75 kD (α -frustulin), 105 kD (β -frustulin), 140 kD (γ -frustulin), and 200 kD (δ -frustulin).^{3,11} Further purification has shown that there are three additional isoforms of α -frustulin.¹¹ The function of frustulins is thought to be dependant on the pH of the SDV, since the protein contains acidic, cysteine rich domains.¹² As silica polymerization occurs, the SDV environment becomes more acidic, therefore the

frustulins are thought to be expressed in the latter stage of valve formation.^{12,13} The frustilins are calcium binding proteins with characteristic EF hand calcium binding domains.³ They do not play a role in silica precipitation, but they crosslink using Ca²⁺ bridges to form the cell wall outer protein coating.¹²

Pleuralins

Acid hydrolysis of the diatom cell wall revealed a high molecular weight protein family associated with the silica scaffold denoted as pleuralins, originally termed HEPs (HF extractable proteins).¹ Peptide sequence analysis of pleuralin-1, a 200 kD protein, revealed five repeating domains. Proline, serine, cysteine, and aspartic acid constitute approximately 50% of the amino acid residues in each domain.¹ Unlike frustalins, the proteins are not incorporated into the cell wall via a SDV mediated pathway.¹⁴ A general exocytosis mechanism is proposed to be responsible for the protein secretion. To date, the precise function of the pleuralins is unknown; however, they are found in the region of the hypotheca/epitheca overlap. In cell division, pleuralins become associated with a distinct girdle band, the pleural band, during hypotheca/epitheca differentiation, indicating that pleuralins are involved in the developmental control of the thecas.^{11,14}

Silaffins

A protein family with a low molecular weight (ranging from 4 to 17 kD), termed silaffins were also isolated from the cell wall upon acid hydrolysis.² Upon further investigation, three silaffins are present in the cell wall identified as silaffin-1A (4 kD), silaffin-1B (8 kD), and silaffin 2 (17 kD). Silaffin-1A contains repeating units rich in

lysine, arginine and serine amino acid residues. Silaffin-1B is almost identical to silaffin-1A, except it contains an additional repeat of the 1A sequence. Kroger and coworkers amplified a fragment of cDNA from silaffin-1B using PCR. Using this fragment, the *C. fusiformis* genomic library was screened and a 265 amino acid protein, Si11p, was identified (**Figure 14**). *In vivo*, the protein is cleaved, resulting in the smaller polypeptides. When silicic acid is introduced into a solution of silaffin-1A, silica nanoparticles ranging in size from 500 to 700 nm rapidly form. Similarly, silaffin-1B forms nanoparticles less than 50 nm in diameter when exposed to silicic acid. The ability of silaffins to form silica *in vitro* indicates that they are involved in silica polymerization in the diatom cell.²

The high concentration of hydroxyamino acids in Si11p makes the protein a candidate for posttranslational modifications, such as phosphorylation and glycosylation.² However, these can be easily cleaved during the harsh HF extraction process. A gentler

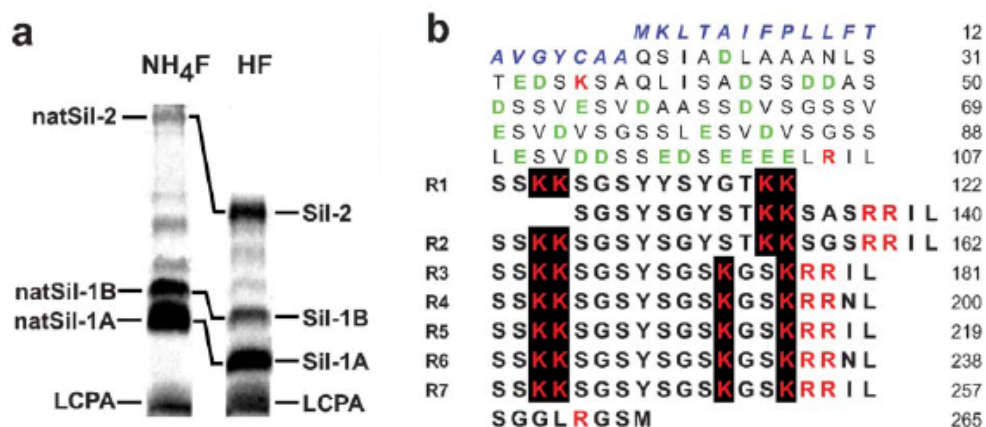


Figure 14: A) Comparison of the SDS/PAGE gel of ammonium fluoride and HF extracted silaffins B) Amino acid sequence of Si11p. Acidic amino acid residues are in green, basic amino acid residues are in red, the blue residues are the signal peptide, the bold black amino acids are responsible for silaffin generation.¹⁵

ammonium fluoride extraction of the cell wall revealed that the lysines are post-translationally modified forming either ϵ -N,N-dimethyllysine, ϵ -N,N,N-trimethyl- δ -hydroxylysine, or long chain polyamines, a derivative of polypropylenimine.⁶ The ammonium fluoride extracted silaffins are denoted native silaffins and abbreviated natSil-1A, natSil-1B, and natSil-2 (**Figure 14**).² In addition to the lysine post-translational modifications of the natSil-1A, the serines are phosphorylated (**Figure 15**).

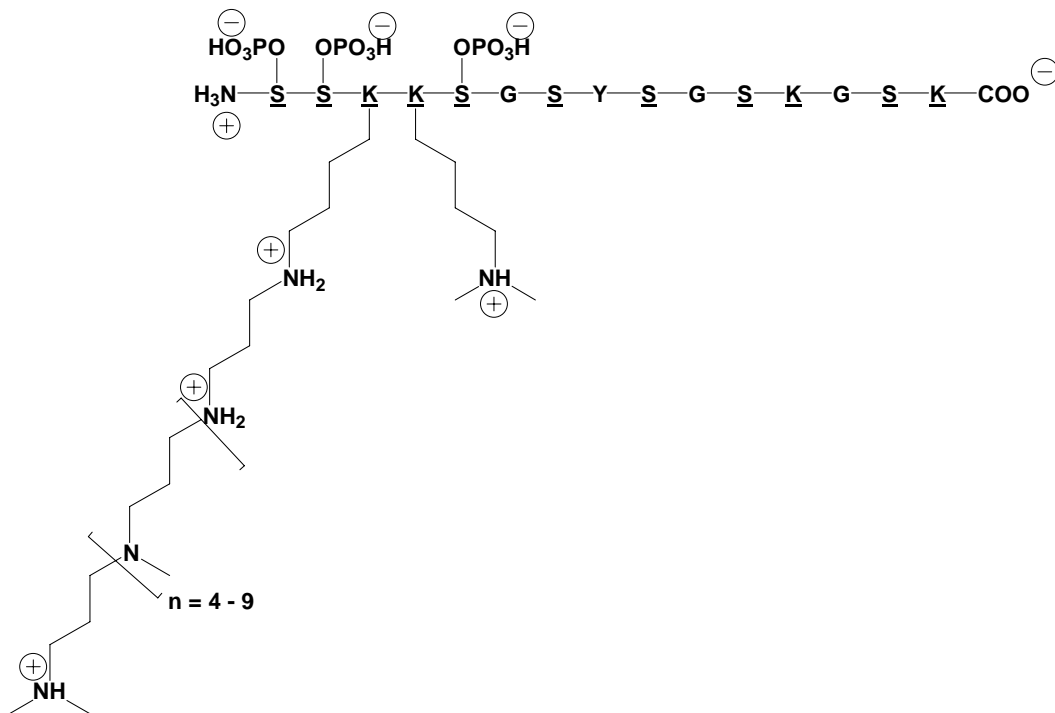


Figure 15: Structure of natSil-1A, underlined amino acids are post-translationally modified.¹⁵

Phosphorylation of the serine residues result in a large self-assembled structure of approximately 700 peptide molecules.¹⁶ High local amine concentration of the self assembled structure leads to silica precipitation at pH 5.5, the physiological pH of the silica deposition vesicle.¹³

When Si11p is compared to the native silaffins extracted from the diatom shell, important information about the *in vivo* processing of the protein is revealed.¹⁵ The protein is proteolytically cleaved, releasing the repeat units R1-R7 as individual peptides. During the proteolytic processing, the RRIL or RRNL motif is cleaved, resulting in similar 15mer sequences. Silaffin 1-A is derived from a mixture of the peptide repeat units R2-R7, while silaffin 1-B originates from repeat unit R1. The function of the acidic N-terminal region of the peptide (20-107) is unknown, as it is not incorporated into the siliceous diatom wall. Additionally, sequence information obtained from silaffin 2 indicated that it is not derived from Si11p.¹⁵

Kroger and coworkers have studied the role of silaffin-2 or natSil-2 in silica biomineralization.¹⁷ While the protein does not form silica *in vitro*, it does direct the morphology of silica formed in the presence of natSil-1A or long chain polyamines. When natSil-2 is combined with natSil-1A or polyamines, a porous silica matrix is formed rapidly, with pore sizes ranging from 100-1000 nm, comparable to biosilica.¹⁸ NatSil-2 also acted as an inhibitor at higher concentrations, leading the researchers to conclude that natSil-2 may regulate silica formation. Unfortunately, a gene was unable to be cloned for natSil-2, so the specific amino acid sequence responsible for morphology control could not be isolated. However, the amino acid composition was analyzed by phenyl isothiocyanate derivation followed by HPLC to separate the amino acids and

determine the relative amounts. Electrospray mass spectrometry (ESI-MS) was also used to identify modified amino acids not detected by isothiocyanate derivation.¹⁷ NatSil-2 has a high concentration of glycine and hydroxyamino acids similar to natSil-1A; however, unlike natSil-1A there is also a considerable amount of methionine and leucine present.⁶ Even though lysines with long chain polyamine modifications were found in high concentrations similar to natSil-1A, natSil-2 was unable to form silica nanoparticles, indicating that the long chain polyamine moieties in natSil-2 may just be devoted to the electrostatic assembly of the peptide.¹⁷

The R5 Peptide

A synthetic silaffin derived from a repeat unit of NatSil-1A, the R5 peptide SSKKSGSYSGSKGSKRRIL (**1**), also precipitates silica under ambient, aqueous conditions.² In contrast to the post-translationally modified peptide, the R5 peptide forms silica at pH 7. A site-directed mutagenesis study by Wright and Knecht indicates that several truncated forms of the R5 peptide also produce silica nanoparticles (**Table 3**).¹⁰ Initially, two regions of the R5 peptide, SSKKSGSY (**2**) and SGSKGSKRRIL (**3**), were analyzed. Truncate 3 and the R5 peptide produced similar amounts of silica, while truncate 2 formed considerably less. However, silica precipitating activity returned if the RRIL was attached to either the N-terminus or C-terminus of **3**. According to DLS data the R5 peptide self-assembles into a structure of about 825 nm. Truncates **3** and **7** form self assembled structures that are roughly 700 nm and 925 nm in diameter; however, peptides lacking of the RRIL motif do not self assemble in solution. The RRIL motif is proposed to be responsible for the self assembled structure with this structure

Table 3: Silica Precipitating ability of the R5 peptide and truncates¹⁰

Peptide	Peptide Sequence	Specific activity (nmoles TiO ₂ per min • nmole peptide)	Particle size (nm)
1	SSKKSGSYSGSKGSKRRIL	3.59 ± 0.16	250-450
2	SSKKSGSY	0.08 ± 0.05	n/a
3	SGSKGSKRRIL	3.35 ± 0.25	180-400
4	KSGSYSGSKGSKRRIL	3.29 ± 0.21	125-200
5	SGSKGSKRR	2.70 ± 0.19	150-300
6	SSKKSGSYSGSKGSK	1.09 ± 0.23	85-130
7	LIRRSSKKSGSY	3.17 ± 0.22	60-300
8	SSKKSGSYRRIL	2.88 ± 0.32	60-300
9	SGSKGSKAAIL	0.24 ± 0.16	n/a
10	SGSKGSKEEIL	0.17 ± 0.08	n/a
11	SGSKGSKNNIL	0.16 ± 0.07	n/a

resulting in a high local concentration of amines, facilitating silica production. Longer peptides lacking the R5 motif (**5** and **6**) displayed silica precipitating activity, albeit at a lower level, which is not surprising since small amine containing molecules have been shown to produce silica¹⁹.

Site directed mutagenesis of the R5 peptide (**9-11**) studied the effects of hydrogen bonding, linear amine groups, and charge on the biosilification process. The arginines in

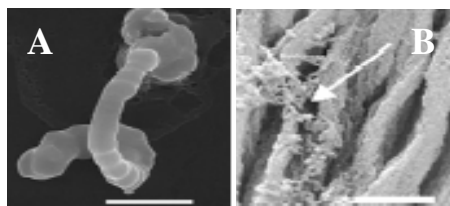


Figure 16: A) SEM of arch-like silica structures formed from flowing nitrogen through the reaction. B) SEM of silica fibrous structures formed when shear is applied.²⁰

the RRIL motif were replaced with alanines, aspartic acid, or asparagines with minimal silica precipitation as a result. The lack of silica condensation indicates that the position of the guanidinium groups with respect to the hydrophobic leucine and isoleucine may function in the self assembly process of the R5 peptide. Silica produced from the R5 peptide and truncates range in diameter from 60 to 400 nm.¹⁰

Morphology Control

External conditions can be varied in solution to change the morphology of the silica formed in the presence of the R5 peptide. In an attempt to duplicate the intricate silica structures that diatoms produce, Naik and coworkers have investigated silica formation under varied mechanical conditions.²⁰ When nitrogen gas was slowly bubbled through the reaction vessel during the biosilification reaction, arched silica structures formed (**Figure 16 A**). The structures are composed of discernable silica spheres approximately 500 nm in diameter. An interface between the forming silica nanospheres and the nitrogen bubbles is proposed to direct the formation of the interconnected arch-like structures. As expected, silica production was not observed in control reactions lacking the R5 peptide. Additionally, when shear was applied during the R5

condensation reaction, fibers of silica were formed (**Figure 16 B**). Again, the authors suggest that the liquid/air/tube interface is proposed to direct the morphology of the forming silica nanoparticles. SEM analysis of the fibers shows that they are actually composed of smaller fibers ranging from 100 to 300 nm in diameter and silica spheres.²⁰

By combining the R5 peptide and a spider silk protein, films and fibers can be produced by film casting or electrospinning the proteins. Foo and coworkers designed a novel silk fusion protein that incorporated the R5 peptide into domains of the Major Ampullate Spidroin 1 (MaSp1) protein from *Nephila calvipes* spider silk.²¹ Major ampullate dragline silk has unique mechanical and physical properties such as strength comparable to Kevlar, making it interesting for materials applications.²² Films of the fusion proteins were cast and treated with methanol to induce β -sheet formation.²¹ The morphology of the silk protein films lacking the R5 peptide did not exhibit any change when exposed to silicic acid. Silica nanoparticles with sizes ranging from .5 to 2 μm were formed in the presence of the fusion protein with the R5 peptide attached to the C-terminus. Thermal analysis of the nanoparticles determined that approximately 90% of the nanocomposite consisted of organic material, while only 10% was silica, indicating that the protein acts as a scaffold for silica formation. Electrospinning of the proteins into fibers resulted in much smaller nanoparticles, 200 to 400 nm in diameter. If the fibers are electrospun during the biosilification polymerization, then the silica coats the fibers.²¹ By controlling the process of fiber assembly, the morphology of biosilica can be altered to include silica fibers.

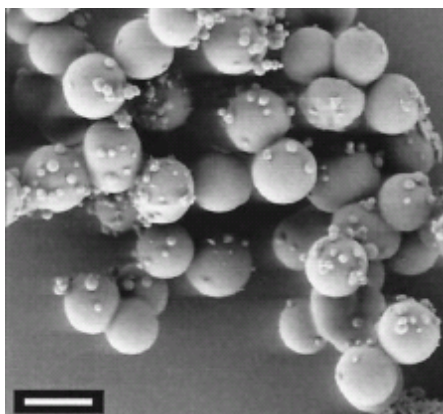


Figure 17: Silica nanoparticles formed from polyamines isolated from *N. angularis* diatom, scale bar 1 μm .⁴

Polymers

Diatoms not only contain silica precipitating peptides that have been functionalized with polyamines, but they also contain free polyamines located in the cell wall.^{2,4} The polyamines are long chains of N-methyl-propylamine attached to a putrescine.^{2,4} The polyamines isolated from the diatoms have been shown to form silica spheres in vitro from the monosilicic acid precursor (**Figure 17**).⁴ Several polymers have been utilized for the catalysis of silica including poly-L-lysine (PLL)^{5,23}, poly-L-arginine^{24,25}, poly(allylamine hydrochloride) (PAA)²⁶, 2-(dimethylamino)ethyl methacrylate (DMAEMA)²⁷, and several block copolypeptides.²⁸ Additionally, PLL has been used as templates for GeO_2 .⁸ In general, all the polymers that have been used to synthesize silica and GeO_2 have been cationic, similar to silaffins and silicateins. Furthermore, several studies have investigated the ability of polymers to control the nanoparticle size, pore size, and structure of metal oxide nanoparticles. The molecular

weight of the polymer, secondary structure, and functional groups of polymers are instrumental in controlling silica nanoparticle morphology.²⁸⁻³¹

Synthesis of Metal Oxides

Patwardhan and coworkers have investigated the ability of PLL, poly-L-arginine, and PAA to precipitate silica from hydrolyzed tetramethyl orthosilicate (TMOS).^{5,24-26,32} PLL forms silica nanospheres, ranging in size from 40 to 600 nm, rapidly when silicic acid was introduced in the solution.⁵ EDS was used to identify the composition of the nanoparticles, which was mostly silica and oxygen with smaller peaks of sodium, magnesium, phosphate, and potassium corresponding to the buffer solution.⁵ Poly-L-arginine also forms silica nanoparticles that have been identified using SEM and EDS.²⁵ In general, as the molecular weight of the polymer decreases, the nanoparticles become more defined. For example, poly-L-arginine with an average molecular weight of 55,300 g/mol produces interconnected silica nanoparticles that are less than 100 nm in diameter. When poly-L-arginine with a molecular weight of 13,000 g/mol is used, defined nanoparticles with a diameter of 300 to 500 nm form. An opposite trend was observed when PAA was used as the template for biosilicification.^{24,26} Silica spheres ranging in diameter from 500 to 3000 nm in diameter were formed when 70,000 g/mol PAA was used as a template. In contrast, the size of silica spheres formed in the presence of lower molecular weight PAA, 15,000 g/mole, were between 50 to 100 nm. Additionally, when shear force is applied to the reaction, elongated silica nanostructures form that are 1.5 to 2 μm with a diameter of 100 to 200 nm.³³

Morphological Control

Polymers have been used to not only synthesize silica, but to investigate chemical and physical properties of the metal oxide, as well as external effects on silica formation. Control of the nanoparticle pore size, silica size, and architecture are particularly important for drug delivery device development. Previously, silica had not been used as drug delivery devices because the high synthetic temperatures are not compatible with organic molecules and there is a lack of control of the structure of the nanoparticle.³⁴

Morse and coworkers have investigated the silica precipitating activity of amino acid polymers and copolymers, as well as their ability to direct the shape of the resultant silica.²⁸ Single amino acid polymers of L-lysine, L-histidine, D/L-serine, L-threonine, and L-glutamic acid did not precipitate silica. Additionally, mixtures of the individual polymers did not form silica nanospheres, with the exception of poly(L-cysteine) in an

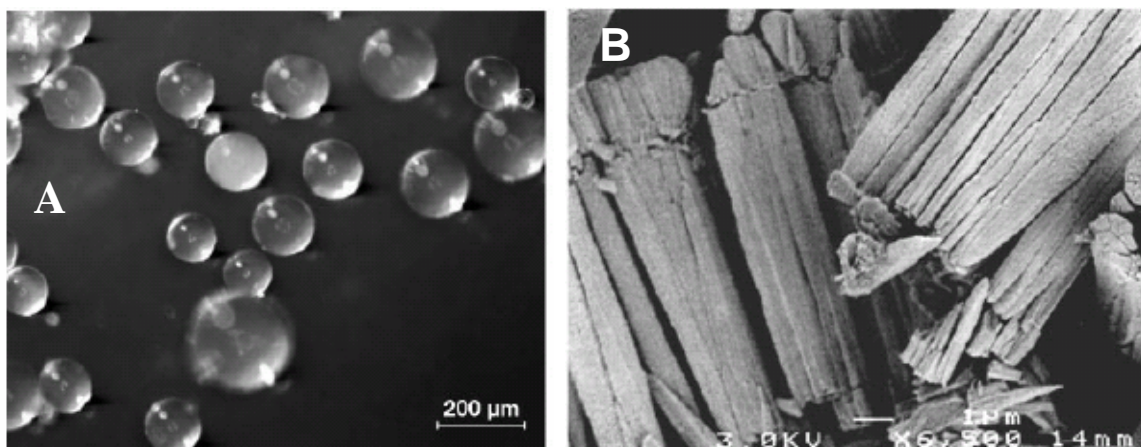


Figure 18: A) Silica nanoparticles formed from poly(L-cysteine₃₀-L-lysine₂₀₀) under nitrogen. B) Silica columns formed from poly(L-cysteine₃₀-L-lysine₂₀₀) in air.²⁸

anaerobic environment. The nucleophilic nature of the sulphhydryl group is proposed to facilitate condensation of the silicic acid. In an aerobic environment, disulfide bonds form, preventing the hydrolysis of TEOS.²⁸

Block copolymers of L-cysteine with L-glutamic acid or L-lysine were synthesized to study the effects of a combination of cationic and anionic amino acid groups.²⁸ Similar to silicatein and the R5 peptide, copolymers containing the cationic residue L-lysine result in silica precipitation. On the other hand, copolymers of L-cysteine and L-glutamic acid did not produce silica. The anionic effect of L-glutamic acid may repel the negative precursor, preventing polymerization. The shape of the silica produced from the copolymers in the presence of nitrogen and under air was drastically different. Under nitrogen, poly(L-cysteine₃₀-L-lysine₂₀₀) self assembled into a structure about 600 nm in diameter according to DLS, and upon addition of TEOS, transparent silica nanospheres approximately 100 nm in diameter formed (**Figure 18 A**). In the presence of oxygen, the disulfide bonds of the cysteine crosslink, resulting in a self assembled structure of about 1300 nm, and exposure to TEOS results in the formation of silica columns (**Figure 18 B**). Block copolymers of different lengths were studied to determine if the morphology of the silica could be controlled. Decreasing the length of the cysteine block or increasing the length of the lysine block resulted in silica spheres similar to those formed by poly(L-cysteine₃₀-b-L-lysine₂₀₀). However, when the length of the cysteine block was increased, the silica nanoparticles formed were elongated rather than spherical.²⁸ The amino acid composition of the polymer can be tailored to form specific nanostructures, increasing the versatility of the nanoparticles formed.

Similar to the R5 peptide biosilification pathway, several external factors can be altered that influence the formation of nanoparticles. The morphology of silica structure can be altered by PLL secondary structure, exposure of PLL to an electric field, exposure of PLL to a hydrodynamic field, or by increasing the amount of cations present in solution.^{9,29,35} The effect of PLL molecular weight on silica structures was investigated by Rodriguez and coworkers.²⁹ Silica structures form from PLL with a variety of molecular weights (2.9, 27.4, 57.9, 240.1, and 708.5 kD). PLL with a molecular weight of 2.9 kD formed silica nanoparticles approximately 500 nm in diameter while the higher molecular weight polymers (27.4 to 708.5 kD) formed platelets that range in size from 300 to 2000 nm.²⁹ Circular dichroism (CD) experiments indicate that the secondary structure of the polymers dictates the morphology of the silica structures.^{9,35} PLL undergoes a transformation from a random coil conformation to an alpha helix in the presence of silicic acid, resulting in silica platelets. Lower molecular weight PLL does not undergo the conformation change and silica spheres form.^{9,35} Further work by Parwarden and coworkers indicate that the handedness of the helix does not affect silica formation.⁹

Rodriguez and coworkers exposed variable molecular weight PLL to an electrostatic field with a potential -1.0 V for 20 minutes, then introduced silicic acid.²⁹ Lower molecular weight PLL form silica nanoparticles ranging from 380 to 760 nm, while mid-weight PLL (27.4 and 57.9 kD) produces platelets with a size range of 121 to 3000 nm. In contrast, high molecular weight polymers (240.1 and 708.5 kD) template formed fibrous silica nanostructures. Rodriguez and coworkers propose that the electrostatic field changes the conformation of the PLL, resulting in the different silica

structures.²⁹ However, to date, CD experiments have not been conducted to confirm this hypothesis.

The effect of hydrodynamic forces after the application of electrostatic fields also produced altered silica morphologies.²⁹ PLL was deposited on a spherical cathode utilizing the previously described electric field. Immediately after the addition of silicic acid, the cathode was spun at a variable angular velocity. The silica produced from the 2.9 kD PLL was branched, while the 27.4, 57.9, and 240.1 kD PLL templated silica formed plates with a size range of 65 nm to 3000 nm. Additionally, silica platelets formed from 708.5 kD PLL; however, the size was much larger with a range of 2120 to 7500 nm. The morphology of the forming silica nanoparticles can be altered by external forces, as was also the case in the presence of hydrodynamic flow.²⁹

Alternate Substrates

In addition to forming silica nanoparticles, polymers have also been used to form GeO₂ nanoparticles.⁸ GeO₂ was produced in the presence of PAA and PLL when either tetra(iso-propoxy)germane or germanium (IV) isopropoxide were introduced into the solution. As expected, in the absence of either polymer, no GeO₂ formed. Three approximate sizes of nanoparticles (400 nm, 1 μm and 3 μm) were observed in the SEM images of GeO₂ nanoparticles synthesized with PAA. Similar to the silica nanoparticles formed with PAA, when the GeO₂ reaction is stirred instead of shaken, elongated structures form. The composition of the GeO₂ nanoparticles was confirmed with EDS. No peaks were present in the XRD analysis, indicating that the nanoparticles were

amorphous. GeO_2 particles formed in the presence of PLL are currently being investigated.⁸

Increasingly, biomimetic approaches are being applied to the synthesis of a wide variety of abiological materials.^{8,36-42} The ability of both ferritin and silicatein to mineralize non-natural metal oxides has been extensively investigated.^{39,42-45} However, the ability of the silica precipitating R5 peptide to form alternate metal oxides has not been investigated. In contrast the typical high temperatures, pressures and caustic chemicals required for the chemical synthesis of TiO_2 , the R5 peptide and the polymer PLL condense nanoparticles of TiO_2 from a titanium bis(ammonia lactato) dihydroxide (TBALDH, $[\text{CH}_3\text{CH}(\text{O}^-)\text{CO}_2\text{NH}_4]_2\text{Ti}(\text{OH})_2$) precursor under ambient conditions.⁴⁶⁻⁴⁹ The resulting nanoparticles were characterized by SEM, EDS, IR, and XRD. The results presented here expand the known reactivity of this biomimetic peptide assembly and provide methods that can be readily adapted for a range of metal oxide syntheses.⁴⁹

Experimental

Peptide Synthesis: All peptides were synthesized on single substituted 2-chlorotrityl resins (Synpep and Adv. Chemtech) using an Advanced Chemtech Apex 396 DC automated peptide synthesizer. A standard 9-Fluorenylmethoxycarbonyl (Fmoc) and tert-butyl protection scheme was used.⁵⁰ All coupling were carried out with 5 equivalents excess to the resin capacity. Couplings were achieved by the addition of Fmoc amino acid, 2-(1H-benzotriazole-1-yl)-1,1,3,3,-tetramethyluronium hexafluorophosphate (HBTU; Anaspec), 1-hydroxybenzotriazole (HOBt; Anaspec), and diisopropylethylamine (DIPEA; Adv. Chemtech) (1:1:1:2) followed by mixing for 1

hour. Fmoc was removed with 25% piperidine in a dimethyl formamide (v/v) solution. Peptides were cleaved in 1.5 mL of trifluoroacetic acid (TFA); anisole; thianisole ; 1,2 ethanedithiol (EDT) (90:5:3:2) per 100 mg of resin and collected with cold diethyl ether precipitation followed by centrifugation and 3 washes of diethyl ether. The peptides were purified using reverse phase HPLC on a Waters Prep LC 4000 with water (0.1% TFA) and acetonitrile (0.1% TFA) on a Waters 25 mm module C₁₈ column and a Waters 2487 Dual λ absorbance detector (210 nm and 254 nm). The identity of the peptides were confirmed using a matrix assisted laser desorption ionization mass spectrometry with time of flight detector (MALDI-TOF). Purified peptides were lyophilized (Labconco Freezone 4.5) and stored at -40°C.

TiO₂ Precipitation Assay: Titanium (IV) bis(ammonium lactato) dihydroxide (20 μ L, 1M) was added to 200 μ L of variable concentration of R5 peptide or PLL·HBr (average molecular weight: 55,000 g/mol) dissolved in either phosphate buffer or water and shaken for 5 minutes. The samples were centrifuged for 5 minutes at 10,000 RPM and washed three times with deionized water. To examine the effect of pH on TiO₂ formation (supplementary information), fresh solutions, using phosphate buffers ranging from pH 5.5 to 7.5, were used. All other experiments were conducted at a pH of 7.5.

Titanium Quantitation: The 5-chlorosalicylic acid assay was used to quantify TiO₂ production.⁵¹ TiO₂ was dissolved in 1 mL of concentrated sulfuric acid and incubated at 95°C for 2 hours. 5-chlorosalicylic acid (2.5 mL of 2.5% in ethanol), sodium perchlorate (2.5 mL, 1 M), ethanol (7.5 mL), and deionized water (10 mL) were added to the dissolved titanium solution. The solution was adjusted to pH 4 using concentrated NH₄OH and diluted to 50 mL using deionized water. The colorimetric product was

monitored at 355 nm using an Agilent 8453 UV-Vis spectrophotometer and quantified using a standard curve.

Template Characterization: All DLS measurements were conducted on a Malvern Nano Series Zetasizer with a 633 nm laser. The duration of the individual scans were 60s and each measurement was an accumulation of 10 scans. Circular dichroism spectra were collected on an Aviv 215 CD spectrophotometer over the wavelength range of 180 to 230 nm with a resolution of 3 nm and a bandwidth of 1 nm. The samples were analyzed in a strain free quartz cell with a 0.5 s averaging time. For in situ experiments, 30 μ L of 1M TBALDH was added to 250 μ L of 7.5 mg/mL PLL solution in either water or phosphate buffer. An average of 20 scans was taken and phosphate and TBALDH blanks were manually subtracted from the spectra.

Nanoparticle Characterization: Powder X-ray diffraction (XRD) scans were obtained on a Scintag X₁ θ/θ automated powder diffractometer with a Cu target, a Peltier-cooled solid state detector, and a zero background Si(510) sample support. The step size was 0.02, preset time 25 s. All samples were scanned from 20 to 60 2θ . For high temperature runs, the samples (15 mg) were heated in a sealed quartz tube with nitrogen flowing in a 79300 Thermolyne tube furnace. All peaks were identified according to JCPDS. For crystal size analysis, each XRD scan was corrected for background scattering and was stripped of the $K_{\alpha 2}$ portion of the diffracted intensity using the DMSNT software (version 1.30c), provided by Scintag. Observed peaks were fitted with a profile function to extract the full-width-at-half-maximum (fwhm) values. Average crystallite size, L , was calculated from Scherrer's equation, $L = K\lambda/\beta\cos\theta_B$, assuming that peak broadening arises from size effects only (where β is the peak at fwhm

measured in radians on the 2θ scale, λ is the wavelength of X-rays used, θ_B is the Bragg angle for the measured hkl peak, and K is a constant equal to 0.90 for L taken as the volume-average crystallite dimension perpendicular to the hkl diffraction plane). Additionally, the nanoparticles were examined by a Hitachi S4200 scanning electron microscope operating at variable voltages. The samples were suspended in ethanol and added dropwise to an aluminum SEM puck (Ted Pella Inc.). After evaporation of the solvent, the samples were sputter coated with a thin layer of gold (Pelco Model 3 Sputtering Instrument) to avoid charging. The nanoparticles were analyzed on a Phillips CM 20T transmission electron microscope (TEM) operating at 200 kV. Samples were prepared by pipetting the nanoparticle solution on a 3 mm diameter nickel or copper grid covered with carbon film as a substrate (SPI supplies) and allowed to evaporate. The TEM contains an EDAX DX-4 package for energy dispersive X-ray spectrometry (EDS). Samples were tilted at a 15° angle for EDS analysis.

Results and Discussion

R5 Peptide Mediated Formation of TiO_2

The R5 peptide catalyzed the condensation of an aqueous solution of TBALDH to form amorphous TiO_2 nanoparticles at room temperature in a concentration dependent fashion (**Figure 19**). As the concentration of peptide increased, the amount of TiO_2 increased linearly until approximately 6 mg/mL, where the yield approached 5000 nmols of TiO_2 . In the absence of peptide, no precipitate was observed at room temperature. Previous

studies, using the aqueous TBALDH precursor alone, report no formation of TiO_2 at temperatures lower than 100°C .⁴⁸ The specific activity of the R5 peptide was

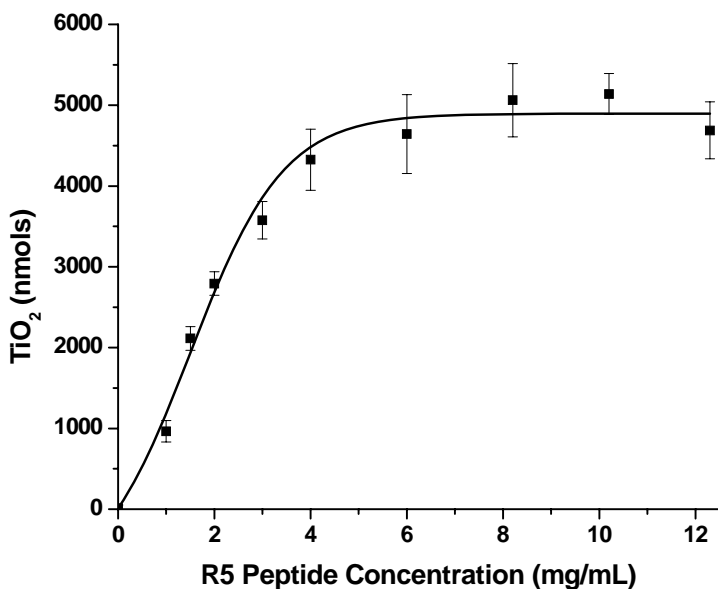


Figure 19: TiO_2 production as a function of R5 concentration. Reactions were run for 5 minutes in 100 mM phosphate buffer, pH 7.5 as detailed in the experimental section.

2.16 ± 0.23 nmols of titanium per min-nmol peptide, comparable to the silica specific activity of the R5 peptide reported by Knecht and Wright (**Table 4**),¹⁰ with a molar ratio of titanium to R5 peptide of approximately 11. This is comparable to both the molar ratio of silica to the R5 peptide or NatSil1A, which has been reported as 13 and 12, respectively.^{2,10} Approximately 20% of the available precursor was converted to TiO_2 , suggesting that the precipitating TiO_2 nanoparticles may have removed the catalytic

Table 4: Characterization of TiO_2 precipitating peptides and the resulting nanoparticles.

Peptide Template ^a	Template Size ^b (nm)	Specific Activity ^c	Particle Size (nm)
SSKKSGSYSGSKGSKRRIL	758 ± 82	2.16 ± 0.23	50 ± 20
SSKKSGSYSGSKGSKRRIL in H₂O	746 ± 150	0.75 ± 0.4	50 ± 20
SSKKSGSY	n/a	0.16 ± 0.03	n/a
SGSKGSKRRIL	637 ± 117	1.63 ± 0.09	60 ± 30
SSKKSGSYRRIL	567 ± 40	1.17 ± 0.11	50 ± 20
PLL	1570 ± 192	27.0 ± 2.0	140 ± 60
PLL in H₂O	797 ± 136	31.4 ± 5.6	40 ± 20

^aunless specified, reaction was performed in 100 mM phosphate buffer, pH 7.5 ^bas measured by DLS ^cSpecific activity is reported as nmoles TiO₂ per min • nmole peptide

peptide from solution by encapsulation. The pH profile of TiO₂ production reached a maximum between pH 6.0 to 7.5 (**Figure 20**) with well-defined nanoparticles at pH 7.5. One notable difference between the R5 mediated formation of SiO₂ and TiO₂ was that the R5 peptide exhibited TiO₂ precipitating activity in the absence of phosphate ions, albeit at reduced levels.^{15,16} Given the noted similarity of the reactivity space occupied by the R5 assembly, it is likely that condensation of the TBALDH precursor occurs in a fashion similar to that of monosilicic acid. As has been suggested by several groups,^{2,10} the peptide assembly can concentrate the anionic precursor through a combination of electrostatics and hydrogen bonding to promote condensation. Subsequently, the amine

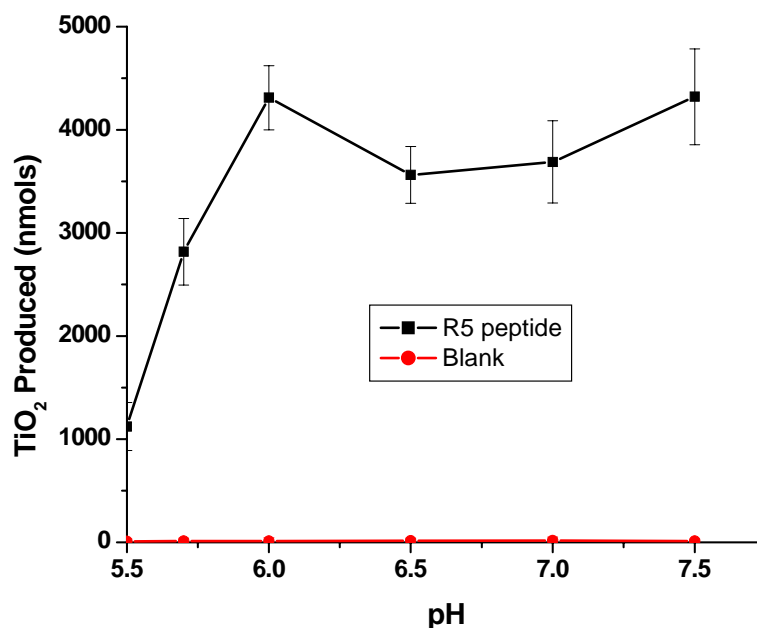


Figure 20: Titanium dioxide production as a function of pH.

rich peptide template can be seen to act as a general acid/base catalyst by protonating the coordinated lactate ligand and priming the precursor for subsequent hydrolysis. To explore the role of the R5 peptide in TiO₂ formation, a series of related peptides was examined (**Table 4**). While truncates SSKKSGSYRRIL (**1**) and SGSKGSKRRIL (**2**) precipitated TiO₂, the RRIL deficient truncate SSKKSGSY (**3**), was inactive. The lack of TiO₂ precipitation catalyzed by **3** suggests that the self assembled peptide structure is vital for the production of TiO₂ in a manner similar to the R5 mediated silica results of Knecht and Wright.¹⁰ DLS experiments of the self assembled peptide structure reveal no self assembly for truncates without the RRIL motif or mutations within the motif.¹⁰ Consequently, the RRIL motif may be seen to mediate the assembly of the R5 template

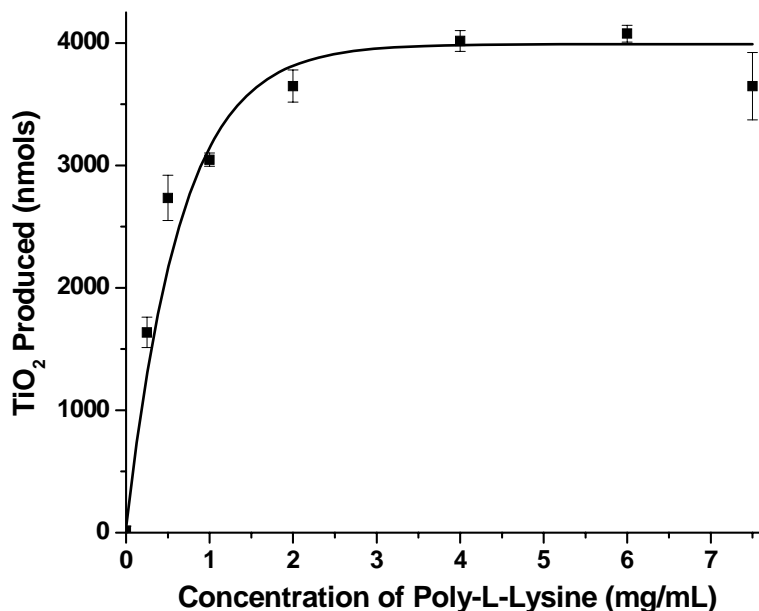


Figure 21: TiO₂ produced as a function of PLL concentration. Reactions were run for 5 minutes in 100 mM phosphate buffer, pH 7.5 as detailed in the experimental section.

creating a highly cationic complex capable of interacting with multiple anionic TBALDH precursor molecules and driving subsequent condensation.

PLL Mediated Formation of TiO₂

PLL has been examined as a template for the biomimetic synthesis of metal oxides including silica and germanium oxide.^{5,8,23} When TBALDH was added to variable concentrations of PLL in either phosphate buffer or water, a white precipitate formed rapidly. No precipitate was observed in the absence of polymer. As concentration of PLL increased up to approximately 2 mg/mL, the amount of TiO₂

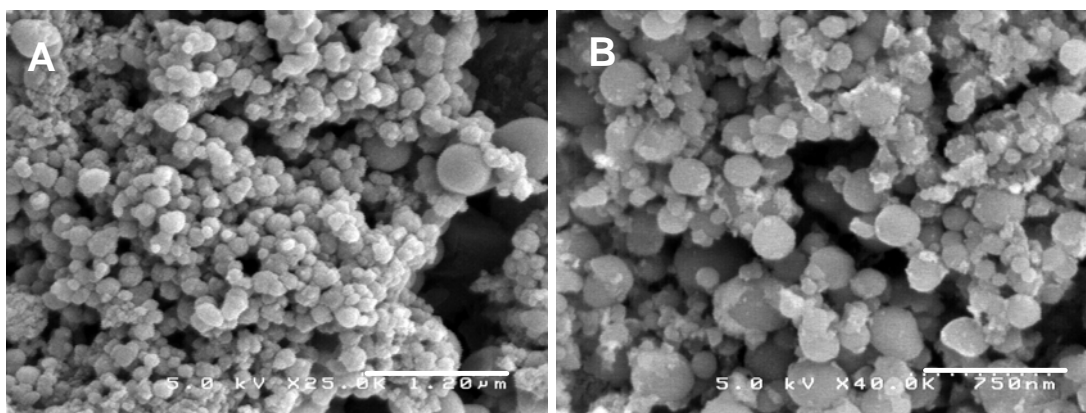


Figure 22: A) SEM micrograph of R5 templated TiO₂ nanoparticles (scale bar 1.20 μm). B) SEM micrograph of PLL templated TiO₂ nanoparticles (scale bar 750 nm). Particles were obtained by reacting 20 μL of 1M TBALDH with 200 μL of 2 mM R5 or PLL dissolved in 100 mM phosphate buffer, pH 7.5.

produced increased linearly until production plateaued near 4000 nmols of TiO₂ (**Figure 21**). The specific activity of PLL is 27.0 ± 2.0 nmols of titanium per min·nmol peptide (**Table 4**). However, when the specific activity of the R5 peptide and PLL is normalized to the number of primary amines available, it is roughly equivalent. During the course of the reaction, 20% of the starting material formed TiO₂. Analogous to the R5 mediated TiO₂ formation, TiO₂ is also formed when phosphate ions are absent. DLS studies show that the polymer is approximately the size of the self assembled structure of the R5 peptide. The reactivity and self-assembled nature of the PLL template and the R5 peptide suggests that the mechanism of metal oxide formation is similar.^{8,52,53}

Nanoparticle Characterization

SEM images of R5 peptide templated TiO₂ showed a Gaussian size distribution with a mean of 50 ± 20 nm (**Figure 22 A**). The presence of phosphate did not affect the

size or morphology of the nanoparticles. EDS of R5 templated TiO₂ particles confirmed the presence of titanium (**Appendix A**). Samples synthesized in phosphate buffer displayed an additional phosphate emission line, indicating the association of phosphate with the nanoparticle. IR spectra of R5 templated TiO₂ nanoparticles synthesized in water and phosphate buffer revealed the peptide amide stretching frequency at 1640 cm⁻¹, indicating the association of R5 peptide with the nanoparticles (**Appendix A**).⁵⁴ Additionally, particles prepared in phosphate buffer showed a broad transition at 998 cm⁻¹, attributed to the P-O vibration similar to that observed in other metal oxides synthesized in the presence of phosphate ions.⁵⁵⁻⁵⁸ The presence of the peptide frequencies in the IR, as well as the fact that only 20% of the starting material is consumed in the reaction, suggests that the peptide may be encapsulated in the forming nanoparticles.⁵⁹

The nanoparticles formed in the presence of PLL displayed a Gaussian size distribution, with an average of approximately 140 ± 60 nm, according to SEM images (**Figure 22 B**). In the case of PLL, it has been suggested that the secondary structure of the polymer can direct the morphology of the nanoparticles.^{9,35} PLL with chain lengths ranging from 100 to 840 amino acids results in the formation of silica platelets, while silica nanospheres are formed from PLL with chain lengths under 100 amino acids.^{9,35} Previously, circular dichroism (CD) studies have shown that in the presence of phosphate and silicic acid, PLL with a chain length above 100 amino acids adopts an α -helical structure, resulting in the formation of silica platelets.^{9,35} In contrast, CD spectra of PLL with 266 amino acids in the presence of TBALDH showed little, if any, indications of secondary structure, consistent with the formation of spherical nanoparticles

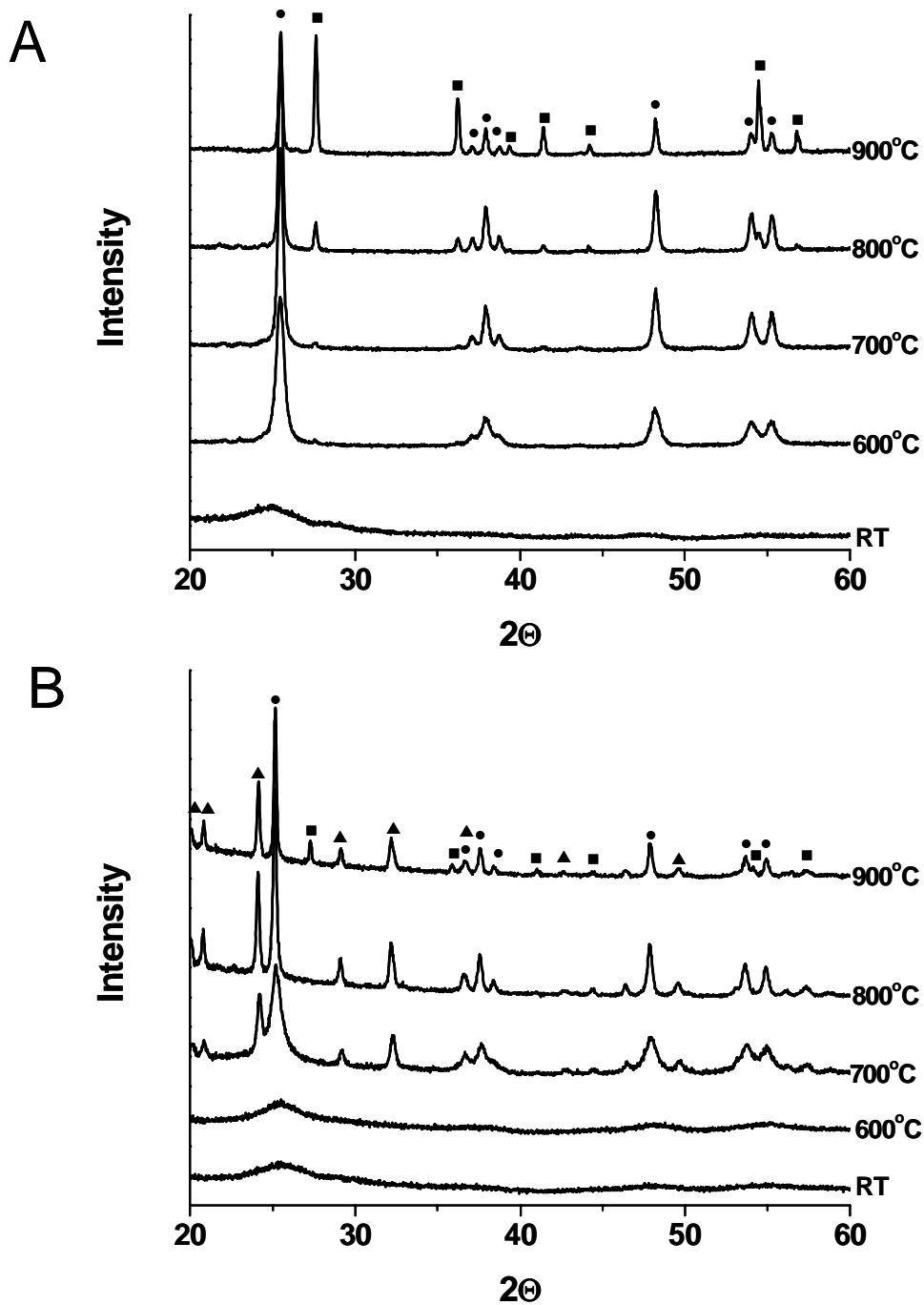


Figure 23: A) Variable temperature XRD of R5 templated TiO_2 synthesized in water. B) Variable temperature XRD of R5 templated TiO_2 synthesized in 100 mM phosphate buffer, pH 7.5. (● anatase, ■ rutile, and ▲ titanium phosphate)

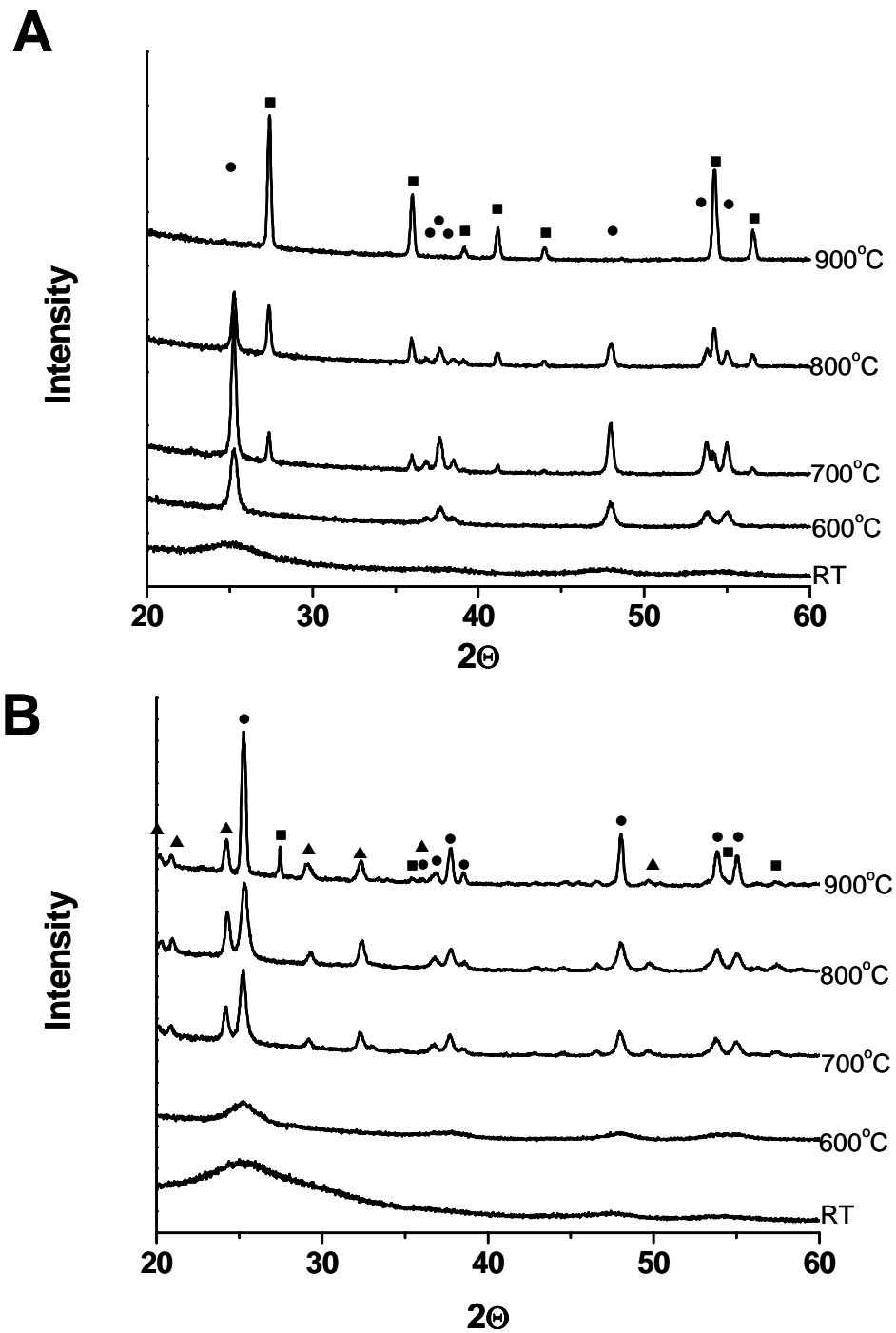


Figure 24: A) Variable temperature XRD of PLL templated TiO_2 in the presence of water. B) Variable temperature XRD of PLL templated TiO_2 synthesized in 100 mM phosphate buffer, pH 7.5 (● anatase, ■ rutile, and ▲ titanium phosphate).

(**Appendix A**). EDS of the nanoparticles confirmed the presence of titanium, as well as phosphate, if buffer was present (**Appendix A**).

X-Ray Diffraction Analysis

An X-ray diffraction study of the phase transition in R5 and PLL templated TiO₂ synthesized in the absence and presence of phosphate was performed (**Figure 23 and 24**) with results summarized in **Table 5**. The transition from anatase to rutile has been generally classified as an intermediate topotactic phase transition, with two Ti-O bonds breaking and reforming in the transition from distorted face centered cubic anatase to distorted hexagonal closest packed rutile.⁶⁰ Observed increases in crystallite sizes from anatase to rutile are consistent with the proposed mechanism of TiO₂ phase transition. R5 templated TiO₂ synthesized *sans* phosphate buffer was amorphous at room temperature (**Figure 23 A**). The crystalline anatase phase was observed at 600°C. At 700°C, the phase transition from anatase to rutile was evident. At 900°C, approximately 50% of the anatase phase is converted to rutile. PLL templated TiO₂ was also poorly crystalline at room temperature (**Figure 24 A**). Similar to R5 TiO₂, the anatase phase is present at 600°C and the transition from anatase to rutile occurs at 700°C. Unlike the R5 templated TiO₂, anatase to rutile phase conversion is complete at 900°C. In contrast, for TiO₂ templated on protein fibers of silicatein, the anatase to rutile phase transition occurred at 825°C, 125°C higher than observed here.³⁹ This delay in transition temperature was previously attributed to the presence of carbon^{61,62} from the silicatein

filaments or the precursor. This seems unlikely, however, as the R5 template or PLL would also have similar amounts of carbon from constituent amino acids. A more likely

Table 5: Scherrer's analysis of R5 peptide and PLL templated TiO₂

Peptide Template	Temperature	Water		Phosphate Buffer (100 mM, pH 7.5)		
		Anatase Size (nm)	Rutile Size (nm)	Anatase Size (nm)	Rutile Size (nm)	Ti ₄ P ₆ O ₂₃ Size (nm)
R5 peptide	25°C	n/a	n/a	n/a	n/a	n/a
	600°C	12.9 ± 2.5	n/a	2.58 ± 0.41	n/a	n/a
	700°C	20.1 ± 1.4	n/a	10.8 ± 0.25	n/a	26.2 ± 0.55
	800°C	29.7 ± 0.63	42.3 ± 0.89	28.6 ± 0.87	n/a	38.4 ± 1.2
	900°C	37.3 ± 0.52	53.1 ± 0.74	31.1 ± 1.4	49.7 ± 2.3	43.0 ± 1.9
PLL	25°C	n/a	n/a	n/a	n/a	n/a
	600°C	14.7 ± 2.4	n/a	3.65 ± 0.72	n/a	n/a
	700°C	26.5 ± 3.2	27.2 ± 2.23	17.4 ± 1.36	n/a	21.7 ± 2.3
	800°C	28.6 ± 1.60	34.9 ± 1.82	17.6 ± 0.58	n/a	24.9 ± 0.87
	900°C	n/a	36.1 ± 1.69	25.8 ± 1.52	67.9 ± 3.2	25.5 ± 1.5

n/a indicates that no peak was present

explanation, as proposed by Morse *et al.*, is that the strain energies imposed from the interacting template result in the delay of transition temperature, suggesting tighter interactions between the self-assembled peptide templates.³⁹

The XRD variable temperature study for PLL and R5 templated TiO₂ in phosphate buffer are remarkably similar. TiO₂ synthesized by either of the peptides in the presence of phosphate buffer is amorphous at room temperature (**Figure 23 B and 24 B**). Calcination of the sample revealed a crystalline anatase phase at 700°C. Additionally, a small amount of titanium phosphate (Ti₄P₆O₂₃) is formed at 700°C and higher temperatures. The formation of Ti₄P₆O₂₃ has been previously seen in deamination of NH₄Ti₂P₃O₁₂ at 770°C.^{63,64} Here, the release of NH₄⁺ from degradation of the R5 peptide or NH₄⁺ counter ion present from the precursor could facilitate the formation of Ti₄P₆O₂₃. At 900°C, there was a transition from anatase to rutile, an increase in transition temperature of some 200°C. Phosphate that has either been trapped, absorbed on the surface, or incorporated into the crystal lattice has been shown to inhibit movement of oxygen atoms necessary for the phase transition, thereby, increasing the transition temperature.⁶⁵ Such a mechanism would be consistent with these experimental observations.

Conclusions

The often extreme conditions of metal oxide synthesis can be limiting when working with biological materials or constructing delicate nanodevices. Increasingly, biomimetic

processing is being adapted for the synthesis of non-natural materials. For example, PLL has been used to form not only silica, but germanium dioxide.⁸ More recently, the R5 peptide has been used to form composite carbon nanotube/metal oxide structures.⁶⁶ Given that the proposed mechanism of silica formation by the R5 peptide is based on a combination of interactions that effectively concentrate the negatively charged silicate species at the peptide template primed to drive acid/base hydrolysis and condensation, the R5 peptide should be able to form alternative metal oxides as well. Using the non-natural precursor TBALDH, the R5 peptide assembly readily formed TiO₂ nanoparticles under ambient conditions. Additionally the interaction between the template and the TiO₂ modulated the anatase to rutile phase conversion, resulting in generally lower transition temperatures than other biogenic TiO₂. Similar behavior was observed for the primary amine rich PLL template. The ability of the R5 peptide to form other non-natural metal oxides is currently under investigation.

References

1. Kroger, N.; Lehmann, G.; Rachel, R.; Sumper, M., *Eur. J. Biochem.* **1997**, *250*, 99-105.
2. Kroger, N.; Deutzmann, R.; Sumper, M., *Science* **1999**, *286*, 1129-1132.
3. Kroger, N.; Deutzmann, R.; Bergsdorf, C.; Sumper, M., *EMBO J.* **1994**, *13*, 4676-4683.
4. Kroger, N.; Deutzmann, R.; Bergsdorf, C.; Sumper, M., *Proc. Natl. Acad. Sci.* **2000**, *97*, 14133-14138.
5. Patwardhan, S. V.; Mukherjee, N.; Clarson, S. J., *J. Inorg. Organomet. Polym.* **2002**, *11*, 193-198.
6. Kroger, N.; Deutzmann, R.; Sumper, M., *J. Biol. Chem.* **2001**, *276*, 26066-26070.

7. Noll, F.; Sumper, M.; Hampp, N., *Nano Letters* **2002**, *2*, 91-95.
8. Patwardhan, S. V.; Clarson, S. J., *Polymer* **2005**, *46*, 4474-4479.
9. Patwardhan, S. V.; Maheshwari, R.; Mukherjee, N.; Kiick, K. L.; Clarson, S. J., *Biomacromolecules* **2006**, *7*, 491-497.
10. Knecht, M. R.; Wright, D. W., *Chem. Comm.* **2003**, *24*, 3038-3039.
11. Kroger, N.; Bergsdorf, C.; Sumper, M., *Eur. J. Biochem.* **1996**, *239*, 259-264.
12. van der Poll, W. H.; Vrieling, E. G.; Gieskes, W. W. C., *J. Phycol.* **1999**, *35*, 1044-1053.
13. Vrieling, E. G.; Gieskes, W. W. C.; Beelen, T. P. M., *J. Phycol.* **1999**, *35*, 538-559.
14. Kroger, N.; Wetherbee, R., *Protist* **2000**, *151*, 263-273.
15. Sumper, M.; Kroger, N., *J. Mater. Chem.* **2004**, *14*, 2059-2065.
16. Kroger, N.; Lorenz, S.; Brunner, E.; Sumper, M., *Science* **2002**, *298*, 584-586.
17. Poulsen, N.; Sumper, M.; Kroger, N., *PNAS* **2003**, *100*, 12075-12080.
18. Pickett-Heaps, J.; Schmid, A. M. M.; Edgar, L. A. *Prog. in Phycol. Res.*; Biopress: Bristol, 1990; Vol. 7.
19. Roth, K. M.; Zhou, Y.; Yang, W.; Morse, D. E., *J. Am. Chem. Soc.* **2004**, *127*, 325-330.
20. Naik, R. R.; Whitlock, P. W.; Rodriguez, F.; Brott, L. L.; Glawe, D. D.; Clarson, S. J.; Stone, M. O., *Chem. Comm.* **2003**, *2*, 238-239.
21. Foo, C. W. P.; Patwardhan, S. V.; Belton, D. J.; Kitchel, B.; Anastasiades, D.; Huang, J.; Naik, R. R.; Perry, C. C.; Kaplan, D. L., *PNAS* **2006**, *103*, 9428-9433.
22. Rising, A.; Nimmervoll, H.; Grip, S.; Fernandez-Arias, A.; Storchenfeldt, E.; Knight, D. P.; Vollrath, F.; Engstrom, W., *Zoological Science* **2005**, *22*.
23. van Bommel, K. J. C.; Jung, J. H.; Shinkai, S., *Adv. Mater.* **2001**, *13*, 1472-1476.
24. Patwardhan, S. V.; Clarson, S. J., *Silicon Chemistry* **2002**, *1*, 207-214.
25. Patwardhan, S. V.; Clarson, S. J., *J. Inorg. Organomet. Polym.* **2003**, *13*, 193-203.

26. Patwardhan, S. V.; Mukherjee, N.; Clarson, S. J., *Silicon Chemistry* **2002**, *1*, 47-55.
27. Kim, D. J.; Lee, K.-B.; Chi, Y. S.; Kim, W.-J.; Paik, H.-j.; Choi, I. S., *Langmuir* **2004**, *20*, 7904-7906.
28. Cha, J. N.; Stucky, G. D.; Morse, D. E.; Deming, T. J., *Nature* **2000**, *403*, 289-292.
29. Rodriguez, F.; Glawe, D. D.; Naik, R. R.; Hallinan, K. P.; Stone, M. O., *Biomacromolecules* **2004**, *5*, 261-265.
30. Hawkins, K. M.; Wang, S. S.-S.; Ford, D. M.; Shantz, D. F., *J. Am. Chem. Soc.* **2004**, *126*, 9112-9119.
31. Tannenbaum, R.; Zubris, M.; Goldberg, E. P.; Reich, S.; Dan, N., *Macromolecules* **2005**, *38*, 4254-4259.
32. Patwardhan, S. V.; Clarson, S. J., *J. Inorg. Organomet. Polym.* **2003**, *13*, 49-53.
33. Patwardhan, S. V.; Mukherjee, N.; Clarson, S. J., *J. Inorg. Organomet. Polym.* **2002**, *11*, 117-121.
34. Barbe, C.; Bartlett, J.; Kong, L.; Finnie, K.; Lin, H. Q.; Larkin, M.; Calleja, S.; Bush, A.; Calleja, G., *Advanced Materials* **2004**, *16*, 1959-1966.
35. Tomczak, M. M.; Glawe, D. D.; Drummy, L. F.; Lawrence, C. G.; Stone, M. O.; Perry, C. C.; Pochan, D. J.; Deming, T. J.; Naik, R. R., *J. Am. Chem. Soc.* **2005**, *127*, 12577-12582.
36. Allen, M.; Willits, D.; Young, M.; Douglas, T., *Inorg. Chem* **2003**, *42*, 6300-6305.
37. Flynn, C. E.; Mao, C.; Hayhurst, A.; Williams, J. L.; Georgiou, G.; Iverson, B.; Belcher, A. M., *J. Mater. Chem.* **2003**, *13*, 2414-2421.
38. Okuda, M.; Iwahori, K.; Yamashita, I.; Yoshimura, H., *Biotechnology and Bioengineering* **2003**, *84*, 187-194.
39. Sumerel, J. L.; Yang, W.; Kisailus, D.; Weaver, J. C.; Choi, J. H.; Morse, D. E., *Chem. Mater.* **2003**, *12*, 4804-4809.
40. Dickerson, M. B.; Naik, R. R.; Stone, M. O.; Cai, Y.; Sandhage, K. H., *Chem. Comm.* **2004**, 1776-1777.

41. Hosein, H.-A.; Strongin, D. R.; Allen, M.; Douglas, T., *Langmuir* **2004**, *20*, 10283-10287.
42. Kisailus, D.; Choi, J. H.; Weaver, J. C.; Yang, W.; Morse, D. E., *Adv. Mater.* **2005**, *17*, 314-318.
43. Curnow, P.; Bessette, P. H.; Kisailus, D.; Murr, M. M.; Daugherty, P., S.; Morse, D. E., *J. Am. Chem. Soc.* **2005**, *127*, 15749-15755.
44. Douglas, T.; Young, M., *Adv. Mater.* **1999**, *11*, 679-681.
45. Douglas, T.; Stark, V. T., *Inorg. Chem* **2000**, *39*, 1828-1830.
46. Wold, A., *Chem. Mater.* **1993**, *5*, 280-283.
47. Trentler, T. J.; Denler, T. E.; Bertone, J. F.; Agrawal, A.; Colvin, V. L., *J. Am. Chem. Soc.* **1999**, *121*, 1613-1614.
48. Mockel, H.; Giersig, M.; Willig, F., *J. Mater. Chem.* **1999**, *9*, 3051-3056.
49. Sewell, S. L.; Wright, D. W., *Chem. Mater.* **2006**, *18*, 3108-3113.
50. Chan, W. C., White, P. D., Ed. *Fmoc Solid Phase Peptide Synthesis*; Oxford Univeristy Press: New York, 2000.
51. Abdel-Aziz, M. S.; Idriss, K. A.; Sedaira, H., *The Analyst* **1996**, *121*, 1079-1084.
52. Coradin, T.; Lopez, P. J., *ChemBioChem* **2003**, *4*, 251-259.
53. Coradin, T.; Durupthy, O.; Livage, J., *Langmuir* **2002**, *18*, 2331-2336.
54. Pretsch, E.; Buhlmann, P.; Affolter, C., Eds. *Structure Determination of Organic Compounds*; Springer: Berlin, 2000.
55. Conner, P. A.; McQuillan, A. J., *Langmuir* **1999**, *15*, 2916-2921.
56. Yu, J. C.; Zhang, L.; Zheng, Z.; Zhao, J., *Chem. Mater.* **2003**, *15*, 2280-2286.
57. Combes, C.; Rey, C.; Freche, M., *Colloids ans Surfaces B: Biointerfaces* **1998**, *11*, 15-27.
58. Isabel, T.-T. M.; Anderson, M. A., *Langmuir* **1990**, *6*, 602-611.
59. Knecht, M. R.; Wright, D. W., *Langmuir* **2004**, *20*, 4728-4732.
60. Shannon, R. D.; Pask, J. A., *Am. Mineral.* **1964**, *49*, 1707-1717.

61. Hahn, H.; Logas, J.; Averback, R. S., *J. Mater. Res.* **1990**, *5*, 609-614.
62. Gruy, F.; Pijolat, M., *J. Am. Cer. Soc.* **1992**, *75*, 663-666.
63. Ono, A., *J. Sol. State Chem.* **1985**, *56*, 260-262.
64. Horiuchi, S.; Ono, A., *J. Sol. State Chem.* **1986**, *62*, 335-341.
65. Criado, J.; Real, C., *J. Chem. Soc. Faraday Trans.* **1983**, *79*, 2765-2771.
66. Pender, M. J.; Sowards, L. A.; Hartgerink, J. D.; Stone, M. O.; Naik, R. R., *Nano Letters* **2006**, *6*, 40-44.

CHAPTER III

SIZE CONTROL OF DENDRIMER TEMPLATED SILICA

Introduction

Recent efforts in biomimetic silica synthesis have focused on improving the ability to control nanoparticle size and dispersity.^{1,2} Using self-assembled biological and biomimetic polyamine templates, researchers have developed strategies to control particle size distributions. Brunner and coworkers have investigated the ability of phosphate ions to regulate the size of silica nanoparticles formed using polyamines isolated from *Stephanopyxis turris* and the polymer, PAA.^{1,2}

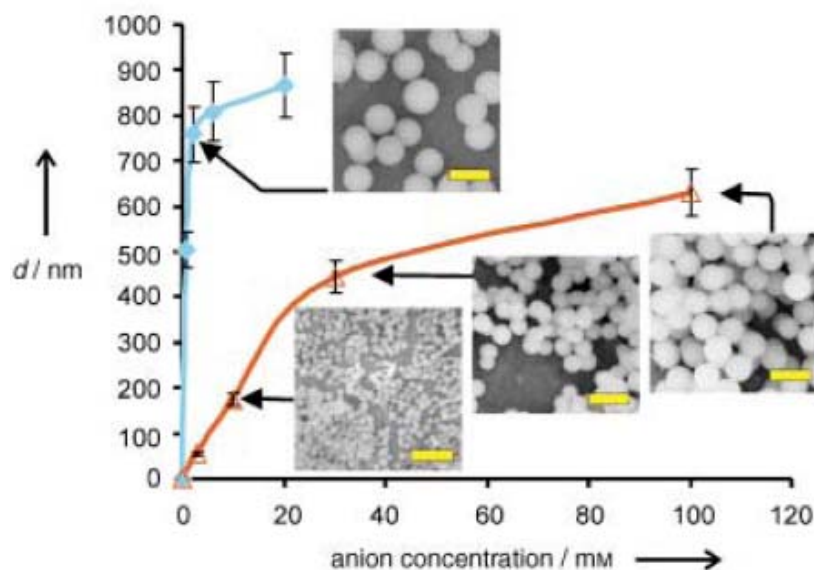


Figure 25: Silica nanoparticle diameter as a function of phosphate buffer concentration red line – orthophosphate, blue line - pyrophosphate, scale bar 1000 nm.¹

Polyamines isolated from *S. turris*, consisting of 15-21 repeating units of N-methylpropyleneimine attached to putrescine, precipitated silica within a few minutes upon exposure to silicic acid.¹ As the concentration of phosphate ions increase, the size of the resulting nanoparticles increases accordingly. Silica nanoparticles grow in size from 30 nm at a phosphate concentration of 3 mM to approximately 600 nm at a phosphate concentration of 100 mM (**Figure 25, red line**). When pyrophosphate (a higher charged anion) replaces orthophosphate, nanoparticles approximately 900 nm in size are formed at 20 mM phosphate concentration (**Figure 25, blue line**). Additionally, other multivalent buffer systems such as sulfate can form silica nanoparticles, however,

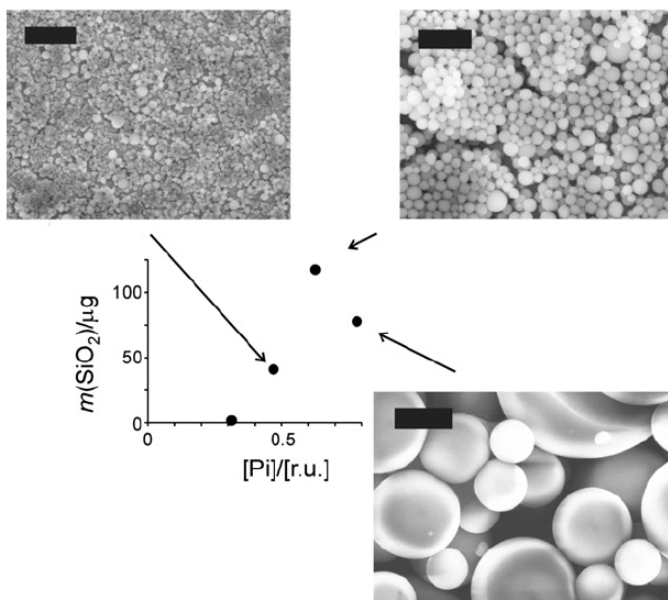


Figure 26: Amount of silica produced as a function of phosphate concentration (phosphate ions per repeat unit). SEM images of corresponding nanoparticles, scale bar 2000 nm.²

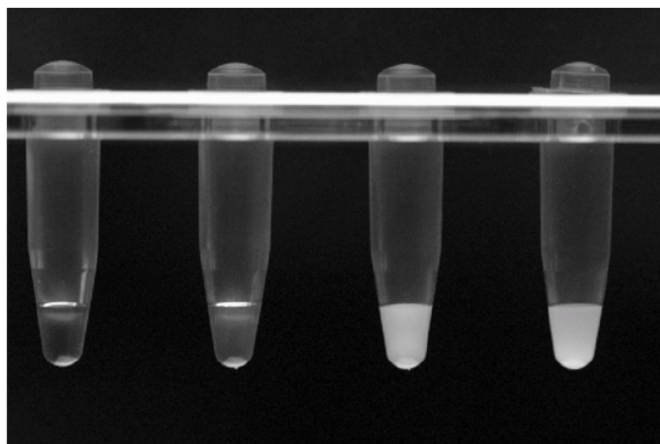


Figure 27: Aggregation of PAA at various phosphate concentration. From left to right: 0.15, 0.31, 0.47, 0.62 [Pi]/[r.u].²

monovalent anions, such as chloride or acetate, cannot form silica in this system. NMR experiments indicate that the polyamines self assemble into a large structure in the presence of phosphate.¹

When PAA is used as a biomimetic template for silica formation, the concentration of phosphate buffer affects the size of the resulting nanoparticles.² Similar to polyamines from *S. turris*, as the concentration of phosphate buffer increases, nanoparticle size also increases (**Figure 26**). At 0.5 [Pi]/[r.u.] (phosphate ions per repeat unit), the average nanoparticle size is 170 ± 70 nm. At 0.7 [Pi]/[r.u.], the average size of the nanoparticles grow to 2400 ± 1100 nm. DLS of PAA shows that as the concentration of phosphate buffer is increased, the aggregation of the template increases (**Figure 27**). Aggregates of approximately 1 nm in diameter were observed for PAA lacking phosphate

buffer, consistent with one molecule of PAA. Aggregates of 120 nm and 600 nm were observed at concentrations of 0.31 and 0.5 [Pi]/[r.u.], respectively.²

In addition to nanoparticle size, the amount of silica produced by the polyamine template is also affected by phosphate concentration.^{1,2} These results suggest that the size and condensation activity of silica can be linked to the degree of aggregation of the biomimetic templates. However, the observed phosphate concentration dependence may be involved only in template aggregation, while the growth mechanism of silica may be dependent upon other conditions. Unfortunately, in both systems, it is difficult to separate the self-assembly process from probable silica growth mechanisms. By using a monomeric biomimetic template, additional conditions that influence silica growth can be examined.

Dendrimers

Dendrimers are unique globular polymers that branch from a central core.³⁻⁵ They possess three distinct structural features: the core, interior area containing branching repeat units (generations), and the exterior with surface functional groups. By changing any of the features, the chemical properties of the dendrimer can be altered. As the generation of the dendrimers increases, the number of surface groups and molecular weight of the dendrimer effectively doubles. Dendrimers are unique in the fact that their properties can be tuned by varying a generation and/or functional group.³⁻⁵

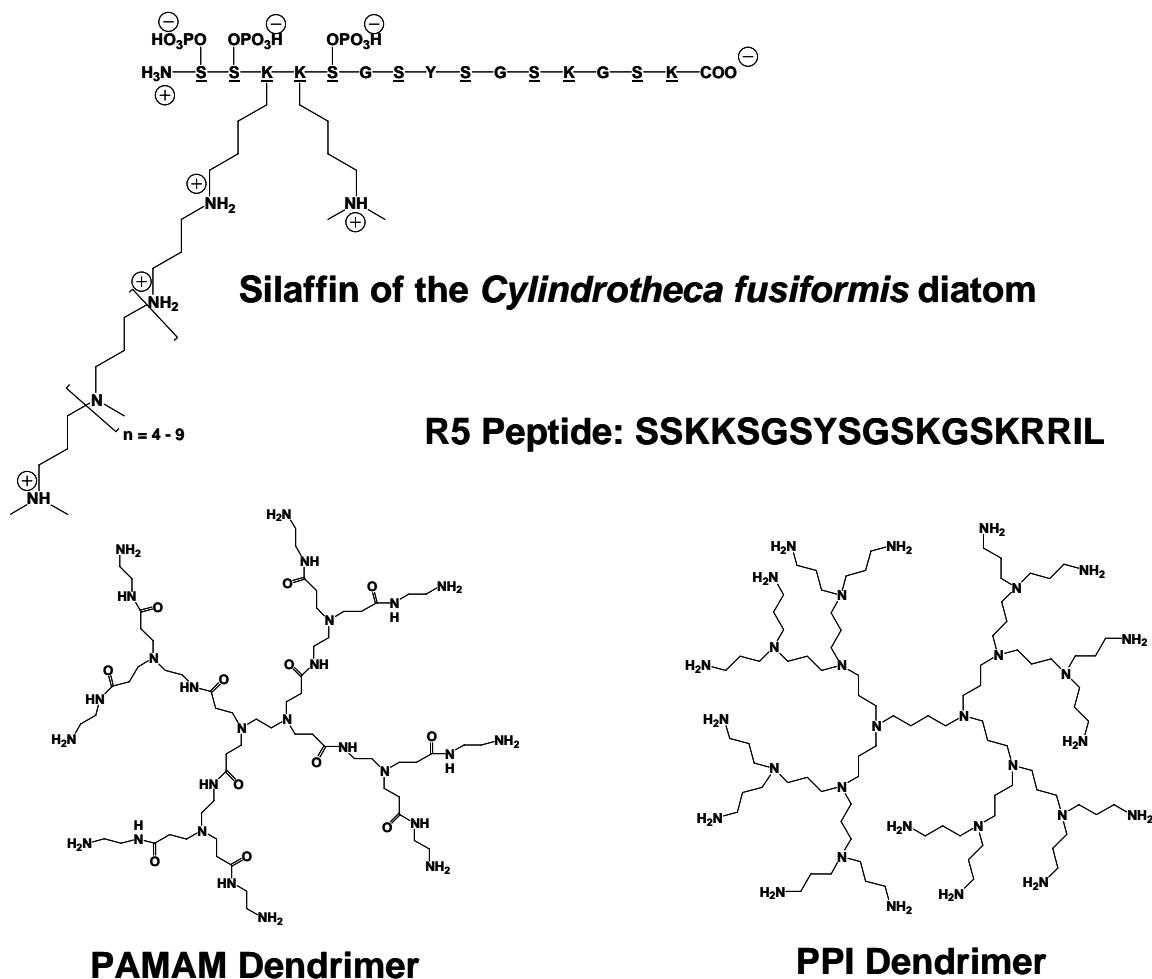


Figure 28: The structure of the silaffin from *C. fusiformis*, the R5 peptide, PAMAM dendrimer and PPI dendrimer.⁶

Amine Terminated Dendrimer Metal Oxide Synthesis

Polyamidoamine (PAMAM) dendrimers are composed of ethylenediamine units with surface amine groups, similar to the unmodified lysine in the R5 peptide.

Polypropyleneimine (PPI) dendrimers consists of repeating polyenimine units that are similar to the modified lysines in native silaffins (**Figure 28**).⁶ Amine terminated

PAMAM dendrimers and PPI dendrimers have similar structural properties comparable

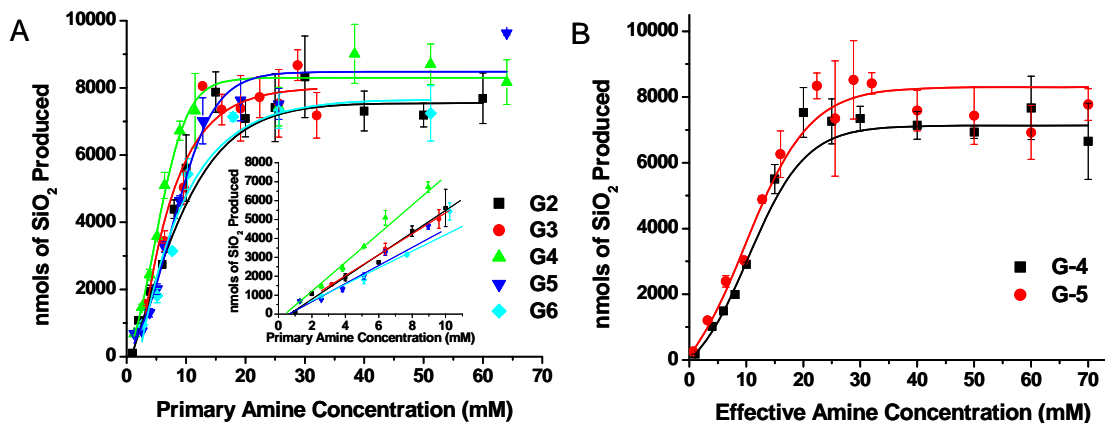


Figure 29: A) The nmols of silica produced as a function of PAMAM primary amine concentration B) The nmols of silica produced as a function of PPI primary amine concentration⁶

to the R5 peptide and natural silaffins, which make dendrimers excellent biomimetic templates.

Amine terminated PAMAM dendrimers and PPI dendrimers precipitate silica nanoparticles when silicic acid is introduced into the solution. PAMAM dendrimers (G0-G6) and PPI dendrimers (G1 – G5) precipitated silica nanospheres rapidly in the presence of phosphate buffer at pH 7.⁶ Solutions lacking amine terminated dendrimers or containing hydroxyl-terminated PAMAM dendrimers were also investigated but did not precipitate silica. The amount of silica produced was determined using the β -silicomolybdate assay.⁷ For PAMAM dendrimers, the amount of silica varied linearly as a function of the primary amine concentration (0-15 mM) until the monosilicic acid became limiting and the silica production plateaued (**Figure 29**).⁶ PPI mediated silica precipitation displayed a sigmoidal correlation between silica production and primary amine concentration. The difference between the silica production for PAMAM and PPI

dendrimers is probably due to the size difference of the dendrimers. PPI dendrimers are approximately 60% of the size of PAMAM dendrimers, with the same number of primary amines.⁸ Knecht and Wright suggest that the size difference leads to a higher surface charge and amine density, causing the silica to precipitate out of solution faster with the PPI dendritic template.

IR analysis of the PAMAM templated silica contains the amine stretching frequency of the dendrimer, indicating the dendrimer is associated with the silica (**Figure 30**).⁶ The silica was etched with a dilute solution of NaOH, resulting in a decrease in size of roughly 60 to 100 nm. IR analysis of the etched silica also contains the amine stretching frequency of the dendrimer suggesting the dendrimer is encapsulated in the

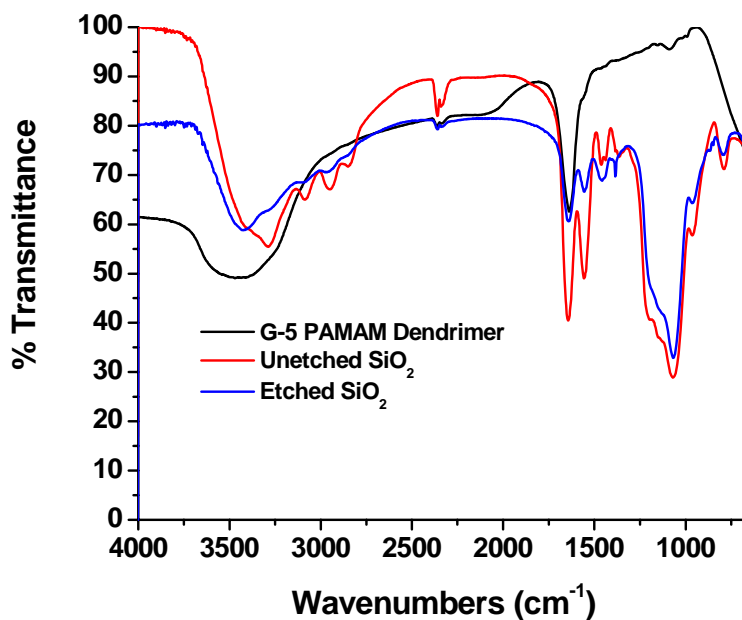


Figure 30: IR of dendrimer templated nanoparticles⁶

silica matrix. Additionally, reseeded experiments support the theory that the dendrimer template is encapsulated in the silica nanosphere. Silica nanoparticles were isolated from the dendrimer mediated reaction and extensively washed to remove any trace of silicic acid. The silica particles were introduced into a fresh solution of monosilicic acid. The amount of silica produced dramatically decreased, reinforcing the hypothesis that the dendrimer is buried in the nanoparticle. The silica particles synthesized in the presence of G1 and G2 PPI dendrimers range in diameter from 170 to 180 nm, while the particles produced from G2-G5 PPI dendrimer are between 220 and 260 nm. G0 and G1 PAMAM dendrimers produce two distinct sizes of silica nanoparticles ranging from 95 to 130 nm and 350 to 400 nm. The larger PAMAM templates (G2-G6) formed nanoparticles ranging in size from 275 to 390 nm. The dendrimer's positively charged surface is proposed to concentrate the developing silanol groups, leading to encapsulation of the dendrimer and precipitation of the silica nanoparticle.⁶

Previous studies have shown that PAMAM and PPI dendrimers are effective biomimetic analogs of the self-assembled templates used by diatoms for silica production.⁶ Dendrimers also remain in an unaggregated state in solution as determined by small angle x-ray scattering.⁹ Similar results from DLS studies at various concentrations of additives in solution confirm these findings. With such a well-defined template, the silica growth process can be examined independent of the buffer conditions required for self-assembly of biological systems.

As dendrimers of higher generation do not self assemble, but remain as discreet globular spheres in solution,⁹ they represent unique templates for the study of the biomimetic silica production. Through the use of these dendrimer templates, we have

been able to determine key conditions for the controlled *in vitro* synthesis of silica nanospherical materials. Under these conditions, we are able to grow and develop the materials at discreet size regimes without negatively impacting the template's overall activity.

Experimental

Silica Precipitation Assays: Silica precipitation assays were based on a variation of previous procedures.¹⁰⁻¹² To varying concentrations of phosphate buffer (0 – 100 mM, pH 7.5), a dendrimer solution of 200 μ L was prepared to a primary amine concentration of 20 mM. Silicic acid was prepared from the hydrolysis of TMOS in 1 mM HCl. To the dendrimer solutions, 20 μ L of 1 M silicic acid was added. After shaking for 5 minutes, the assay mixture was centrifuged for five minutes at 10,000 RPM, the supernatant was decanted and the pellet was washed thrice with water. The silica pellet was then either quantified using the β -silicomolybdate assay⁷ or examined using SEM. Silica precipitation was also performed using various concentrations of main group metal chloride salts (0.255 mM – 400 mM, pH 7.5). The salts included LiCl, NaCl, KCl, RbCl, CsCl and MgCl₂. Silica precipitation assays were conducted as described above.

Silica Quantitation:⁷ Silica samples to be quantified were dissolved in 1 mL of 500 mM NaOH, incubated at 95°C for 30 minutes. After complete dissolution, the samples were filtered using molecular weight cut off centrifuge filtration devices (Amicon Centricon filtration devices, Millipore Inc.) to remove the dendrimer as it interfered with the molybdate assay.⁶ Due to readily available molecular weight cutoff filters, only silica produced from PAMAM generations 2 and greater and generations 4 and higher for

PPI dendrimers were quantified. To the filtered samples, the molybdate reagent was added and allowed to react for 15 minutes to produce the colorimetric product that was monitored at 410 nm on an Agilent 8453 UV-Vis spectrophotometer and quantified using a standard curve.

Scanning Electron Microscopy: Silica samples were prepared as described above. After the final washing, the pellet was suspended in ethanol and added dropwise to an aluminum SEM puck (Ted Pella Inc.). After evaporation of the solvent, the samples were sputter coated with a thin layer of gold using a Pelco Model 3 Sputtering Instrument to avoid charging. The samples were analyzed using a Hitachi S4200 SEM operating at variable voltages. Particle size distributions were manually determined.

Dynamic Laser Light Scattering: G4 PAMAM and G5 PPI dendrimers tested by light scattering were dissolved in appropriate solutions (0.5, 10, 40 mM phosphate buffer or salt solution (NaCl) at pH 7.5) to a primary amine concentration of 20 mM. All DLS measurements were conducted on a Malvern Nano Series Zetasizer with a 633 nm laser. The duration of the scans were 60 s and were the accumulation of 10 scans.

Results and Discussion

Effect of Phosphate Concentration

At various concentrations of phosphate buffer (0–100 mM, pH 7.5), each dendritic template was assayed for silica production and the resulting nanoparticles were characterized.¹³ As discussed in the introduction, previously studied self-assembling amine templates have shown a distinct phosphate concentration dependence on silica

production activity.^{1,2} In contrast, dendritic templates (PAMAM G2-G6 and PPI G4 and G5) produced constant amounts of silica as a function of phosphate concentration.

Assays performed in the absence of phosphate buffer, however, resulted in no silica

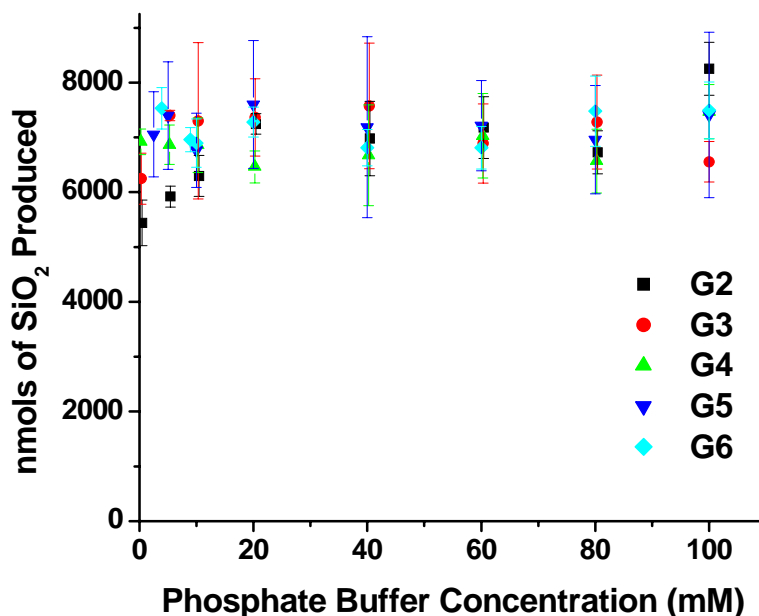


Figure 31: Silica production as a function of phosphate buffer concentration.

production (**Figure 31**). Consistent activity over a wide range of buffer concentrations is the result of the monomeric state of the dendritic template.

While silica production activity was not affected by phosphate buffered solutions, silica nanosphere size appeared to be (**Figure 32**). SEM analysis of particle size distributions demonstrated a linear size dependence for silica particles produced with concentrations below 20 mM phosphate buffer. Above 20 mM phosphate, the silica

spheres had a constant diameter between 250 nm to 350 nm depending on the template. The size selective effects are probably due to the charge neutralization of cations electrostatically interacting with the negatively charged surface silanol groups on the

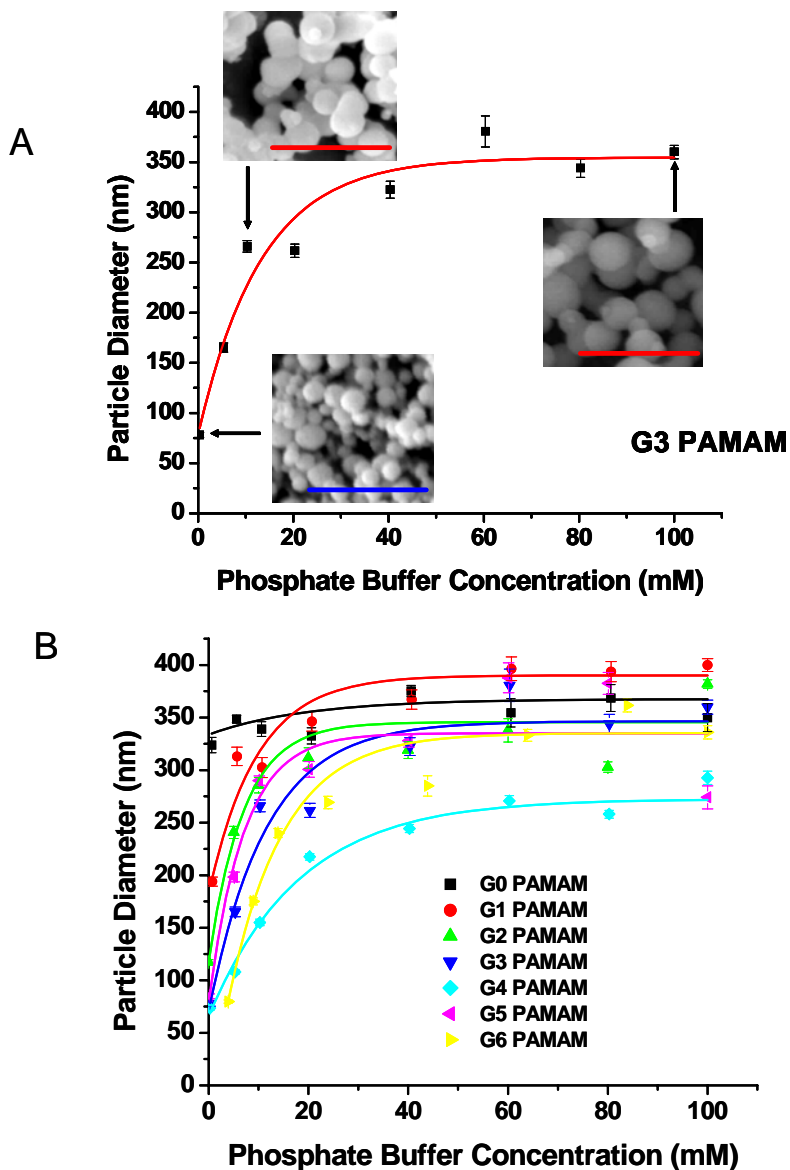


Figure 32: A) Nanoparticle size as a function of phosphate buffer concentration for G3 PAMAM templated silica (blue scale bar 500 nm, red scale bar 1000 nm). B) Size distributions for silica nanoparticles produced from G0-G6 PAMAM templates, error bars represent the standard error associated with the sample size analyzed for the particle size distribution.

silicate surface. It has been previously suggested, from light scattering experiments, that the growth process of dendrimer templated silica demonstrates two dominant phases; the rapid nucleation of silica encapsulating the template followed by a slower ripening phase to the final particle diameter.^{6,10} Electrostatic repulsions between smaller silica nanospheres are minimized by the surface neutralization from cations present in solution, thus allowing for particle growth. Once a certain critical particle size is reached, however, the silica nanoparticles precipitate from solution. In several of the silica samples, bimodal populations were observed as a result of the reaction conditions and the mechanism of particle growth. Due to the limiting amount of reagent, smaller particles could not continue to ripen to a larger size. Additionally, due to electrostatic interactions, the smaller particles could precipitate out of solution concurrently with the larger particles. This is consistent with previously reported dendrimer mediated silica synthesis.⁶

Additionally, a size difference between silica nanoparticles precipitated from PAMAM templates versus PPI templates was observed (**Figure 32 and Appendix B**). As discussed in the introduction, Knecht and Wright have previously shown that silica particles precipitated from PPI templates were approximately 60% of the size of particles precipitated from the associated PAMAM template [PPI G(x) vs. PAMAM (Gx-1)], consistent with the ratio of template diameters.⁶ These effects were also observed in the size distributions of the silica particles of the associated templates at the corresponding buffer concentrations, providing further support for the idea that the small silica encapsulated dendrimers serve as the basic building block of the growing aggregates.

For lower generation dendrimers (PAMAM G0 and G1, PPI G1), cationic concentrations played a lesser role in the particle size distributions. This was attributed to the increased degree of intercalation between the low generational dendritic templates.⁹ Such intercalates result in assembled sheet-like structures of amines. As aggregates present a larger surface area for polycondensation activity, larger silica nanospheres are produced by their extended growth along the sheet-like structures.

Effect of Various Salt Concentrations

These results suggest that the phosphate anions play little role in the actual size determination of the silica nanoparticles from monomolecular templates. Therefore, while phosphate may be critical to the degree of template formation, it is more likely that

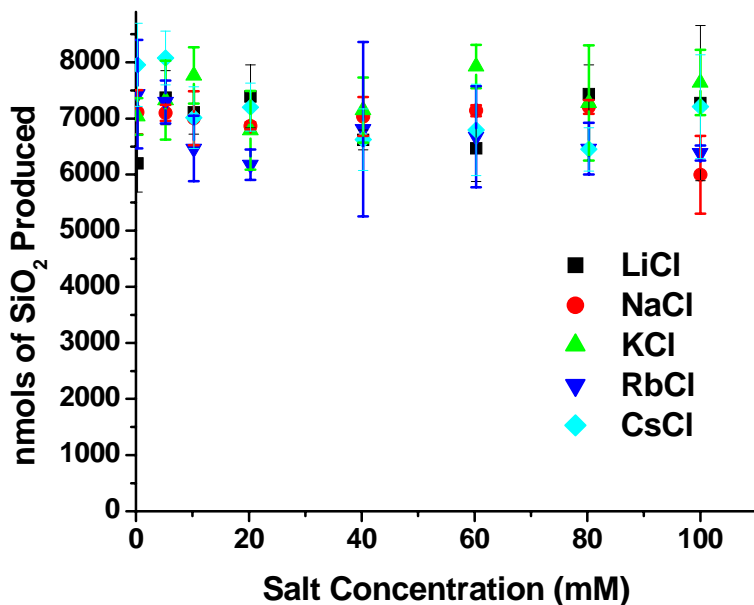


Figure 33: Silica production as a function of salt concentration.

cations mediate silica size. In a biogenic system of silica production, Na^+ or K^+ cations could mediate the controlled synthesis of size-selective silica particles.

To probe the role of cations in silica formation, the activity of the G4 PAMAM

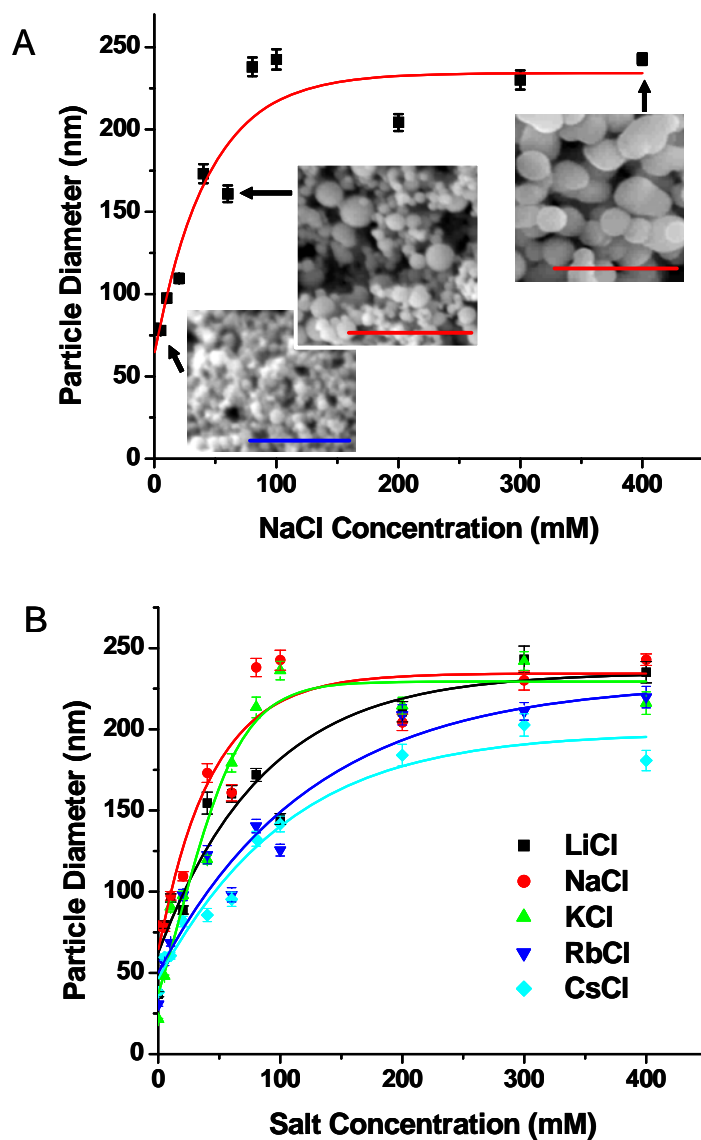


Figure 34: A) Nanoparticle size as a function of NaCl concentration, (blue scale bar 500 nm, red scale bar 1000 nm). B) Size distributions for silica nanoparticles produced from various salts, error bars represent the standard error associated with the sample size analyzed for the particle size distribution.

template was assayed in various concentrations of salt solutions (LiCl, NaCl, KCl, RbCl, CsCl or MgCl₂). Quantitation of the reaction product demonstrated statistically equivalent activity for each assay (**Figure 33**). Furthermore, the activity profile paralleled the activity of silica condensation reactions run in phosphate buffered solutions. Control experiments conducted at constant salt concentrations showed a similar template activity to the phosphate buffered systems (**Appendix B**).⁶ However, under these reaction conditions, the self-aggregating templates of the biological systems would be inactive due to the polyvalent anion requirement for template aggregation.¹⁴

Assays to determine the cation affects upon particle size displayed a dependence on the salt concentration in the reaction. Standard reaction conditions with the G4 PAMAM dendrimer template where phosphate was replaced with individual salt solutions (0.255 mM to 400 mM, pH 7.5) resulted in silica nanoparticles. SEM analysis of the particle size indicates a linear correlation between particle diameter and salt concentrations to 100 mM (**Figure 34 and Appendix B**). Above 100 mM salt, silica sizes stabilize to a constant diameter. Silica precipitated from LiCl, NaCl and KCl all produced nanospheres with a maximum size of approximately 235 nm at salt concentrations higher than 100 mM. RbCl and CsCl produced nanospheres of smaller maximum diameter of 210 nm and 195 nm respectively. The difference in nanosphere sizes may be attributed to the atomic radii of each cation. The smaller cations, with radii between 90 pm and 152 pm, preferentially bind to a single silanol group along the surface of the ripening clusters.^{15,16} The smaller cations may have a stronger affinity to the growing silica structures, resulting in charge neutralization of the surface of the growing silica nanoparticles. The larger cations with radii greater than 166 pm probably bridge

multiple silanol groups.^{15,16} Insufficient surface coverage of the particles leads to less surface charge neutralization. This effect leaves numerous negatively charged silanol groups exposed, increasing the amount of interparticle electrostatic repulsions which leads to diminished particle sizes.

Examination of the divalent magnesium cation resulted in the formation of smaller silica nanospheres approximately 115 nm in diameter. Similarly, the silica production activity showed a marked decrease, indicating that the surface stabilization effects of the divalent magnesium are insufficient for silica production (**Appendix B**). The divalent cation may attempt to bridge multiple singly charged silanol groups along the growing silicate surface, as was seen with Rb^+ and Cs^+ , leading to poor surface coverage and neutralization, thus leading to diminished particle size distributions.

Conclusions

Control of particle size is a principal consideration in nanoscale design and engineering. As discussed in Chapter 1, particle size distributions dictate many of the properties associated with nanomaterials. It is believed that diatoms use highly functionalized organic scaffolds of proteins and polyamines for discrete particle formation and synthesis of highly intricate siliceous materials.¹⁷⁻²⁰ Currently, synthetic size control of biogenic silica has been challenging. Under *in vitro* conditions, particle ripening and aggregation leads to the formation of much larger non-natural silica nanospheres. This process can be controlled by stabilizing the charge of the growing spheres in solution. Particle agglomeration is dictated by the neutralization of negatively charged surface silanol groups. We have shown, through the use of

dendrimer templates, that such interactions are extremely important for the size selectivity of silica nanospheres. The neutralized surface is formed through interactions of cations with the growing negatively charged silicate surface. The effective charge neutralization decreases the electrostatic repulsions, permitting the particles to grow to significantly larger sizes. This study is different than the results of the biologically derived templates that demonstrate a dependence on polyvalent anions, mainly phosphate, for activity. These previous results probably reflect the buffer requirements for template self-assembly, which is unnecessary for activity from monomolecular dendrimers.

References

1. Sumper, M.; Lorenz, S.; Brunner, E., *Angew. Chem. Int. Ed.* **2003**, *42*, 5192-5195.
2. Sumper, M.; Brunner, E.; Lutz, K., *Phys. Chem. Chem. Phys.* **2004**, *6*, 854-857.
3. Padias, A. B.; Hall, H. K.; Tomalia, D. A.; McConnell, J. R., *J. Org. Chem.* **1987**, *52*, 5305-5312.
4. Tomalia, D. A.; Baker, H.; Dewald, J.; Hall, M.; Kallos, G.; Martin, S.; Roeck, J.; Ryder, J.; Smith, P., *Macromolecules* **1986**, *19*, 2466-2468.
5. Tomalia, D. A.; Naylor, A. M.; Goddard, W. A., *Ange. Chem.* **1990**, *102*, 119-157.
6. Knecht, M. R.; Wright, D. W., *Langmuir* **2004**, *20*, 4728-4732.
7. Iler, R. K. *The Chemistry of Silica*; Wiley: New York, 1979.
8. Tande, B. M.; Wagner, N. J.; Mackay, M. E.; Hawker, C. J.; Jeong, M., *Macromolecules* **2001**, *34*, 8580-8585.
9. Prosa, T. J.; Bauer, B. J.; Amis, E. J.; Tomalia, D. A.; Scherrenberg, R., *J. Poly. Sci. B* **1997**, *35*, 2913-2924.
10. Knecht, M. R.; Wright, D. W., *Chem. Comm.* **2003**, *24*, 3038-3039.

11. Knecht, M. R.; Wright, D. W., *Chem. Mater.* **2004**, *16*, 4890-4895.
12. Kroger, N.; Deutzmann, R.; Sumper, M., *Science* **1999**, *286*, 1129-1132.
13. Knecht, M. R.; Sewell, S. L.; Wright, D. W., *Langmuir* **2005**, *21*, 2058-2061.
14. Sumper, M.; Lorenz, S.; Brunner, E., *Angew. Chem. Int. Ed.* **2003**, *42*, 5192-5195.
15. Shannon, R. D., *Acta Crystal. A* **1976**, *A32*, 751-767.
16. Shannon, R. D.; Prewitt, C. T., *Acta Crystal. B* **1969**, *25*, 925-946.
17. Kröger, N.; Bergsdorf, C.; Sumper, M., *Eur. J. Biochem.* **1996**, *239*, 259-264.
18. Kröger, N.; Deutzmann, R.; Bergsdorf, C.; Sumper, M., *Proc. Nat'l. Acad. Sci.* **2000**, *97*, 14133-14138.
19. Kröger, N.; Wetherbee, R., *Protist* **2000**, *151*, 263-273.
20. Poulsen, N.; Sumper, M.; Kröger, N., *Proc. Nat'l. Acad. Sci.* **2003**, *100*, 12075-12080.

CHAPTER IV

AMINE TERMINATED DENDRIMERS: VERSATILE BIOMIMETIC TEMPLATES FOR ALTERNATE SUBSTRATES

Introduction

Dendrimers are extremely robust biomimetic templates. The ability of dendrimer reactivity to be tuned by changing any of the three structural components is extremely advantageous. Additionally, the structure of the dendrimers can be utilized to make complex metal oxides. For example, the electrostatic environment of amine-terminated PAMAM dendrimers has been used to encapsulate metal particles such as gold or quantum dots in silica nanoparticles.¹ Furthermore, carboxylated dendrimers have been used as a template to form ZrO_2 , CeO_2 and Y_2O_3 nanoparticles.² Herein, the ability of amine terminated PAMAM and PPI dendrimers to form metal oxides from alternate substrates has been investigated. When compared to other biomimetic templates, dendrimers have several qualities that make them advantageous for future applications such as patterning. While silicatein filaments form a variety of metal oxides, the rigid structure is unfavorable for patterning applications. Additionally, unlike the peptide-based biomimetic templates, dendrimer mediated metal oxide formation does not depend upon a self assembled structure that can be affected by reaction conditions such as pH or buffer concentrations.³⁻⁷

Dendrimer Mediated Synthesis of Multi-component Nanoparticles

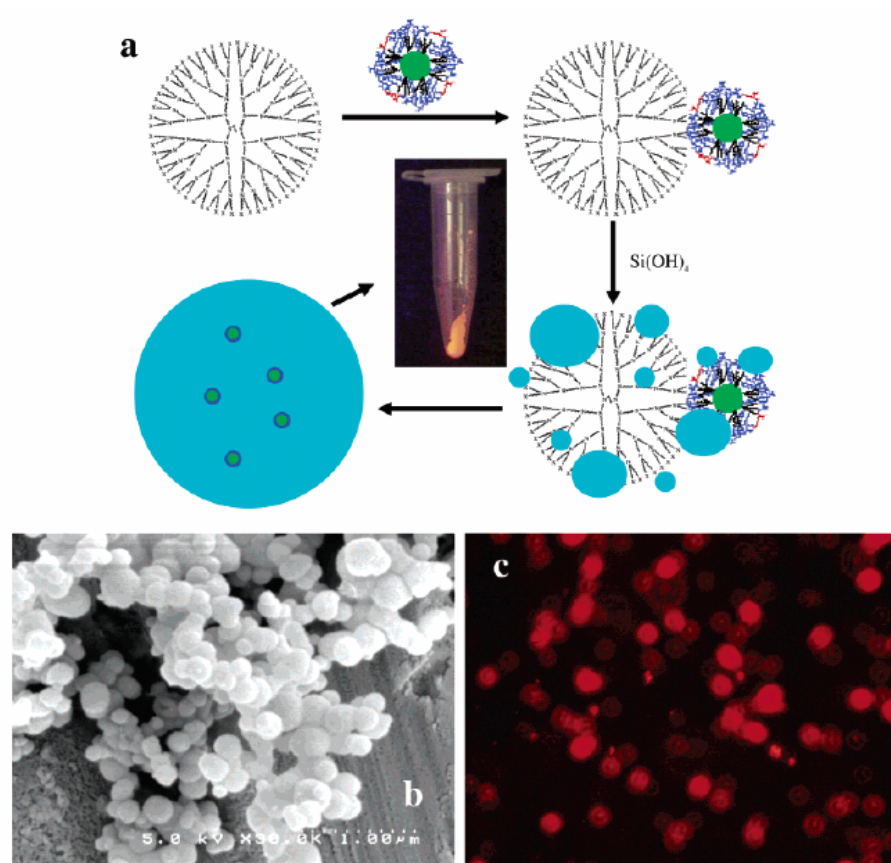


Figure 35: A) A schematic of dendrimer mediated silica encapsulation of quantum dots. B) A SEM image of the silica/quantum dot nanocomposite. C) A confocal image of silica/quantum dot nanocomposite.¹

The electrostatic environment of the amine-terminated dendrimer molecule has been used to encapsulate quantum dots and gold nanoparticle in a silica nanosphere.¹ Quantum dots are fluorescent nanocrystals that have a range of applications from nanosensors to cell labeling.⁸⁻¹¹ Even though quantum dots are being used as imaging

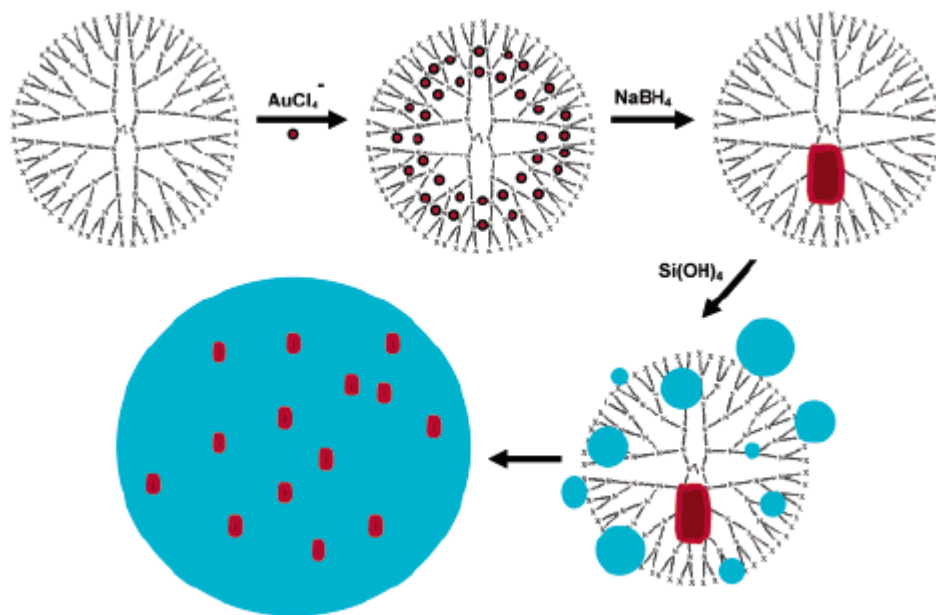


Figure 36: A schematic of dendrimer mediated gold nanoparticle encapsulation in silica nanoparticles.¹

agents, they still have problems such as non-specific binding, aggregation, instability at extreme pHs, and instability in buffers due to the high salt content.¹²⁻¹⁵ Coating quantum dots with silica has several advantages including stability over a broad range of pHs, stability in salt solutions (up to 200 mM), and a retention of the optical properties.¹⁵ Due to the fact that quantum dot photoluminescence quenches at high temperatures, the ambient synthetic conditions of dendrimer mediated silica nanoparticles synthesis is extremely advantageous.¹⁶⁻¹⁹ CdSe/ZnS core shell AMP quantum dots were dispersed in a solution of G4 PAMAM dendrimer at a ratio of 1:1000. The negative surface of the quantum dot interacts electrostatically with the positive surface of the dendrimer.¹ When monosilicic acid is added, silica nanoparticles form, encapsulating quantum dots (**Figure 35**). Fluorescent measurements of the supernatant show that 99% of the quantum dots

are encapsulated in the silica nanospheres. Additionally, confocal images reveal that the fluorescent properties of the quantum dots are retained. SEM images show that the size of the silica was roughly 200 nm, corresponding to silica formed with dendrimers lacking quantum dots.^{1,4,7}

In addition to encapsulating quantum dots in silica, dendrimers have also been used to encapsulate gold nanoparticles.¹ In contrast to the encapsulation mechanism for quantum dots, AuCl_4^- anions coordinate to the amine groups in the interior of the dendrimer (**Figure 36**). Once coordinated, the Au^{3+} ions were reduced to Au^0 by NaBH_4 . TEM analysis showed that the majority of Au nanoparticles were located within the dendrimer, while a few were surface-passivated by the dendrimer. Therefore, free amine groups on the dendrimer surface were available for silification upon the addition of monosilicic acid. UV-vis spectroscopy shows that the characteristic gold plasmon resonance band shifted from 519 nm for the bare gold/dendrimer nanoparticles to 531 nm for the encapsulated dendrimer nanoparticles, consistent with previously published shifts due to gold/silica encasement.²⁰ The layers of silica are proposed to increase the scattering of light and change the refractive index of the particles, resulting in the shift. XRD analysis of the silica/gold nanocomposite reveals the characteristic (111), (220), and (311) peaks of Au^0 .¹ TEM images show that the size of the nanoparticle is roughly 80 nm. The reduced size of the nanoparticles may be due to distortion of the dendrimer caused by the presence of intradendrimer Au^0 clusters. Previously, it has been shown that the size of the dendrimer template affects the size of the nanoparticle formed.^{4,7} Additionally, the gold is solvent accessible, as it can be degraded by KCN, indicating that the silica spheres are mesoporous.

Carboxyl Terminated Dendrimer Metal Oxide Synthesis

Zirconium oxide (ZrO_2), cerium oxide (CeO_2), and yttrium oxide (Y_2O_3) have been formed in the presence of PAMAM (G 5.5) carboxylated dendrimers from the precursors zirconia chloride, cesium chloride, and yttrium chloride, respectively.² The metal oxides were characterized by TEM, XRD and thermogravimetric (TGA) analysis. The average particle sizes, as shown by TEM images, were approximately 12 nm, 18 nm, and 25 nm for ZrO_2 , CeO_2 , and Y_2O_3 , respectively. XRD analysis of the as-synthesized metal oxides show amorphous powders. TGA analysis revealed three weight losses at approximately 110°C, 165°C, and a small change between 500°C and 600°C corresponding to water loss, dendrimer degradation and loss, and surface dehydroxylation, respectively. After 600°C, the mass of the sample remains constant. XRD analysis of the samples that were calcined at 600°C for 2 hours revealed crystalline metal oxides. Scherrer's analysis determined that the crystal sizes were 9, 13, and 21 nm for ZrO_2 , CeO_2 , and Y_2O_3 , respectively, and as such it is estimated that each nanoparticle contains 1 to 2 metal oxide crystals.²

As discussed in Chapters 1 and 2, biomimetic synthesis techniques are being used to form alternate metal oxides not found in natural systems. TiO_2 is a photocatalytic material used in sunscreen and white paint pigment. Additionally, it has the potential to be used in environmental applications such as water purification, wastewater treatment, and air purification.^{21,22} GeO_2 is a blue photoluminescent material with a higher refractive index than silica that is being investigated as a material for optical waveguides in integrated optical systems.^{23,24} At room temperature under ambient conditions, PAMAM (G0, G2, G4 and G6) and PPI (G4 and G5) dendrimers rapidly form TiO_2 and

GeO₂ from the precursors titanium bis(ammonia lactato) dihydroxide (TBALDH, [CH₃CH(O⁻)CO₂NH₄]₂Ti(OH)₂) and germanium ethoxide (TEOG), respectively. The nanoparticles were characterized using scanning electron microscopy (SEM), fourier transform infrared spectroscopy (IR), X-ray diffraction patterns (XRD), and photoluminescent spectroscopy.

Experimental

TiO₂ Precipitation Assay: Titanium (IV) bis(ammonium lactato) dihydroxide (40 μL, 1M) was added to various concentrations of dendrimer solutions diluted in either 200 μL phosphate buffer (100 mM, pH 7.5) or water. The reactions were shaken for 5 minutes, centrifuged for 5 minutes at 10,000 RPM and washed three times with deionized water.

GeO₂ Precipitation Assay: Tetramethoxygermanium (TMOG), tetraethoxy germanium (TEOG), and tetra isopropoxide (TIPG) (5 μL) were added to various concentrations of dendrimer solutions diluted in either 200 μL phosphate buffer (100 mM, pH 7.5) or water. The reactions were shaken for 5 minutes, centrifuged for 5 minutes at 10,000 RPM and washed three times with deionized water. **NOTE: It is absolutely imperative to use fresh bottles of precursor.**

Titanium Quantitation: The 5-chlorosalicylic acid assay was used to quantify TiO₂ production.²⁵ TiO₂ was dissolved in 1 mL of concentrated sulfuric acid and incubated at 95°C for 2 hours. 5-chlorosalicylic acid (2.5mL of 2.5% in ethanol), sodium perchlorate (2.5 mL, 1 M), ethanol (7.5 mL), and deionized water (10 mL) were added to the dissolved titanium solution. The solution was adjusted to pH 4 using concentrated NH₄OH and diluted to 50 mL with deionized water. The colorimetric product was

monitored at 355 nm using an Agilent 8453 UV-Vis spectrophotometer and quantified using a standard curve.

Germanium Quantitation: The β -silicamolybdate assay described by Iler was modified to quantify germanium oxide precipitation.²⁶ Ammonium paramolybdate $(\text{NH}_4)_6\text{Mo}_7\text{O}_{24} \cdot 4\text{H}_2\text{O}$ (4.0 g) was dissolved in 300 mL of deionized water. Concentrated hydrochloric acid (12 mL) was added to the ammonium paramolybdate solution and diluted to 500 mL. Germanium dioxide was dissolved in 1 mL of 0.5 M NaOH at 95°C for 30 minutes. The dendrimers interfered with the assay so they were removed by Centricon filtration (Amicon Centricon filtration devices, Millipore, Inc). Due to available molecular weight cutoff filters, only templates with molecular weights higher than 3000 were assayed. To 0.5 mL of the filtered solution, 5 mL of the ammonium molybdate solution was added and allowed to react for 15 minutes. The colorimetric product was monitored at 410 nm using an Agilent 8453 UV-Vis spectrophotometer and quantified using a standard curve.

X-ray Diffraction: Powder X-ray diffraction (XRD) scans were obtained on a Scintag X₁ θ/θ automated powder diffractometer with a Cu target, a Peltier-cooled solid state detector, and a zero background Si(510) sample support. For titanium dioxide, the samples were scanned from 20 to 60 2θ with a step size of 0.02 and a preset time of 25 seconds. Germanium oxide samples were scanned from 18 to 50 2θ with a step size of 0.03 and a scan time of 10 seconds. For high temperature scans, the samples (15 mg) were heated to the appropriate temperature for 2 hours in a sealed quartz tube in a 79300 Thermolyne tube furnace under nitrogen. All peaks were identified according to JCPDS.

Scanning Electron Microscopy: The nanoparticles were examined by a Hitachi S4200 scanning electron microscope (SEM) operating at variable voltages. The samples were suspended in ethanol and added dropwise to an aluminum SEM puck (Ted Pella Inc.). After evaporation of the solvent, the samples were sputter coated with a thin layer of gold (Pelco Model 3 Sputtering Instrument) to avoid charging.

Infrared Spectroscopy: TiO_2 and GeO_2 were prepared in the precipitation assays stated above. After the final wash, the samples were dried under vacuum and pressed into KBr pellets. The samples were analyzed on a Mattson Genesis Series FTIR.

Photoluminescence Spectroscopy: GeO_2 was prepared in the precipitation assay stated above. After the final wash, the samples were dried under vacuum. The samples were analyzed using a Varian Cary Eclipse fluorescence spectrophotometer. The samples were excited at 325 nm and the photoluminescence spectrum was collected from 350 to 600 nm with data intervals of 0.5 nm and an averaging time of 1.0s.

Results and Discussion

Dendrimer Mediated Metal Oxide Formation

When either TBALDH or TEOG was introduced into a solution of amine terminated PAMAM (G0, G2, G4, and G6) or PPI (G5 and G4) dendrimers in either phosphate buffer or water, a white precipitate formed rapidly. Dendrimers that were carboxylated or hydroxylated did not produce nanoparticles, and in the absence of dendrimer, no particle formation was observed. In the case of TBALDH, the 5-chlorosalicylic acid assay was used to determine the amount of TiO_2 produced.²⁵ As the

generation of dendrimer increased, the specific activity of the template increased accordingly (**Table 6**). However, the amount of TiO_2 produced as a function of primary amine concentration is constant between dendrimer generations, with the exception of G0 (**Appendix C**). There is a linear relationship between the amount of TiO_2 formed and the primary amine concentration between 0 to 40 mM (**Figure 37 A**). After 40 mM, the amount of TiO_2 produced plateaus at approximately 20,000 nmols. Similar reactivity is observed when PPI dendrimers are used as the template (**Figure 37 B**). Unlike the R5 peptide, the amount of TiO_2 does not vary as a function of pH (**Appendix C**).²⁷ The amount of GeO_2 produced was quantified using a variation of the β -silicomolybdate assay described by Iler.²⁶ The dendrimers interfered with the assay and were separated from the solution using molecular weight filtration. Similar to TiO_2 and silica

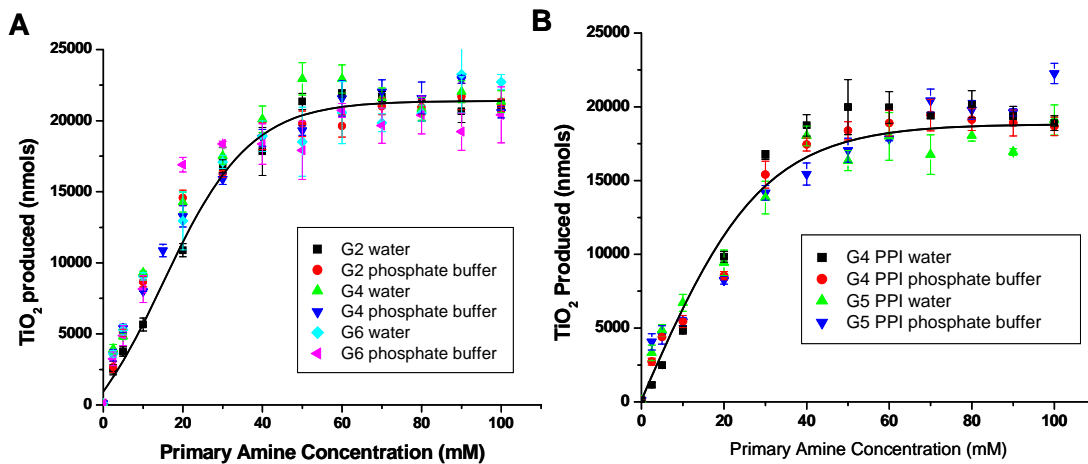


Figure 37: A) G0, G2, G4, and G6 PAMAM templated TiO_2 production as a function of primary amine concentration in phosphate buffer (100 mM, pH 7.5) and water. B) G4 and G5 PPI templated TiO_2 production as a function of primary amine concentration in phosphate buffer (100 mM, pH 7.5) and water.

Table 6: Dendrimer Activity

Dendrimer	Template Size (Å)	Number of Primary Amines	Metal oxide species	Solvent	Specific activity ^a	Size (nm)
G0 PAMAM	15	4	TiO ₂	Water	1.5 ± 0.2	60 ± 15
	15	4	TiO ₂	Phosphate Buffer (100 mM, pH 7.5)	6.9 ± 0.6	310 ± 80
	15	4	GeO ₂	Water	ND	105 ± 40
	15	4	GeO ₂	Phosphate Buffer (100 mM, pH 7.5)	ND	480 ± 170
G2 PAMAM	29	16	TiO ₂	Water	23.1 ± 1.5	60 ± 15
	29	16	TiO ₂	Phosphate Buffer (100 mM, pH 7.5)	20.8 ± 3.1	380 ± 250
	29	16	GeO ₂	Water	ND	115 ± 35
	29	16	GeO ₂	Phosphate Buffer (100 mM, pH 7.5)	ND	470 ± 280
G4 PAMAM	45	64	TiO ₂	Water	89.6 ± 10.4	60 ± 30
	45	64	TiO ₂	Phosphate Buffer (100 mM, pH 7.5)	100.6 ± 8.6	430 ± 150
	45	64	GeO ₂	Water	24.2 ± 2.5	80 ± 60
	45	64	GeO ₂	Phosphate Buffer (100 mM, pH 7.5)	26.4 ± 4.1	350 ± 150
G6 PAMAM	67	256	TiO ₂	Water	273.5 ± 38.9	50 ± 15
	67	256	TiO ₂	Phosphate Buffer (100 mM, pH 7.5)	253.45 ± 35.8	470 ± 90
	67	256	GeO ₂	Water	91.3 ± 13.4	80 ± 20
	67	256	GeO ₂	Phosphate Buffer (100 mM, pH 7.5)	114.9 ± 13.9	460 ± 190
G4 PPI	23.2	32	TiO ₂	Water	31.8 ± 1.9	50 ± 20
		32	TiO ₂	Phosphate Buffer (100 mM, pH 7.5)	34.9 ± 3.0	220 ± 70
	23.2	32	GeO ₂	Water	28.6 ± 3.0	40 ± 20
	23.2	32	GeO ₂	Phosphate Buffer (100 mM, pH 7.5)	19.3 ± 3.3	290 ± 150
G5 PPI	27.8	64	TiO ₂	Water	84.9 ± 13.5	40 ± 20
	27.8	64	TiO ₂	Phosphate Buffer (100 mM, pH 7.5)	104.4 ± 14.0	200 ± 90
	27.8	64	GeO ₂	Water	66.6 ± 3.1	30 ± 10
	27.8	64	GeO ₂	Phosphate Buffer (100 mM, pH 7.5)	44.3 ± 5.5	330 ± 160

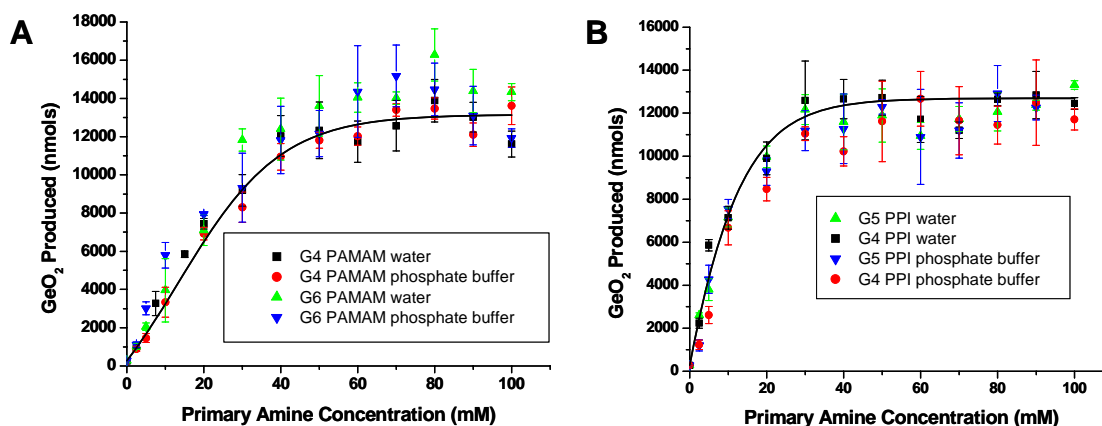


Figure 38: A) G4 and G6 PAMAM templated GeO₂ production as a function of primary amine concentration in phosphate buffer (100 mM, pH 7.5) and water. B) G4 and G5 PPI templated GeO₂ production as a function of primary amine concentration in phosphate buffer (100 mM, pH 7.5) and water.

production, the specific activity of GeO₂ increases with increasing dendrimer generation and varies as a function of primary amine concentration (**Table 6**).⁴ As the germanium substrate becomes limiting, GeO₂ production plateaus at approximately 20,000 nmols (**Figure 38 A**). PPI dendrimer displayed a similar activity profile (**Figure 38 B**). Similar to TiO₂ activity, GeO₂ production did not vary as a function of pH (**Appendix C**).

Both TiO₂ and GeO₂ dendrimer catalyzed synthesis mirrors the dendrimer mediated silica formation presented by Knecht and Wright. However, both these precursors do not need the presence of phosphate buffer to form nanoparticles. In the case of TBALDH, the ammonia cation associated with precursor may act as a flocculating agent. Previously, the positive charge provided by simple salts have been

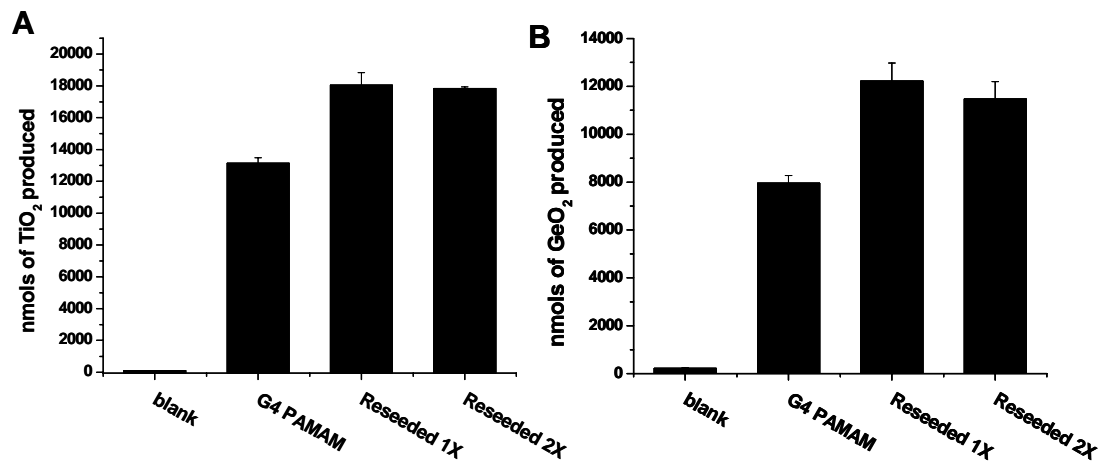


Figure 39: Reseeding experiment for A) TiO₂ and B) GeO₂

shown to stabilize the growing negative charge of forming silica particles.^{4,7}

Additionally, while it has been previously shown that the dendrimer acts as a template for particle formation⁴, in this case, the positive charge of the dendrimer could also neutralize the negative charge of the growing nanoparticles, resulting in precipitation. Reseeding experiments show that when additional precursor is introduced into exhaustively washed TiO₂ nanoparticles, additional TiO₂ forms (**Figure 39 A**). These results support the idea that dendrimers are located on the surface of the nanoparticles, stabilizing the negative charge of the forming metal oxide. In the case of GeO₂, there are no ions associated with the precursor, yet nanoparticles are still formed in water. Similar to TiO₂, when TEOG is introduced into exhaustively washed GeO₂ particles, additional GeO₂ forms, indicating that the dendrimers are on the surface of the particles and could shield the negative charge of the growing particles, resulting in precipitation (**Figure 39 B**).

The expansion of substrates that dendrimers can utilize to form metal oxides under ambient conditions indicates that this process is not species specific, but probably driven by electrostatic interactions of the negative substrate and the positive dendrimer.

Nanoparticle Characterization

SEM images of TiO_2 formed in the presence of G4 PAMAM dendrimers show

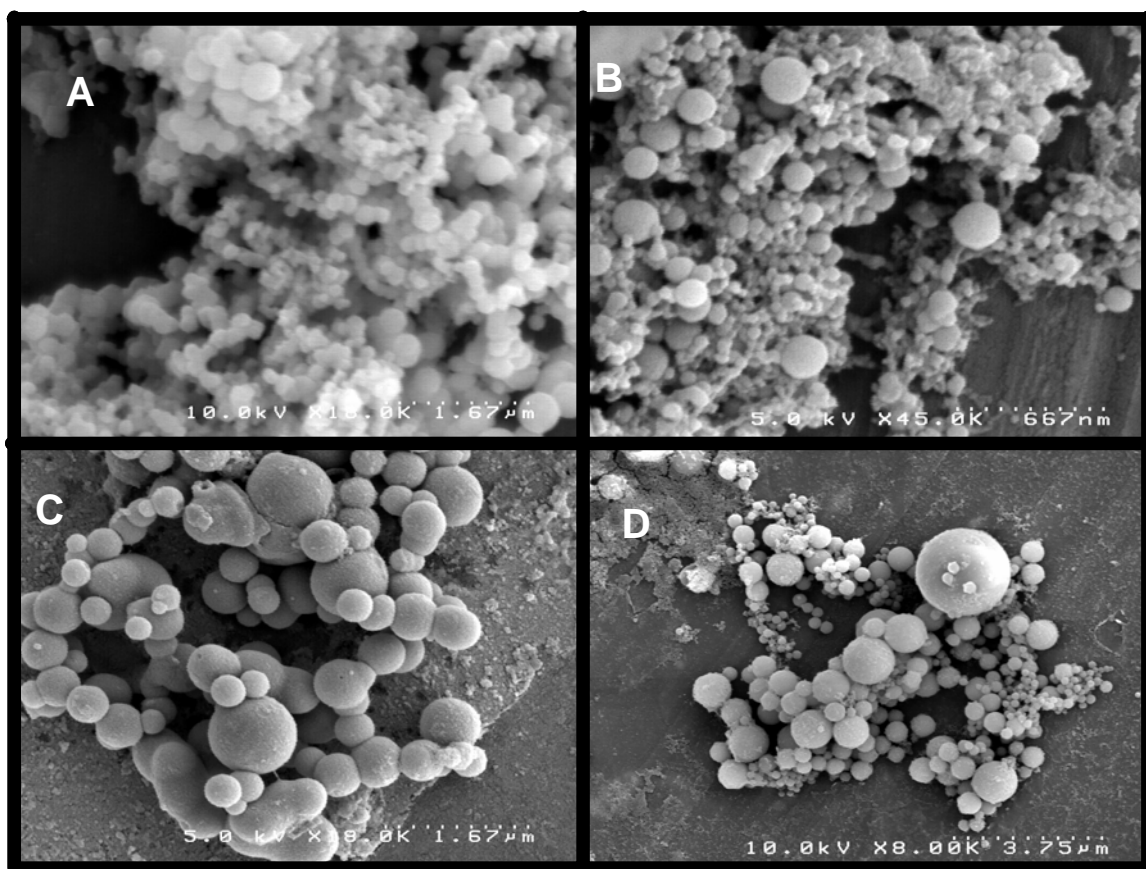


Figure 40: A) SEM of G4 PAMAM templated TiO_2 formed in water, scale bar 1.67 μm . B) SEM of G4 PAMAM templated GeO_2 formed in water, scale bar 667 nm. C) SEM of G4 PAMAM templated TiO_2 formed in phosphate buffer (100 mM, pH 7.5), scale bar 1.67 μm . D) SEM of G4 PAMAM templated GeO_2 formed in phosphate buffer (100 mM, pH 7.5).

round nanoparticles with a Gaussian size distribution (**Figure 40 A**). In water, the average size of PAMAM templated TiO₂ ranges from 30 to 90 nm, while PPI templated TiO₂ ranges in size from 20 to 70 nm in diameter (**Table 6 and Appendix C**). In water, GeO₂ nanoparticles produced from the PAMAM template range in size from 20 to 145 nm, while PPI templated particles range in size from 20 to 60 nm (**Figure 40 B**). When phosphate ions are introduced, the size of the PAMAM and PPI templated TiO₂ and GeO₂ nanoparticles increases. A similar trend was seen with silica nanoparticle formation by Knecht and coworkers.⁷ The presence of cations in solution is proposed to neutralize the charge of the ripening nanoparticle, allowing the developing nanoparticles to stay in solution longer, resulting in a larger particle. The PAMAM templated size range for TiO₂ and GeO₂ formed in phosphate buffer are 130 to 630 nm and 190 to 750 nm, respectively (**Figure 40 C and D**). Interestingly, nanoparticles formed using PPI dendrimers as a template in phosphate buffer are much smaller with sizes ranging from 110 to 290 nm for TiO₂ and 140 to 490 nm for GeO₂. PPI dendrimers with the same number of primary amines are smaller in size (**Table 6**) than the corresponding PAMAM dendrimers, indicating that the ratio of dendrimer size to the number of primary amines may affect the size of the forming nanoparticles. A similar phenomenon is seen in dendrimer templated silica formation.^{4,7} The size of the TiO₂ and GeO₂ nanoparticles are consistent with dendrimer templated silica nanoparticles, as well as R5 templates silica and TiO₂ nanoparticles.^{4,7,27,28}

TiO₂ nanoparticles from each generation synthesized in the presence of water or phosphate were analyzed using IR spectroscopy (**Appendix C**). In each PAMAM sample, amide I and II stretching frequencies at approximately 1650 and 1540 cm⁻¹ are

present, indicating the dendrimer is associated with the nanoparticles.²⁹ Additionally, when phosphate buffer is present, broad peaks ranging from 966 to 996 cm^{-1} are observed due to the P-O vibration frequency also seen in a variety of metal oxides synthesized in the presence of phosphate.^{27,30-33} The IR analysis for GeO_2 nanoparticles synthesized in the presence of PAMAM and PPI showed the Ge-O-Ge stretching frequency ranging from 790 to 890 cm^{-1} (**Appendix C**).³⁴⁻³⁷ Additionally, the amide I and II stretching frequencies are observed; however, the samples synthesized in the presence of phosphate buffer, lack these stretching frequencies, indicating a germanium phosphate species is not formed.²⁹ Previously, Knecht and Wright showed through a series of etching experiments that the dendrimers were encapsulated in the forming metal oxide species.⁴ Since the mechanism of formation should be the same for each metal oxide, regardless of species, the presence of the amide I and II peaks indicate that the dendrimer is the template, driving the hydrolysis and condensation of each precursor.

XRD Analysis

To examine the phase transition from anatase to rutile, variable temperature XRD analysis of TiO_2 synthesized in water and phosphate buffer was conducted (**Figure 41 A, B and Appendix C**). The phase transition from distorted face-centered cubic anatase to distorted hexagonal closest packed rutile is an intermediate topotactic phase transition with two Ti-O bonds breaking and reforming in the process.³⁸ Dendrimer templated TiO_2 synthesized with or without phosphate buffer was amorphous at room temperature. At 600°C, TiO_2 synthesized devoid of phosphate buffer formed crystalline anatase. At 700°C, the rutile phase formed, with a complete transition from anatase to rutile present

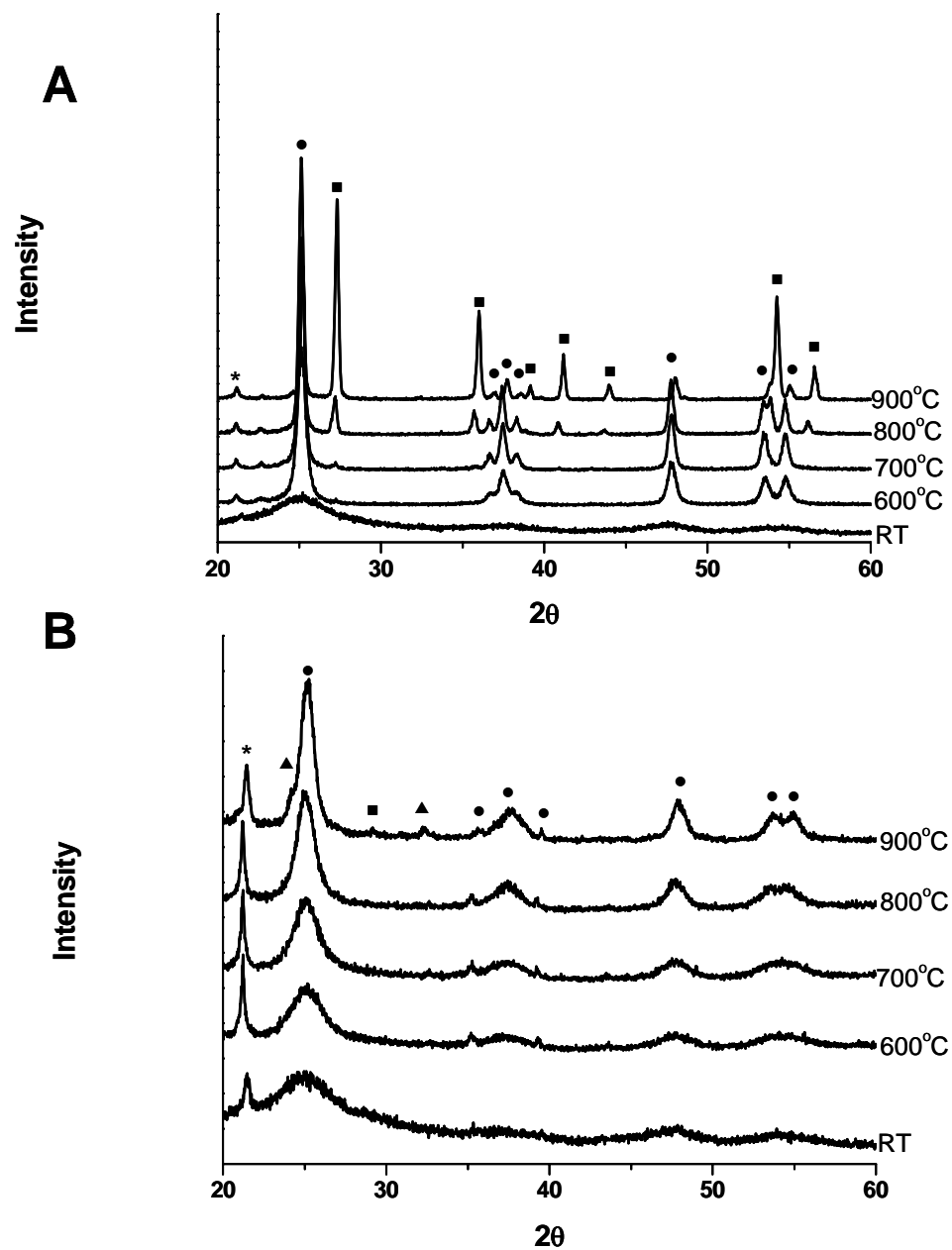


Figure 41: A) Variable temperature XRD of G4 PAMAM templated TiO_2 in water. B) Variable temperature XRD of G4 PAMAM templated TiO_2 in phosphate buffer, 100 mM, pH 7.5 (● anatase, ■ rutile, and ▲ titanium phosphate, * silica plate).

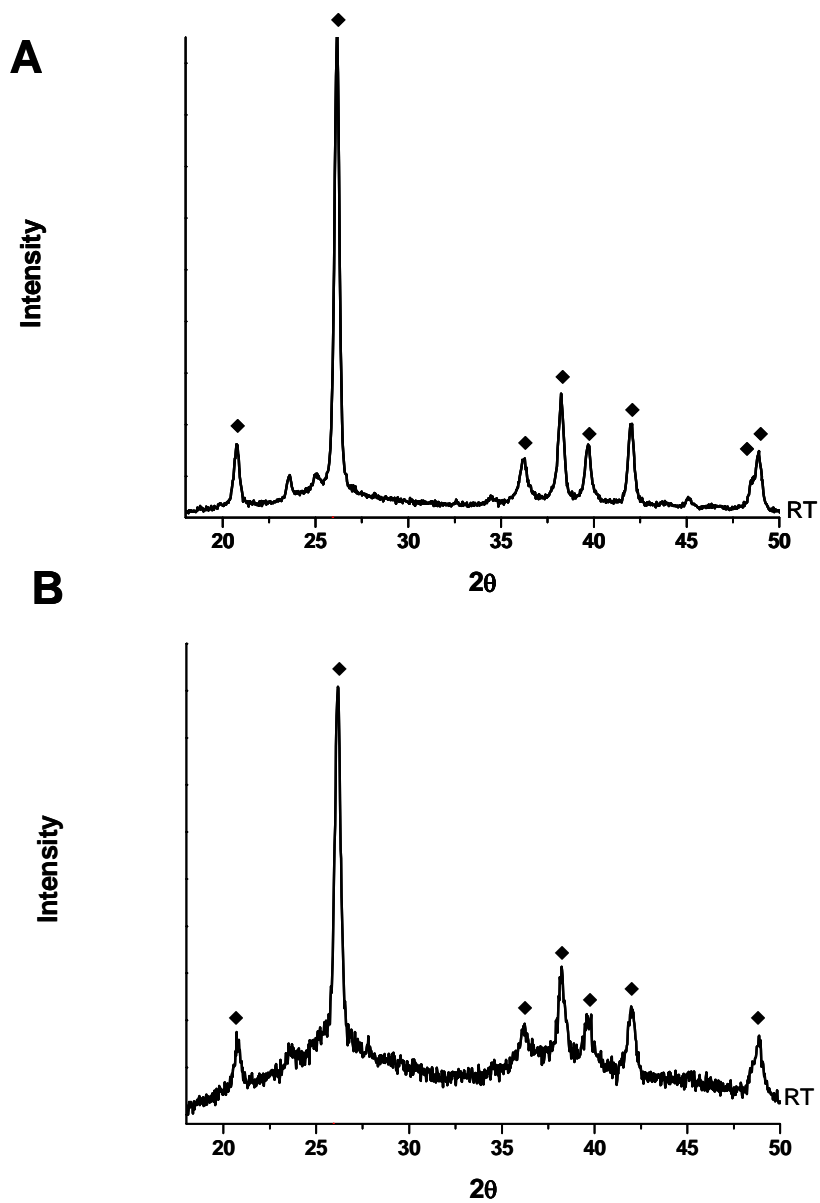


Figure 42: A) XRD of G4 PAMAM templated GeO_2 in water. B) XRD of G4 PAMAM templated GeO_2 in phosphate buffer, 100 mM, pH 7.5. (♦ α -phase)

at 900°C. This transition is consistent with the previously reported transition temperature of R5 templated TiO₂.²⁷ At 600°C crystalline anatase is also observed in the phosphate buffer TiO₂ nanoparticles. A titanium phosphate phase (Ti₄P₆O₂₃) forms at approximately 700°C. Previously this phase has been formed at 770°C in deamination reactions of NH₄Ti₂P₃O₁₂.^{39,40} Here, liberated NH₄⁺ from the degrading dendrimer or the NH₄⁺ counter ion from the precursor could react, forming Ti₄P₆O₂₃. The anatase to rutile phase transition temperature is delayed by 200°C, appearing at approximately 900°C. It has been shown previously that phosphate ions associated with titanium dioxide delay the movement of oxygen atoms necessary for the transition, consistent with these experimental results.⁴¹

XRD analysis of the GeO₂ nanoparticles templated in either water or phosphate buffer revealed crystalline α -GeO₂ (**Figure 42 A and B and Appendix C**). When G4 PAMAM templated GeO₂ in either phosphate buffer or water was heated to 900°C, no phase transition was observed (**Appendix C**). Additionally, a germanium phosphate species was not observed, consistent with the IR results. Previously, crystalline α -GeO₂ has been formed in reverse micelle synthesis, as well as high temperature synthesis procedures.⁴²⁻⁴⁴ To our knowledge, this is the first report of crystalline GeO₂ synthesized under benign, aqueous conditions. Several groups have used biological templates such as poly-L-lysine and peptides isolated from a peptide phage display library to form amorphous germanium dioxide under ambient conditions.^{45,46} The fast rate of hydrolysis and condensation may be a contributing to the formation of crystalline GeO₂. Light scattering profiles of the G4 PAMAM mediated metal oxide synthesis reactions indicate that there is a rapid nucleation followed by nanoparticle growth, then

flocculation out of solution (**Appendix C**). The light scattering profiles also indicate that GeO₂ formation occurs almost three times as quickly as TiO₂ formation (60s versus 175s). To further explore the effect of rate on GeO₂ crystallinity, TMOG and TIPG were investigated as substrates. It is well documented that the steric hindrance of alkoxy group affects the rate of hydrolysis and condensation⁴⁷. When TMOG, which exhibits a faster rate of hydrolysis and condensation, was used as a substrate, crystalline GeO₂ formed (**Appendix C**). However when TIPG, which has a slower rate of hydrolysis and condensation, was used as a substrate, amorphous GeO₂ formed (**Appendix C**). Therefore, the crystalline nature of the metal oxide is probably due to the rate of interaction between precursor and the dendrimer template. Additionally, it is absolutely imperative to use fresh bottles of precursor that have not begun to hydrolyze. It has previously been reported that PLL mediates the formation of amorphous GeO₂ under ambient conditions.⁴⁵ In contrast to these previously reported results, we see the formation of crystalline GeO₂ when fresh TMOG or TEOG are used as the precursor. However, similar to dendrimer mediated GeO₂ formation, when IPG is used as the substrate amorphous GeO₂ forms.

Excitation at 325 nm of the G4 PAMAM templated GeO₂ synthesized in the presence or absence of phosphate buffer produced a blue photoluminescence emission at approximately 420 nm (3.1 eV) (**Figure 43**). The emission is consistent with previously synthesized GeO₂ nanocrystals.⁴⁸ While this is slightly different from commercially available GeO₂, which is approximately 2.3 eV,⁴⁹ the difference in energy could be due to the presence of carbonaceous material in the metal oxide from the presence of the dendrimer.⁴⁸⁻⁵⁰

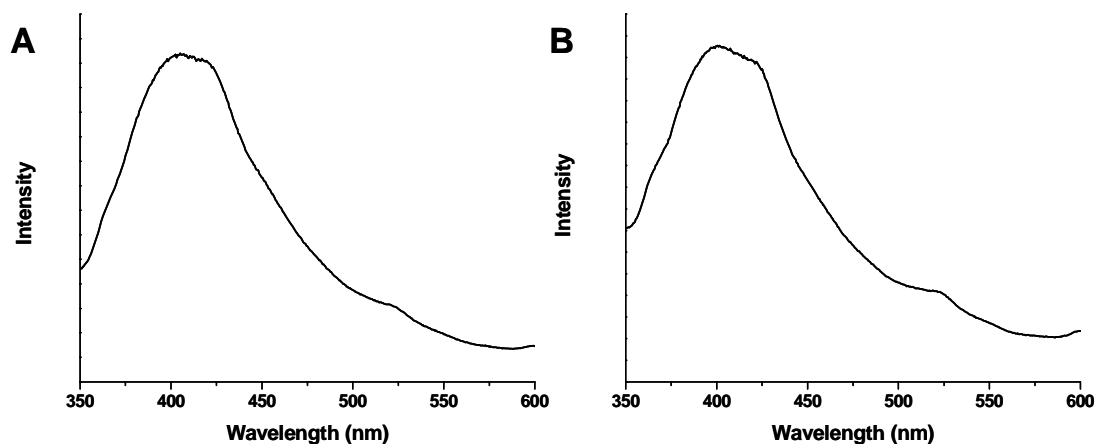


Figure 43: A) Photoluminescence spectrum for G4 PAMAM templated germanium dioxide in phosphate buffer. B) Photoluminescence spectrum for G4 PAMAM templated germanium dioxide in water

Conclusions

Biomimetic synthesis is an attractive alternate route to many abiological materials that avoids harsh chemicals, temperatures, and pressures. The general acid/base dendrimer mediated metal oxide catalysis has been expanded to include alternate substrates. Herein, we have shown that dendrimers are effective biomimetic templates for not only silica formation, but also GeO_2 and TiO_2 nanoparticle synthesis. XRD analysis of dendrimer templated TiO_2 nanoparticles revealed that the presence of phosphate buffer retarded the phase transition from anatase to rutile, similar to previously synthesized biogenic TiO_2 .²⁷ Additionally, to our knowledge this is the first report of crystalline GeO_2 produced under ambient, aqueous conditions. The crystallinity of the material is likely due to the rate of hydrolysis and condensation of the precursor. Furthermore, the dendrimer templated GeO_2 nanoparticles exhibit blue photoluminescence typically observed from this material. These biomimetic synthetic

techniques are increasingly being used in electronic and catalytic applications.

Mineralized ferritin has been used as a catalyst for carbon nanotube formation, as well as chromium reduction.⁵¹⁻⁵³ Recently the 3-dimensional structures of viruses were used as templates for Co₃O₄ wires used in batteries.⁵⁴ Dendrimers have been patterned by a variety of methods, resulting in a reactive spatially deposited surface.^{55,56} Dendrimer mediated metal oxide formation will continue to be used to form 3D structures of silica, titanium dioxide and germanium dioxide.

References

1. Knecht, M. R.; Wright, D. W., *Chem. Mater.* **2004**, *16*, 4890-4895.
2. Yu, X.-B.; Wang, Z.-H.; Chen, H.-M.; Wang, W.-M.; Yang, S.-P.; Zhang, F., *Mater. Lett.* **2004**, *58*, 3285-3289.
3. Kroger, N.; Deutzmann, R.; Sumper, M., *Science* **1999**, *286*, 1129-1132.
4. Knecht, M. R.; Wright, D. W., *Langmuir* **2004**, *20*, 4728-4732.
5. Sumper, M.; Lorenz, S.; Brunner, E., *Angew. Chem. Int. Ed.* **2003**, *42*, 5192-5195.
6. Sumper, M.; Brunner, E.; Lutz, K., *Phys. Chem. Chem. Phys.* **2004**, *6*, 854-857.
7. Knecht, M. R.; Sewell, S. L.; Wright, D. W., *Langmuir* **2005**, *21*, 2058-2061.
8. Parak, W. J.; Pellegrino, T.; Plank, C., *Nanotechnology* **2005**, *16*, R9-R25.
9. Derfus, A. M.; Chan, W. C. W.; Bhatia, S. N., *Adv. Mater.* **2004**, *16*, 961-966.
10. Bentzen, E. L.; House, F.; Utley, T. J.; Crowe, J. E., Jr.; Wright, D. W., *Nano Letters* **2005**, *5*, 591-595.
11. Tran, P. T.; Goldman, E. R.; Anderson, G. P.; Mauro, J. M.; Mattoussi, H., *Phys. Stat. Sol. B* **2002**, *229*, 427-432.
12. Winter, J. O.; Liu, T. Y.; Korgel, B. A.; Schmidt, C. E., *Adv. Mater.* **2001**, *13*, 1673-1677.

13. Pathak, S.; Choi, S.-K.; Arnheim, N.; Thompson, M. E., *J. Am. Chem. Soc.* **2001**, *123*, 4103-4104.
14. Rosenthal, S. J.; Tomlinson, I.; Adkins, E. M.; Schroeter, S.; Adams, S.; Swafford, L.; McBride, J.; Wang, Y.; DeFelice, L. J.; Blackely, R. D., *J. Am. Chem. Soc.* **2002**, *124*, 4586-4594.
15. Gerion, D.; Pinaud, F.; Williams, S. C.; Parak, W. J.; Zanchet, D.; Weiss, S.; Alivisatos, A. P., *J. Phys. Chem. B* **2001**, *105*, 8861-8871.
16. Hjiri, M.; Hassen, F.; Maaref, H., *Mater. Sci. and Engin.* **2002**, *B88*, 255-258.
17. Wu, Y.-h.; Arai, K., *Phys. Rev. B* **1996**, *53*, 485-488.
18. Saint-Girons, G.; Sagnes, I., *J. Appl. Phys.* **2002**, *91*, 10115-10118.
19. Dai, Y. T.; Fan, J. C.; Chen, Y. F.; Lin, R. M.; Lee, S. C.; Lin, H. H., *J. Appl. Phys.* **1997**, *82*, 4489-4492.
20. Liz-Marzan, L. M.; Giersig, M.; Mulvaney, P., *Langmuir* **1996**, *12*, 4329-4335.
21. Hoffmann, M. R.; Martin, S. T.; Choi, W.; Bahnemann, D. W., *Chem. Rev.* **1995**, *95*, 69-95.
22. Wold, A., *Chem. Mater.* **1993**, *5*, 280-283.
23. Xu, X. L.; Zhu, L. X.; Chen, T. P.; Fung, S.; Li, S. M., *Thin Solid Films* **1996**, *283*, 230-234.
24. Margaryan, A.; Liu, W. M., *Opt. Eng.* **1993**, *32*, 1995-1996.
25. Abdel-Aziz, M. S.; Idriss, K. A.; Sedaira, H., *The Analyst* **1996**, *121*, 1079-1084.
26. Iler, R. K. *The Chemistry of Silica*; Wiley: New York, 1979.
27. Sewell, S. L.; Wright, D. W., *Chem. Mater.* **2006**, *18*, 3108-3113.
28. Naik, R. R.; Whitlock, P. W.; Rodriguez, F.; Brott, L. L.; Glawe, D. D.; Clarson, S. J.; Stone, M. O., *Chem. Comm.* **2003**, *2*, 238-239.
29. Pretsch, E.; Buhlmann, P.; Affolter, C., Eds. *Structure Determination of Organic Compounds*; Springer: Berlin, 2000.
30. Conner, P. A.; McQuillan, A. J., *Langmuir* **1999**, *15*, 2916-2921.
31. Yu, J. C.; Zhang, L.; Zheng, Z.; Zhao, J., *Chem. Mater.* **2003**, *15*, 2280-2286.

32. Combes, C.; Rey, C.; Freche, M., *Colloids and Surfaces B: Biointerfaces* **1998**, *11*, 15-27.
33. Isabel, T.-T. M.; Anderson, M. A., *Langmuir* **1990**, *6*, 602-611.
34. Kanno, Y.; Nishino, J., *J. of Mater. Sci. Lett.* **1993**, *12*, 110-112.
35. Kawai, T.; Usui, Y.; Kijiro, K.-N., *Colloids and Surfaces A: Eng. Aspects* **1999**, *149*, 39-47.
36. Wu, H. P.; Lui, J. F.; Ge, M. Y.; Nui, L.; Zeng, Y. W.; Wang, Y. W.; Lv, G. L.; Wang, L. N.; Zhang, G. Q.; Jiang, J. Z., *Chem. Mater.* **2006**, *18*, 1817-1820.
37. Viswanathamurthi, P.; Bhattarai, N.; Kim, H. Y.; Khil, M. S.; Lee, D. R.; Suh, E. K., *J. of Chem. Phys.* **2004**, *121*, 441-445.
38. Shannon, R. D.; Pask, J. A., *Am. Mineral.* **1964**, *49*, 1707-1717.
39. Ono, A., *J. Sol. State Chem.* **1985**, *56*, 260-262.
40. Horiuchi, S.; Ono, A., *J. Sol. State Chem.* **1986**, *62*, 335-341.
41. Criado, J.; Real, C., *J. Chem. Soc. Faraday Trans.* **1983**, *79*, 2765-2771.
42. Wu, H. P.; Liu, J. F.; Ge, N. Y.; Niu, L.; Zeng, Y. W.; Wang, Y. W.; Lv, G. L.; Wang, L. N.; Zhang, G. Q.; Jiang, J. Z., *Chem. Mater.* **2006**, *18*, 1817-1820.
43. Kalyanikutty, K. P.; Gundiah, G.; Govindaraj, A.; Rao, C. N. R., *J. of Nanoscience and Nanotechnology* **2005**, *5*, 421-424.
44. Simanzhenkov, V.; Wiggers, H.; Roth, P., *J. of Nanoscience and Nanotechnology* **2005**, *5*, 436-441.
45. Patwardhan, S. V.; Clarson, S. J., *Polymer* **2005**, *46*, 4474-4479.
46. Dickerson, M. B.; Naik, R. R.; Stone, M. O.; Cai, Y.; Sandhage, K. H., *Chem. Comm.* **2004**, 1776-1777.
47. Interrante, L. V.; Hampden-Smith, M. J., Eds. *Chemistry of Advanced Materials*; Wiley-VCH: New York, 1998.
48. Zacharias, M.; Fauchet, P. M., *Appl. Phys. Lett.* **1997**, *71*, 380-382.
49. Viswanathamurthi, P.; Bhattarai, N.; Kim, H. Y.; Khil, M. S.; Lee, D. R.; Suh, E. K., *J. Of Chem Phys* **2004**, *121*, 441-445.

50. Huang, J.-F.; Luo, H.; Liang, C.; Sun, W.-I.; Baker, G. A.; Dai, S., *J. Am. Chem. Soc.* **2005**, *127*, 12784-12785.
51. Jeong, G.-H.; Yamazaki, A.; Suzuki, S.; Yoshimura, H.; Kobayashi, Y.; Homma, Y., *J. Am. Chem. Soc.* **2005**, *127*.
52. Kim, I.; Hosein, H.-A.; Strongin, D. R.; Douglas, T., *Chem. Mater.* **2002**, *14*, 4874-4879.
53. Bonard, J.-M.; Chauvin, P.; Klinke, C., *Nano Letters* **2002**, *2*, 665-667.
54. Nam, K. T.; Kim, D.-W.; Yoo, P. J.; Chiang, C.-Y.; Meethong, N.; Hammond, P. T.; Chiang, Y.-M.; Belcher, A. M., *Science* **2006**, *312*, 885-888.
55. Xu, F. T.; Street, S. C.; Barnard, J. A., *Langmuir* **2003**, *19*, 3066-3070.
56. Arrington, D.; Curry, M.; Street, S. C., *Langmuir* **2002**, *18*, 7788-7791.

Appendix A

Characterization of the R5 and PLL Template and the Resulting Titanium Dioxide Nanoparticles

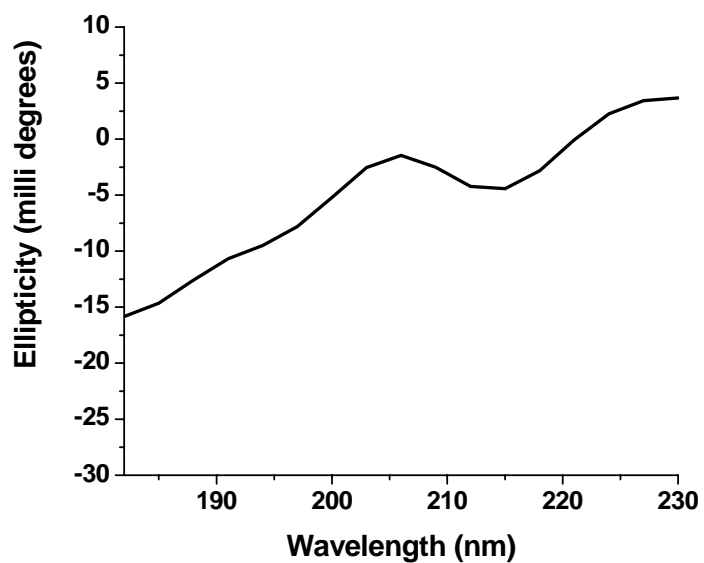


Figure 44: CD of PLL in phosphate buffer (100 mM, pH 7.5)

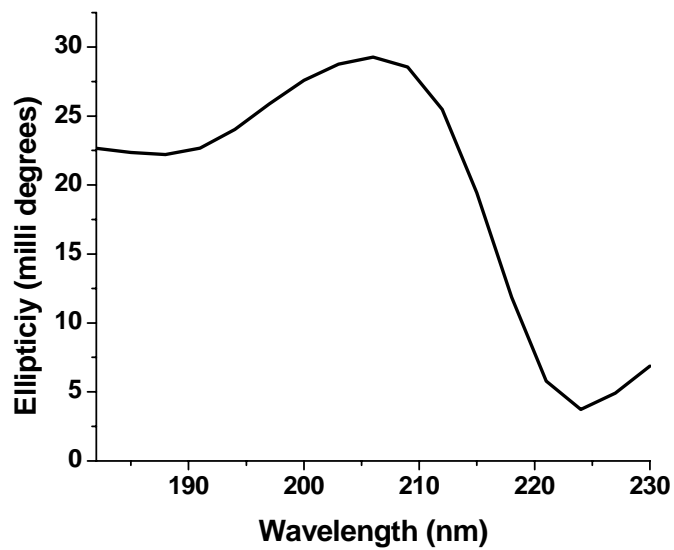


Figure 45: CD of PLL in the presence of phosphate buffer (100 mM, pH 7.5) and TBALDH

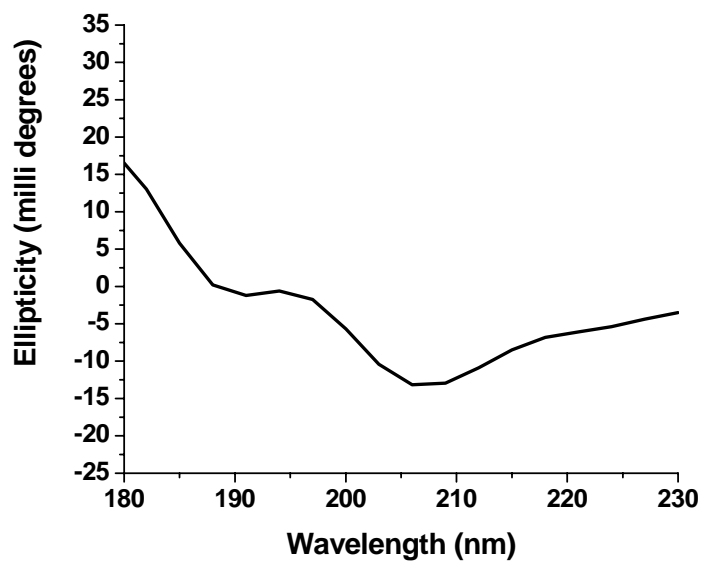


Figure 46: CD of PLL in water

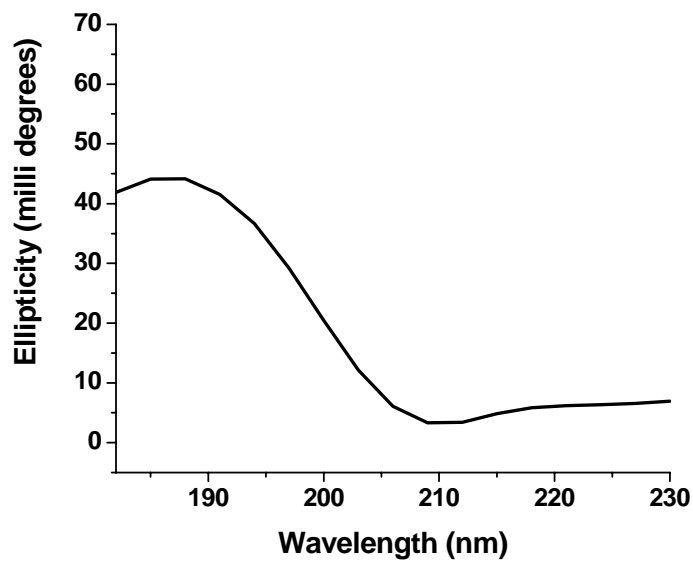


Figure 47: CD of PLL in water and TBALDH

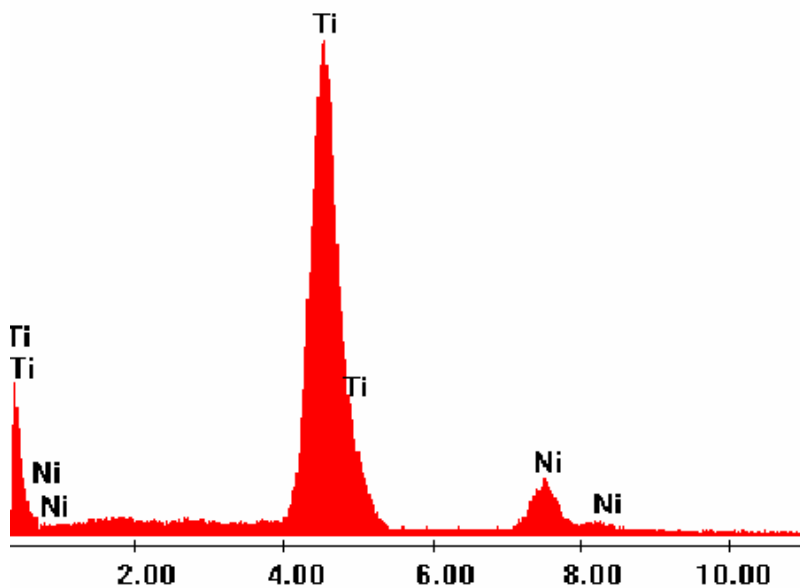


Figure 48: EDS of R5 templated TiO_2 synthesized in the presence of water

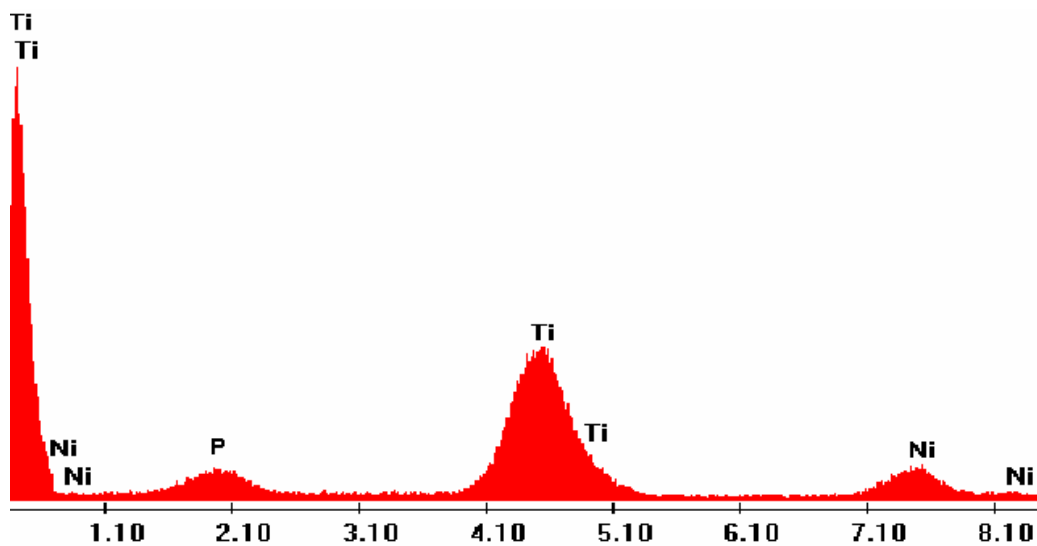


Figure 49: EDS of R5 templated TiO_2 synthesized in the presence of phosphate buffer (100 mM, pH 7.5)

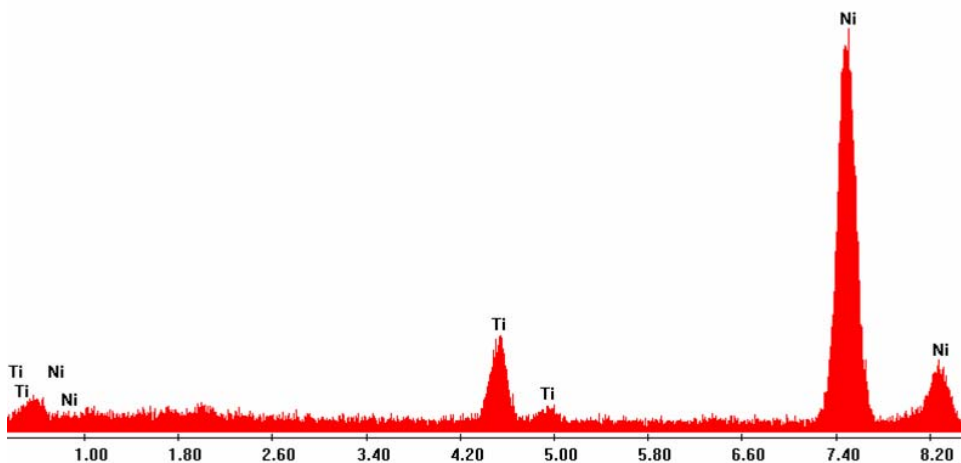


Figure 50: EDS of poly-L-lysine templated TiO_2 synthesized in the presence of water

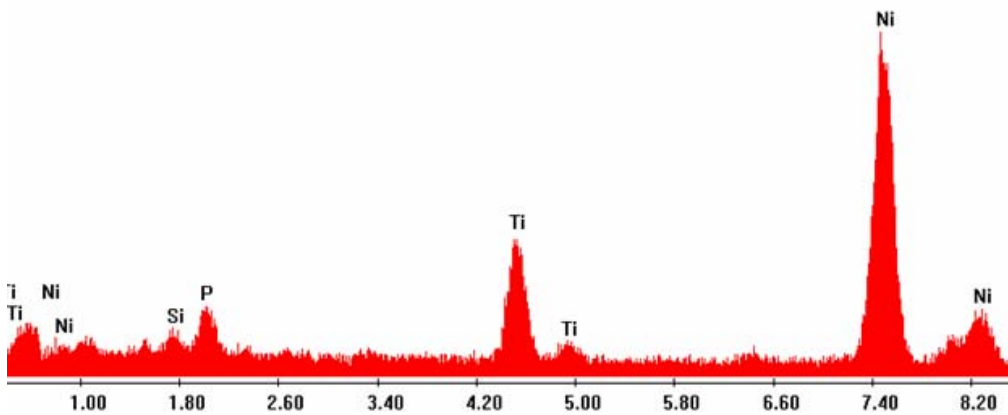


Figure 51: EDS of poly-L-lysine templated TiO_2 synthesized in the presence of phosphate buffer (100 mM, pH 7.5)

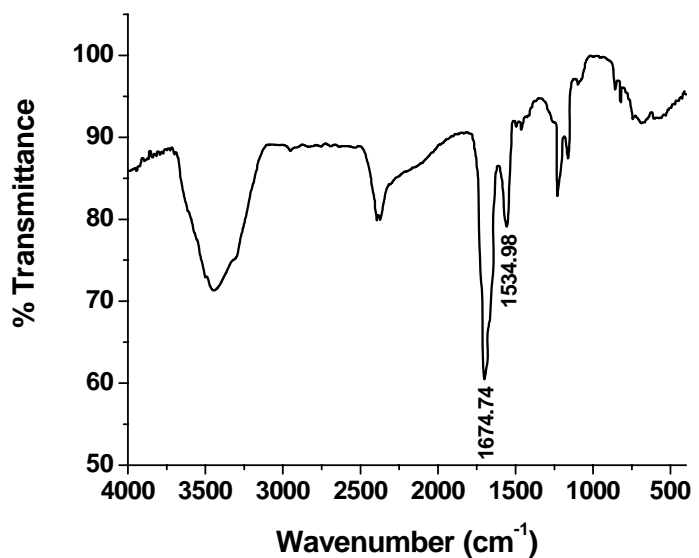


Figure 52: IR of R5 peptide

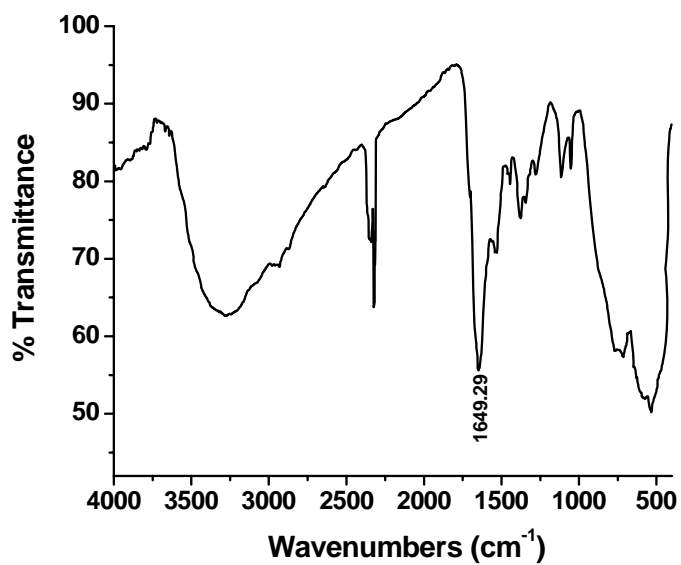


Figure 53: IR of R5 templated TiO₂ synthesized in the presence of water

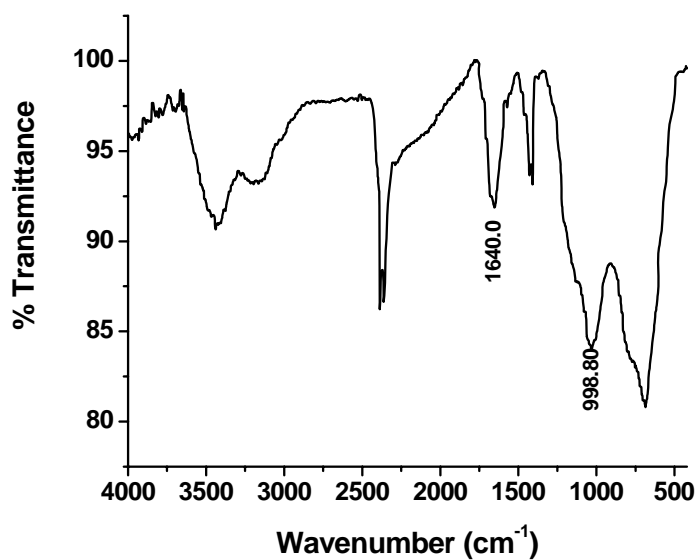


Figure 54: IR of R5 templated TiO₂ synthesized in the presence of phosphate buffer (100 mM, pH 7.5)

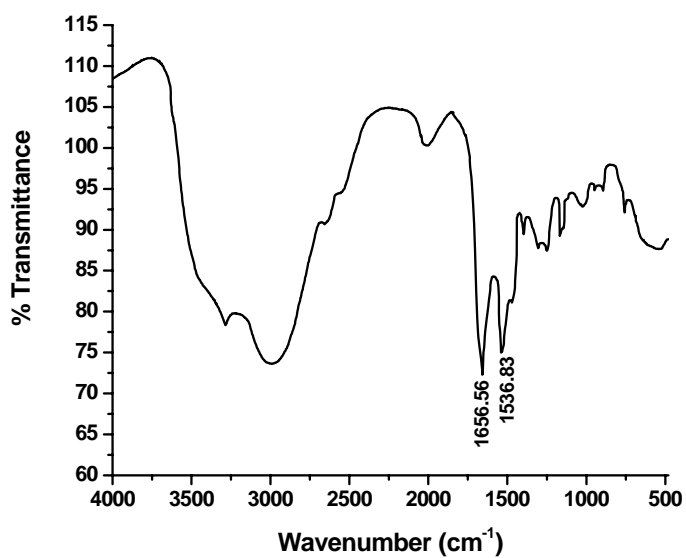


Figure 55: IR of PLL

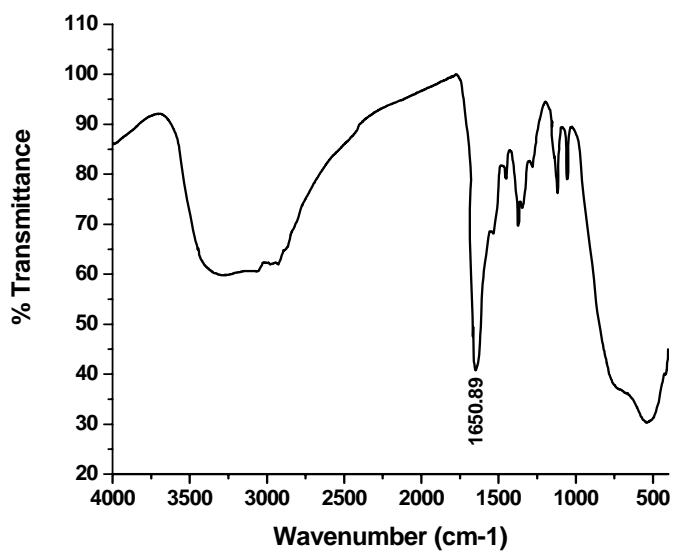


Figure 56: IR of PLL templated TiO_2 synthesized in the presence of water

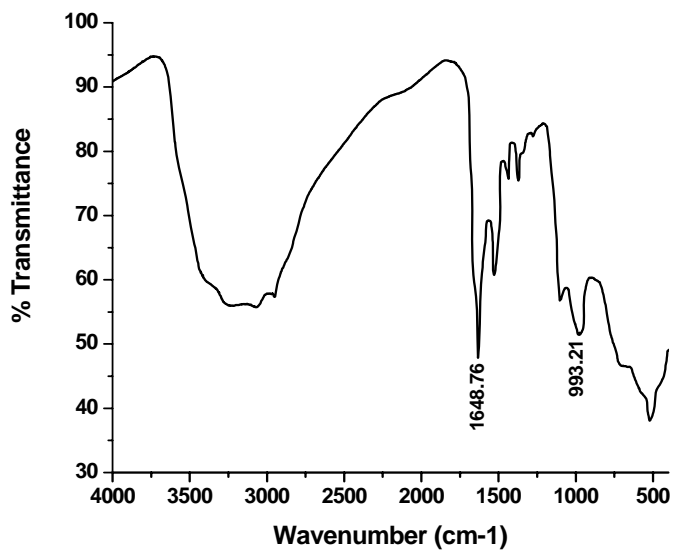


Figure 57: IR of PLL templated TiO_2 synthesized in the presence of phosphate buffer (100 mM, pH 7.5)

APPENDIX B

Characterization of Dendrimer Precipitated Silica Nanoparticles

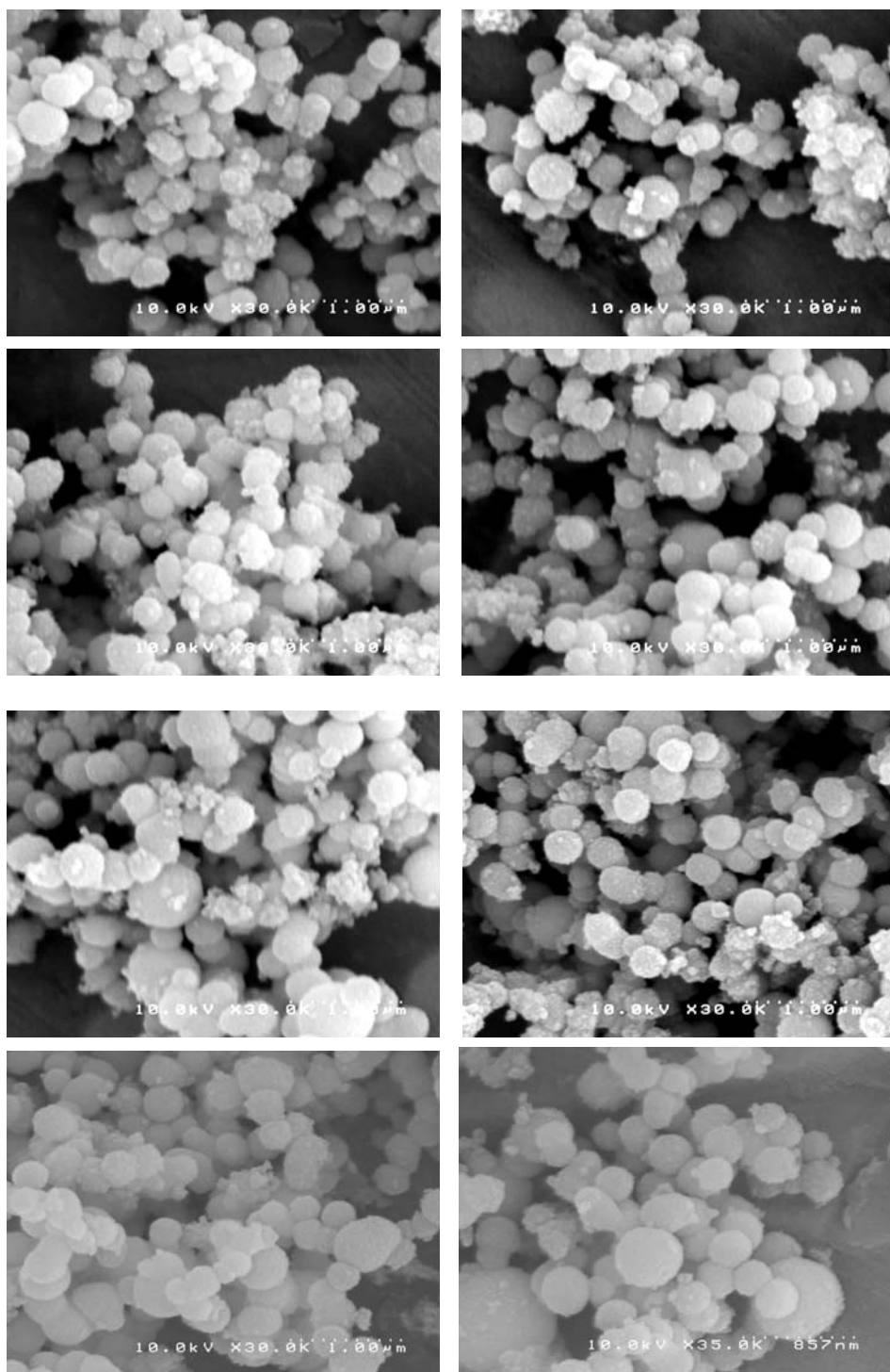


Figure 58: A representative sample of SEMs that were analyzed for each histogram (from G6 PAMAM 60 mM phosphate buffer). **Note:** For each histogram, approximately 150 nanoparticles were counted. Between 8 and 10 SEM pictures were examined to accumulate 150 “countable” nanoparticles.

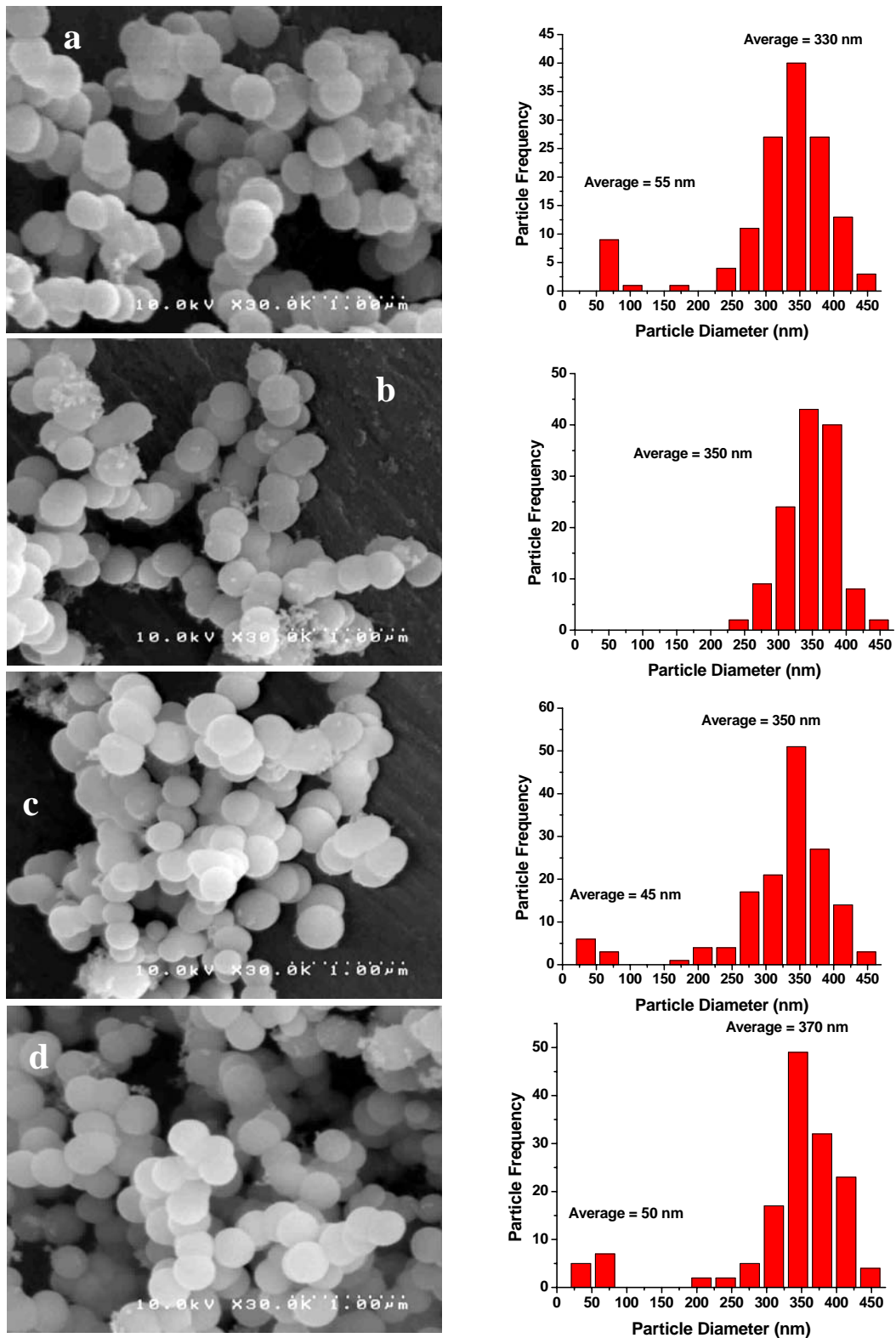


Figure 59: SEM micrographs and histograms of silica nanoparticles produced from the G0 PAMAM template in concentrations of phosphate buffer of a) 0.5 mM, b) 5 mM, c) 10 mM, d) 20 mM, e) 40 mM, f) 60 mM, g) 80 mM and h) 100 mM.

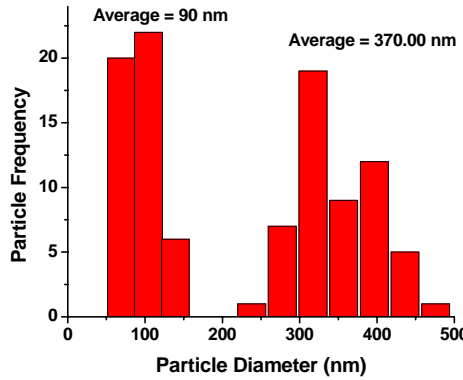
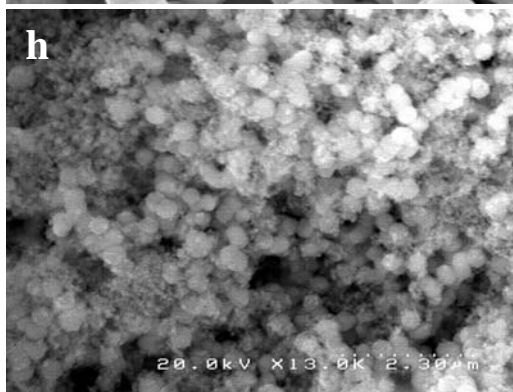
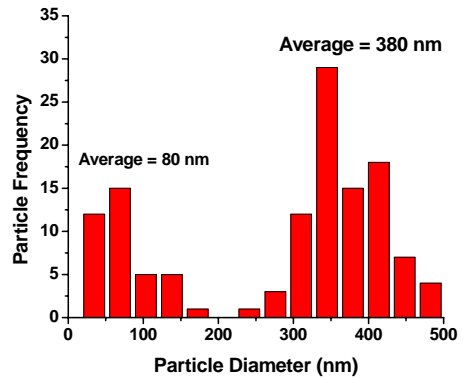
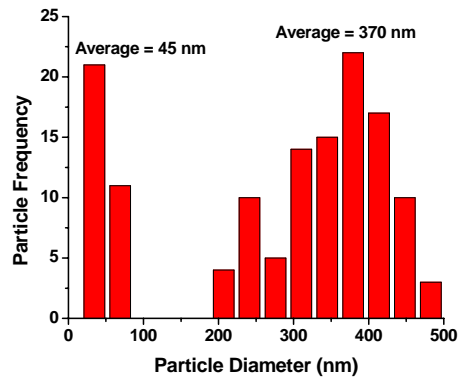
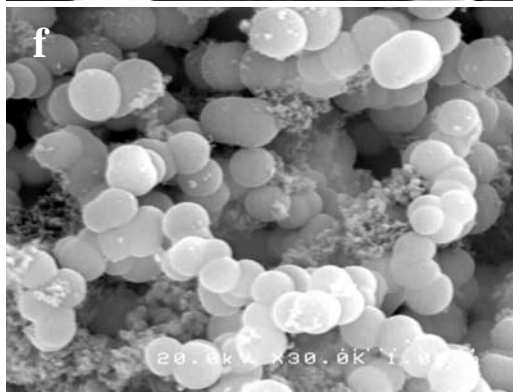
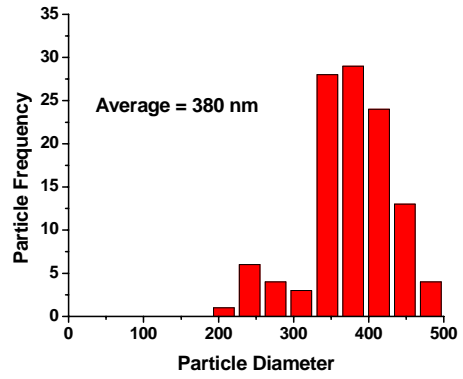
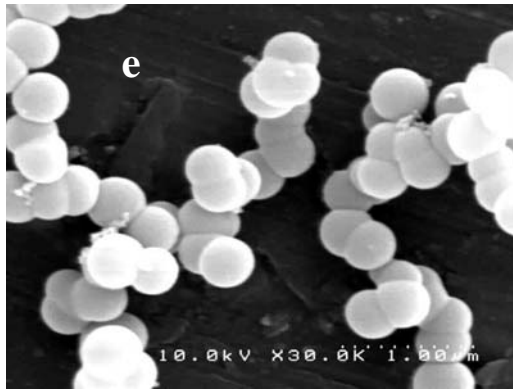


Figure 59. Continued.

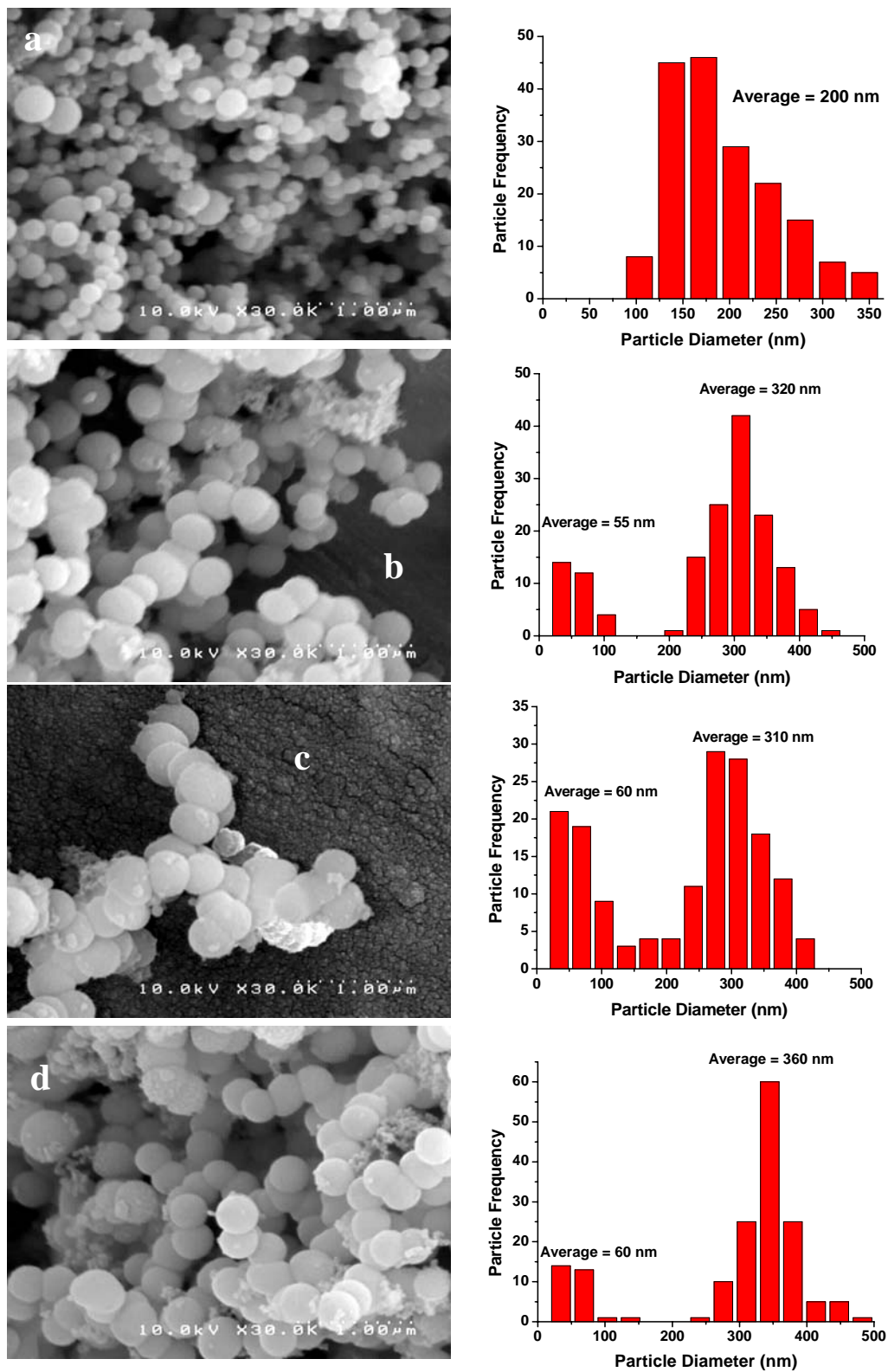


Figure 60: SEM micrographs and histograms of silica nanoparticles produced from the G1 PAMAM template in concentrations of phosphate buffer of a) 0.5 mM, b) 5 mM, c) 10 mM, d) 20 mM, e) 40 mM, f) 60 mM, g) 80 mM and h) 100 mM.

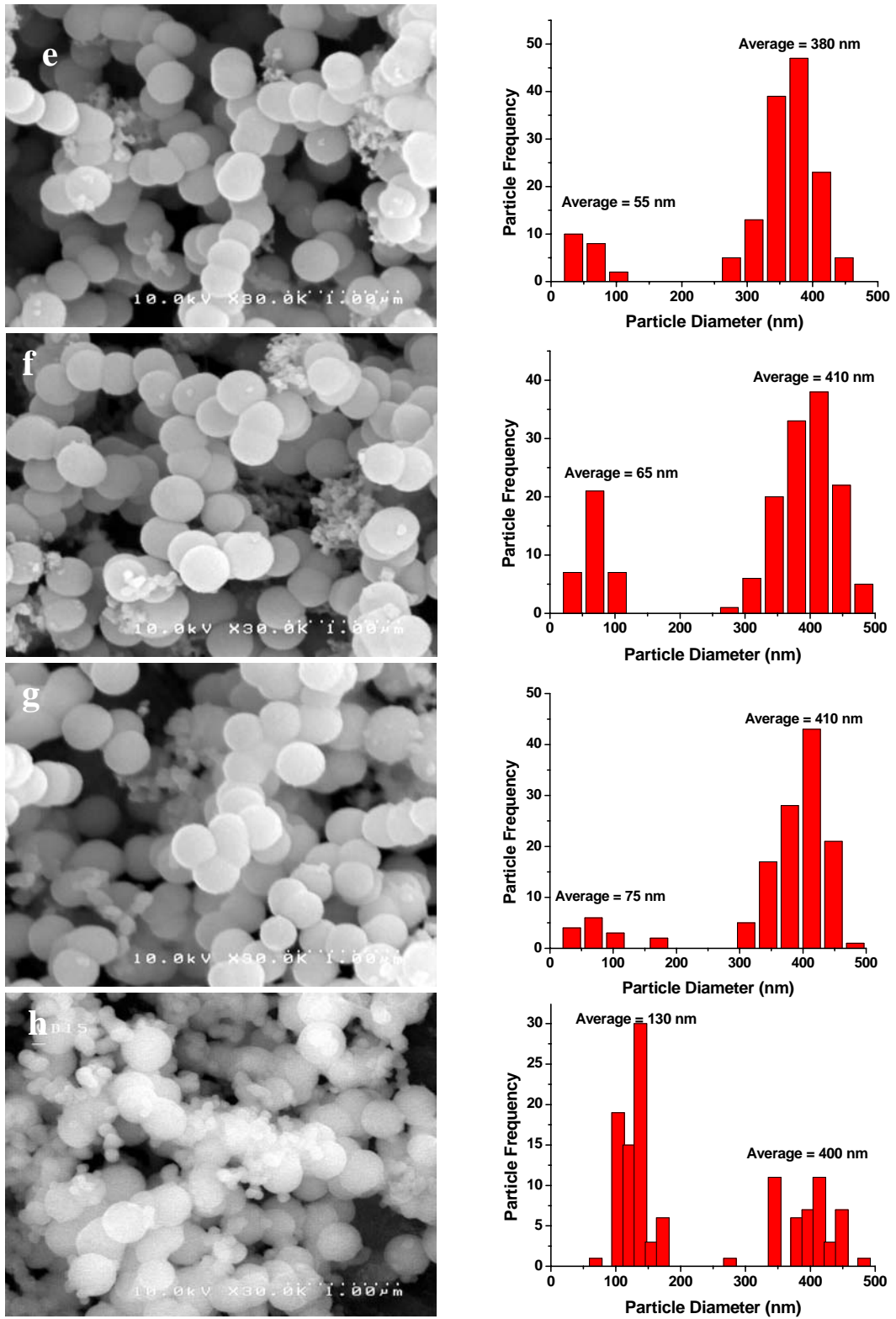


Figure 60. Continued.

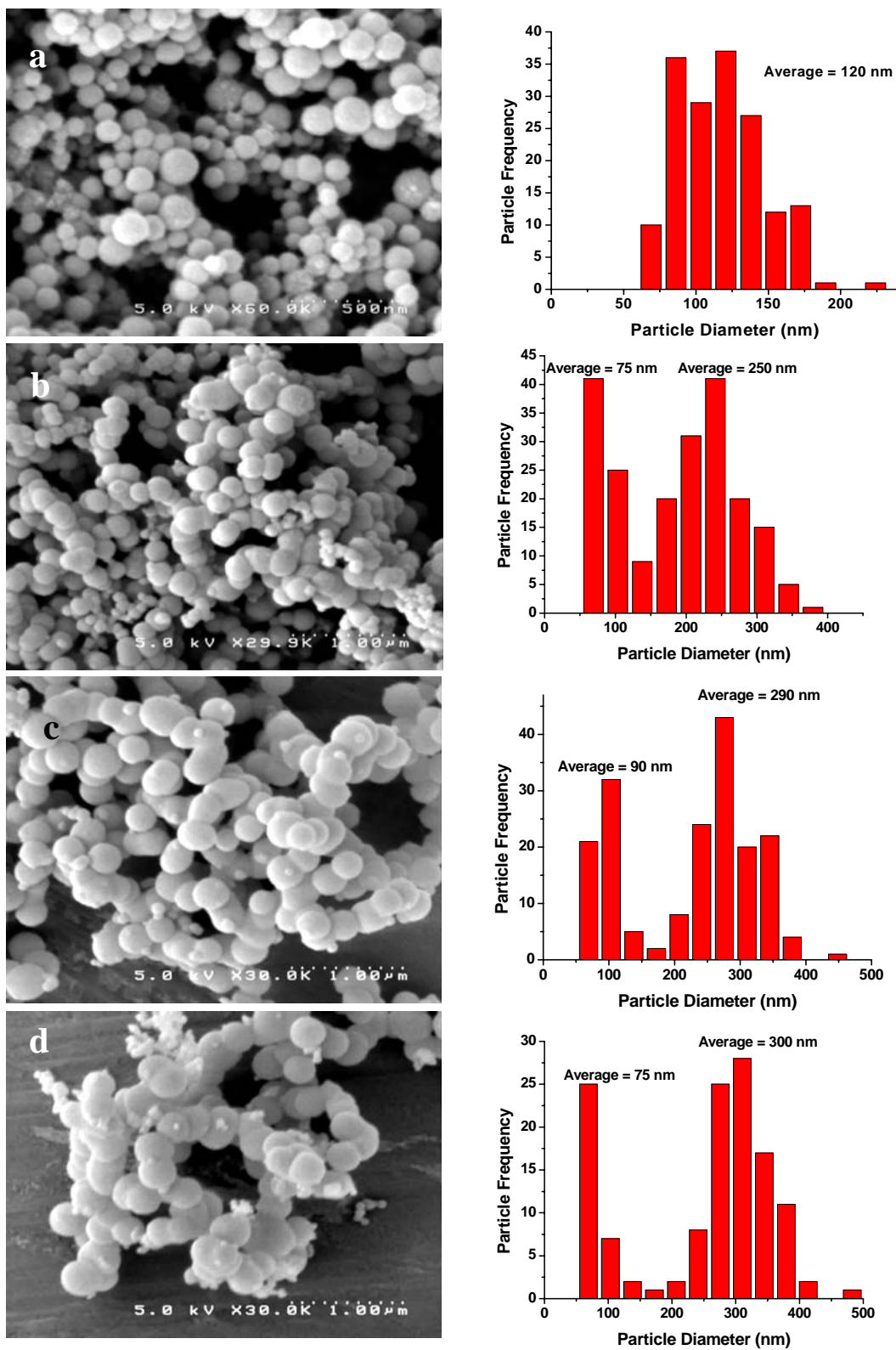


Figure 61: SEM micrographs and histograms of silica nanoparticles produced from the G2 PAMAM template in concentrations of phosphate buffer of a) 0.5 mM, b) 5 mM, c) 10 mM, d) 20 mM, e) 40 mM, f) 60 mM, g) 80 mM and h) 100 mM.

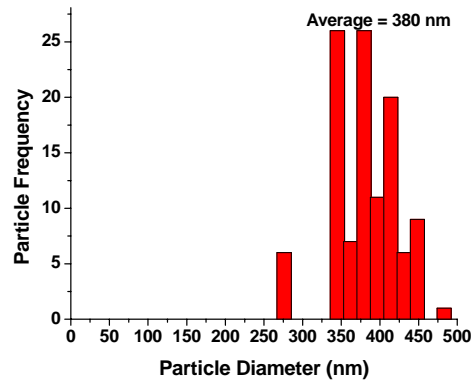
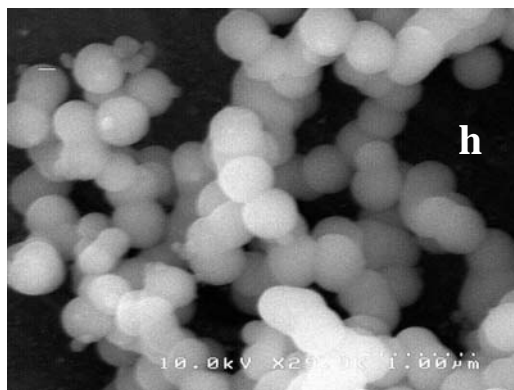
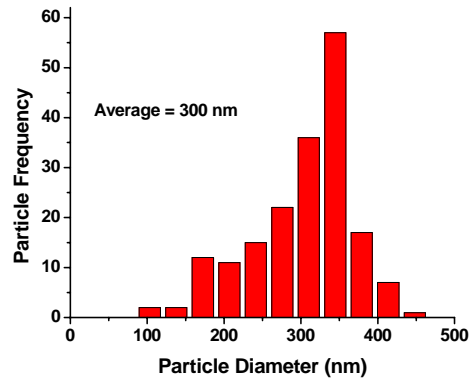
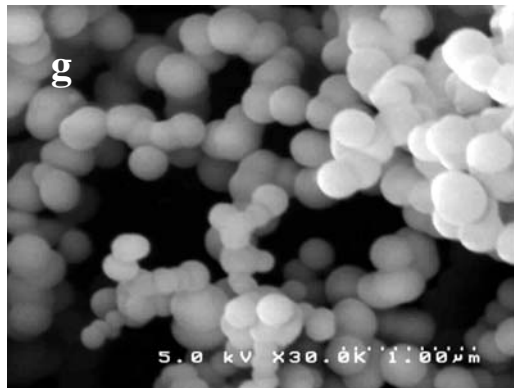
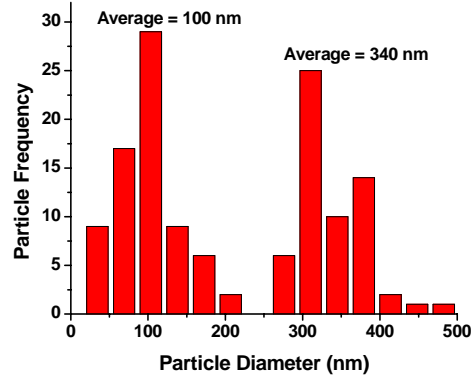
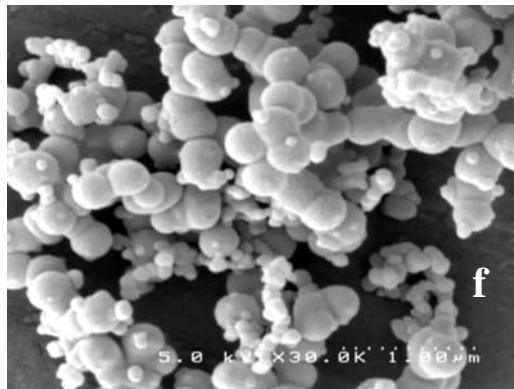
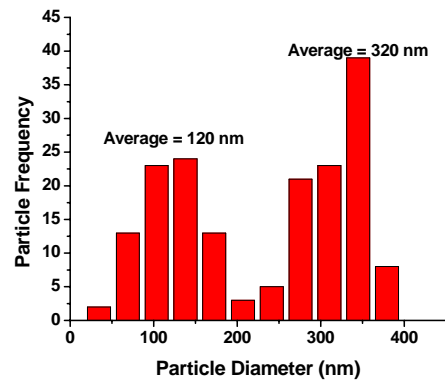
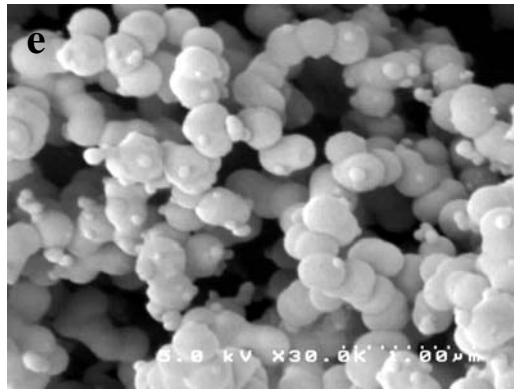


Figure 61. Continued.

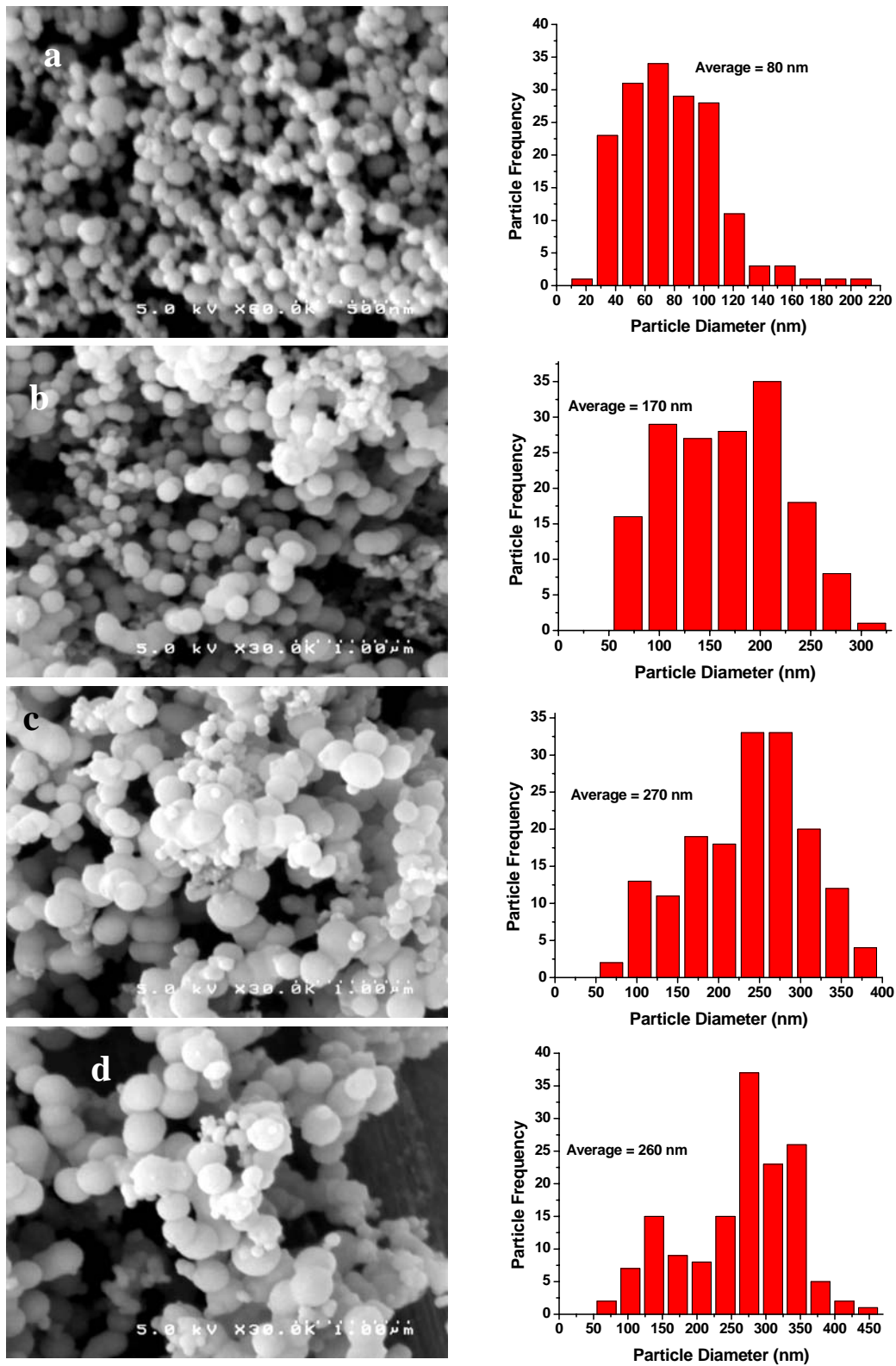


Figure 62: SEM micrographs and histograms of silica nanoparticles produced from the G3 PAMAM template in concentrations of phosphate buffer of a) 0.5 mM, b) 5 mM, c) 10 mM, d) 20 mM, e) 40 mM, f) 60 mM, g) 80 mM and h) 100 mM.

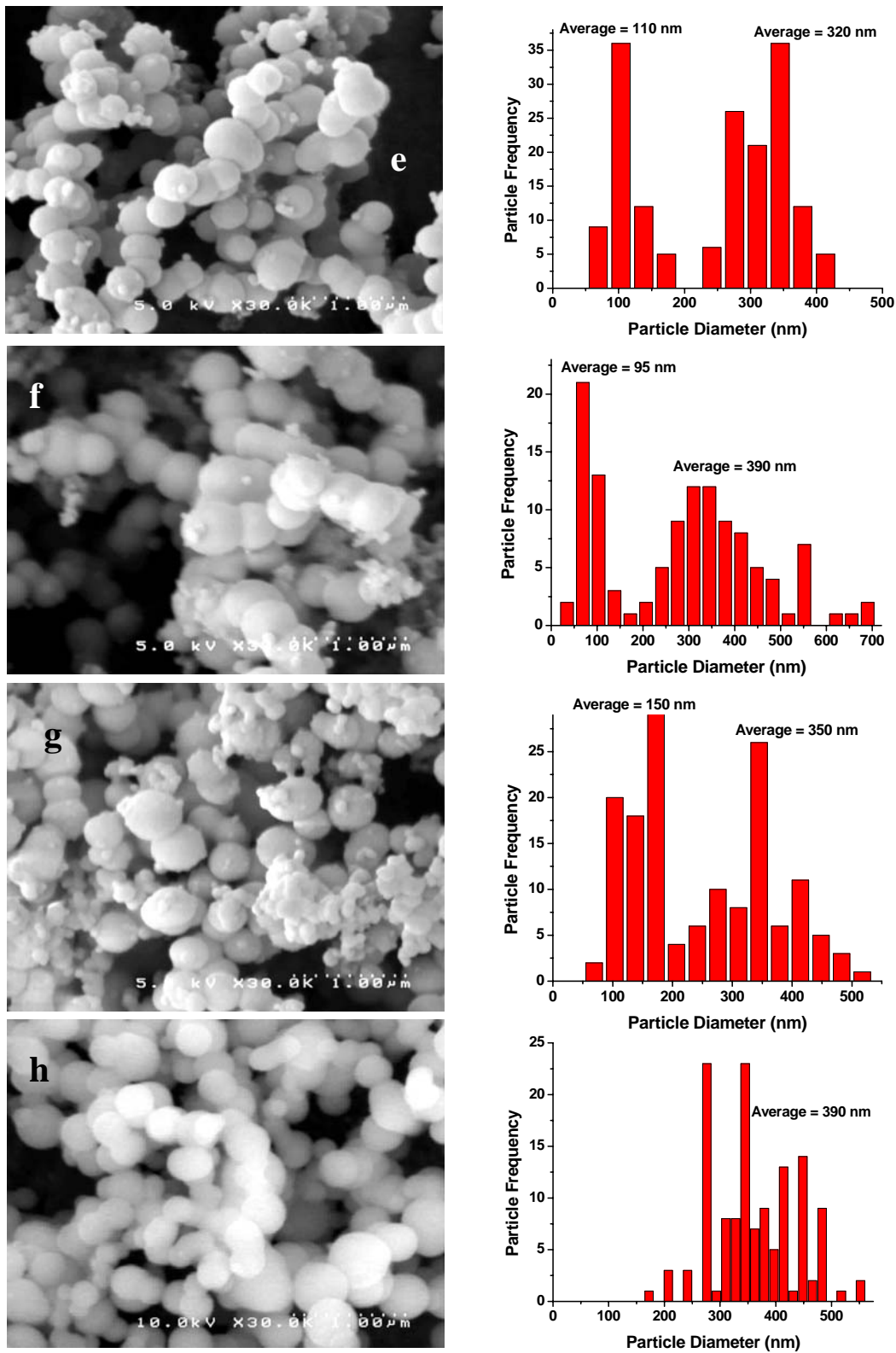


Figure 62. Continued

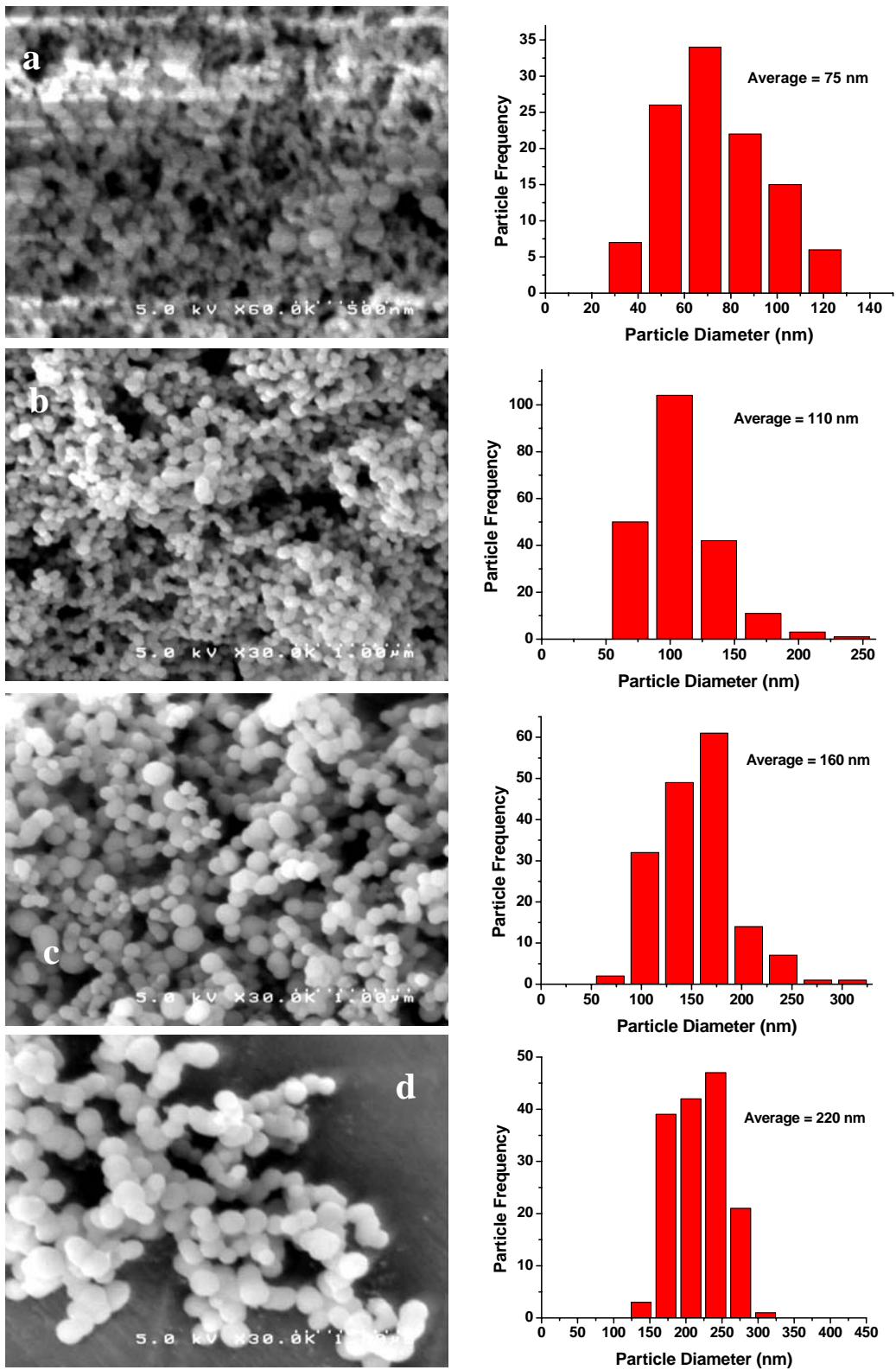


Figure 63: SEM micrographs and histograms of silica nanoparticles produced from the G4 PAMAM template in concentrations of phosphate buffer of a) 0.5 mM, b) 5 mM, c) 10 mM, d) 20 mM, e) 40 mM, f) 60 mM, g) 80 mM and h) 100 mM.

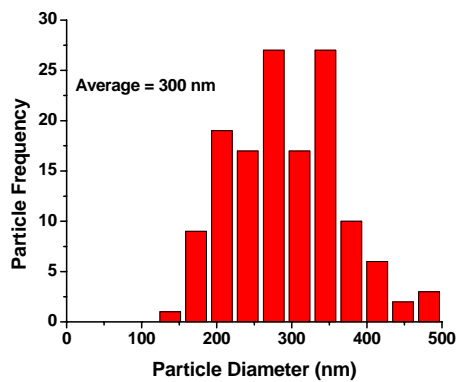
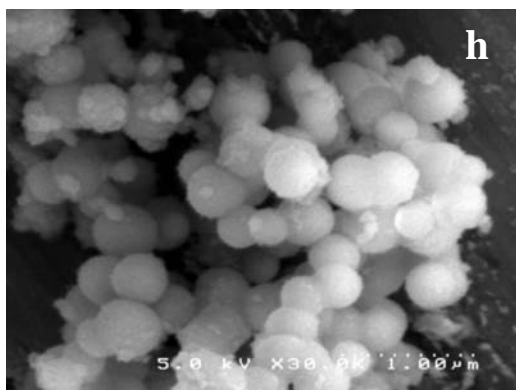
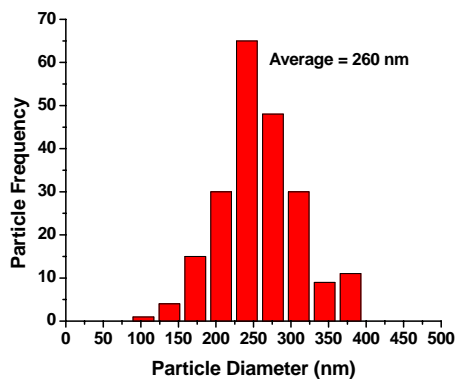
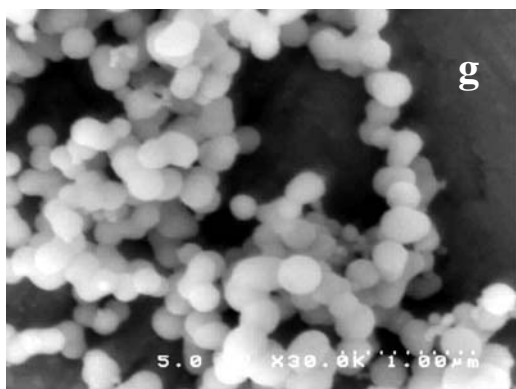
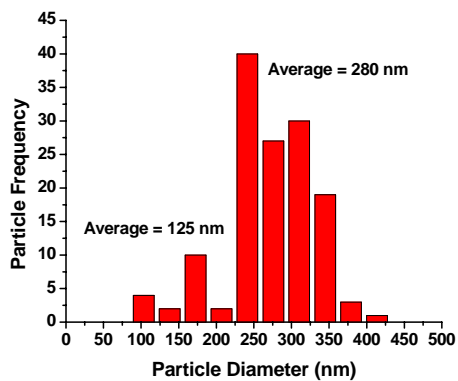
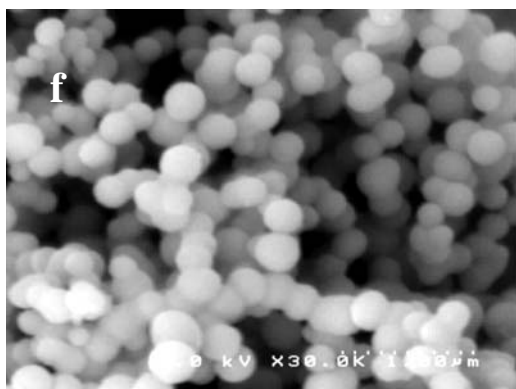
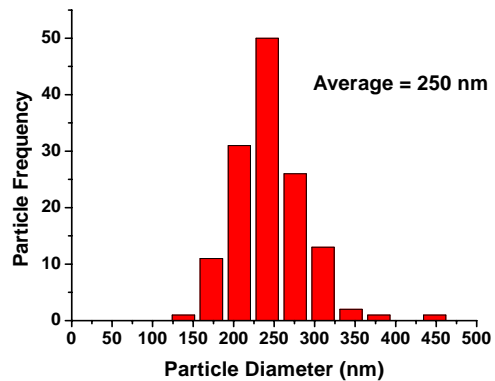
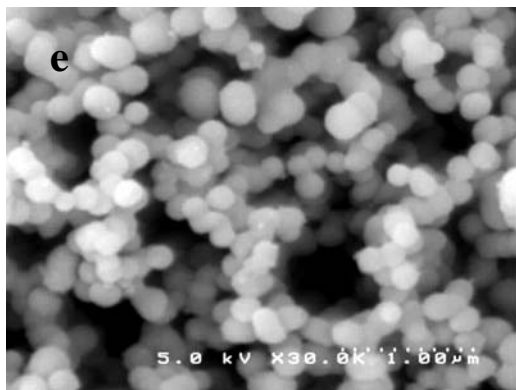


Figure 63. Continued.

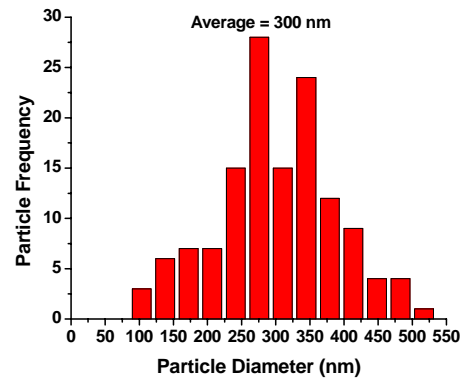
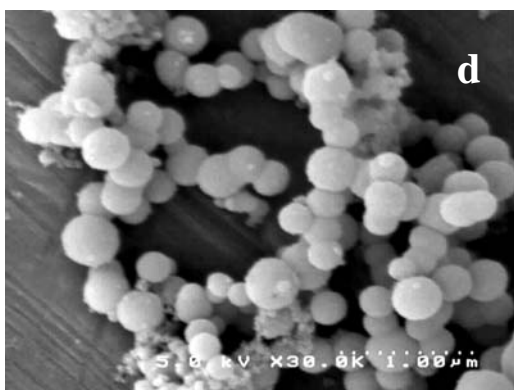
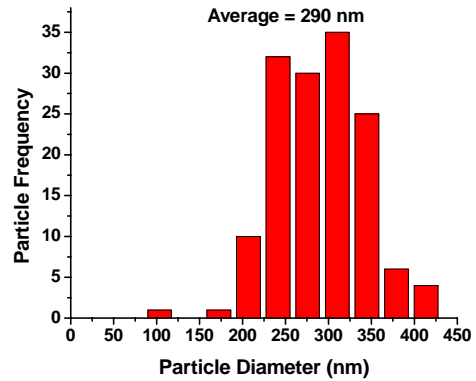
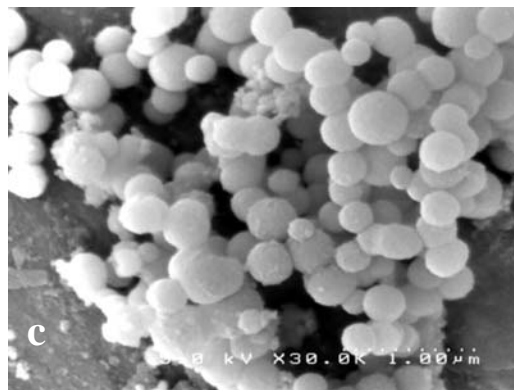
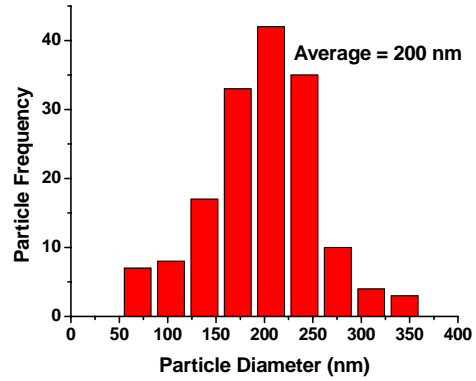
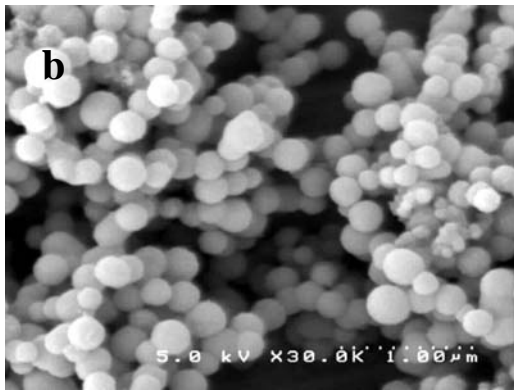
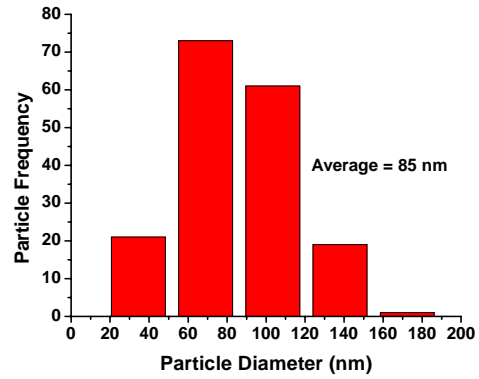
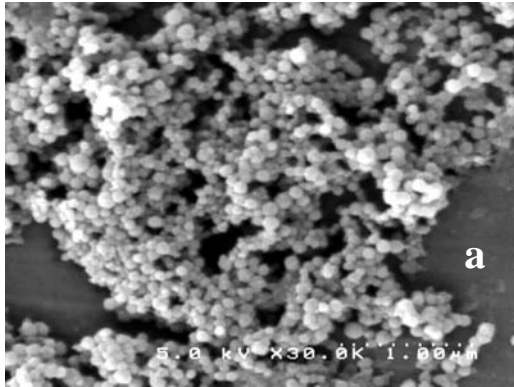


Figure 64: SEM micrographs and histograms of silica nanoparticles produced from the G5 PAMAM template in concentrations of phosphate buffer of a) 0.5 mM, b) 5 mM, c) 10 mM, d) 20 mM, e) 40 mM, f) 60 mM, g) 80 mM and h) 100 mM.

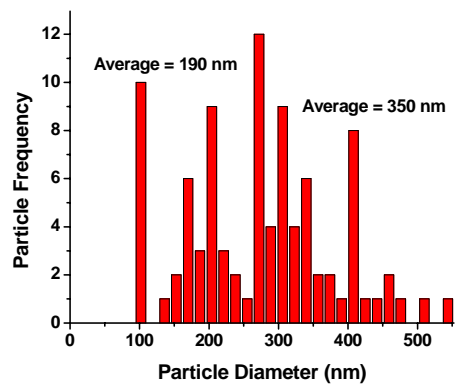
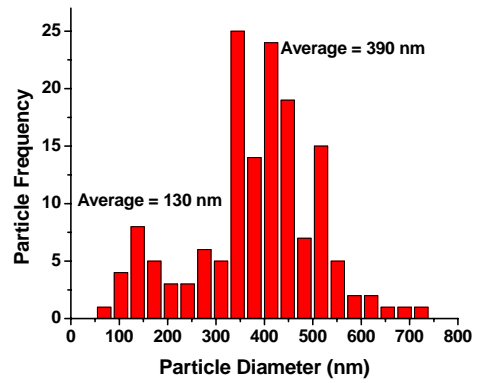
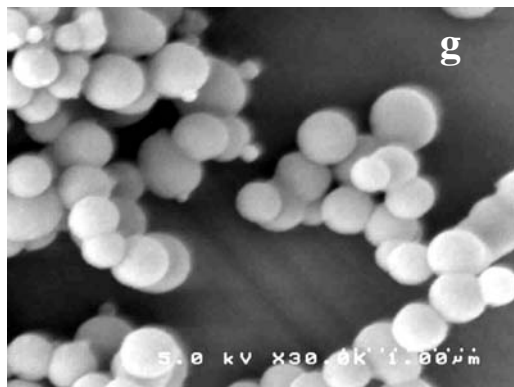
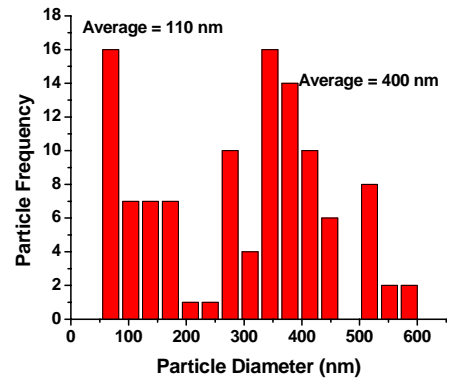
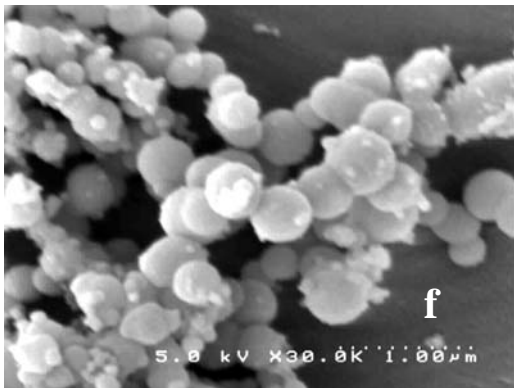
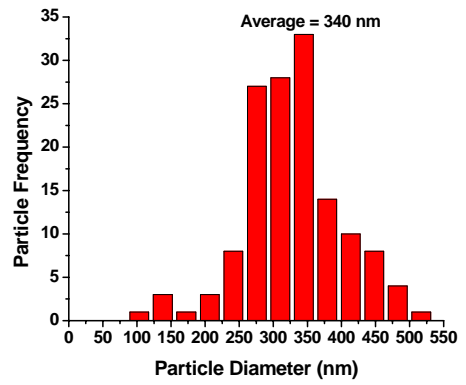
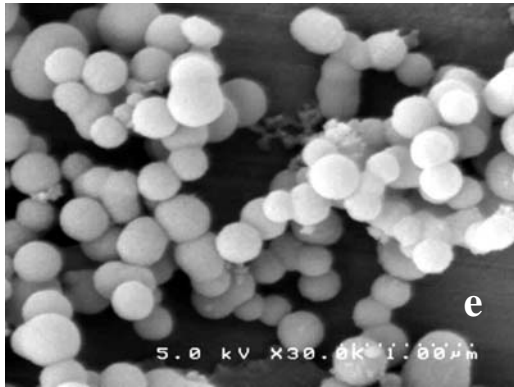


Figure 64. Continued.

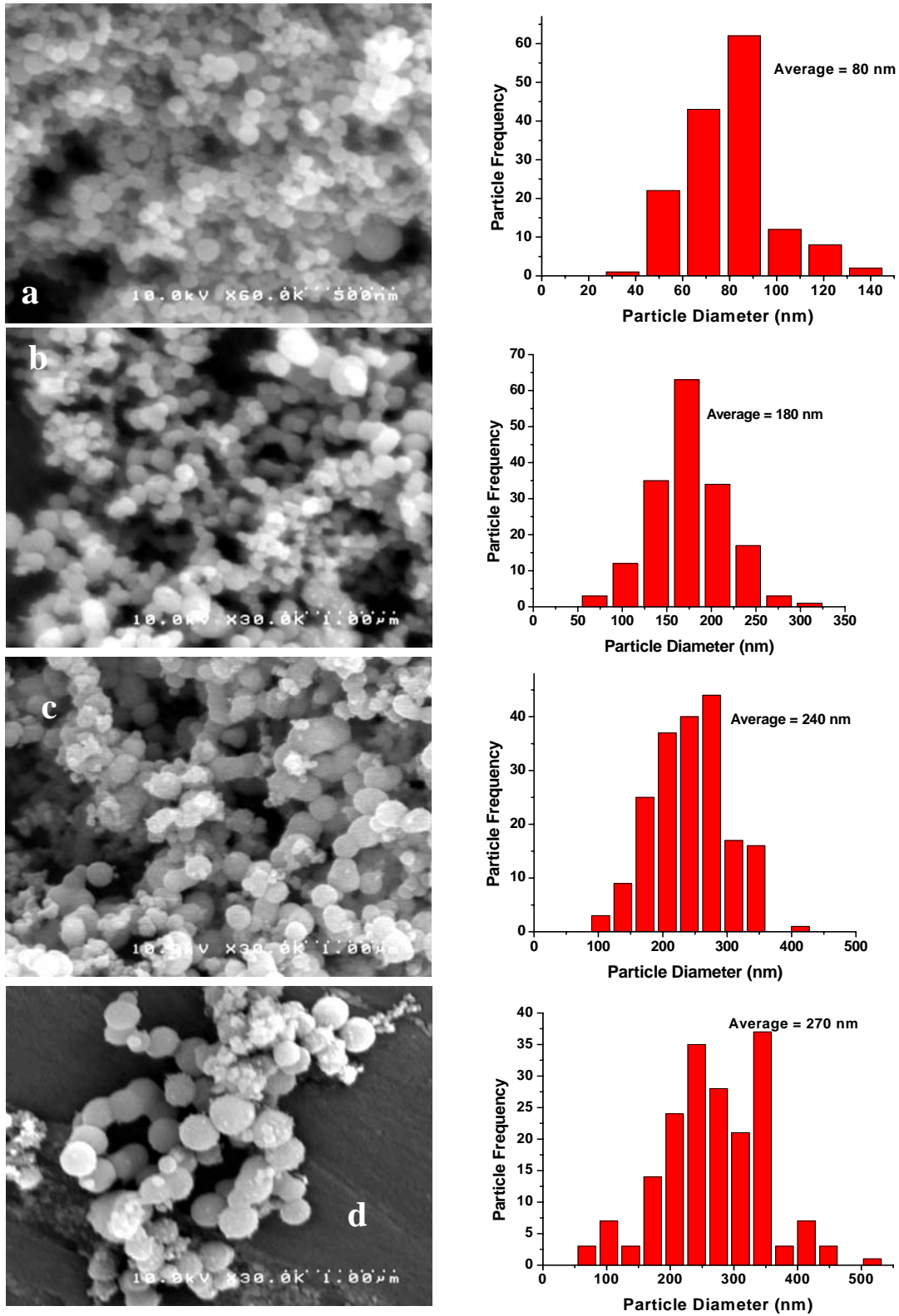


Figure 65: SEM micrographs and histograms of silica nanoparticles produced from the G6 PAMAM template in concentrations of phosphate buffer of a) 0.5 mM, b) 5 mM, c) 10 mM, d) 20 mM, e) 40 mM, f) 60 mM, g) 80 mM and h) 100 mM.

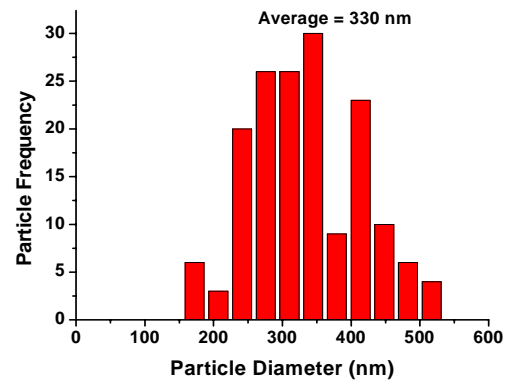
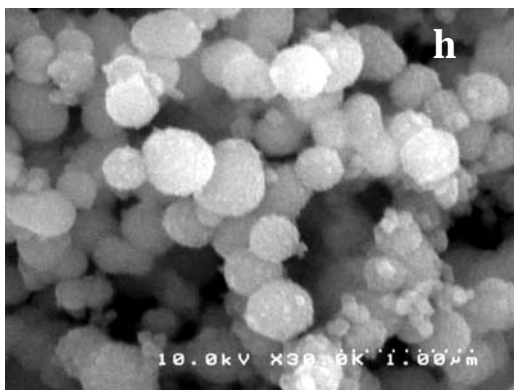
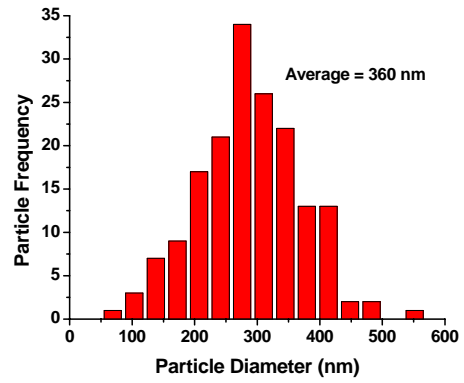
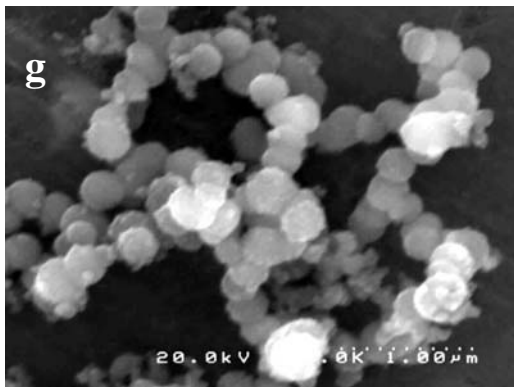
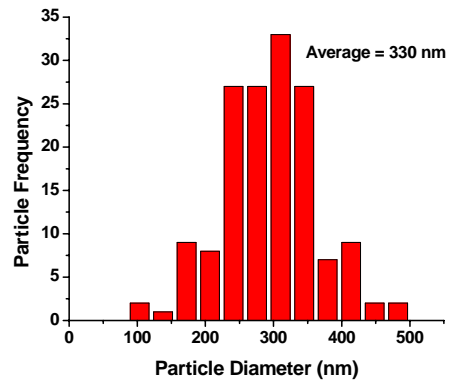
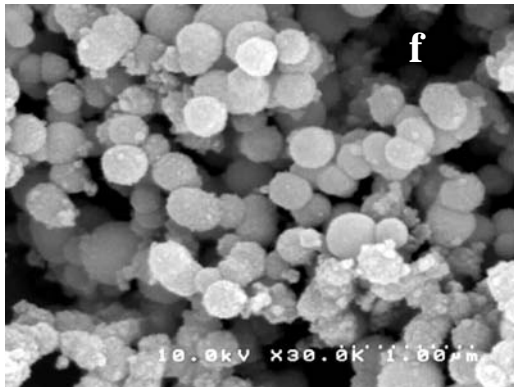
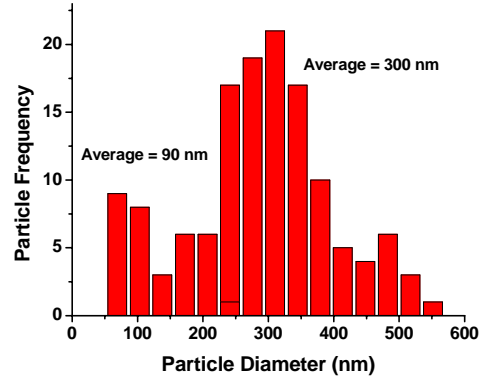
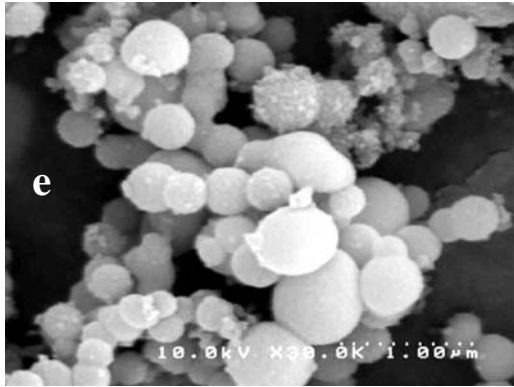


Figure 65. Continued.

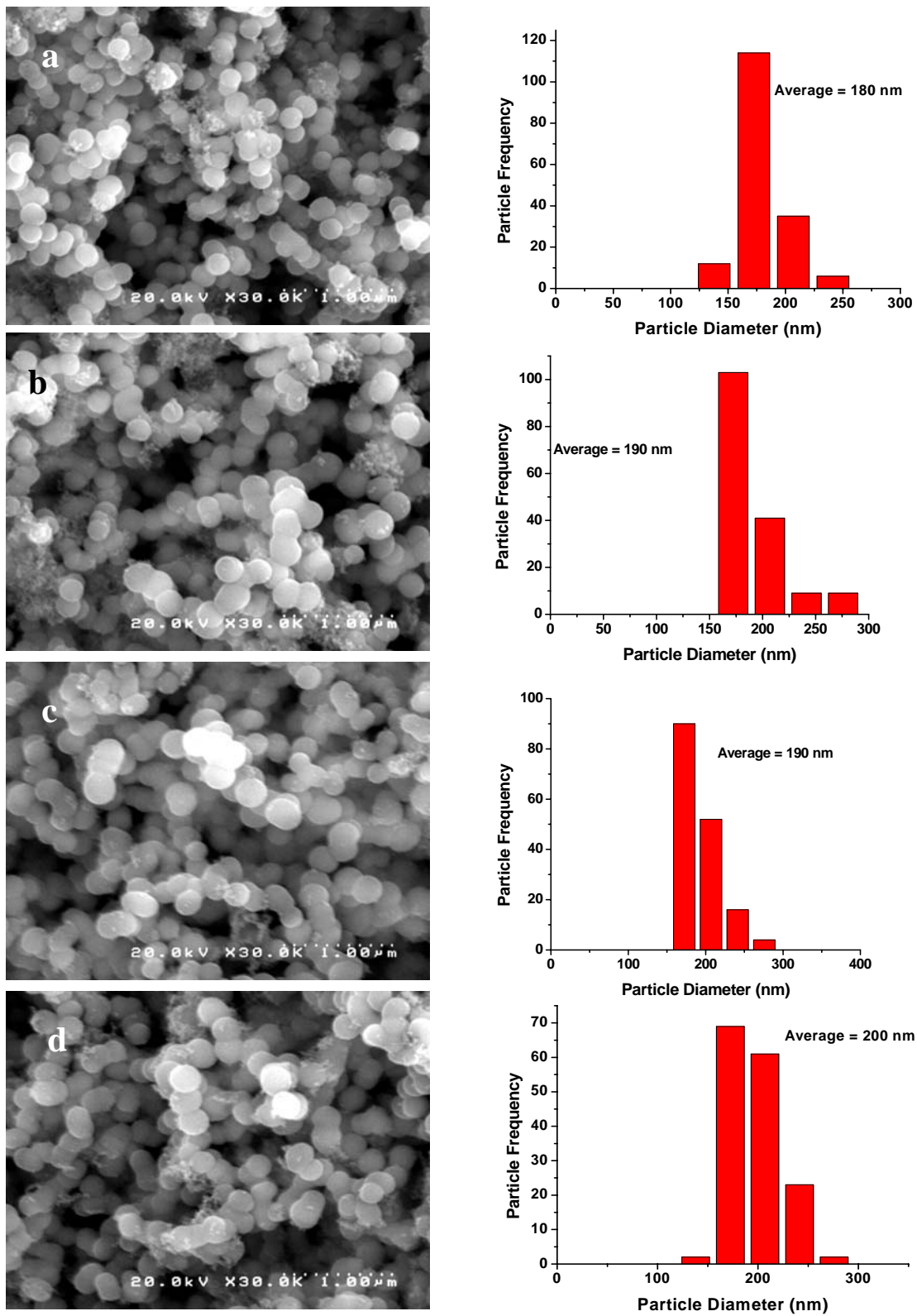


Figure 66: SEM micrographs and histograms of silica nanoparticles produced from the G1 PPI template in concentrations of phosphate buffer of a) 0.5 mM, b) 5 mM, c) 10 mM, d) 20 mM, e) 40 mM, f) 60 mM, g) 80 mM and h) 100 mM.

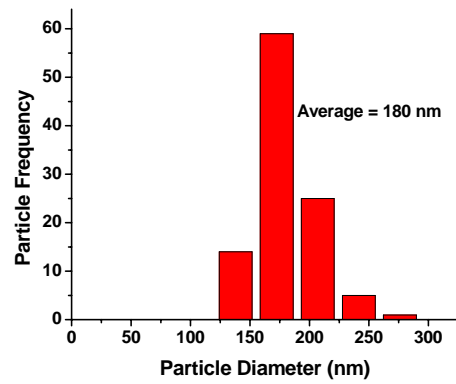
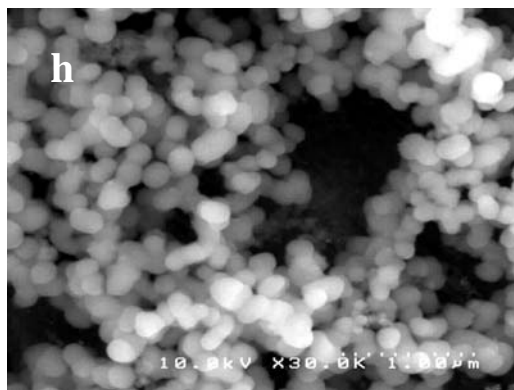
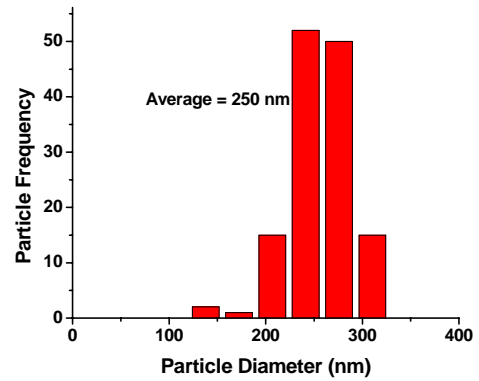
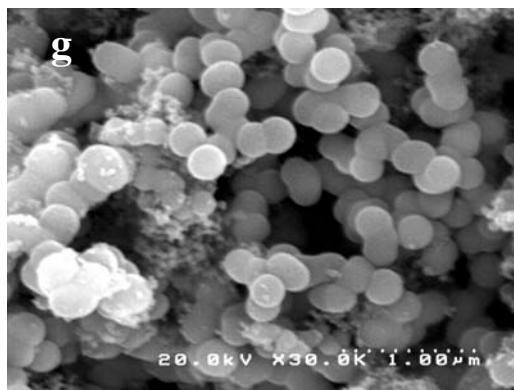
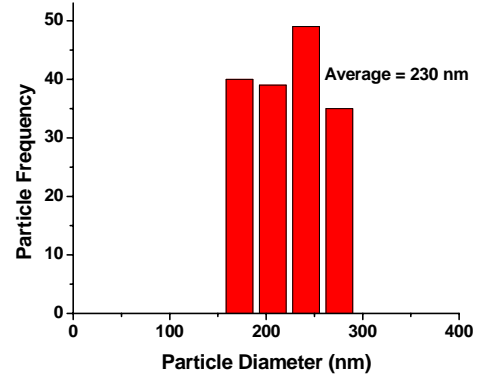
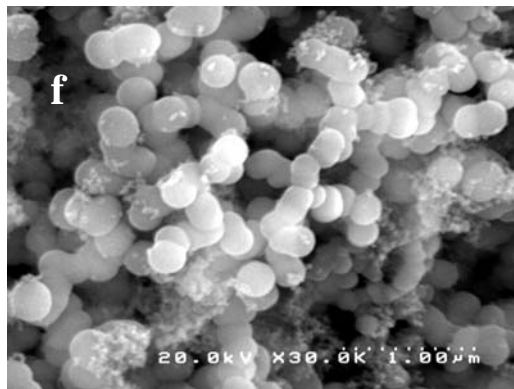
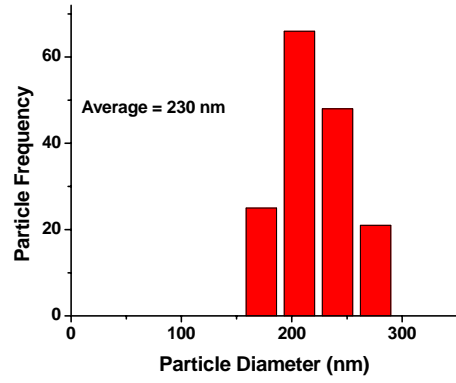
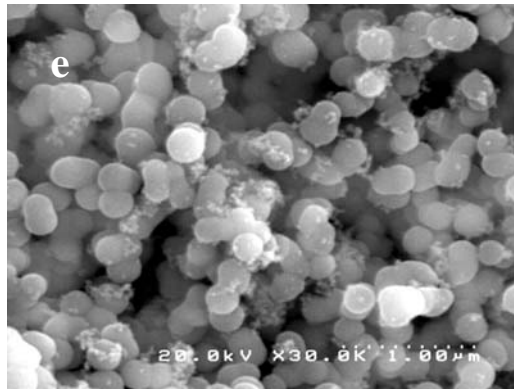


Figure 66. Continued.

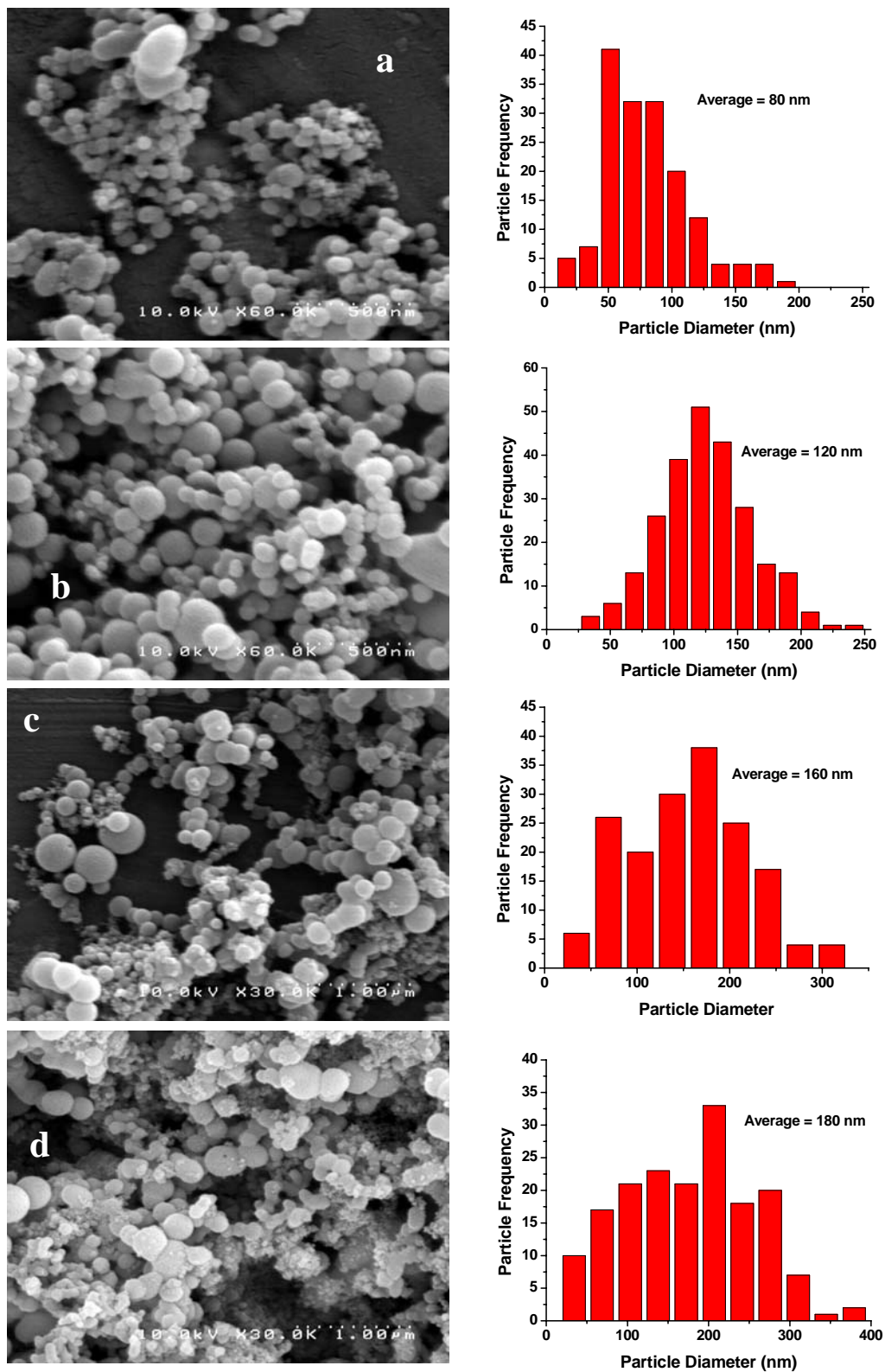


Figure 67: SEM micrographs and histograms of silica nanoparticles produced from the G2 PPI template in concentrations of phosphate buffer of a) 0.5 mM, b) 5 mM, c) 10 mM, d) 20 mM, e) 40 mM, f) 60 mM, g) 80 mM and h) 100 mM.

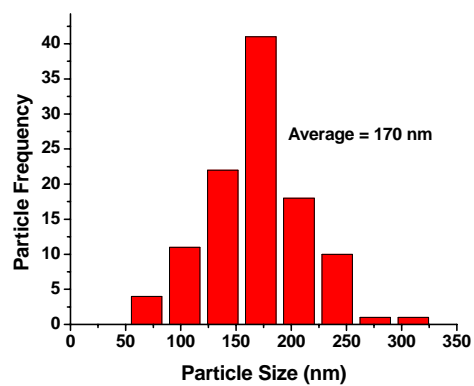
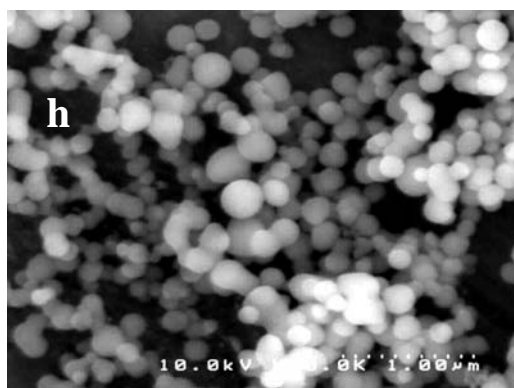
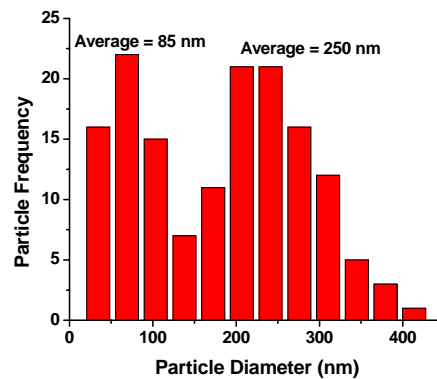
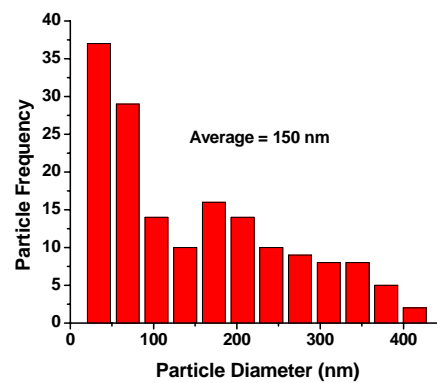
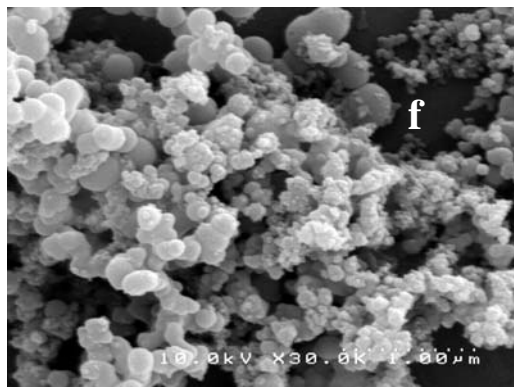
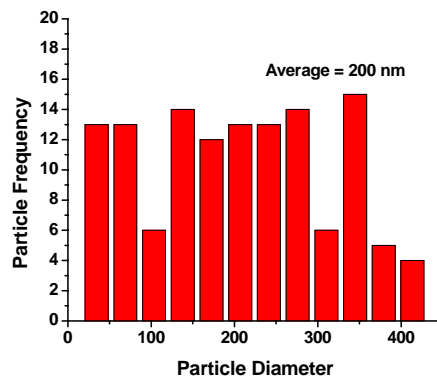
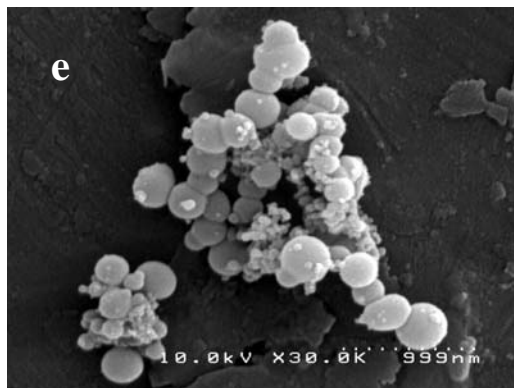


Figure 67. Continued.

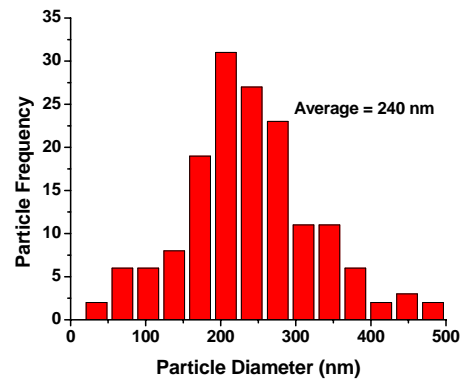
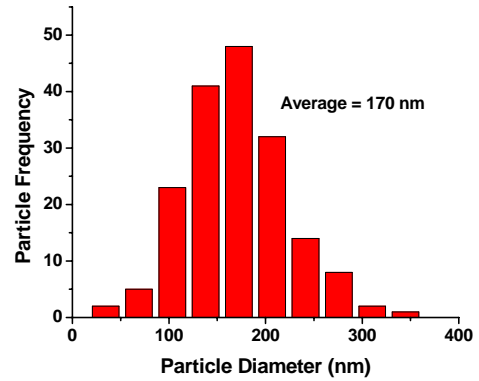
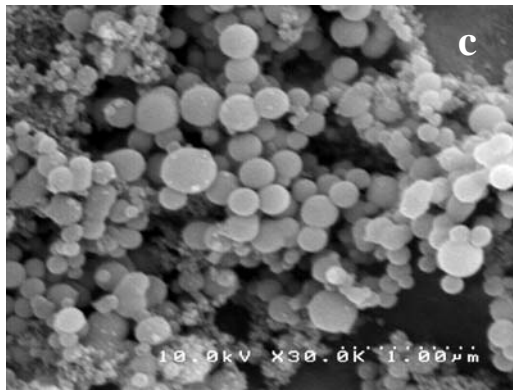
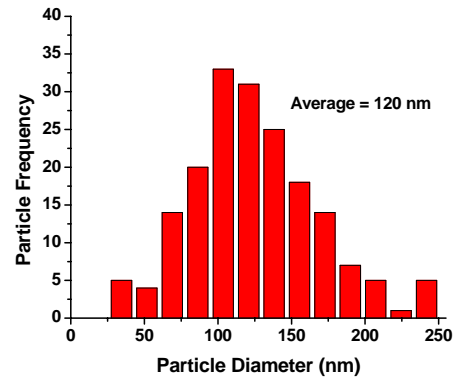
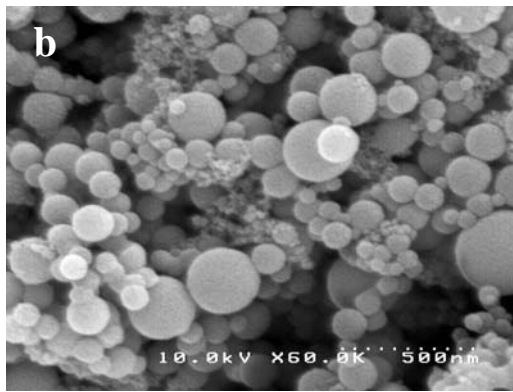
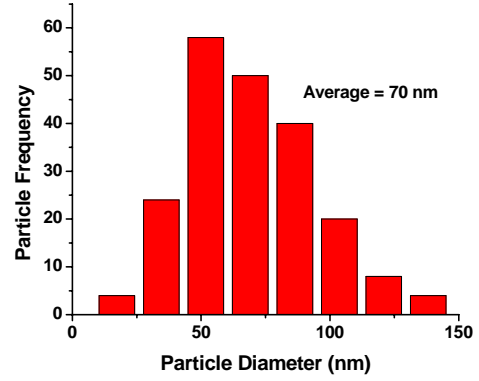
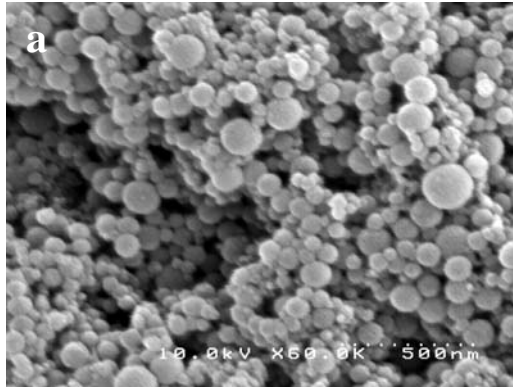


Figure 68: SEM micrographs and histograms of silica nanoparticles produced from the G3 PPI template in concentrations of phosphate buffer of a) 0.5 mM, b) 5 mM, c) 10 mM, d) 20 mM, e) 40 mM, f) 60 mM, g) 80 mM and h) 100 mM.

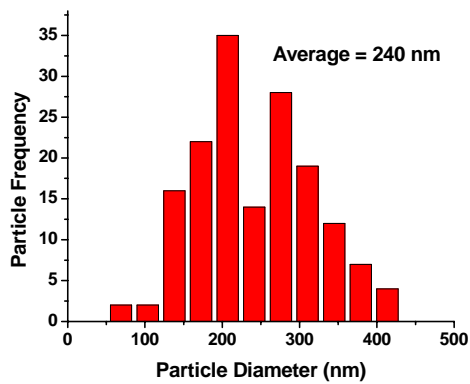
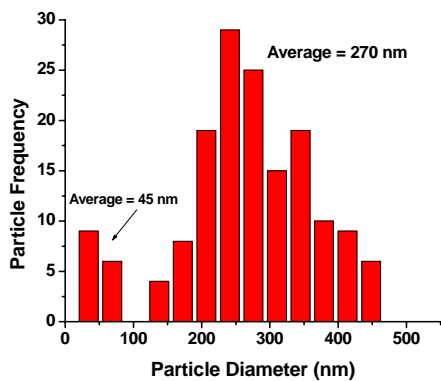
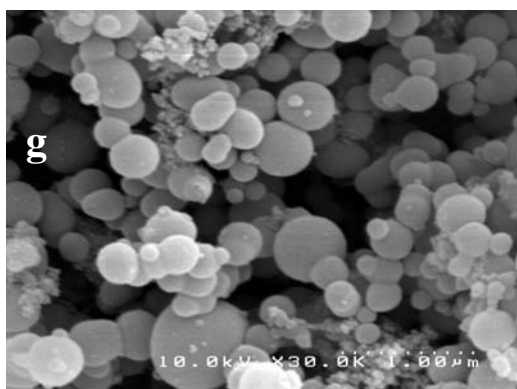
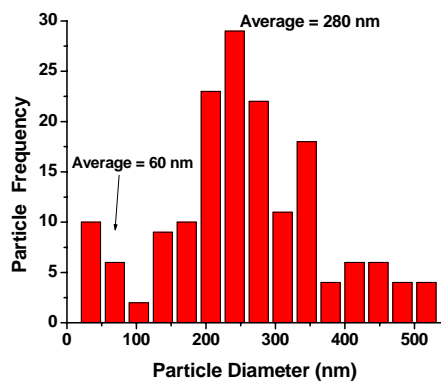
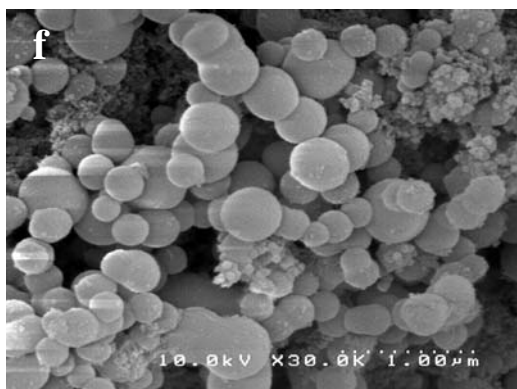
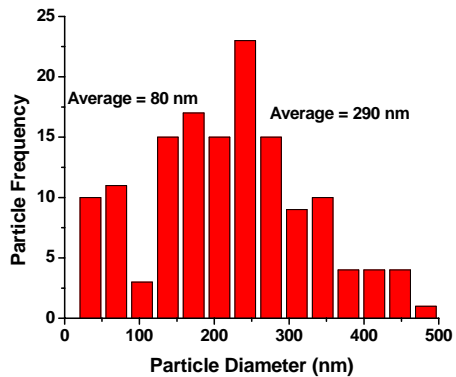
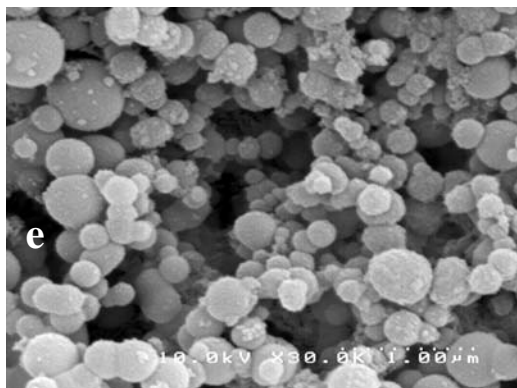


Figure 68. Continued.

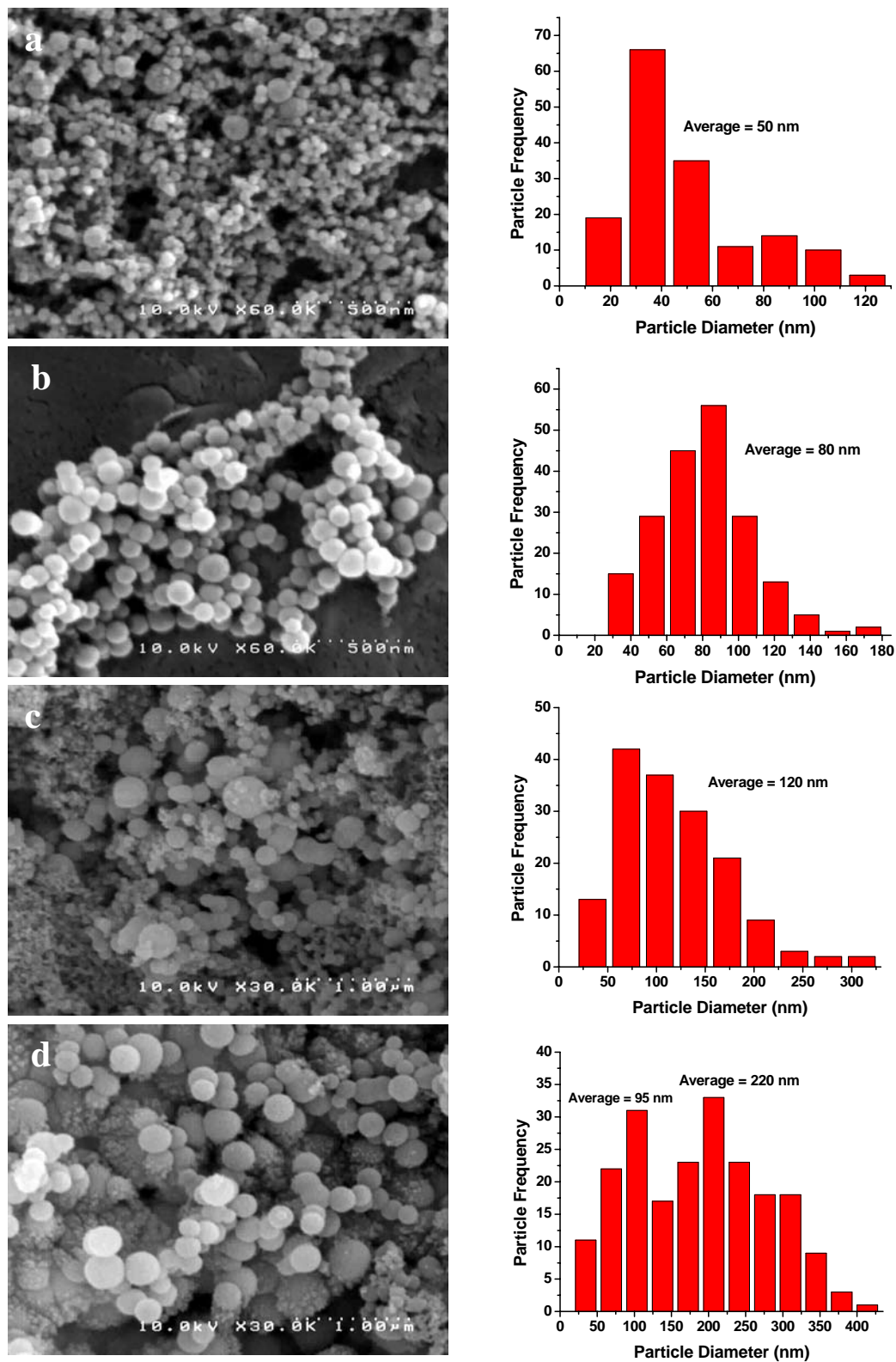


Figure 69: SEM micrographs and histograms of silica nanoparticles produced from the G4 PPI template in concentrations of phosphate buffer of a) 0.5 mM, b) 5 mM, c) 10 mM, d) 20 mM, e) 40 mM, f) 60 mM, g) 80 mM and h) 100 mM.

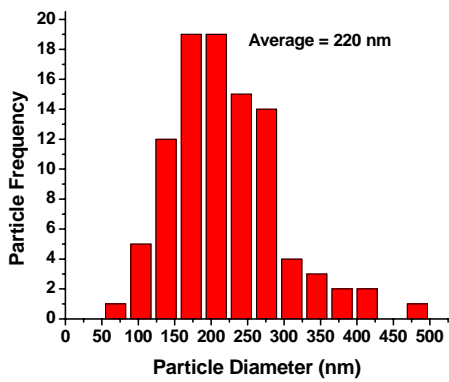
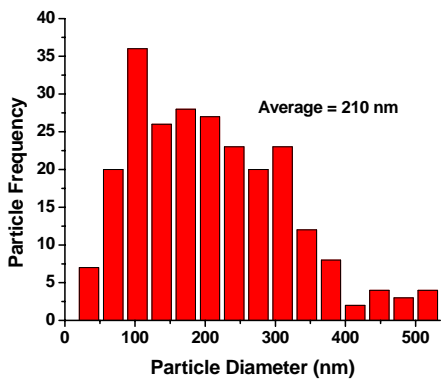
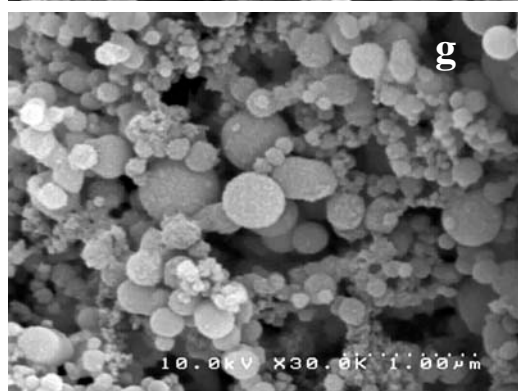
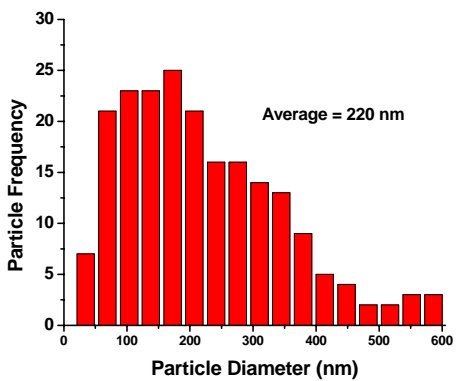
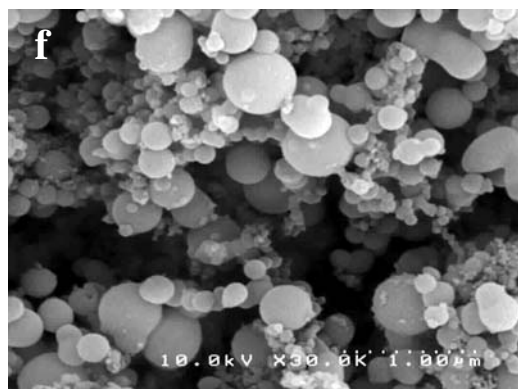
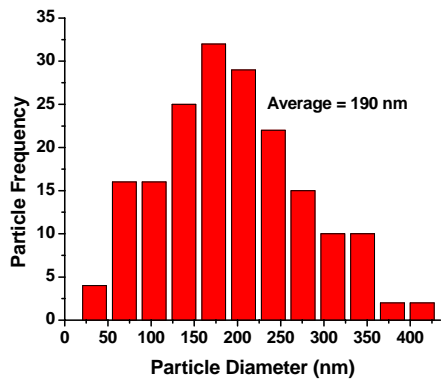
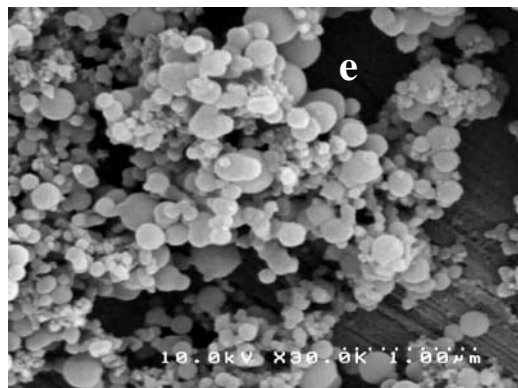


Figure 69. Continued.

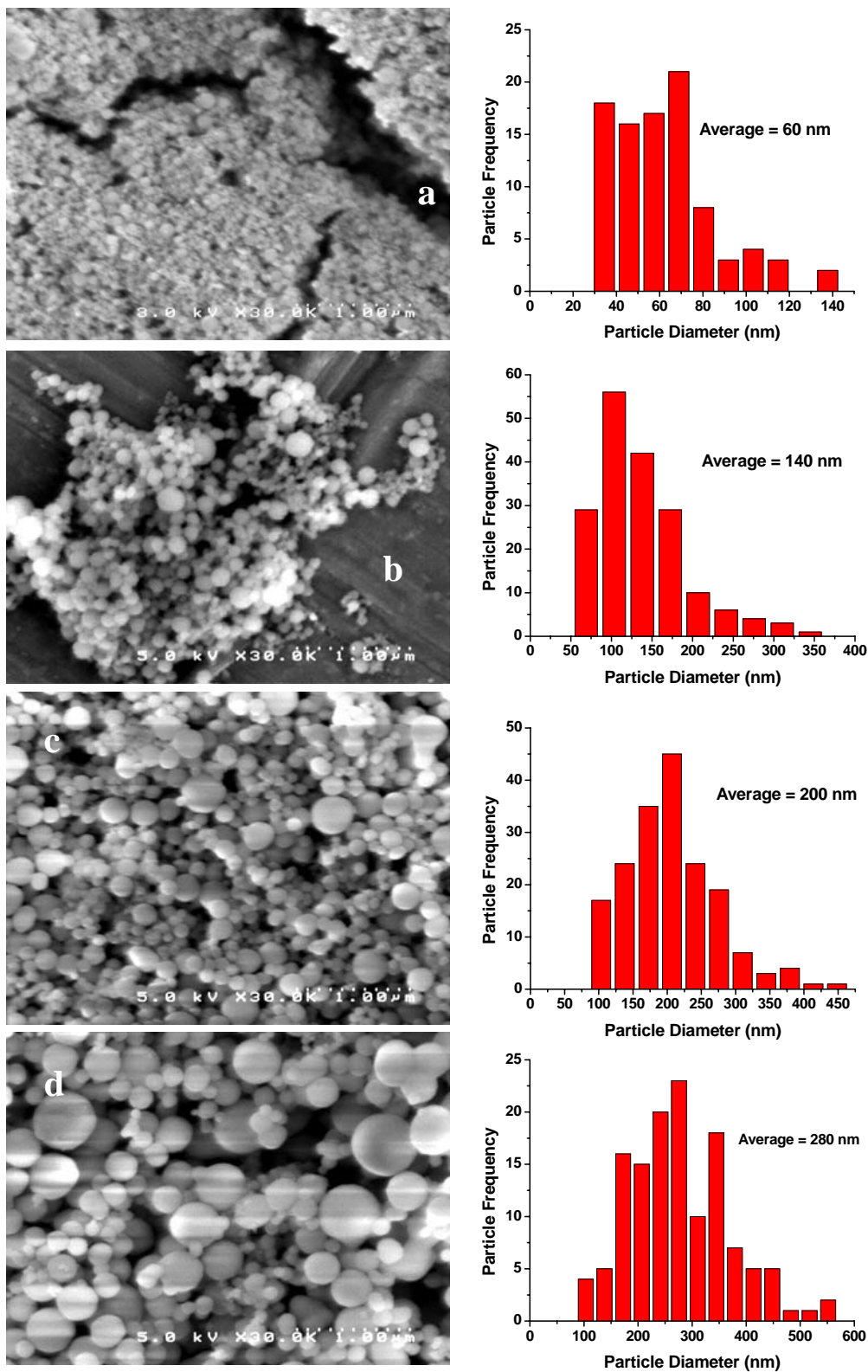


Figure 70: SEM micrographs and histograms of silica nanoparticles produced from the G5 PPI template in concentrations of phosphate buffer of a) 0.5 mM, b) 5 mM, c) 10 mM, d) 20 mM, e) 40 mM, f) 60 mM, g) 80 mM and h) 100 mM.

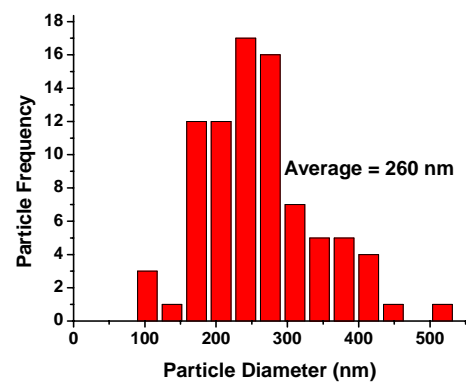
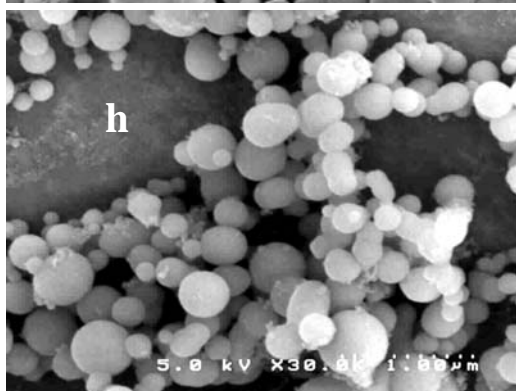
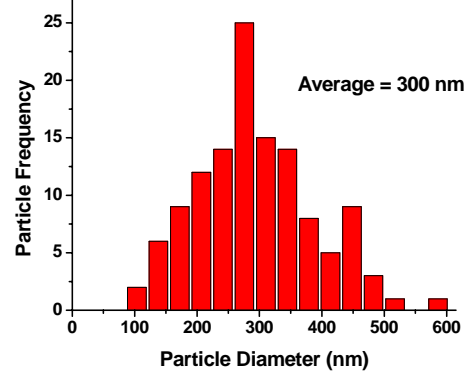
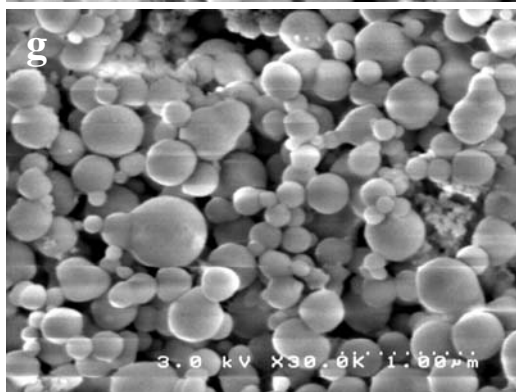
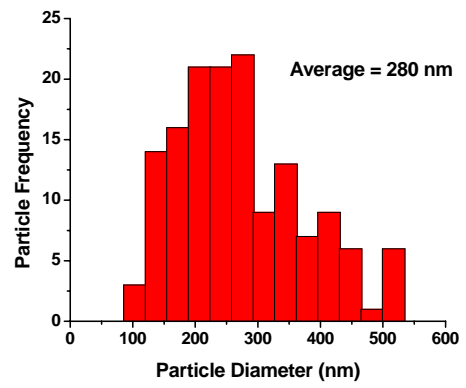
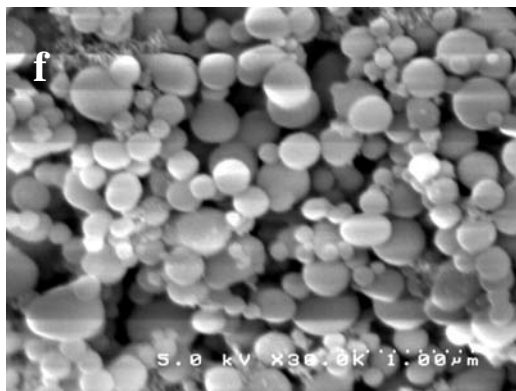
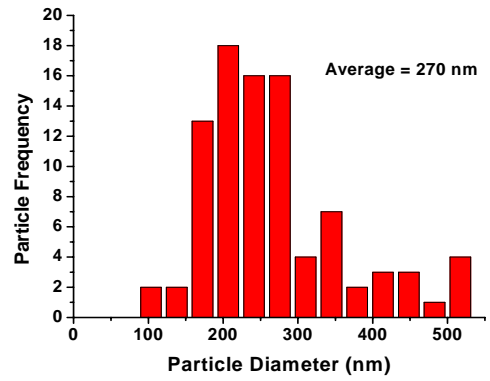


Figure 70. Continued.

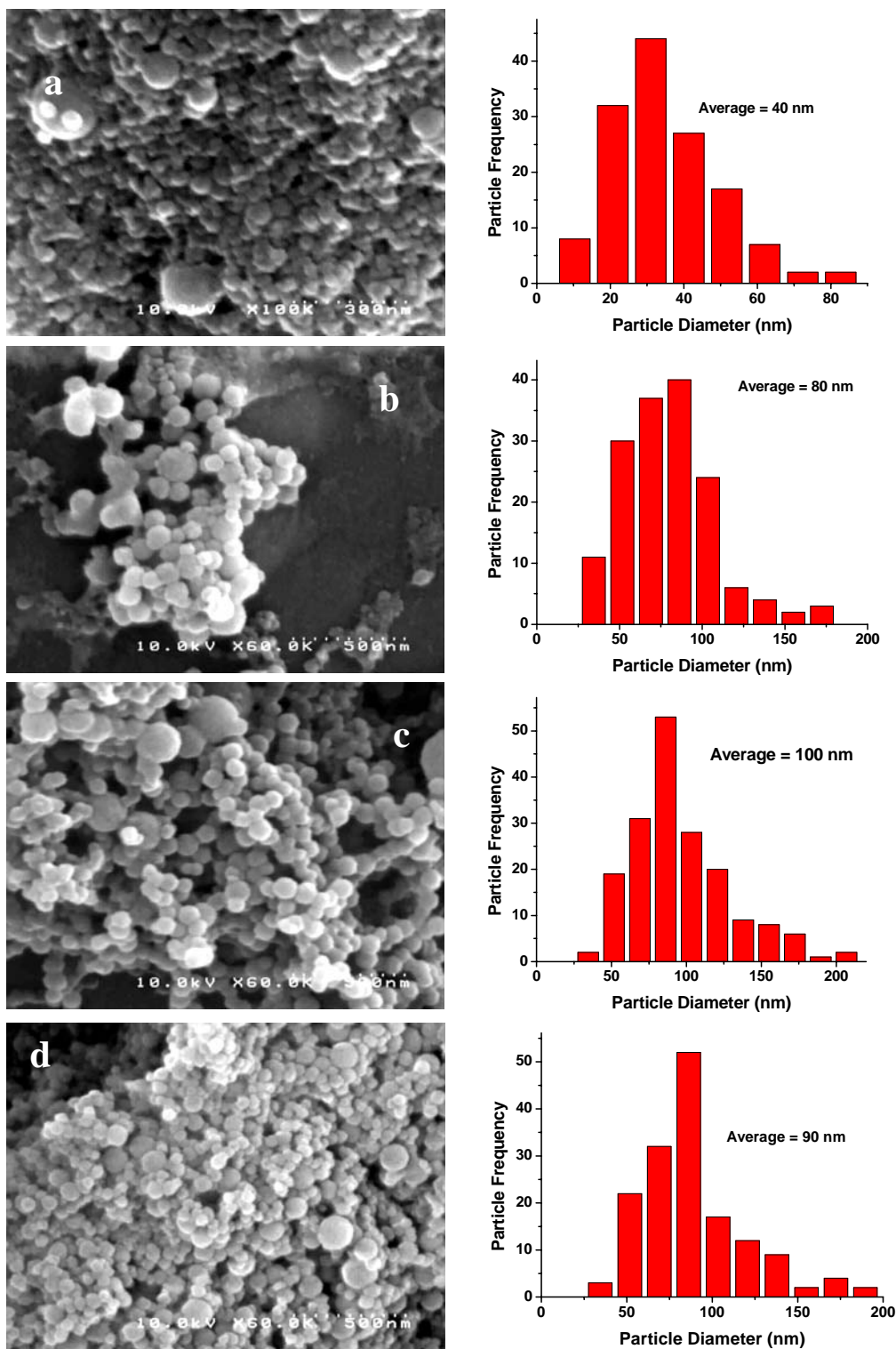


Figure 71: SEM micrographs and histograms of silica nanoparticles produced from the G4 PAMAM template in a LiCl solution with concentrations of a) 0.5 mM, b) 5 mM, c) 10 mM, d) 20 mM, e) 40 mM, f) 60 mM, g) 80 mM, h) 100 mM, i) 200 mM, j) 300 mM and k) 400 mM.

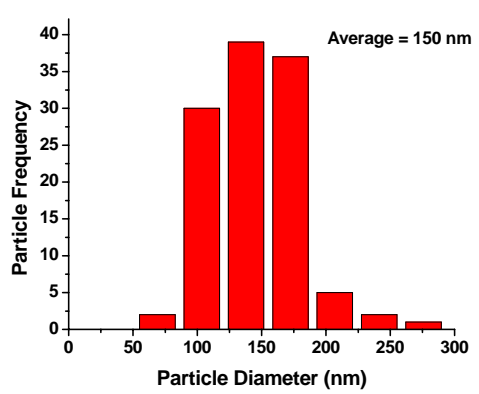
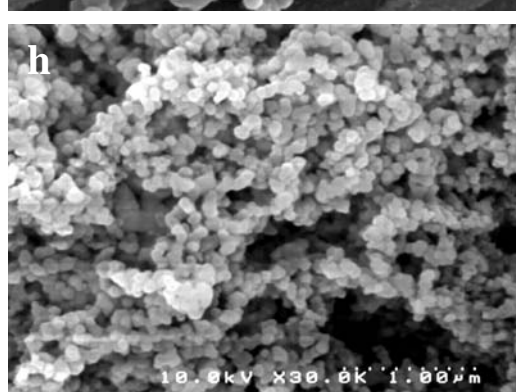
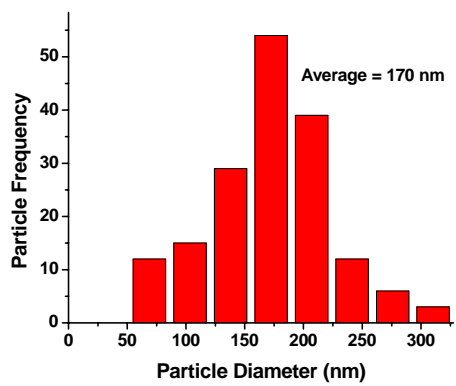
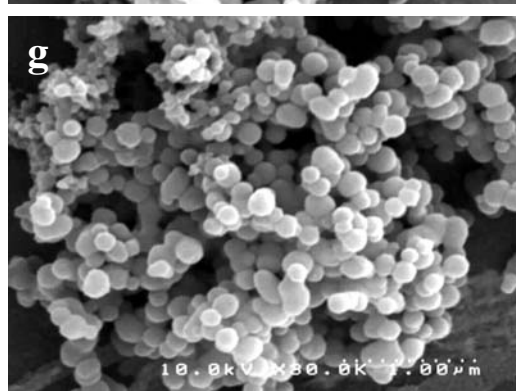
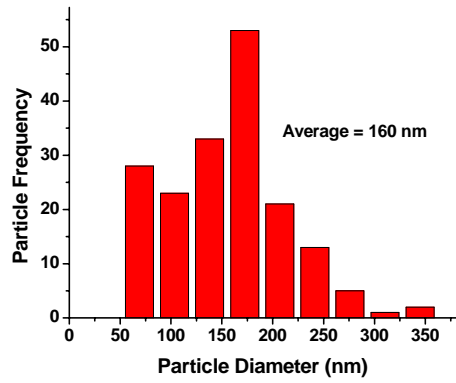
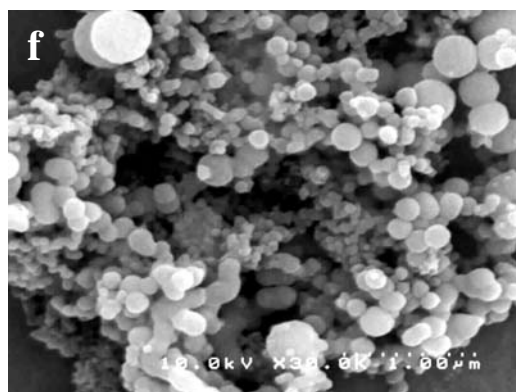
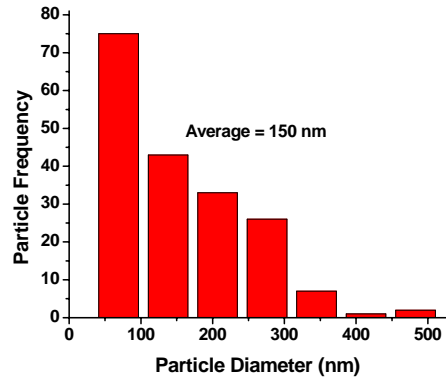
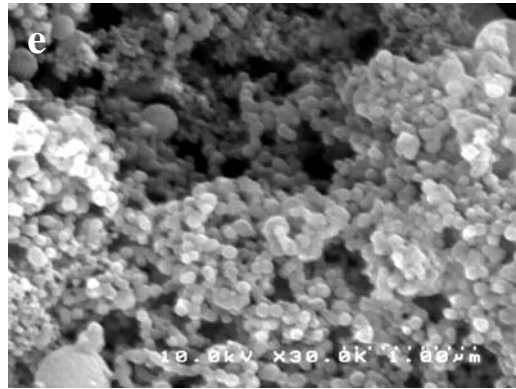


Figure 71. Continued.

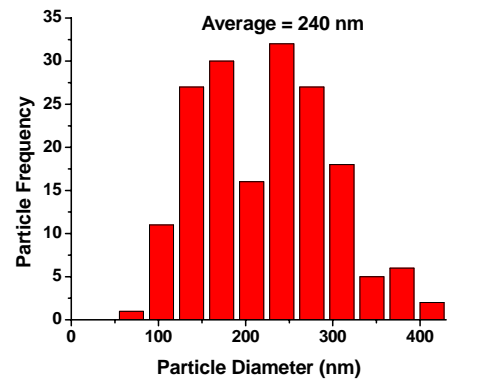
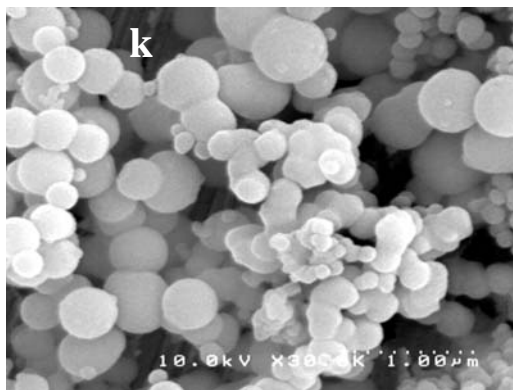
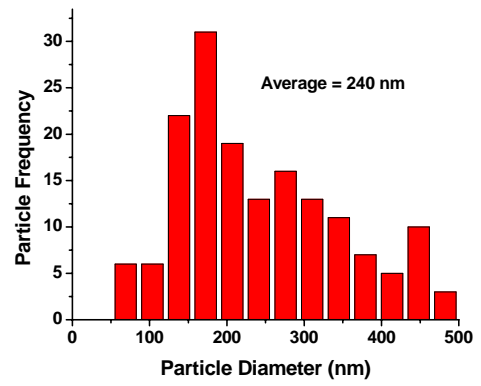
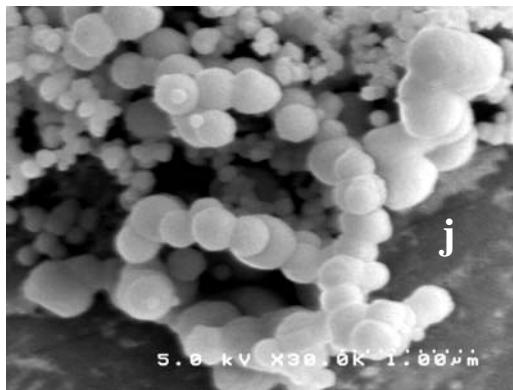
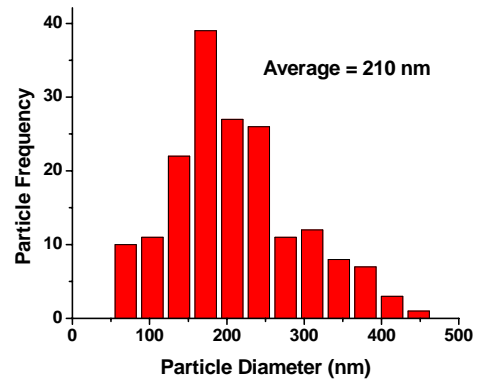
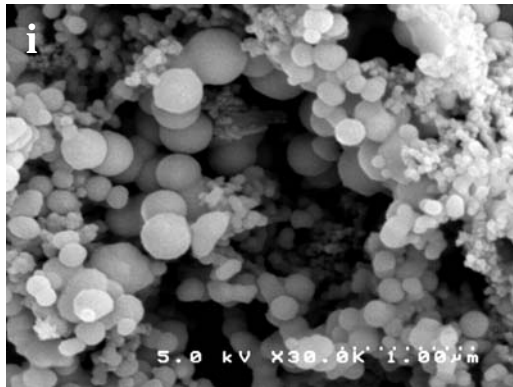


Figure 71. Continued.

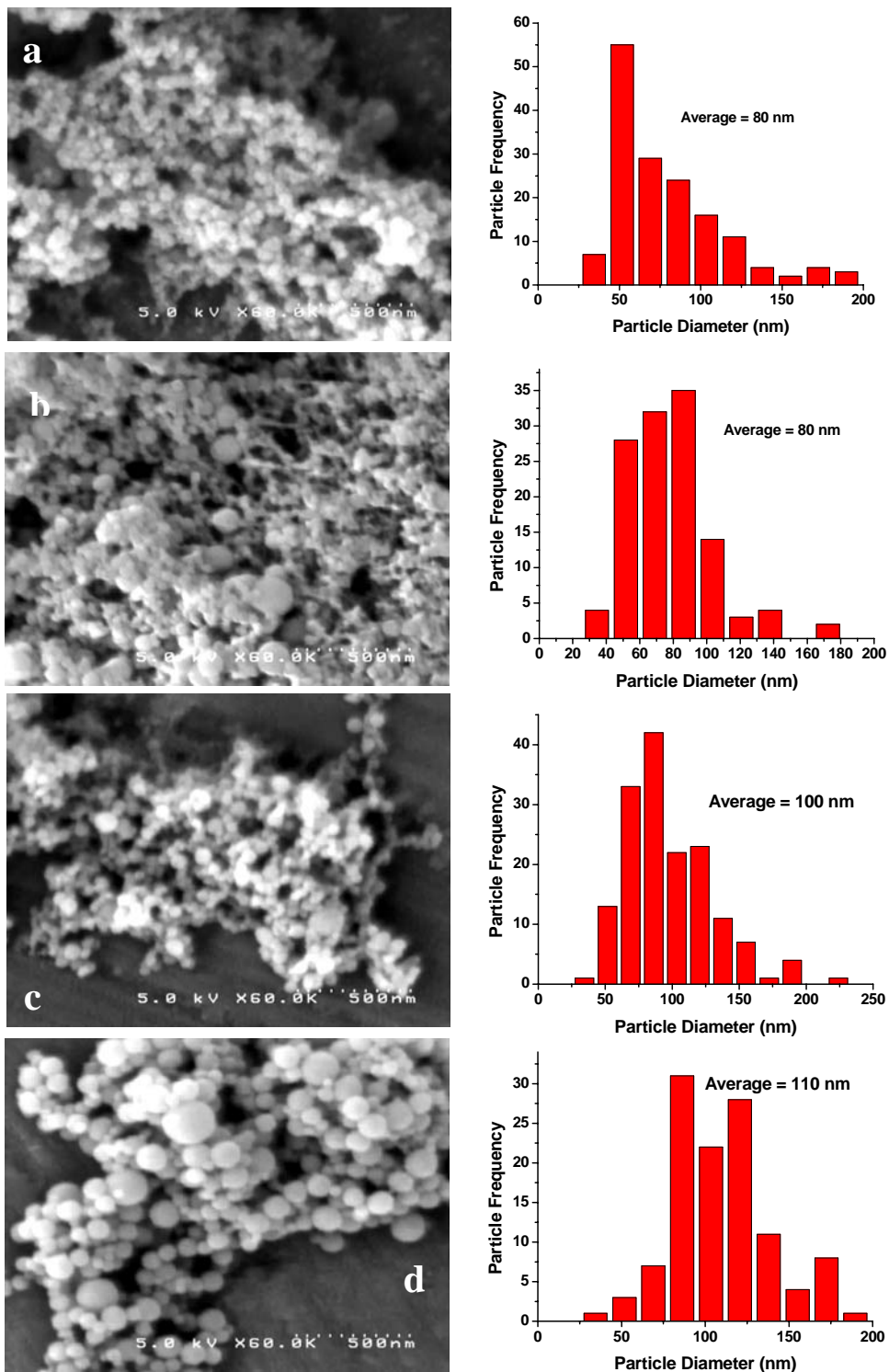


Figure 72. SEM micrographs and histograms of silica nanoparticles produced from the G4 PAMAM template in a NaCl solution with concentrations of a) 0.5 mM, b) 5 mM, c) 10 mM, d) 20 mM, e) 40 mM, f) 60 mM, g) 80 mM, h) 100 mM, i) 200 mM, j) 300 mM and k) 400 mM.

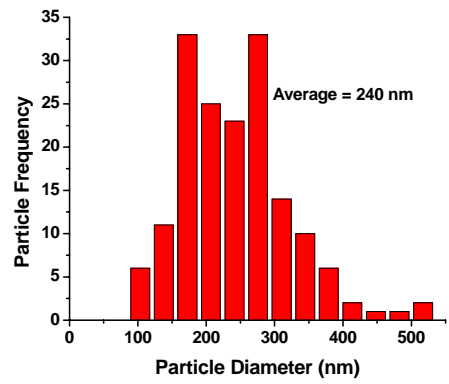
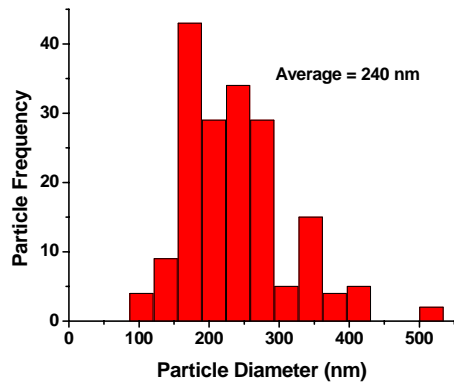
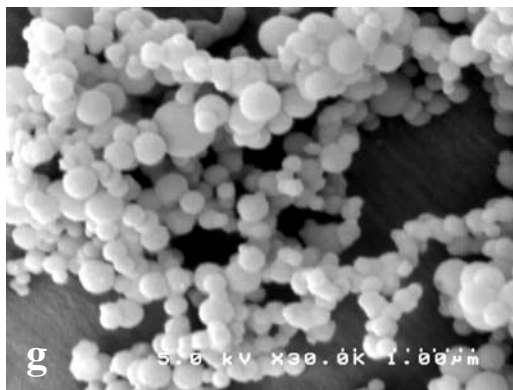
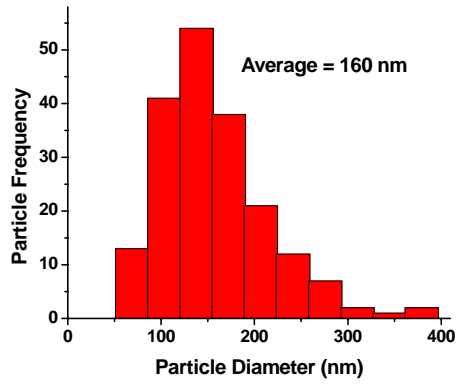
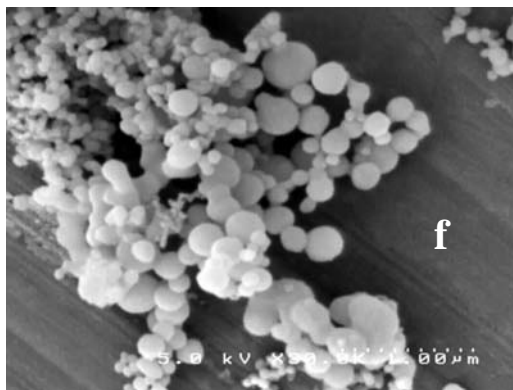
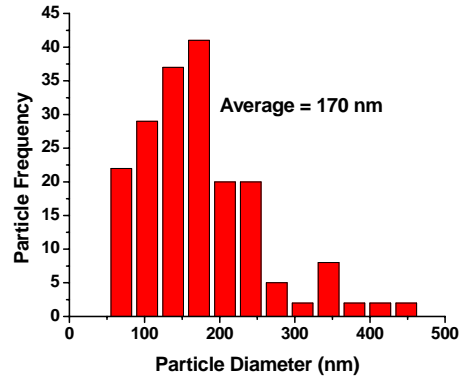
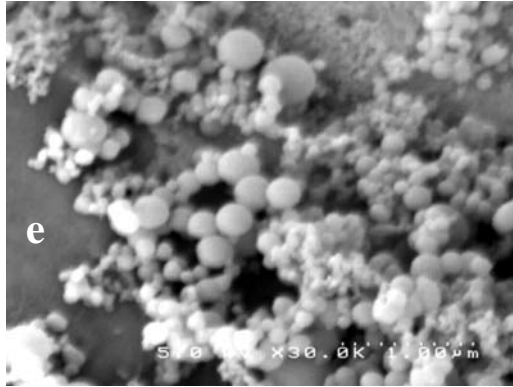


Figure 72. Continued.

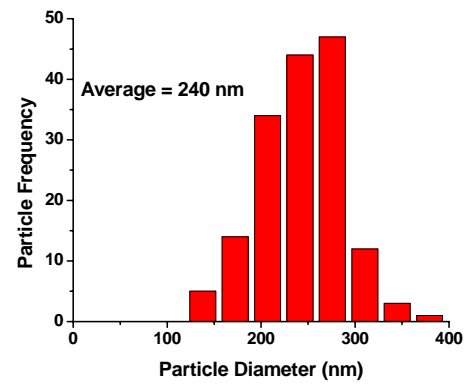
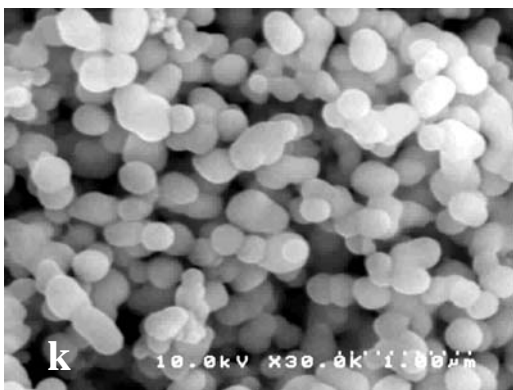
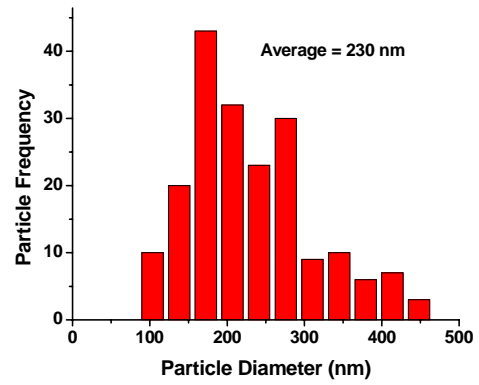
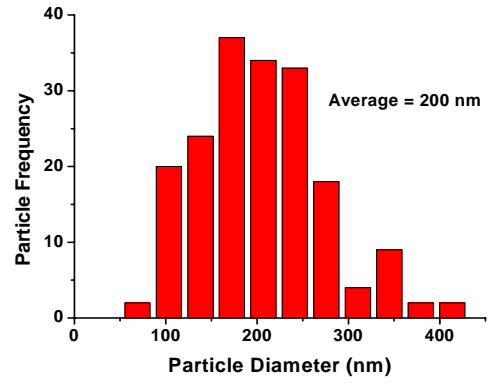
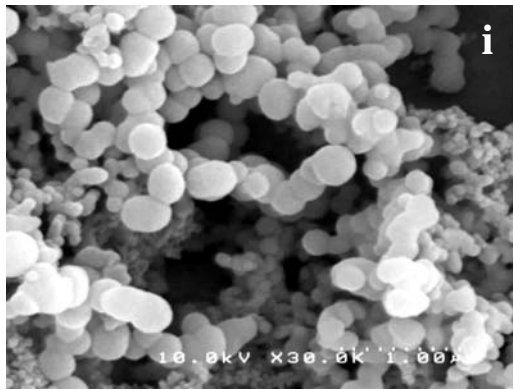


Figure 72. Continued.

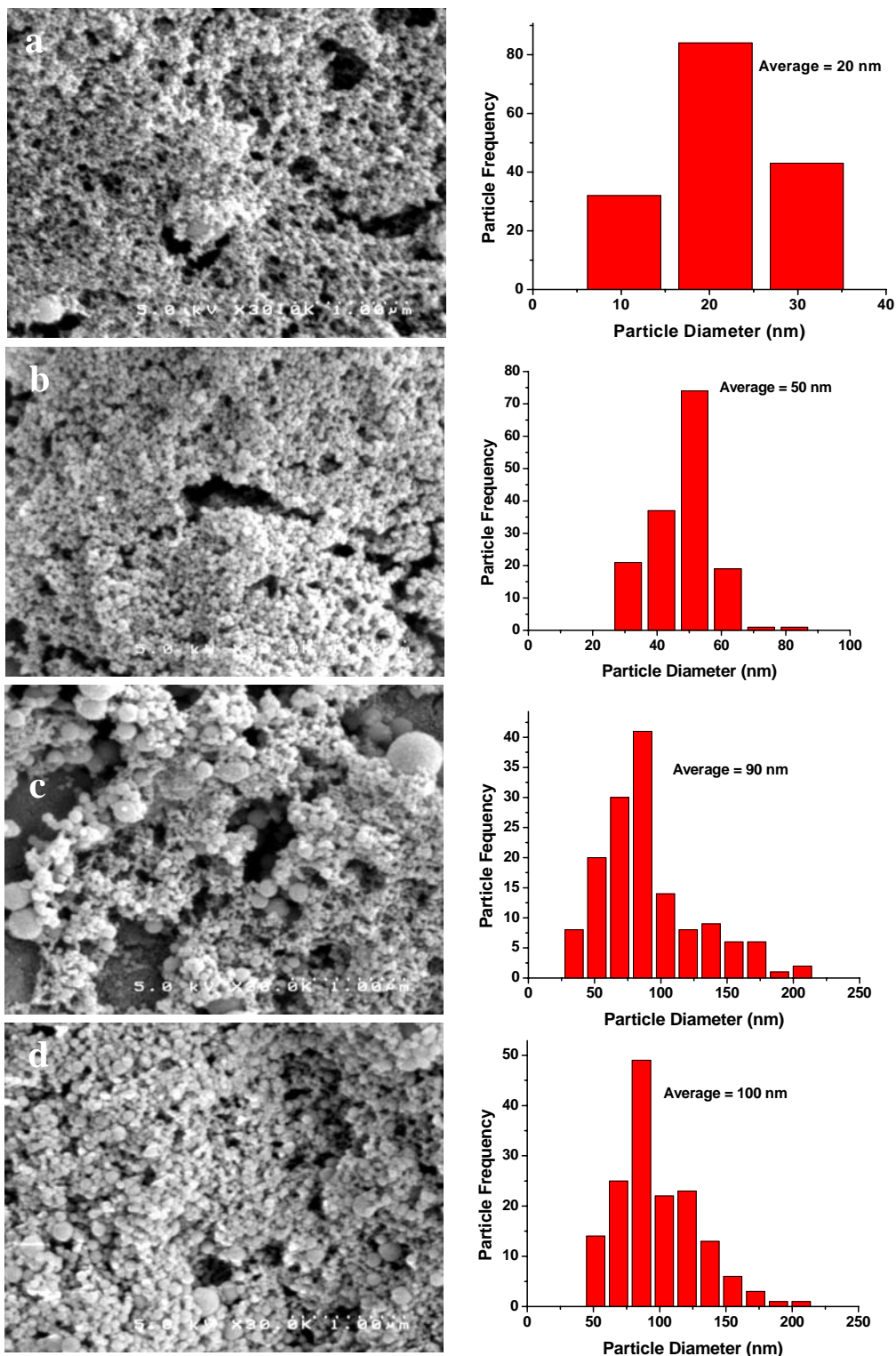


Figure 73: SEM micrographs and histograms of silica nanoparticles produced from the G4 PAMAM template in a KCl solution with concentrations of a) 0.5 mM, b) 5 mM, c) 10 mM, d) 20 mM, e) 40 mM, f) 60 mM, g) 80 mM, h) 100 mM, i) 200 mM, j) 300 mM and k) 400 mM.

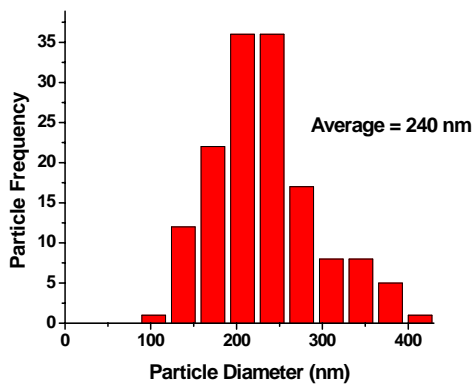
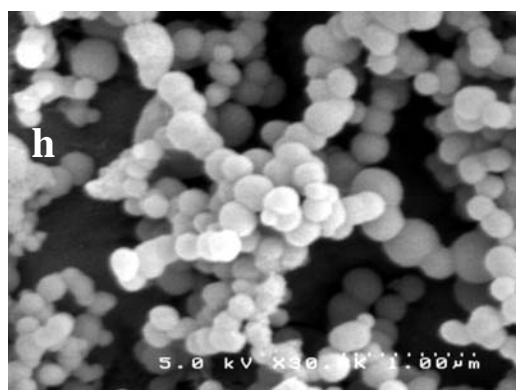
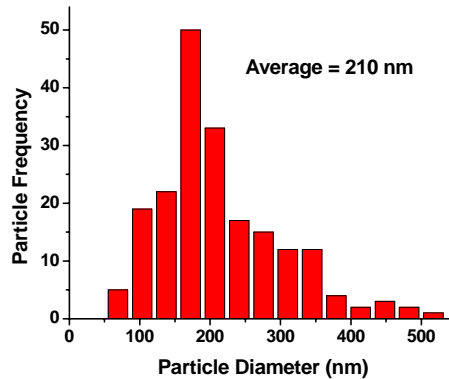
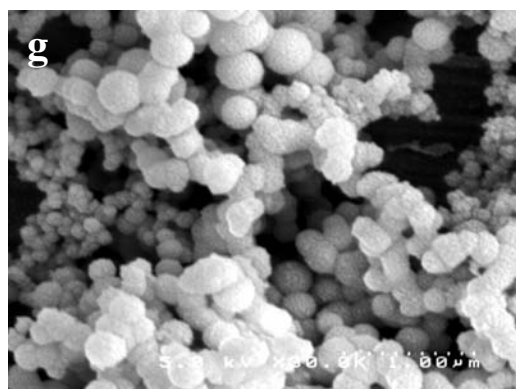
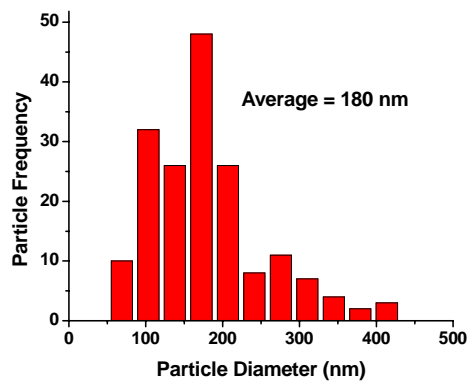
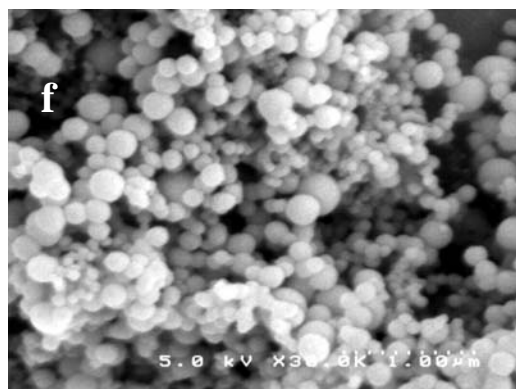
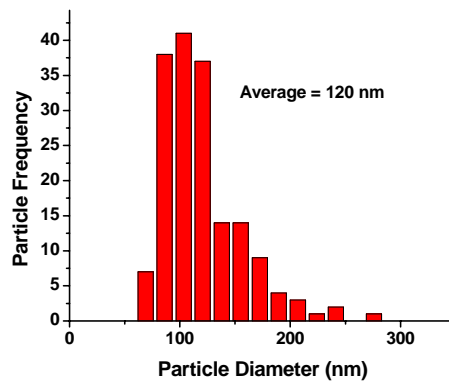
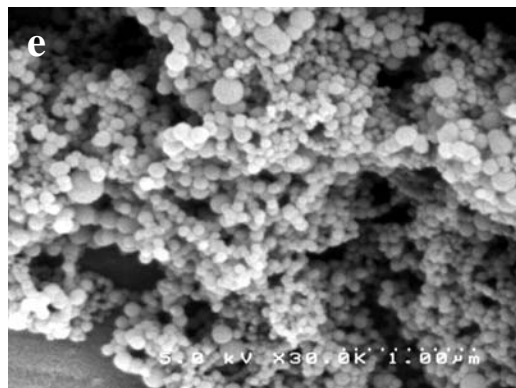


Figure 73. Continued.

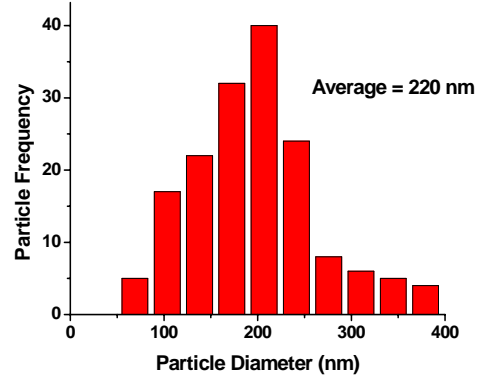
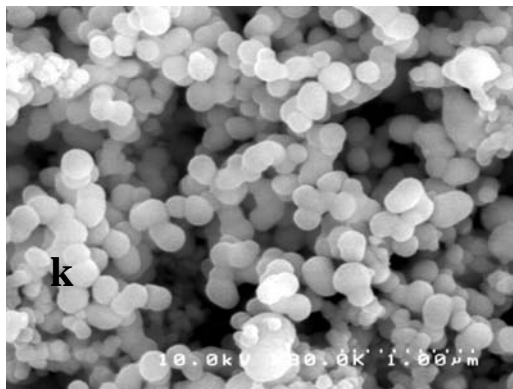
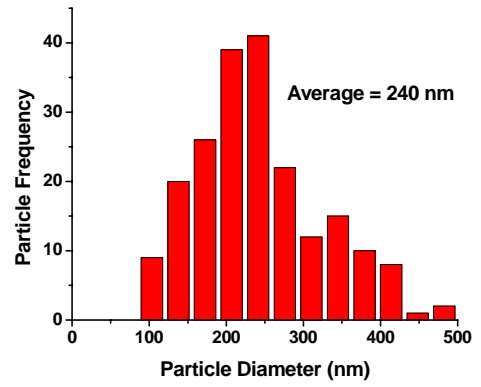
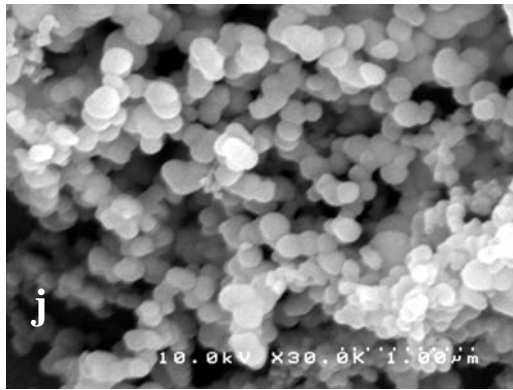
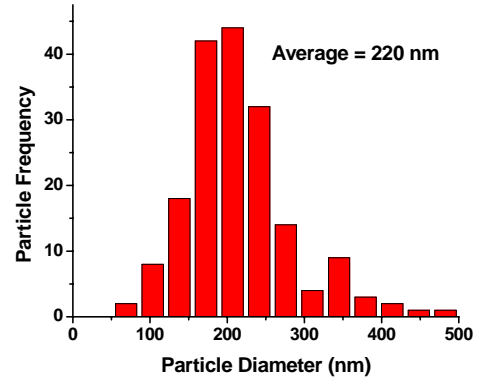
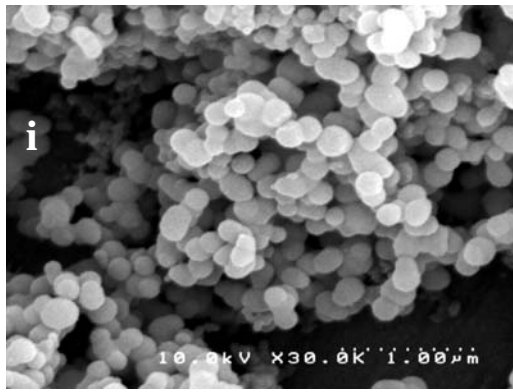


Figure 73. Continued

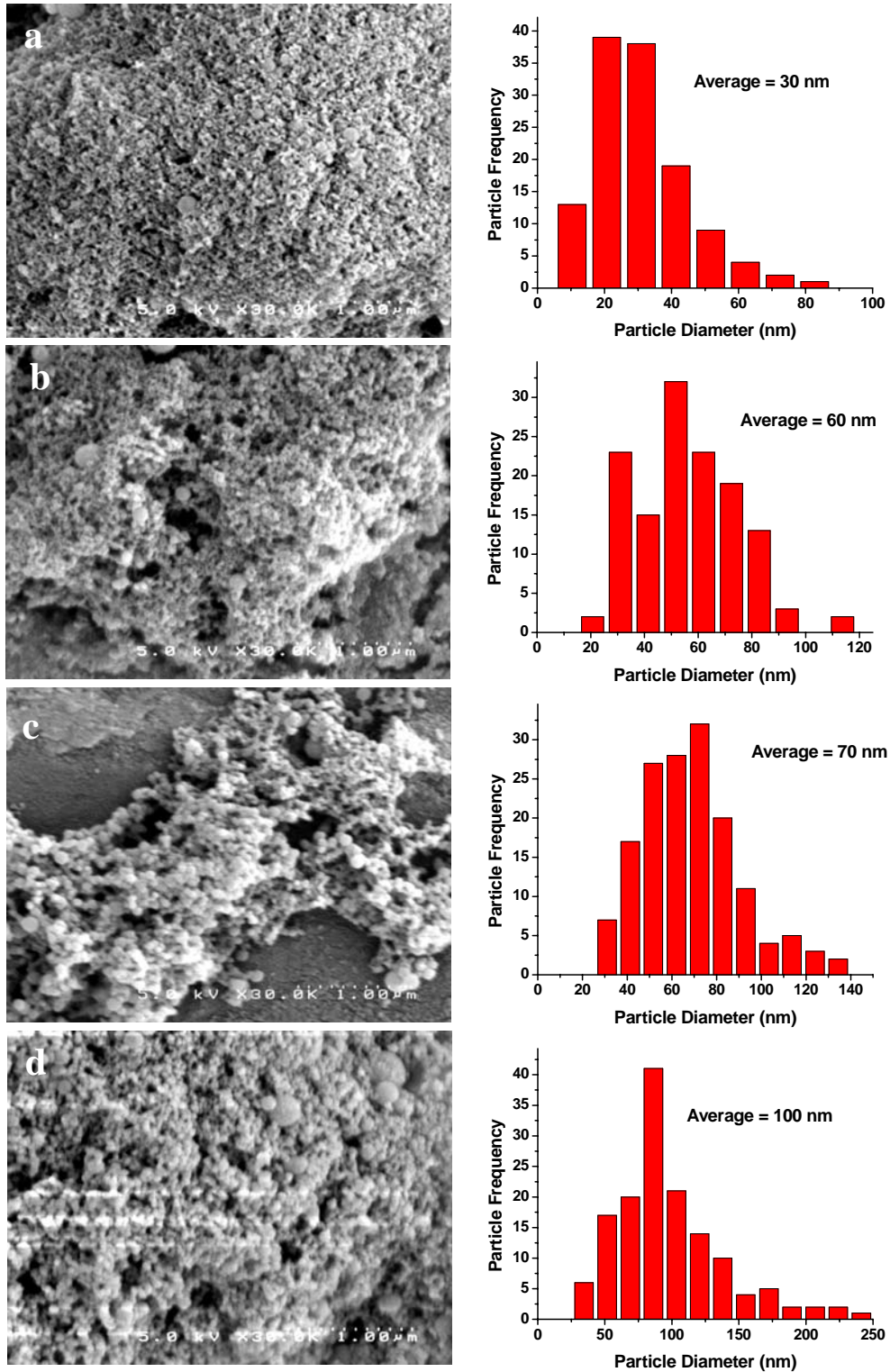


Figure 74: SEM micrograph and histogram of silica nanoparticles produced from the G4 PAMAM template in a RbCl solution with concentrations of a) 0.5 mM, b) 5 mM, c) 10 mM, d) 20 mM, e) 40 mM, f) 60 mM, g) 80 mM, h) 100 mM, i) 200 mM, j) 300 mM and k) 400 mM.

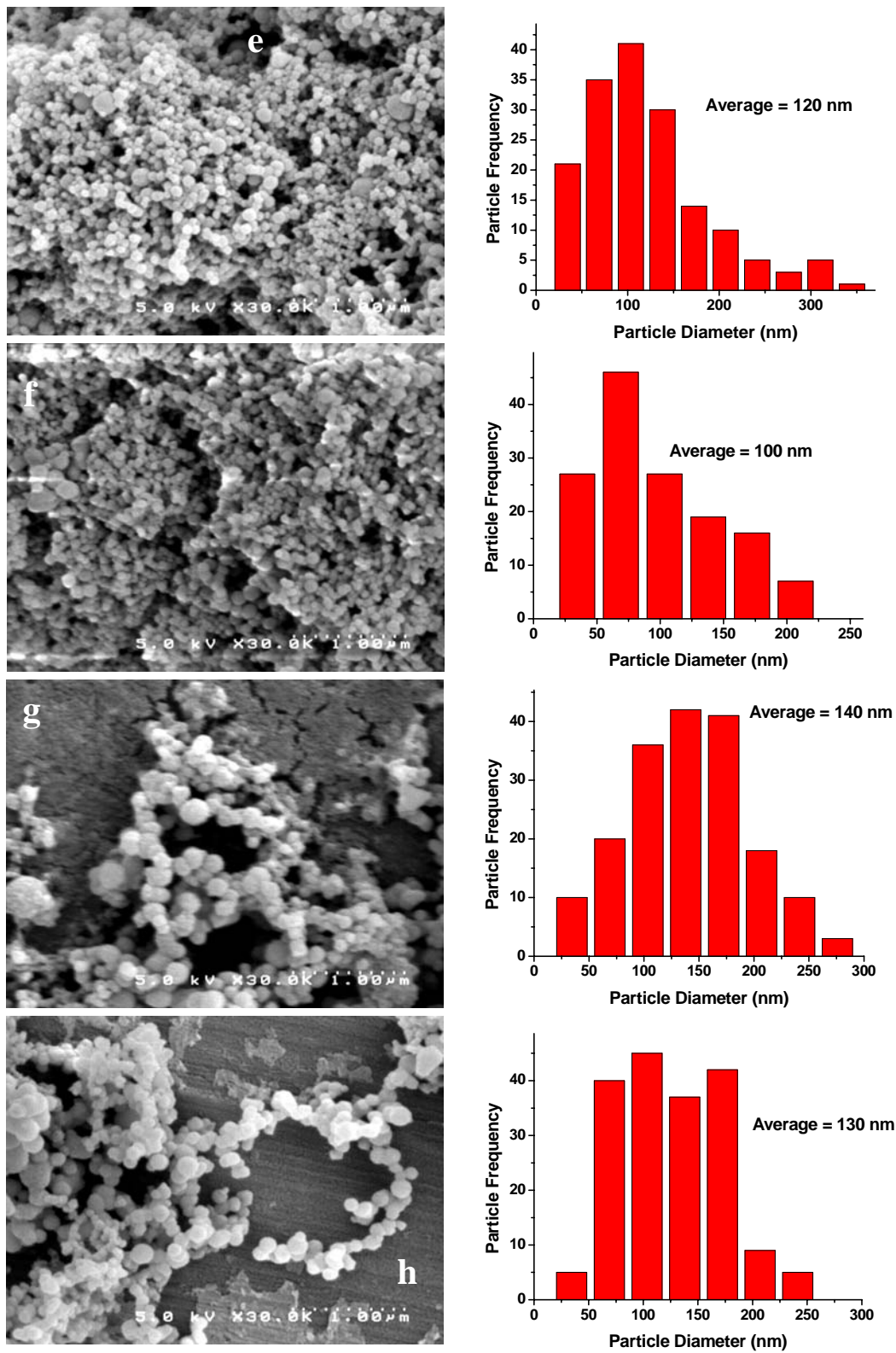


Figure 74. Continued.

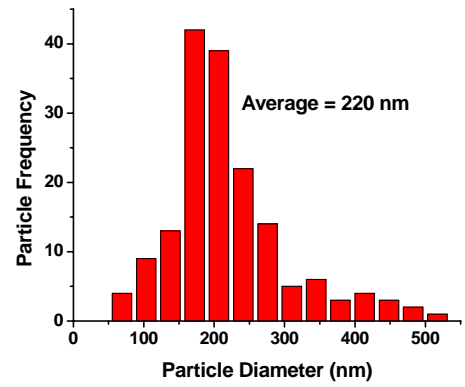
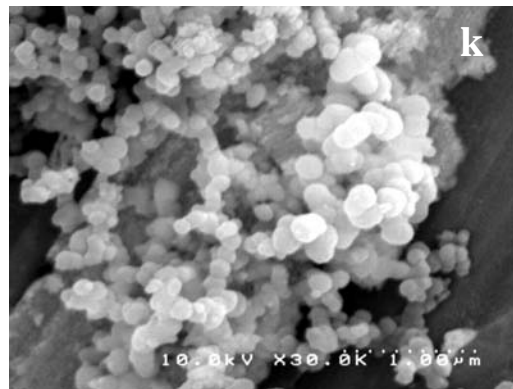
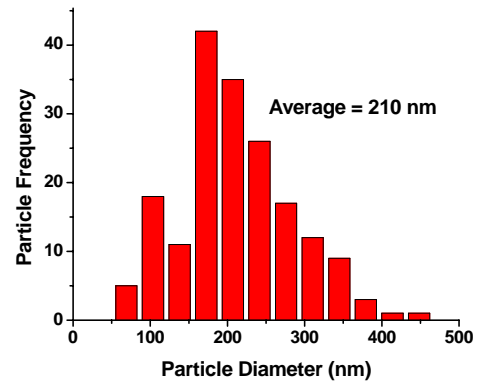
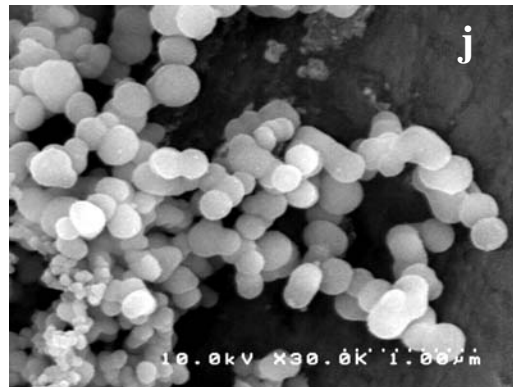
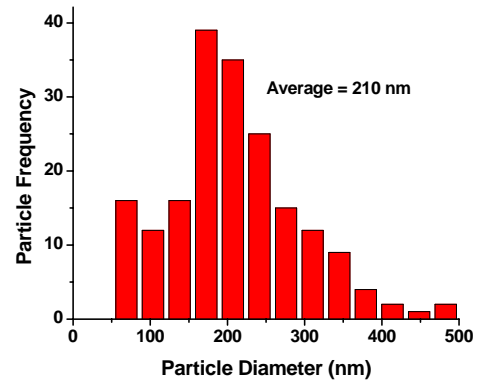
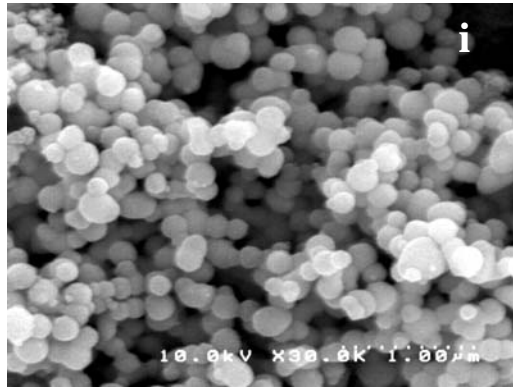


Figure 74. Continued.

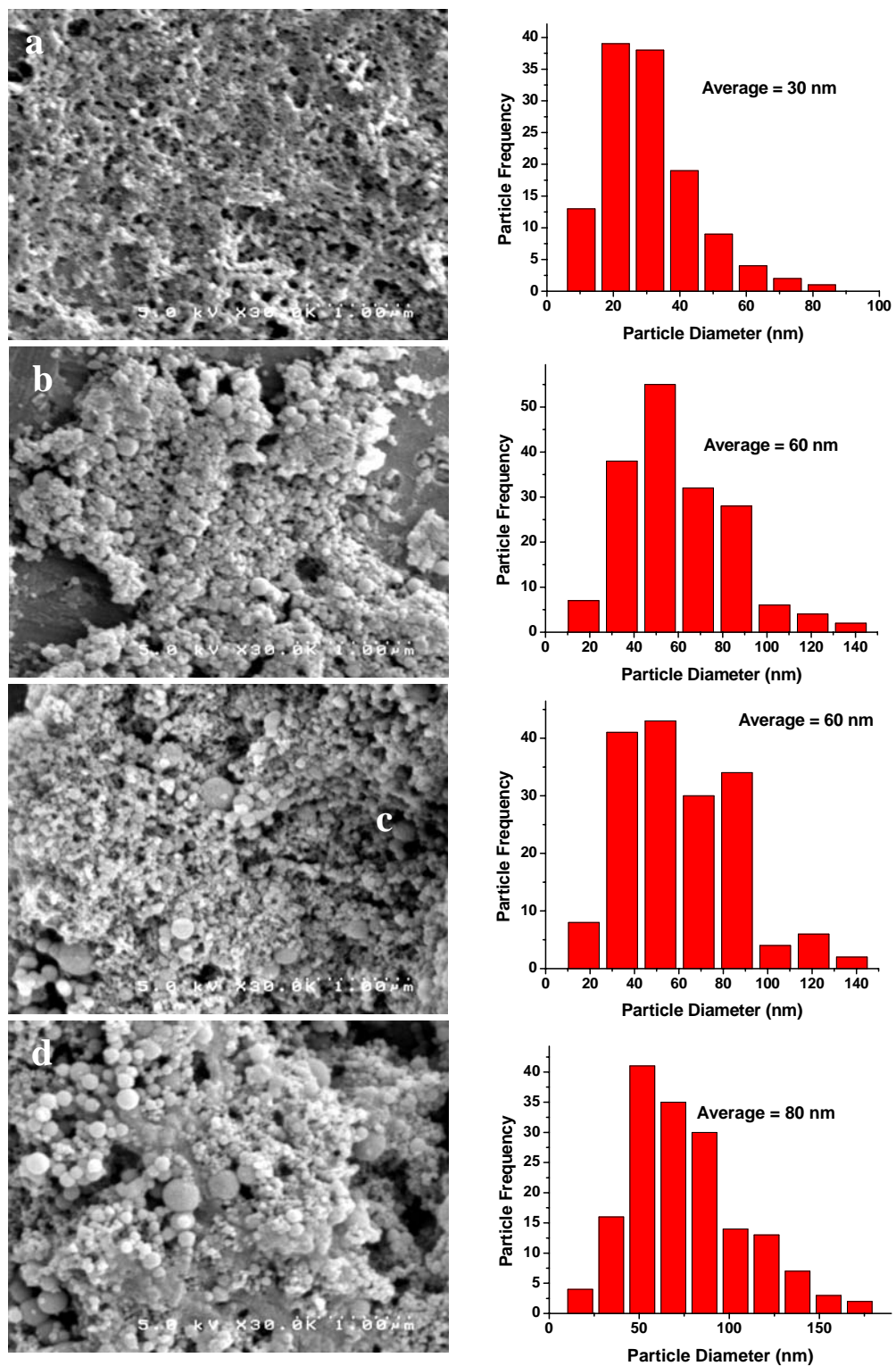


Figure 75: SEM micrographs and histograms of silica nanoparticles produced from the G4 PAMAM template in a CsCl solution with concentrations of a) 0.5 mM, b) 5 mM, c) 10 mM, d) 20 mM, e) 40 mM, f) 60 mM, g) 80 mM, h) 100 mM, i) 200 mM, j) 300 mM and k) 400 mM.

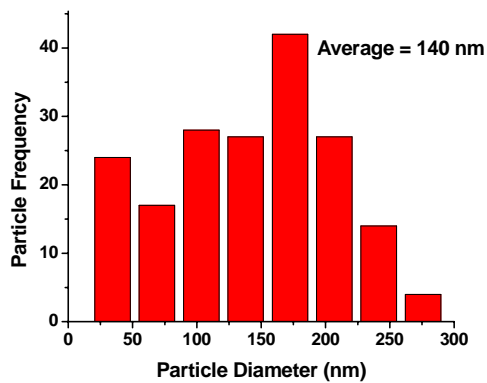
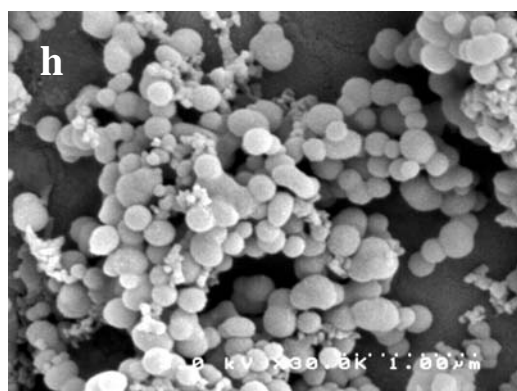
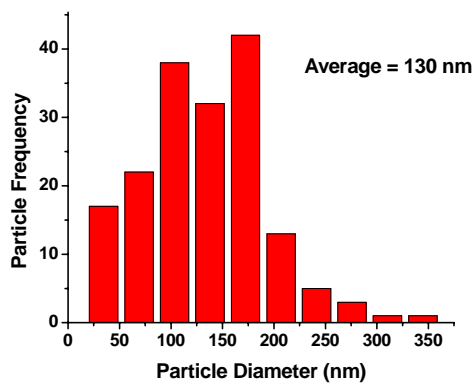
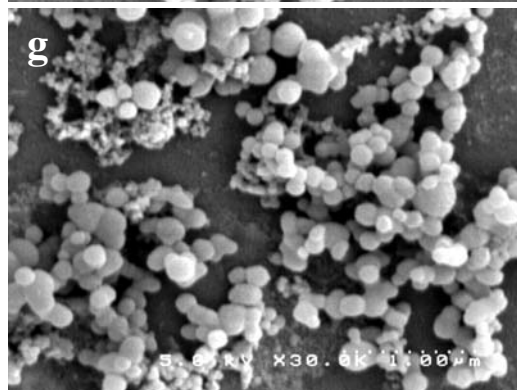
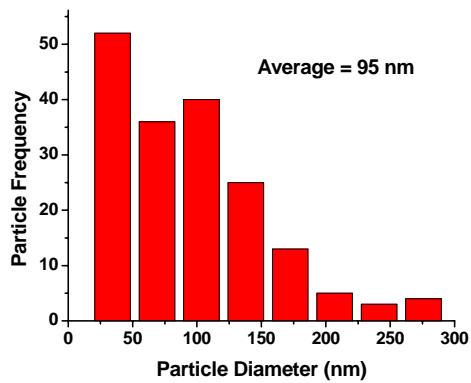
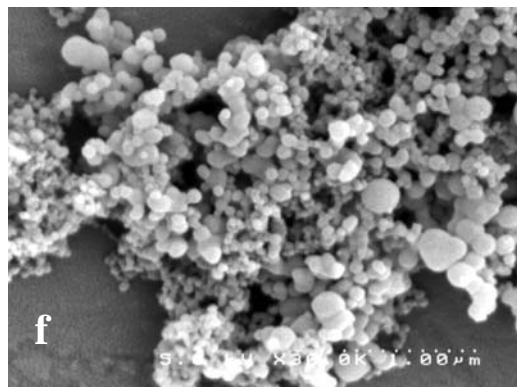
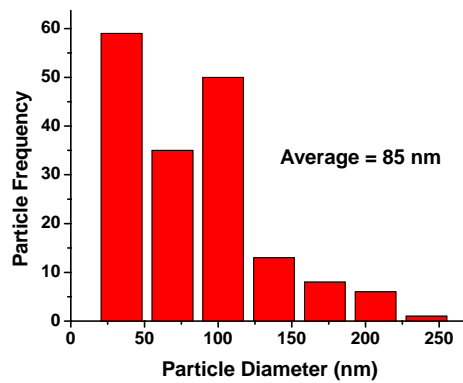
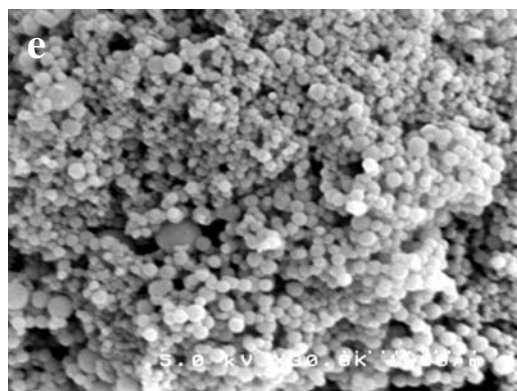


Figure 75. Continued.

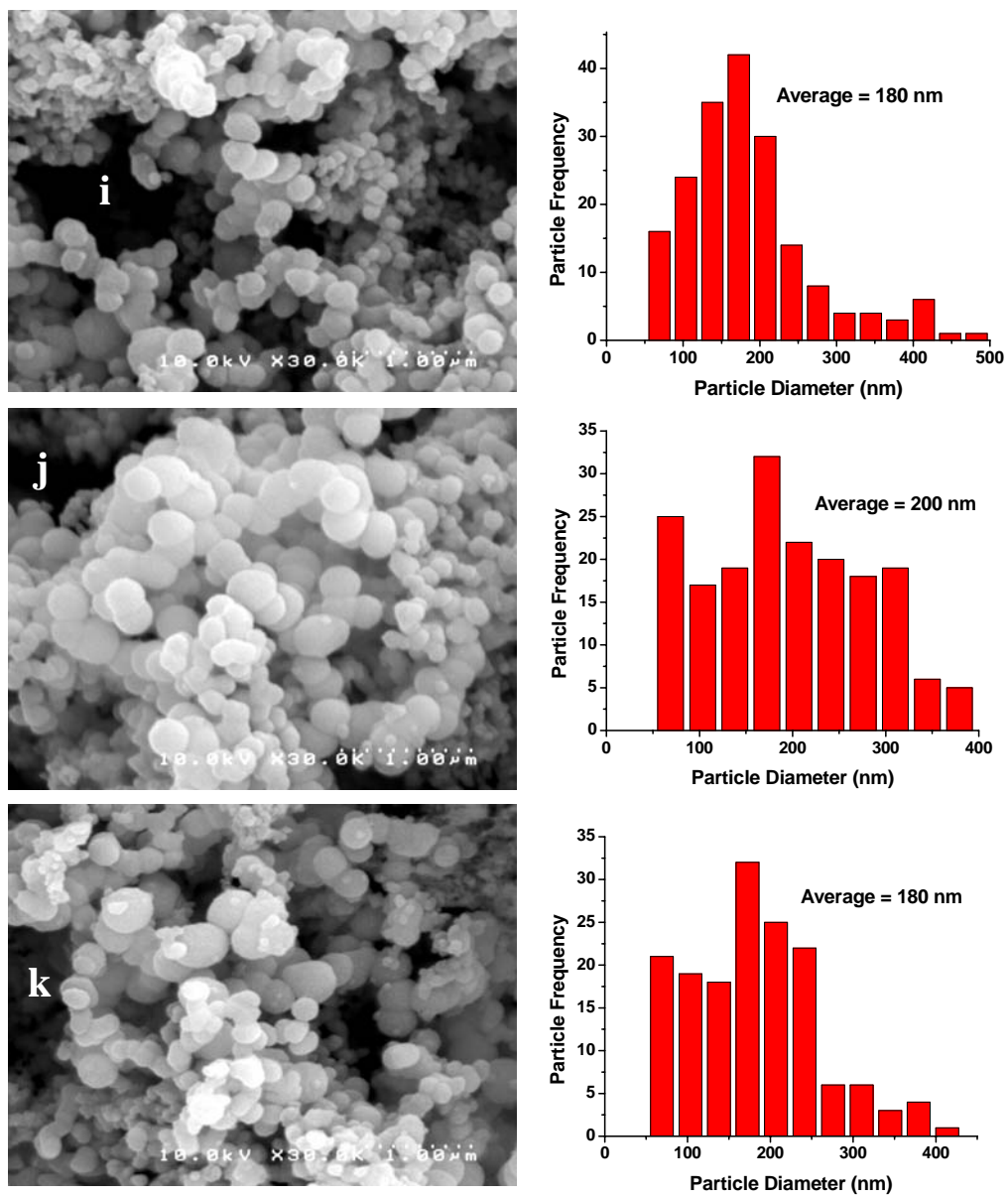


Figure 75. Continued.

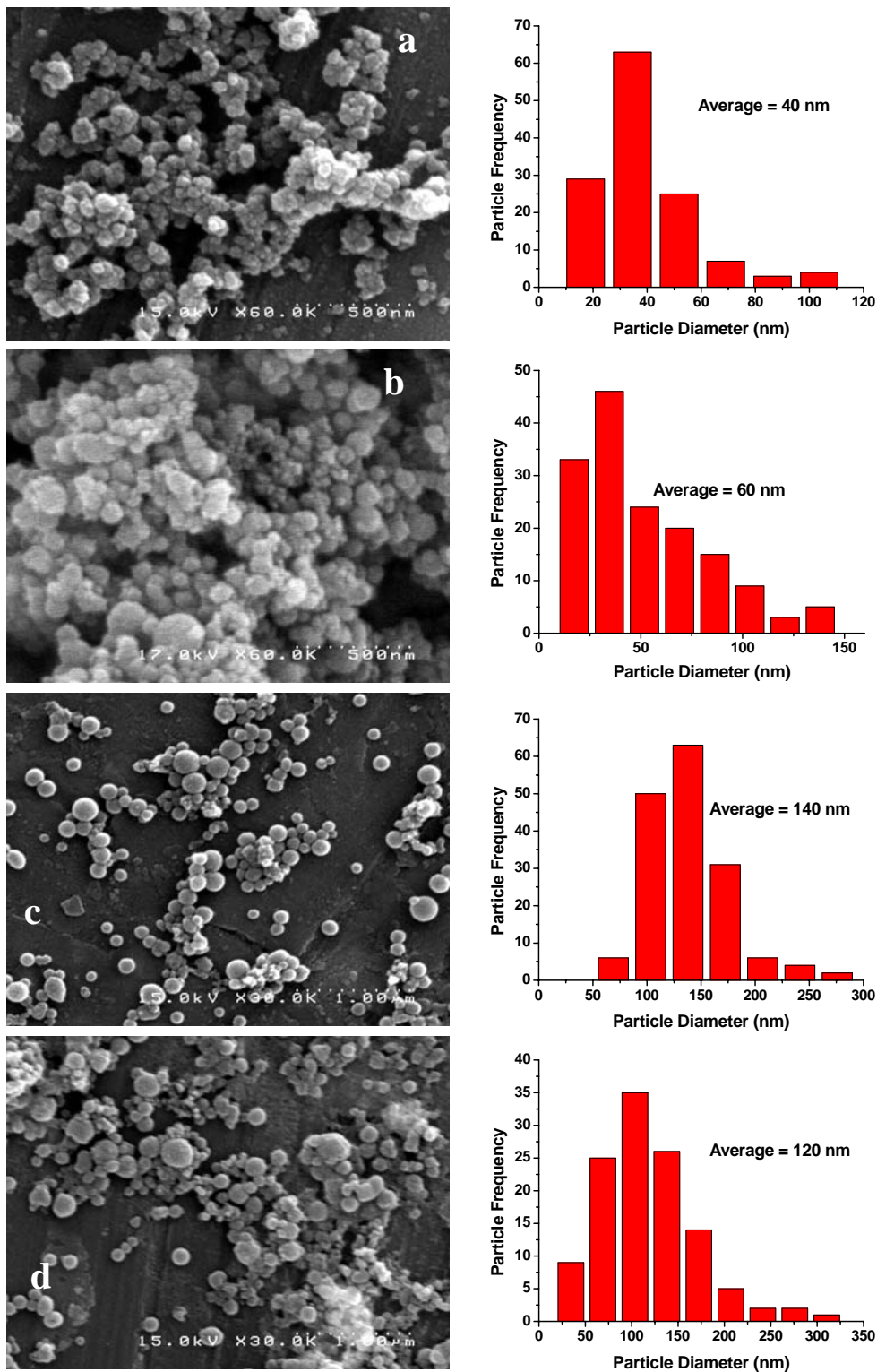


Figure 76: SEM micrographs and histograms of silica nanoparticles produced from the G4 PAMAM template in a $MgCl_2$ solution with concentrations of a) 0.5 mM, b) 5 mM, c) 10 mM, d) 20 mM, e) 40 mM, f) 60 mM, g) 80 mM, h) 100 mM

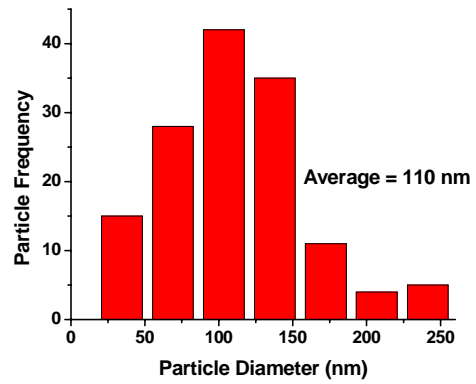
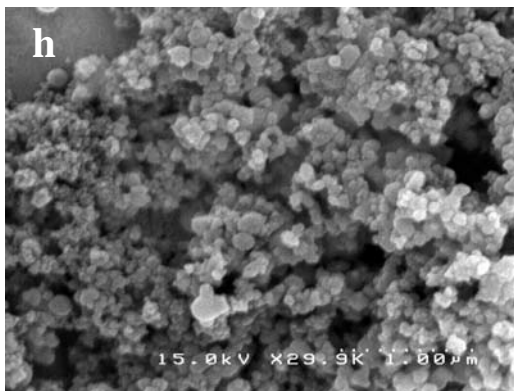
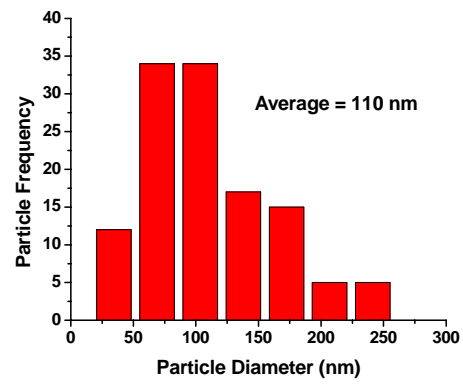
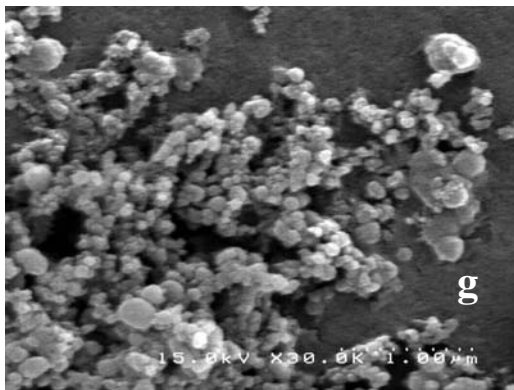
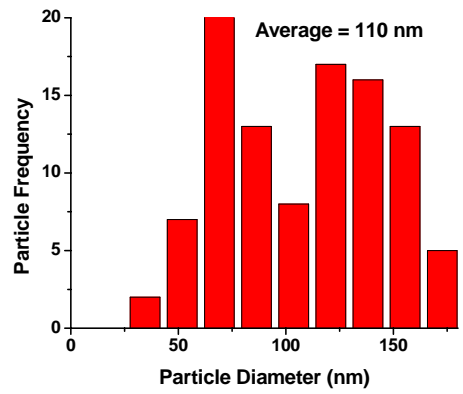
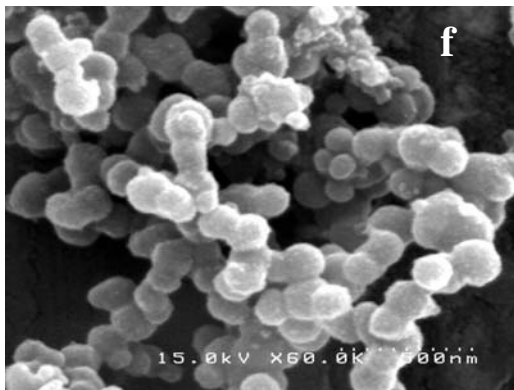
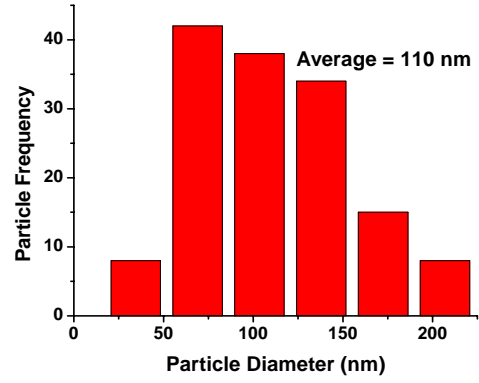
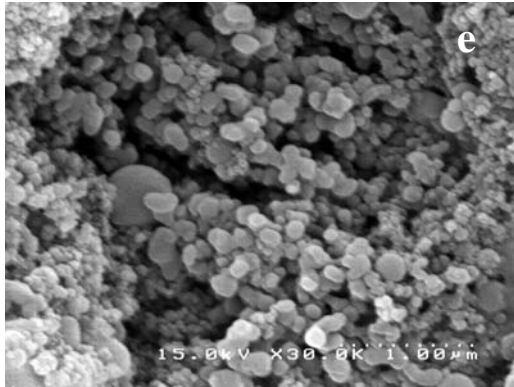


Figure 76. Continued.

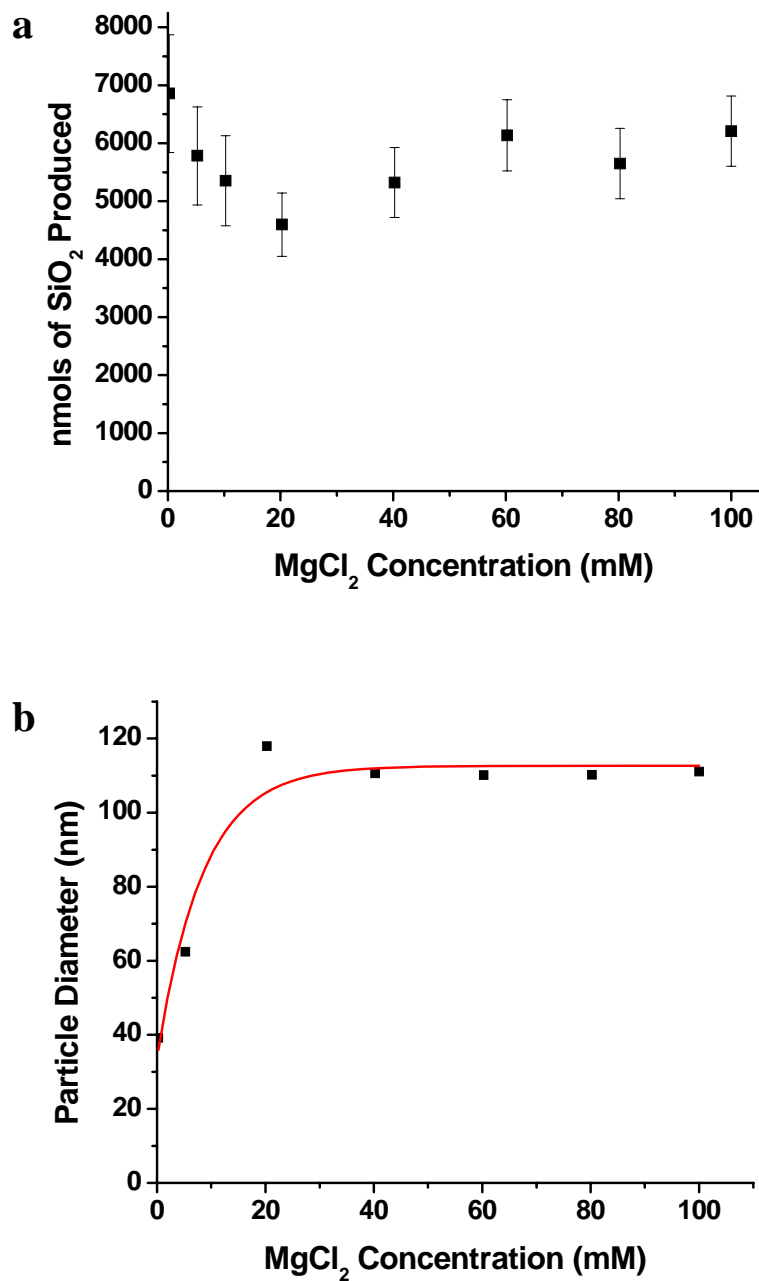


Figure 77: MgCl₂ concentration effects on a) silica production activity of 20 mM primary amine concentration of G4 PAMAM dendrimers and b) particle size distribution.

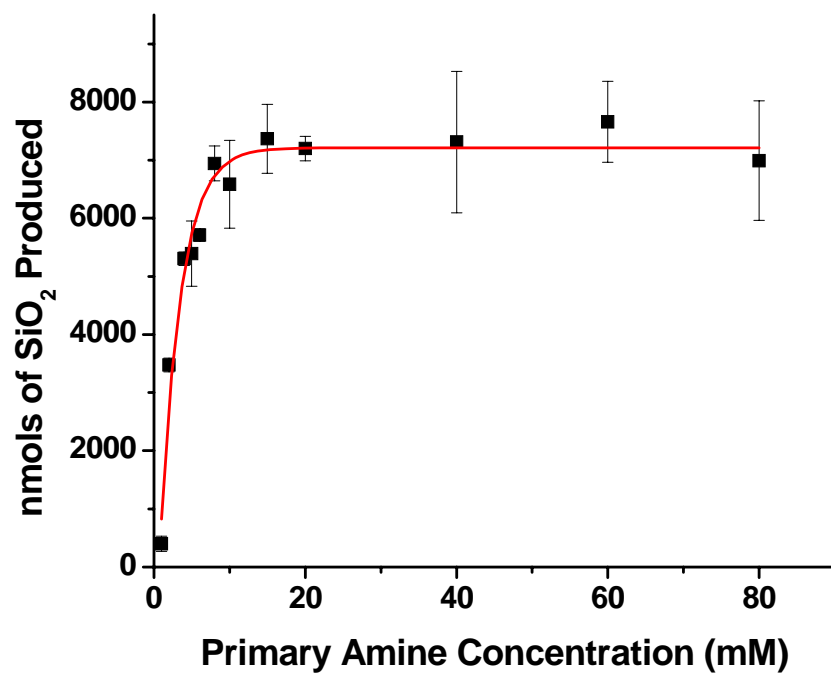


Figure 78: Silica production as a function of the primary amine concentration of the G4 PAMAM template in a 100 mM NaCl solution at pH 7.5.

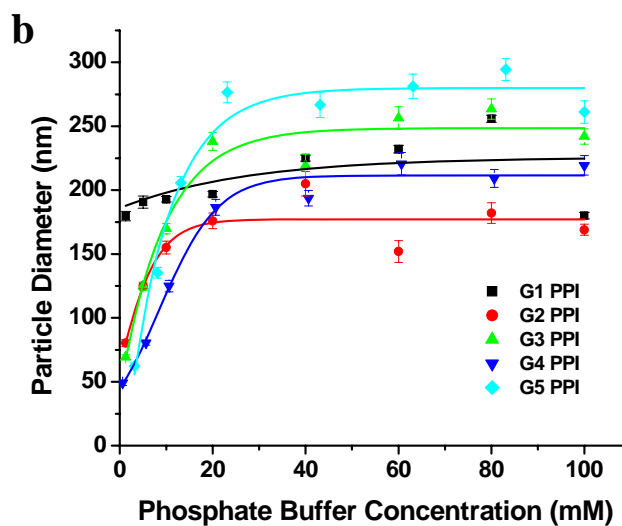
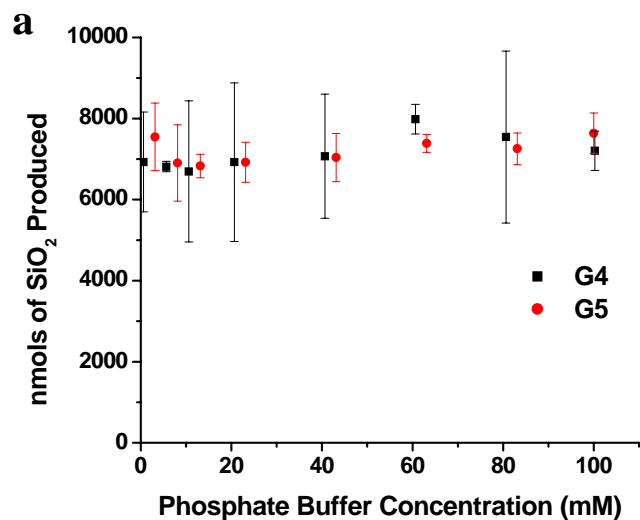


Figure 79: Effects of phosphate buffer concentration on the silica formation activity of PPI dendrimers a) silica production activity and b) size distributions for nanospheres produced from PPI dendrimers. Error bars represent the standard error associated with the sample size analyzed for the particle size distributions.

APPENDIX C

Characterization of Dendrimer Precipitated Titanium Dioxide and Germanium Dioxide Nanoparticles

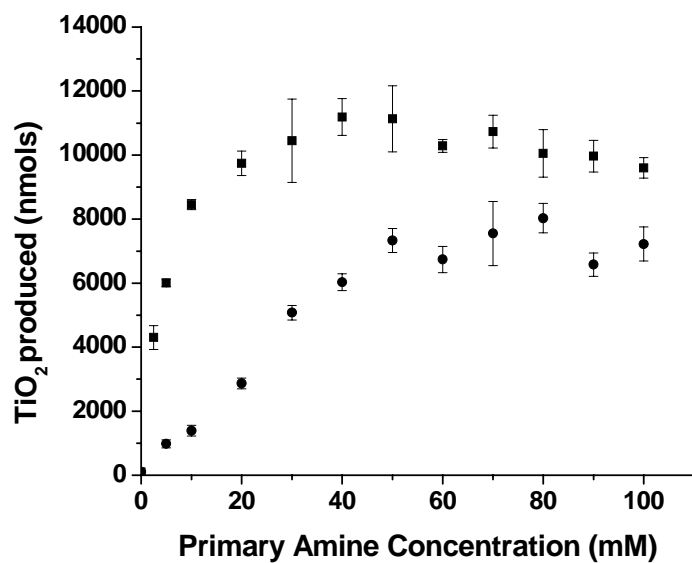


Figure 80: Titanium dioxide production as a function of G0 PAMAM primary amine concentration (● phosphate buffer (100 mM, pH 7.5), ■ water)

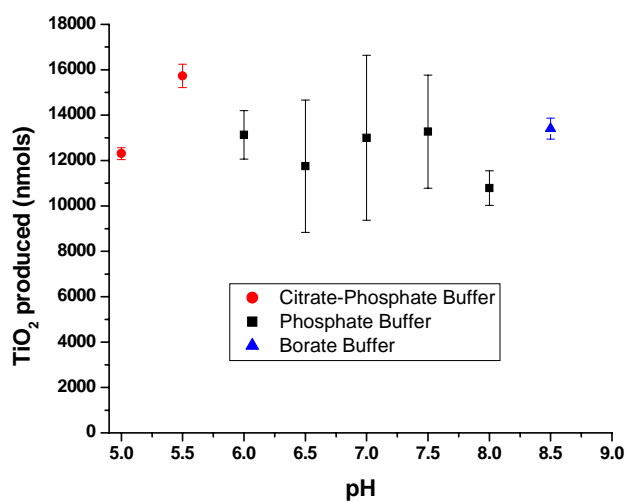


Figure 81: Titanium dioxide production as a function of pH (all buffer concentrations were 100 mM)

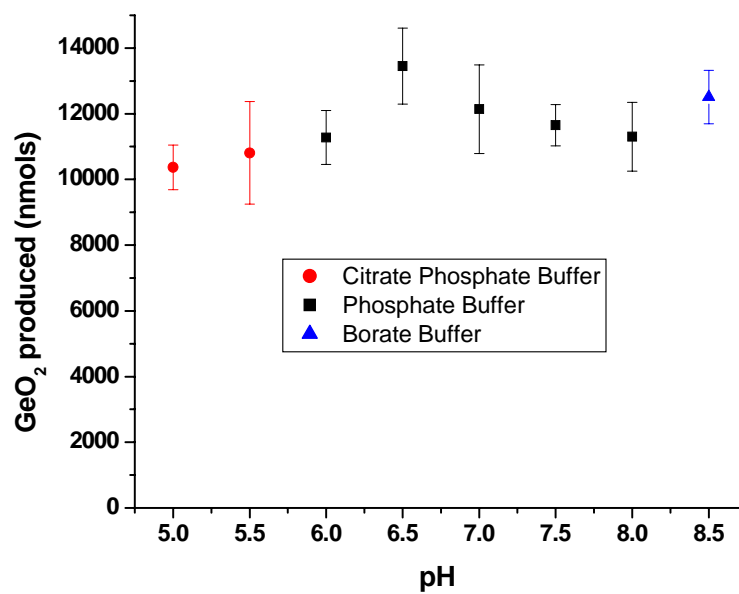


Figure 82: Germanium dioxide production as a function of pH (all buffer concentrations were 100 mM).

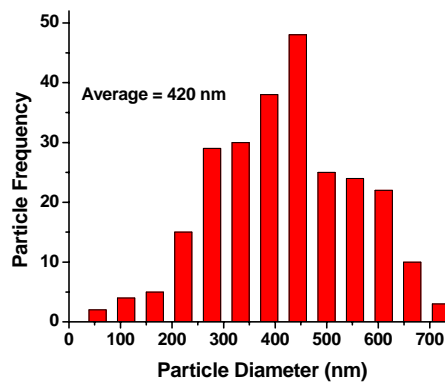
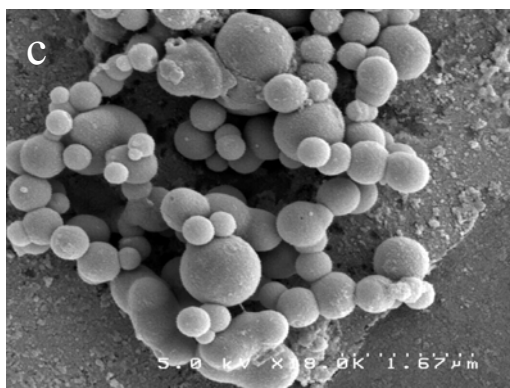
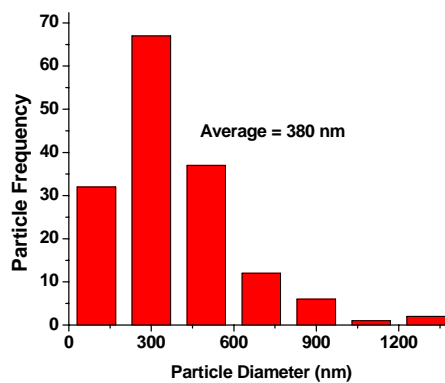
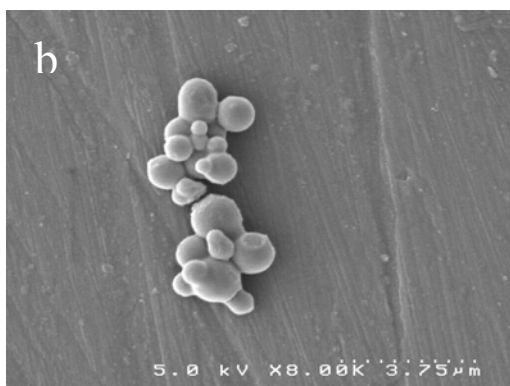
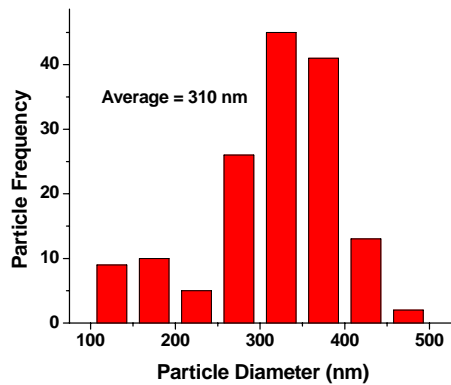
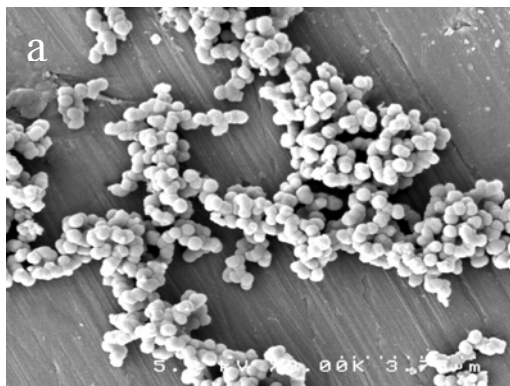


Figure 83: SEM micrographs and histograms of titanium dioxide nanoparticles precipitated in phosphate buffer from: a) G0 PAMAM, b) G-2 PAMAM, c) G-4 PAMAM, d) G-6 PAMAM, e) G4-PPI f) G-5 PPI

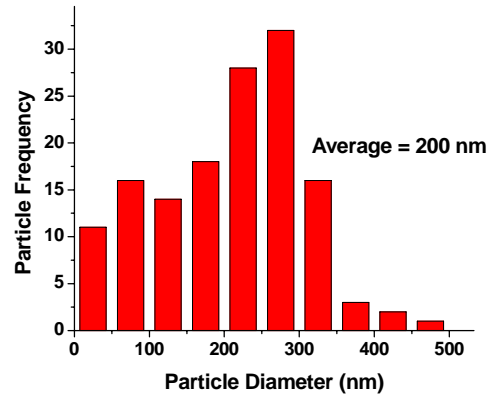
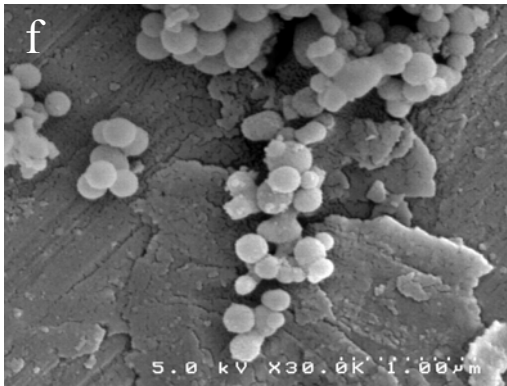
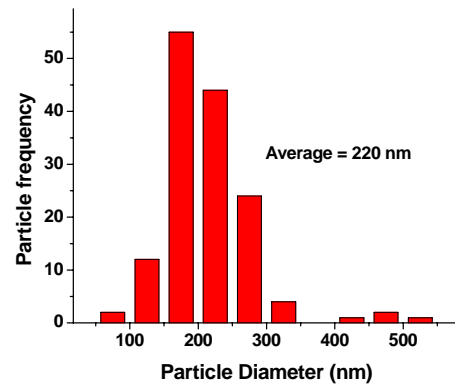
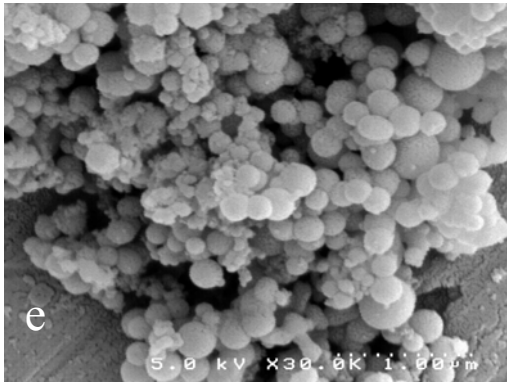
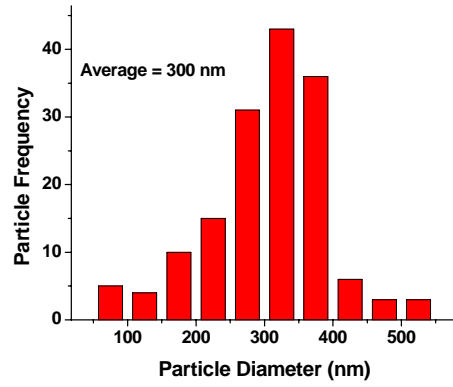
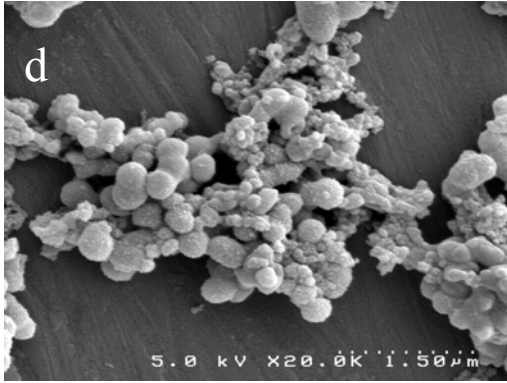


Figure 83. Continued.

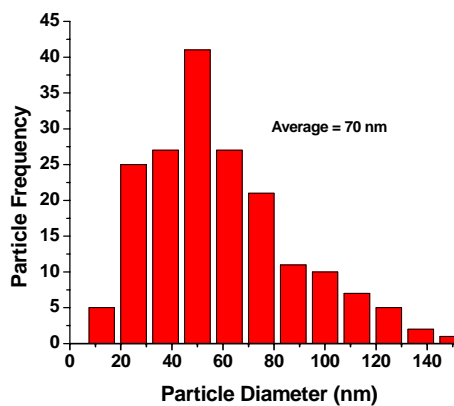
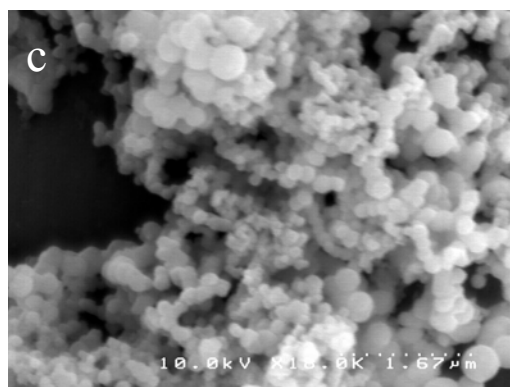
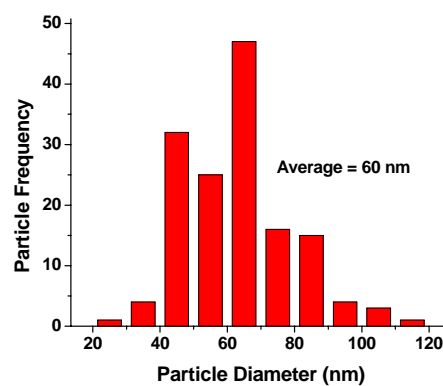
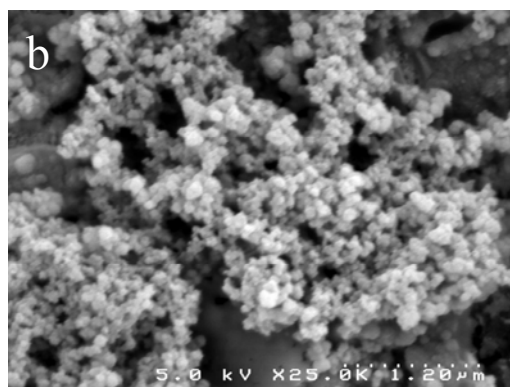
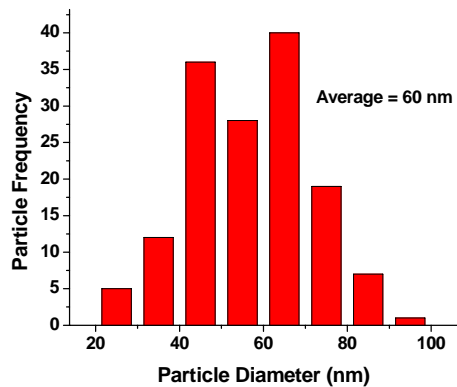
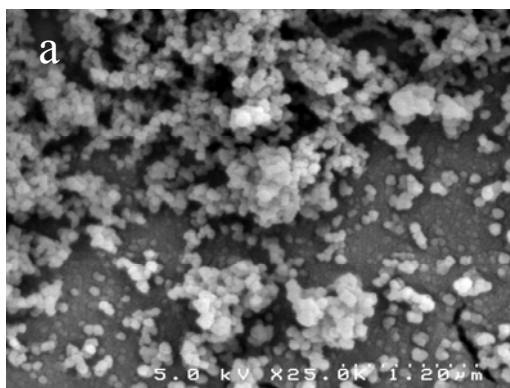


Figure 84: SEM micrographs of titanium dioxide nanoparticles precipitated in water from: a) G-0 PAMAM, b) G-2 PAMAM, c) G-4 PAMAM, d) G-6 PAMAM, e) G4-PPI f) G-5 PPI

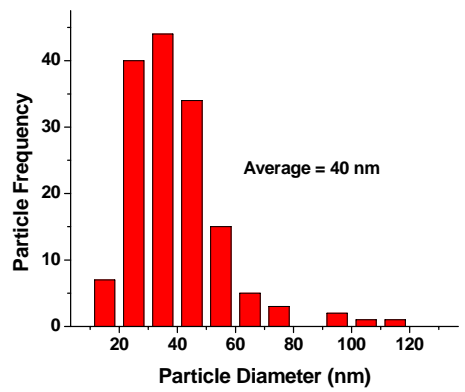
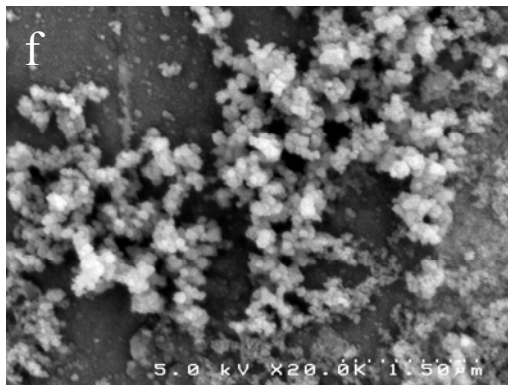
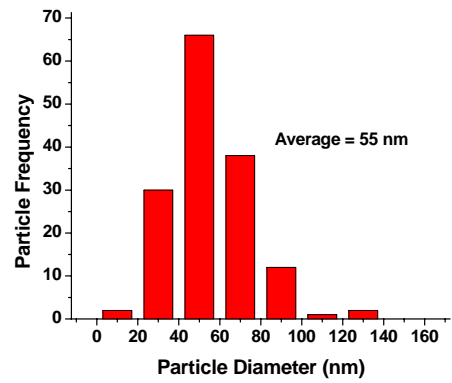
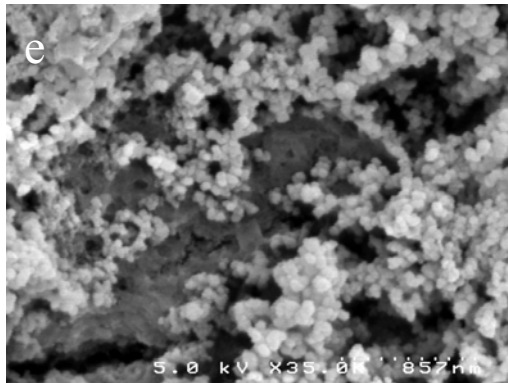
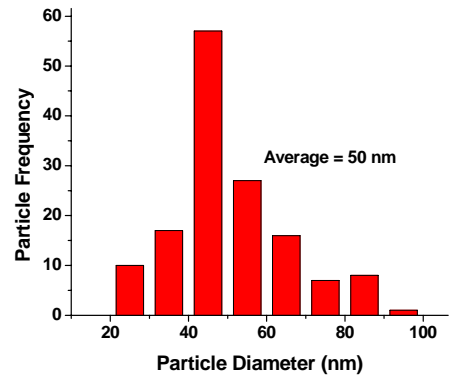
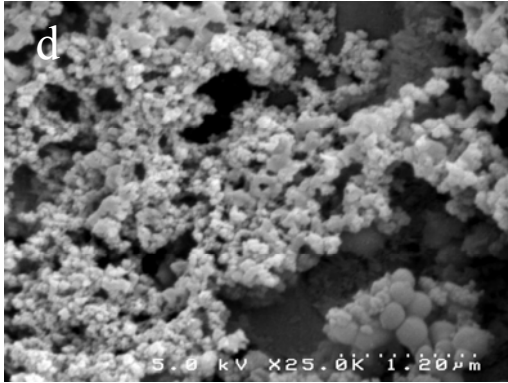


Figure 84. Continued

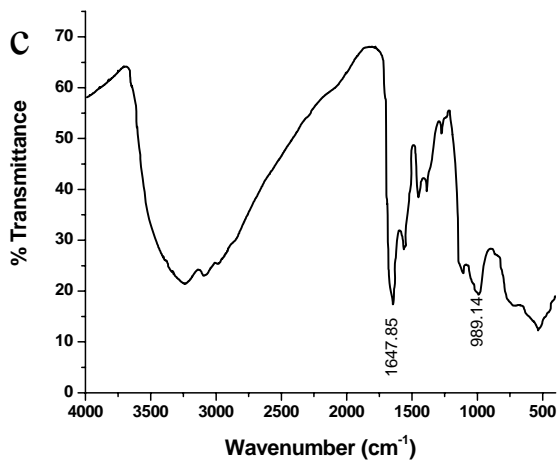
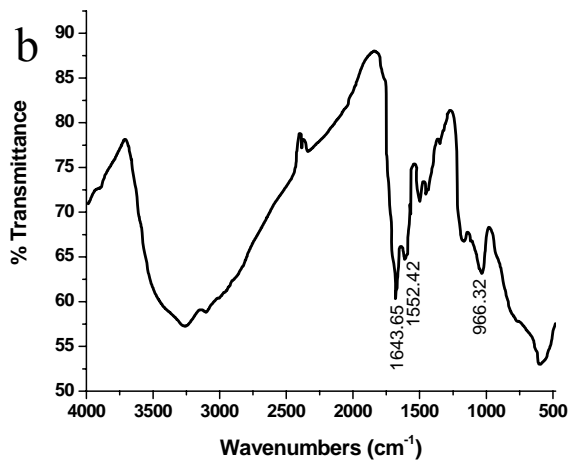
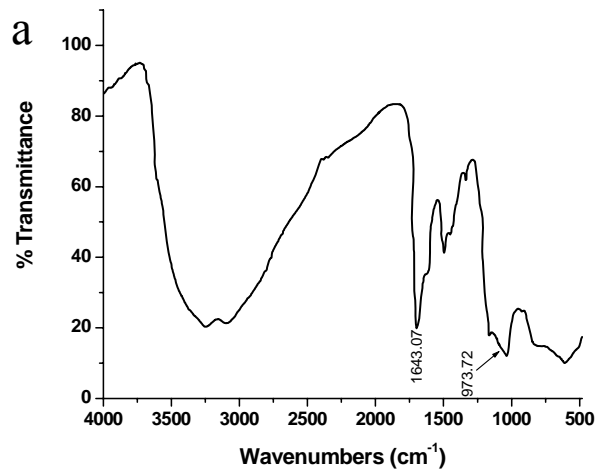


Figure 85: Infra-red spectra of titanium dioxide precipitated in phosphate buffer from: a) G-0 PAMAM, b) G-2 PAMAM, c) G-4 PAMAM, d) G-6 PAMAM, e) G4-PPI f) G-5 PPI

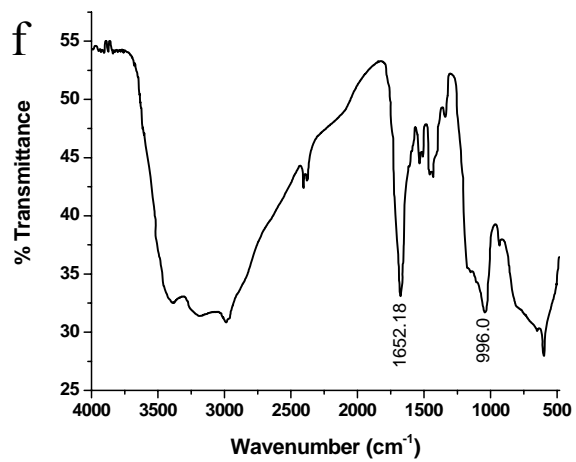
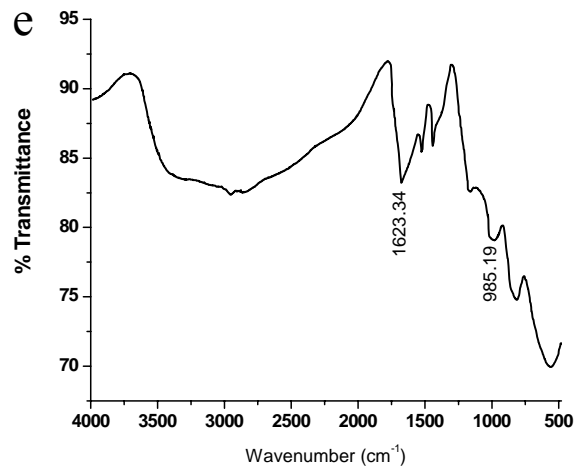
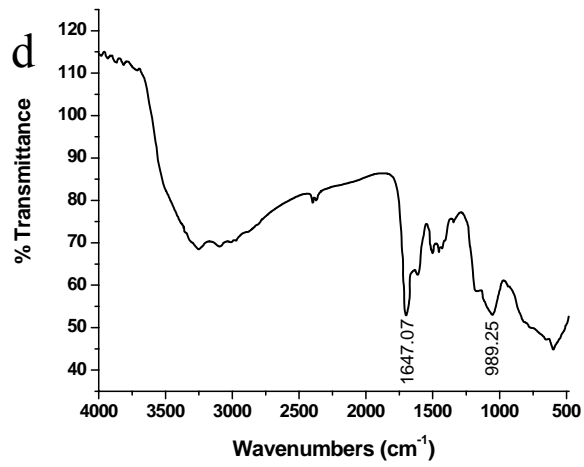


Figure 85. Continued

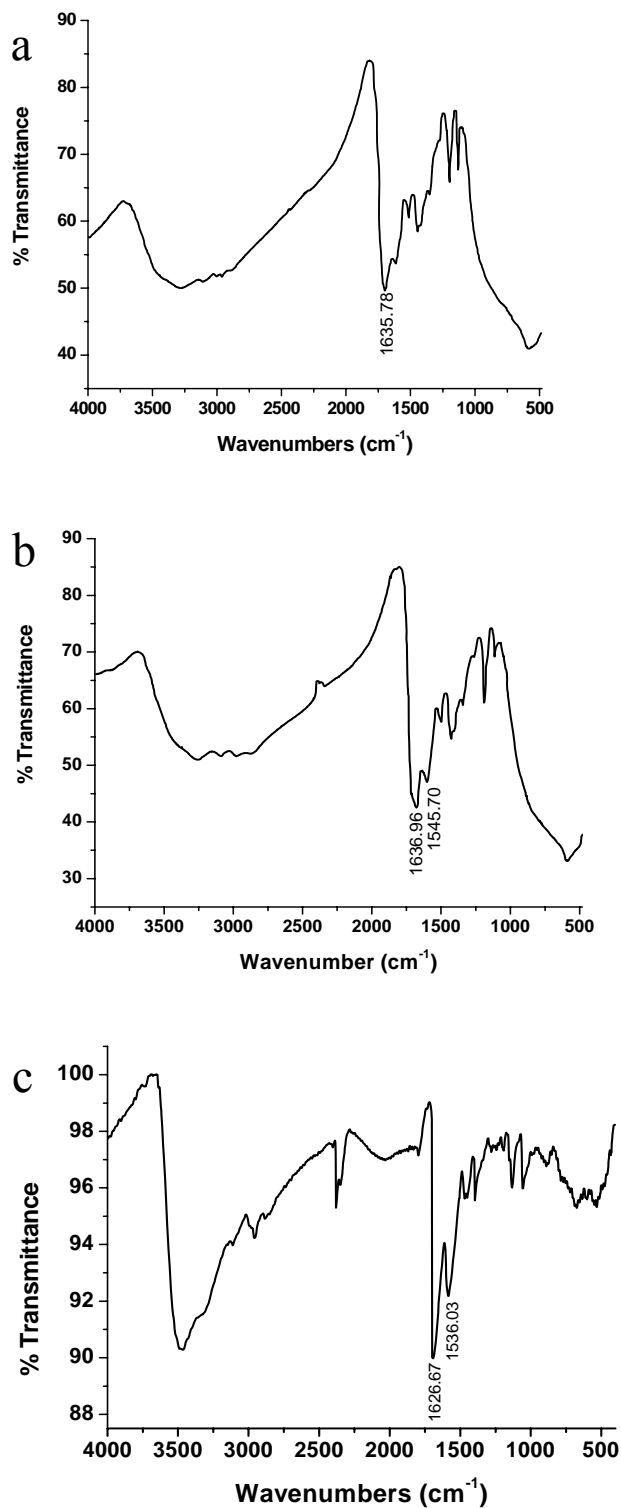


Figure 86: Infra-red spectra of titanium dioxide precipitated in water from: a) G-0 PAMAM, b) G2 PAMAM, c) G-4 PAMAM, d) G-6 PAMAM, e) G4-PPI f) G-5 PPI

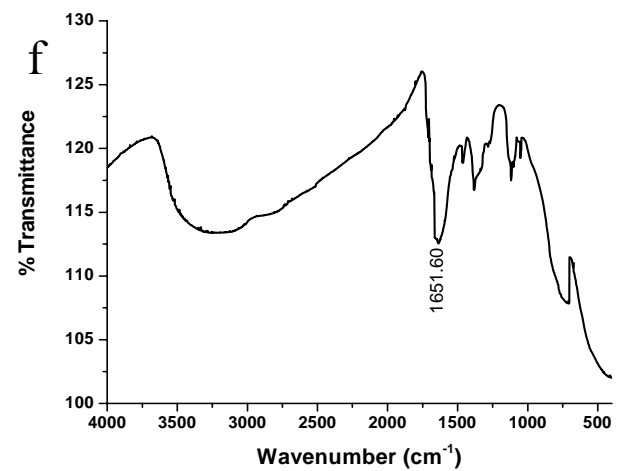
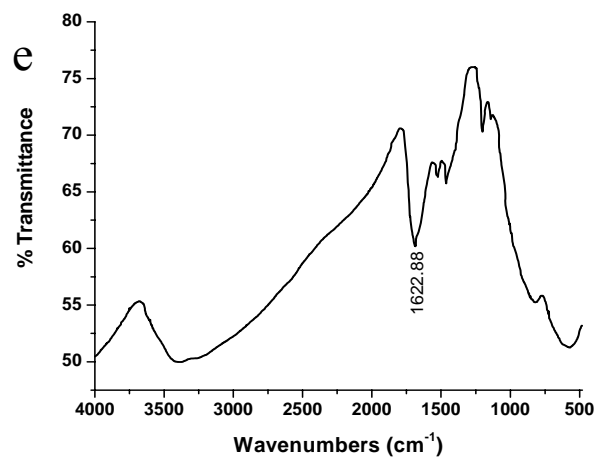
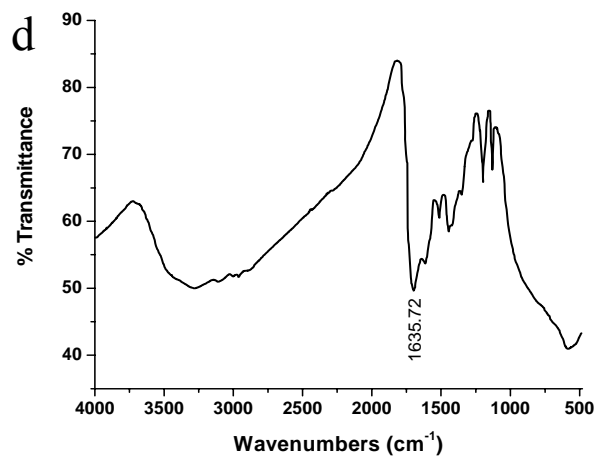


Figure 86: Continued

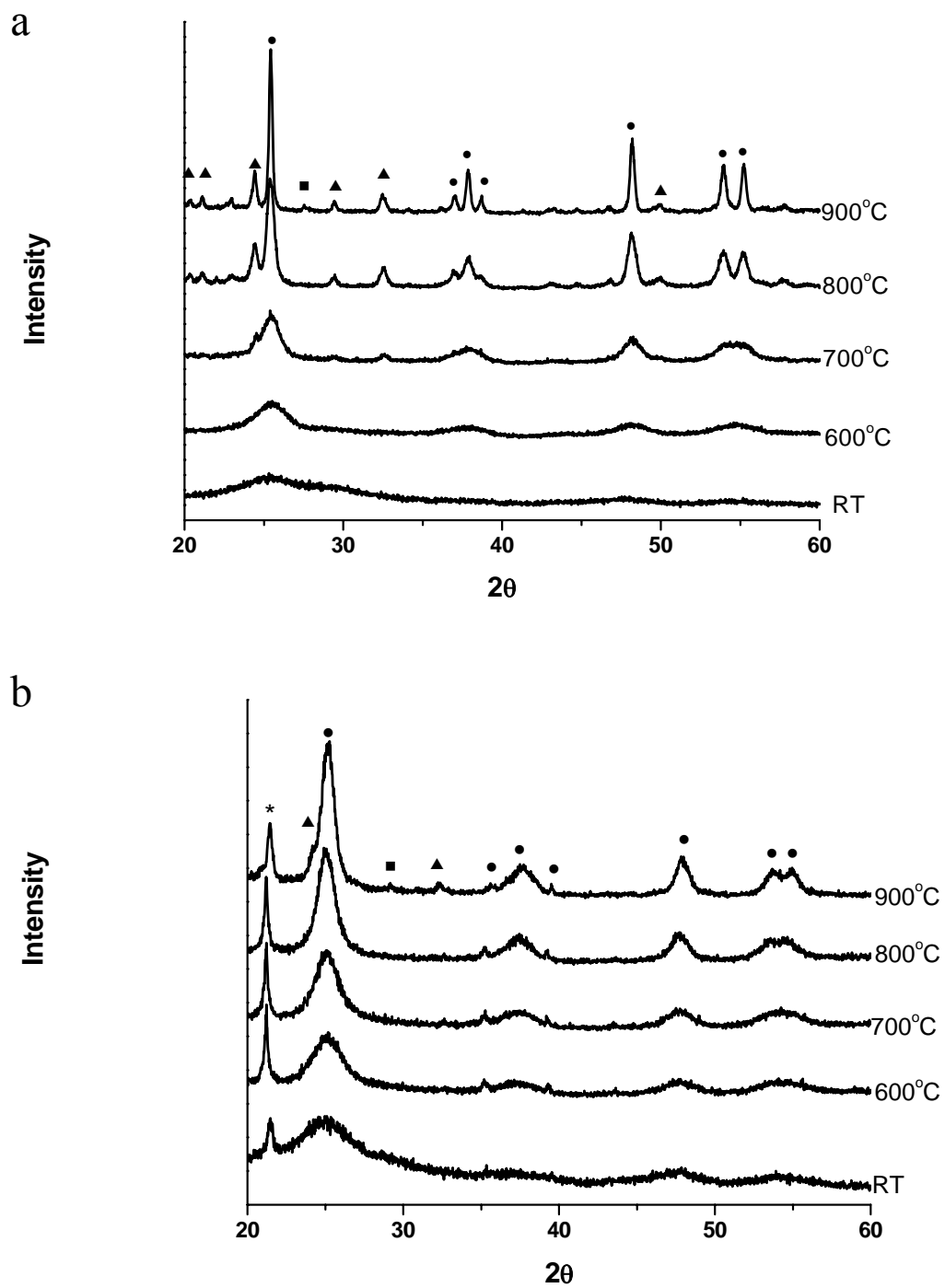


Figure 87. Variable temperature X-ray diffraction spectra of titanium dioxide precipitated in phosphate buffer from a) G-2 PAMAM, b) G-4 PAMAM, c) G-6 PAMAM, d) G4-PPI e) G-5 PPI (● anatase, ■ rutile, ◆ titanium phosphate)

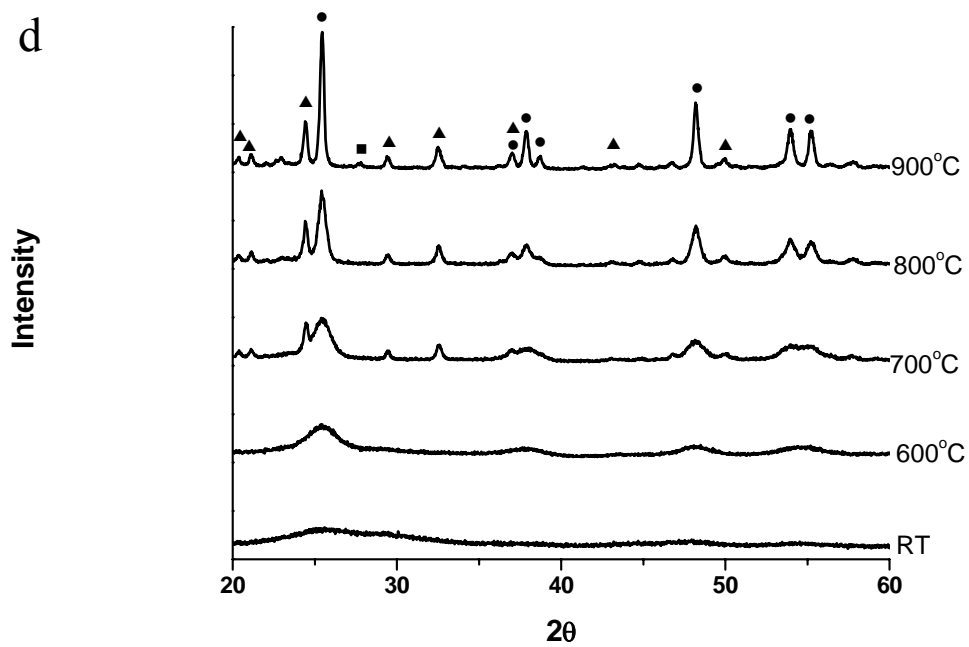
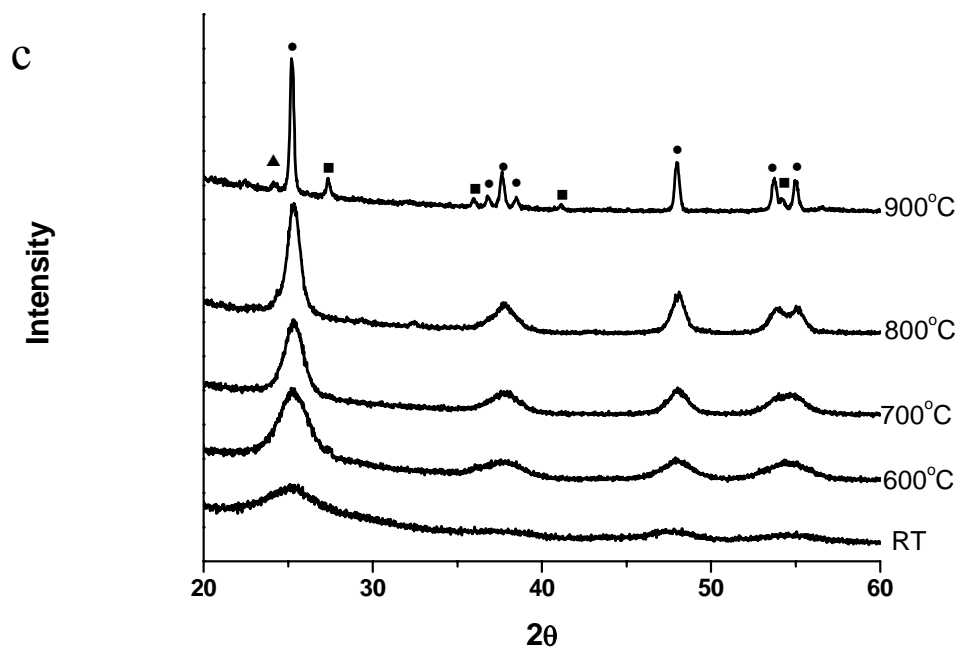


Figure 87. Continued.

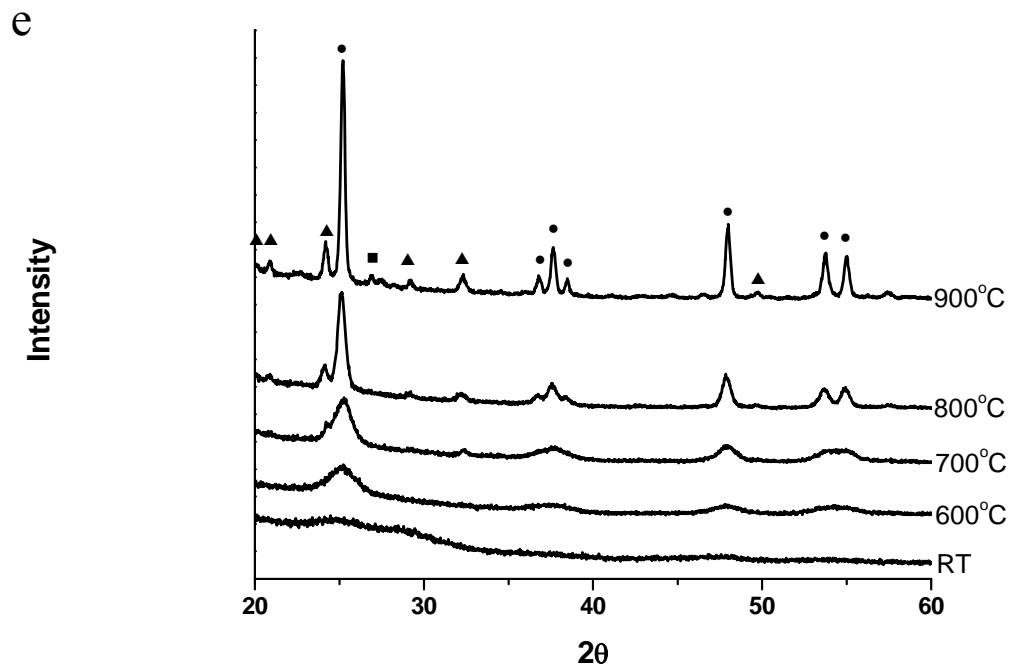


Figure 87. Continued

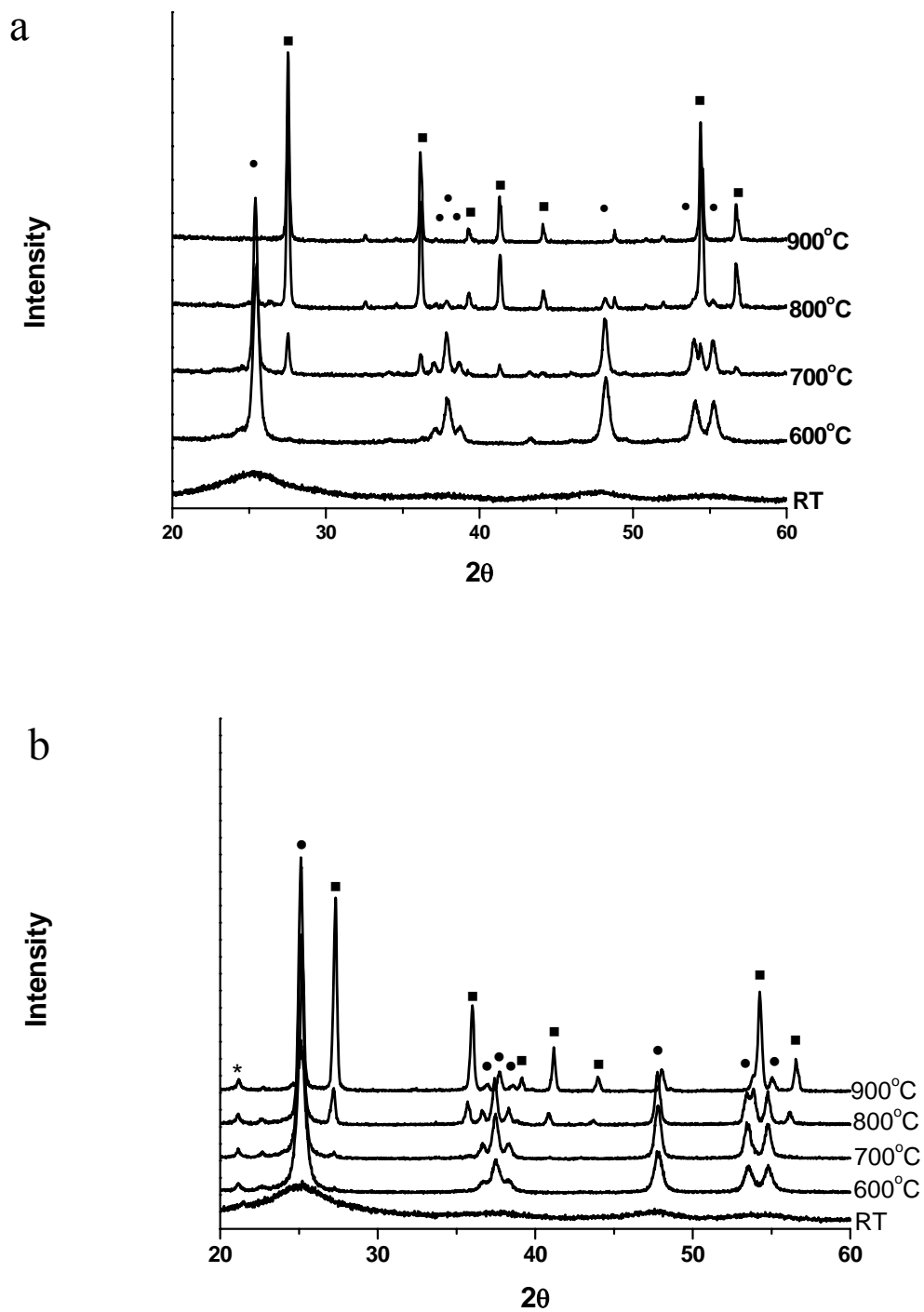


Figure 88: Variable temperature X-ray diffraction spectra of titanium dioxide precipitated in water from a) G-2 PAMAM, b) G-4 PAMAM, c) G-6 PAMAM, d) G4-PPI e) G-5 PPI (● anatase, ■ rutile)

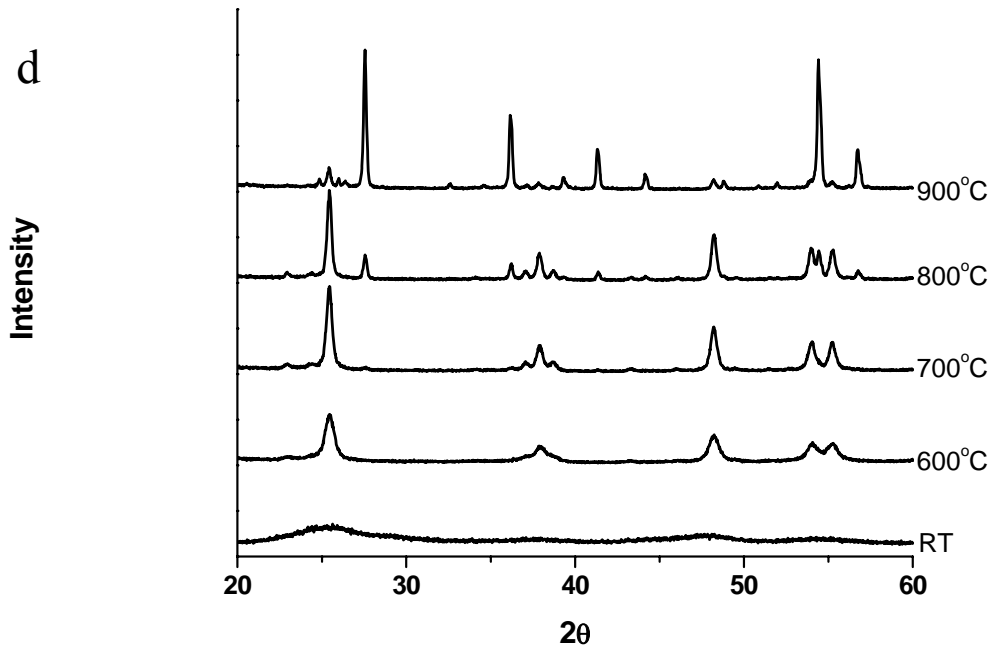
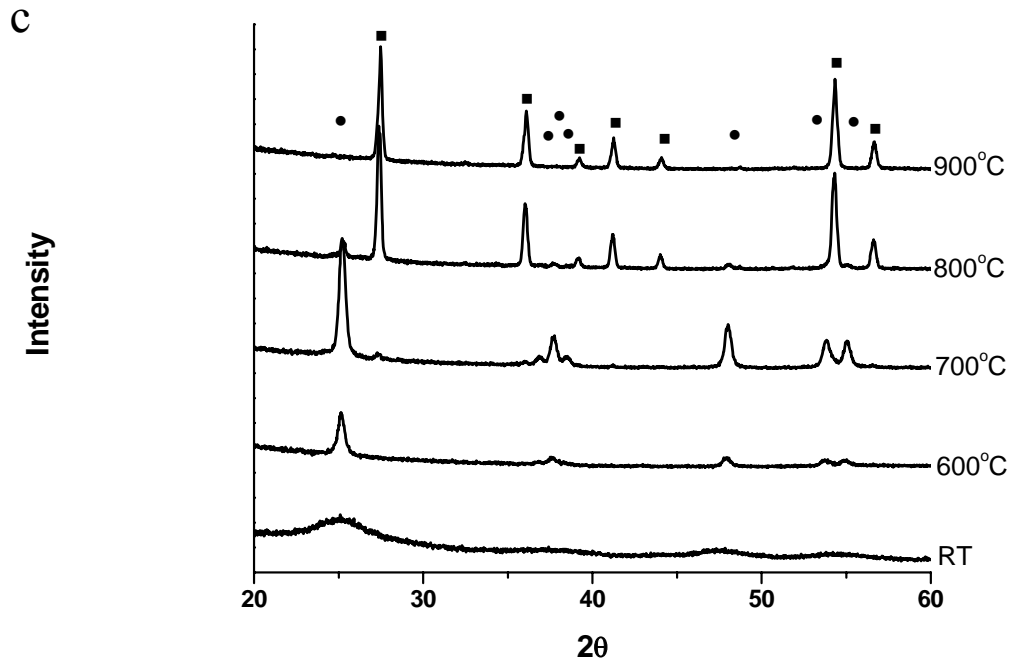


Figure 88. Continued

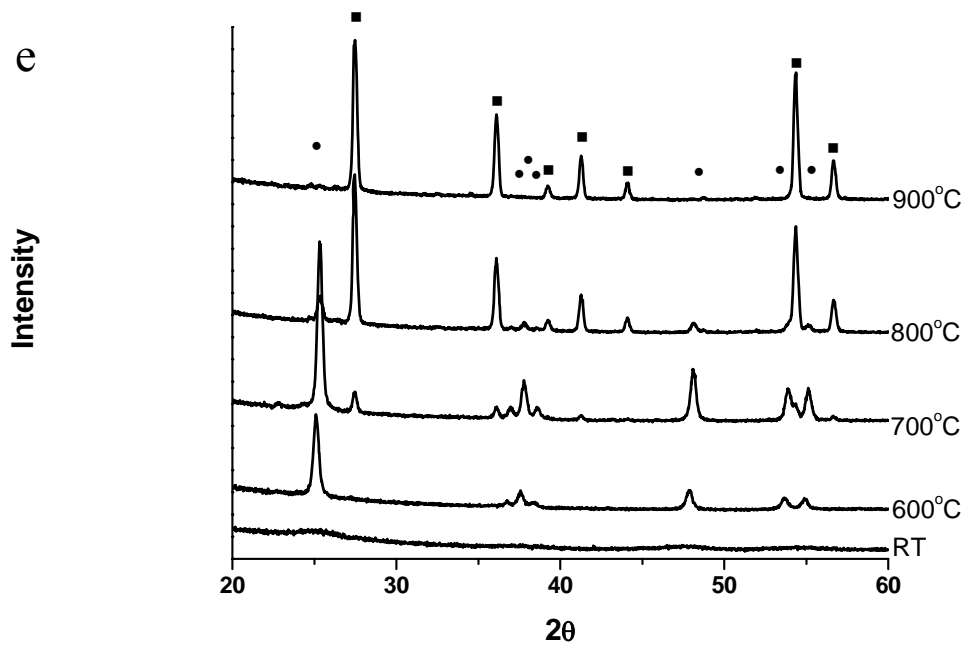


Figure 88. Continued.

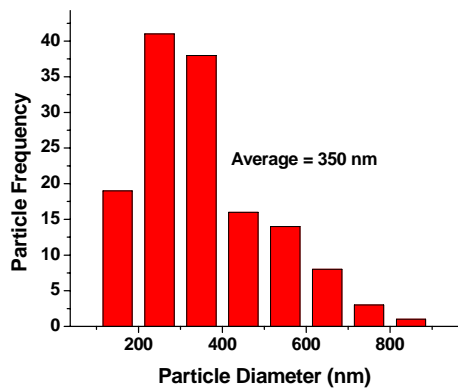
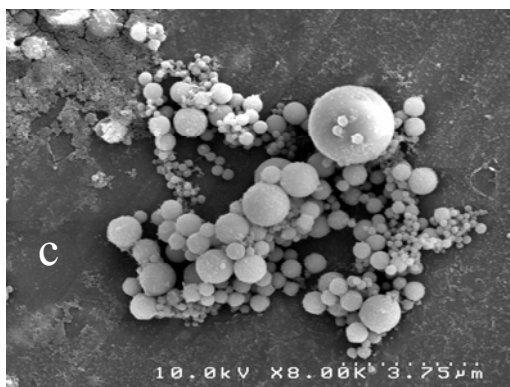
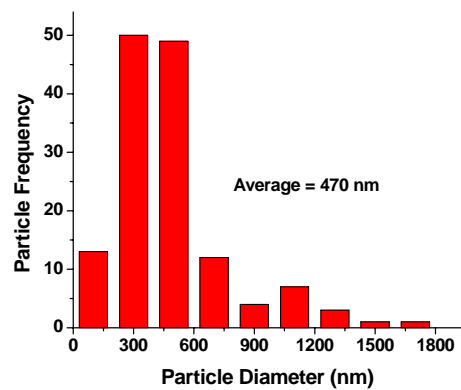
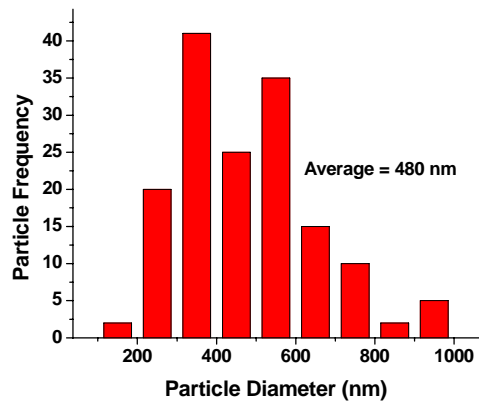
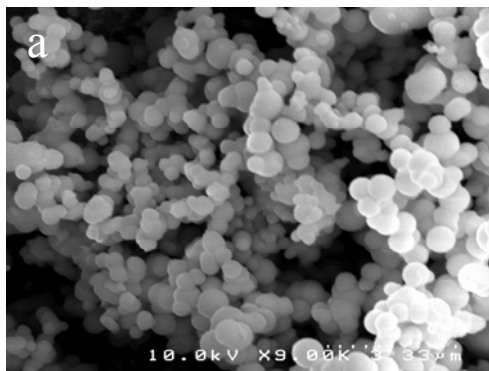


Figure 89: SEM micrographs and histograms of germanium dioxide nanoparticles precipitated in phosphate buffer from: a) G-0 PAMAM, b) G-2 PAMAM, c) G-4 PAMAM, d) G-6 PAMAM, e) G4-PPI f) G-5 PPI

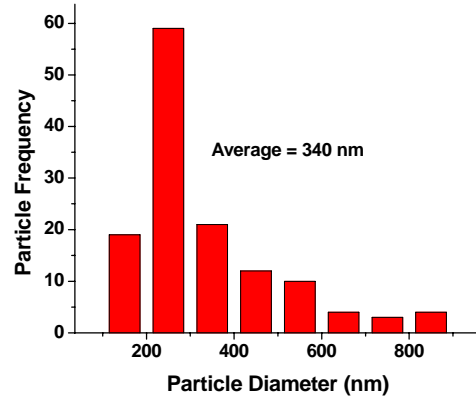
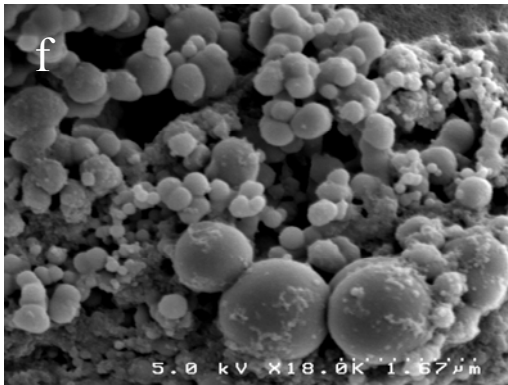
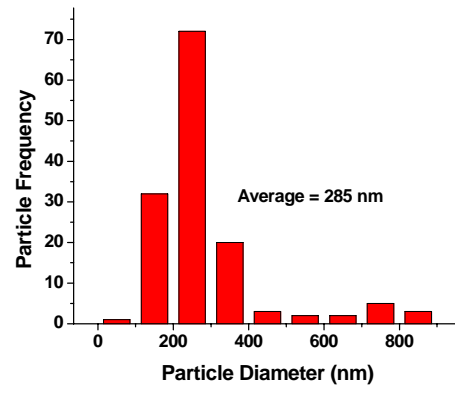
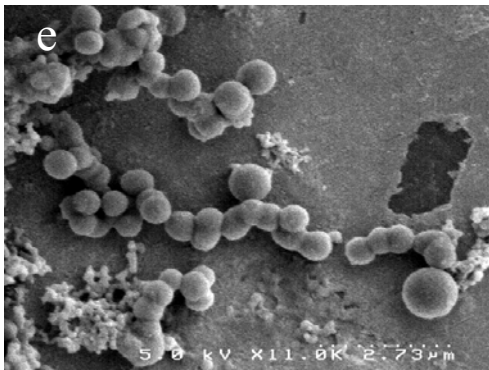
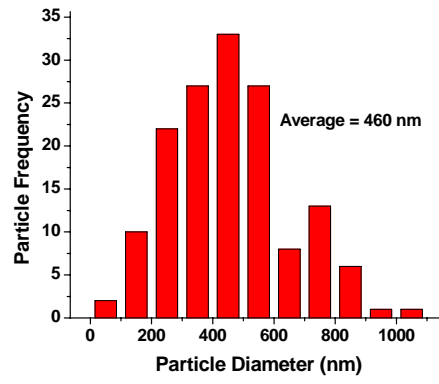
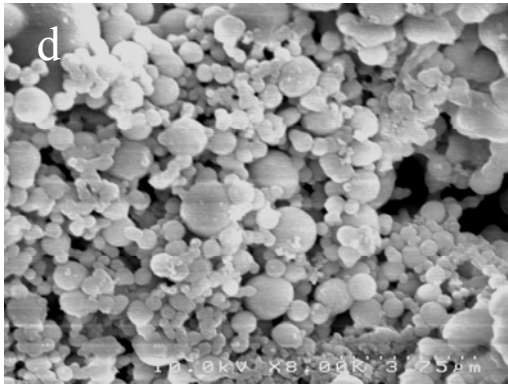


Figure 89. Continued.

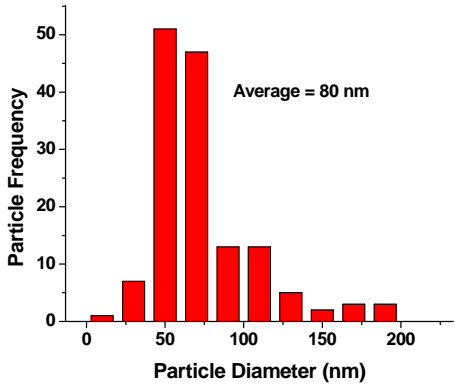
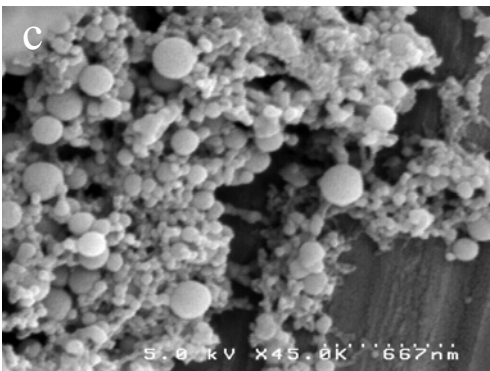
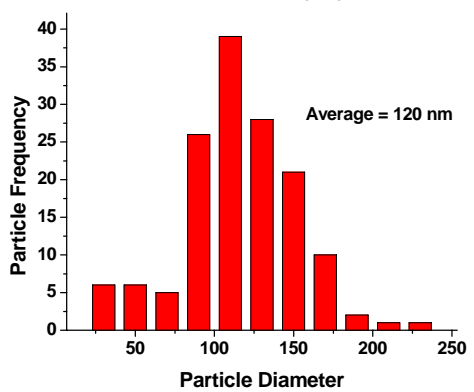
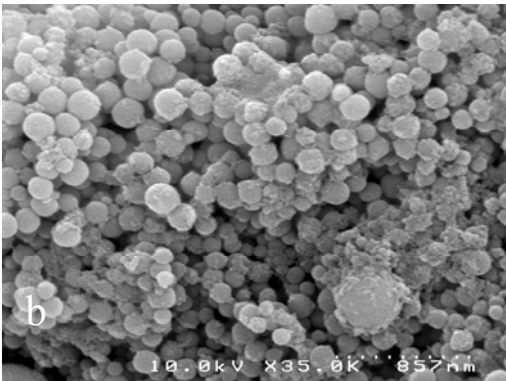
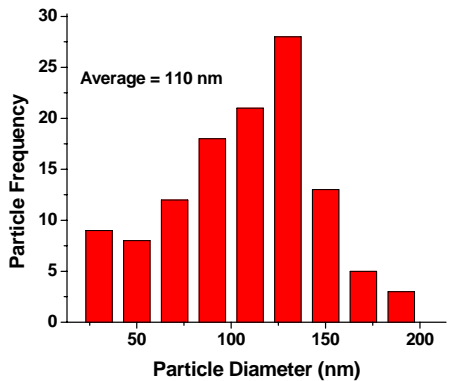
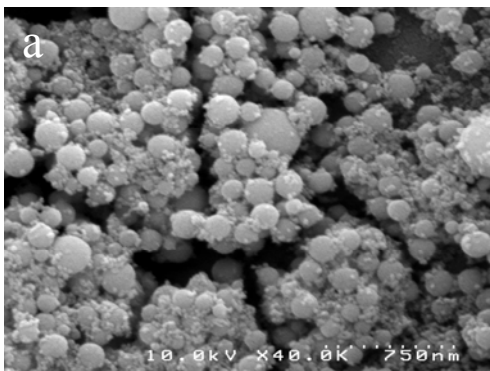


Figure 90: SEM micrographs of germanium dioxide nanoparticles precipitated in water from: a) G-0 PAMAM, b) G-2 PAMAM, c) G-4 PAMAM, d) G-6 PAMAM, e) G4-PPI f) G-5 PPI

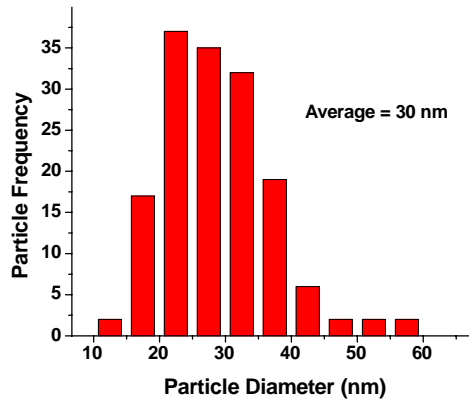
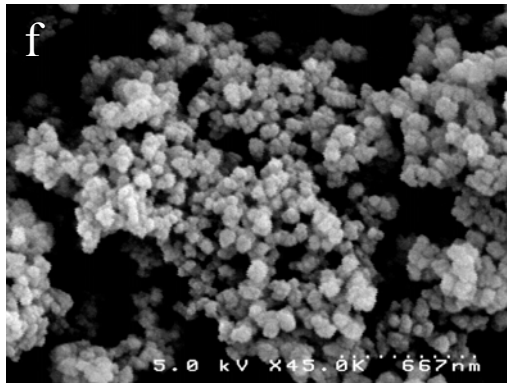
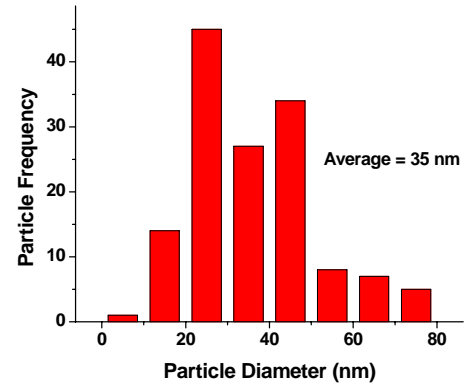
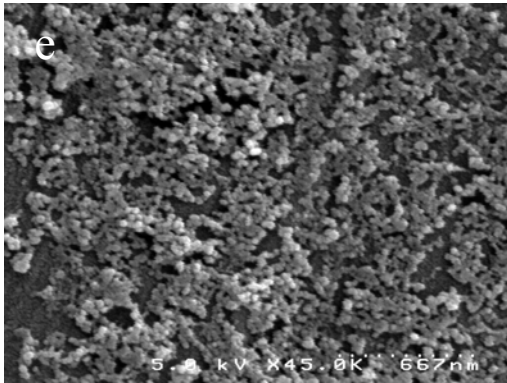
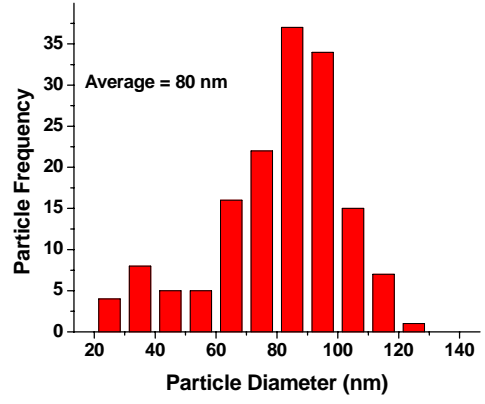
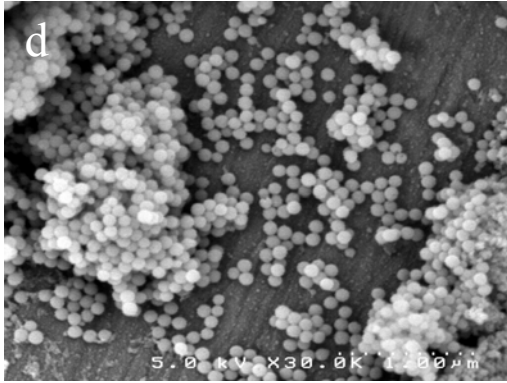


Figure 90. Continued.

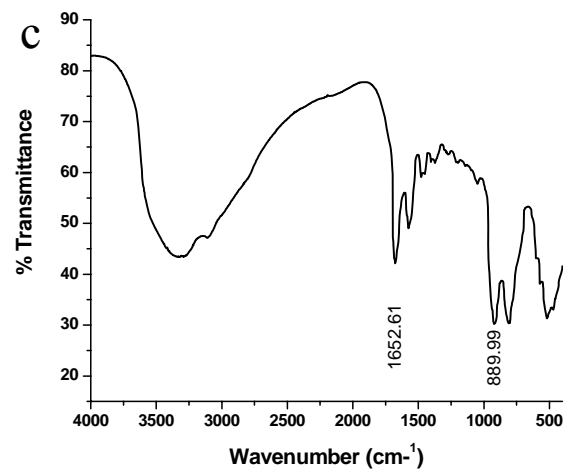
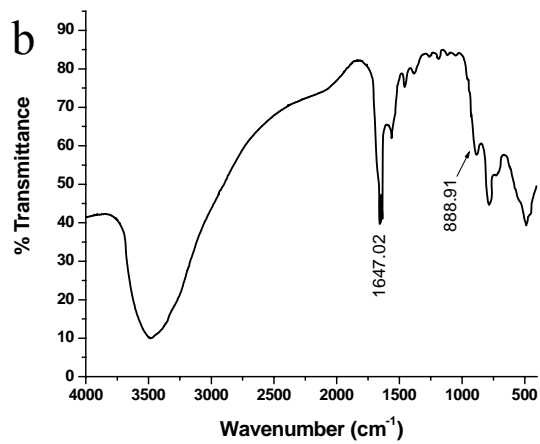
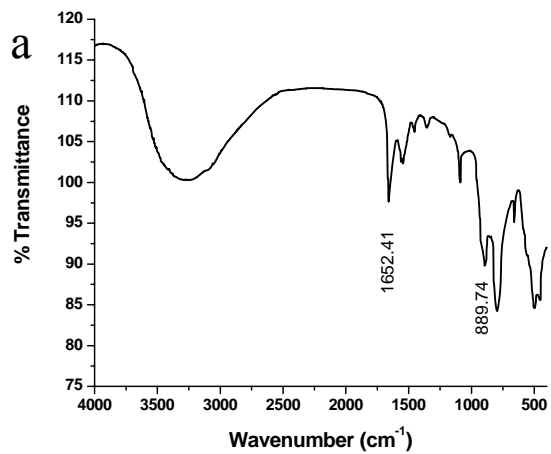


Figure 91: Infra-red spectra of germanium dioxide precipitated in phosphate buffer from: a) G-0 PAMAM, b) G-2 PAMAM, c) G-4 PAMAM, d) G-6 PAMAM, e) G4-PPI f) G-5 PPI

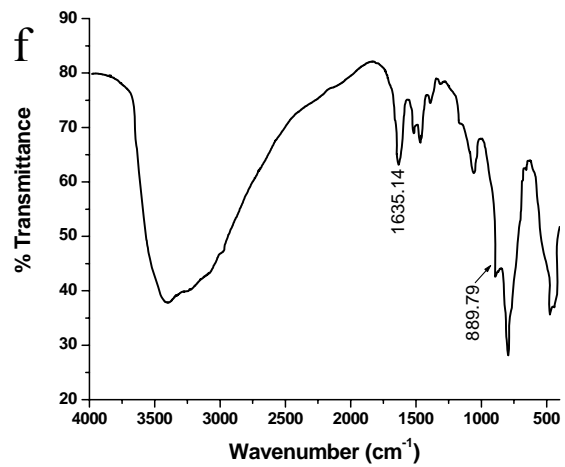
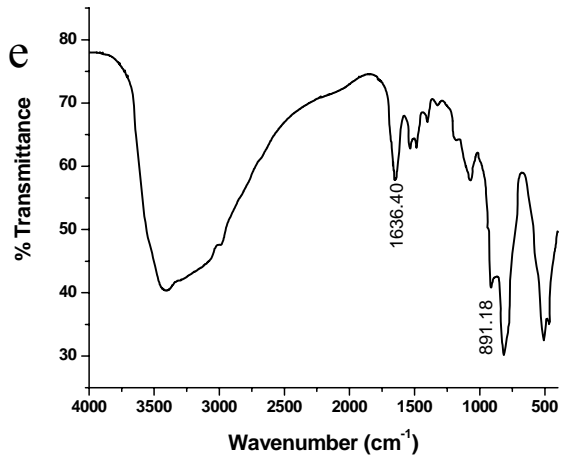
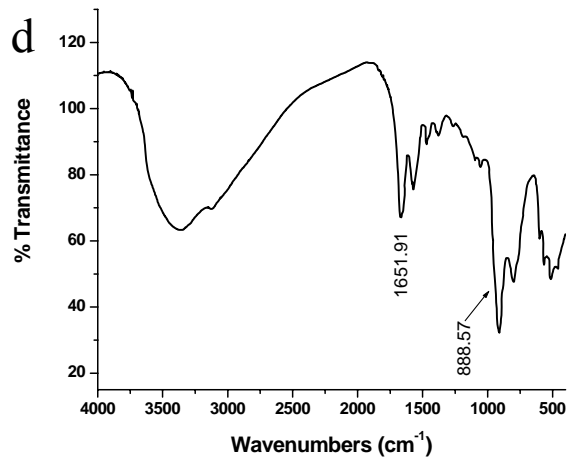


Figure 91. Continued.

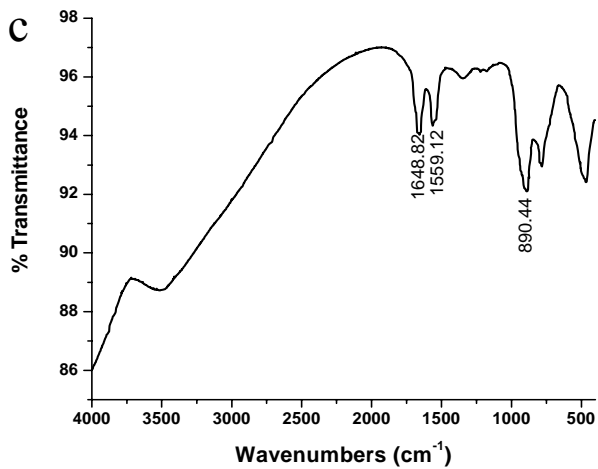
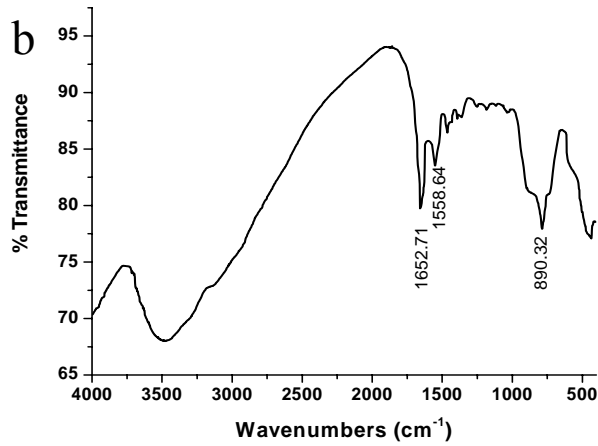
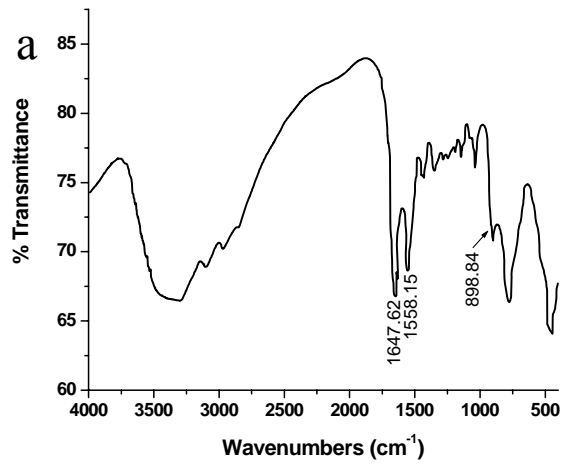


Figure 92: Infra-red spectra of germanium dioxide precipitated in water from: a) G-0 PAMAM, b) G-2 PAMAM, c) G-4 PAMAM, d) G-6 PAMAM, e) G4-PPI f) G-5 PPI

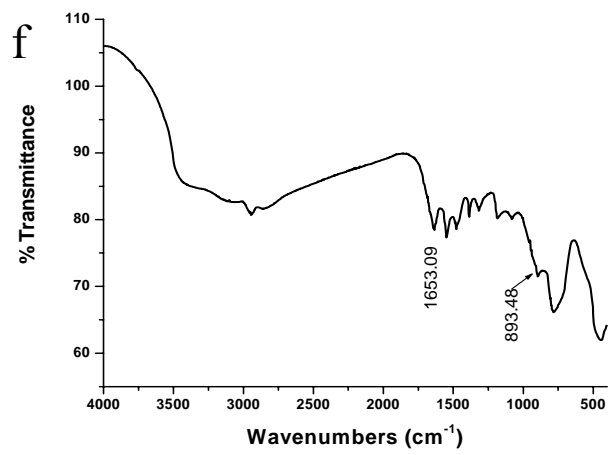
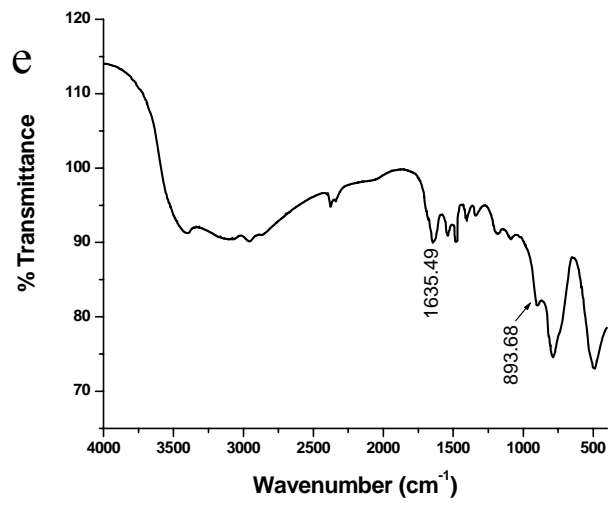
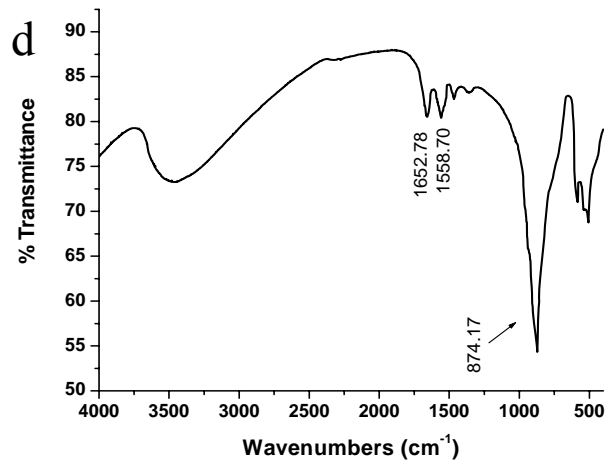


Figure 92. Continued

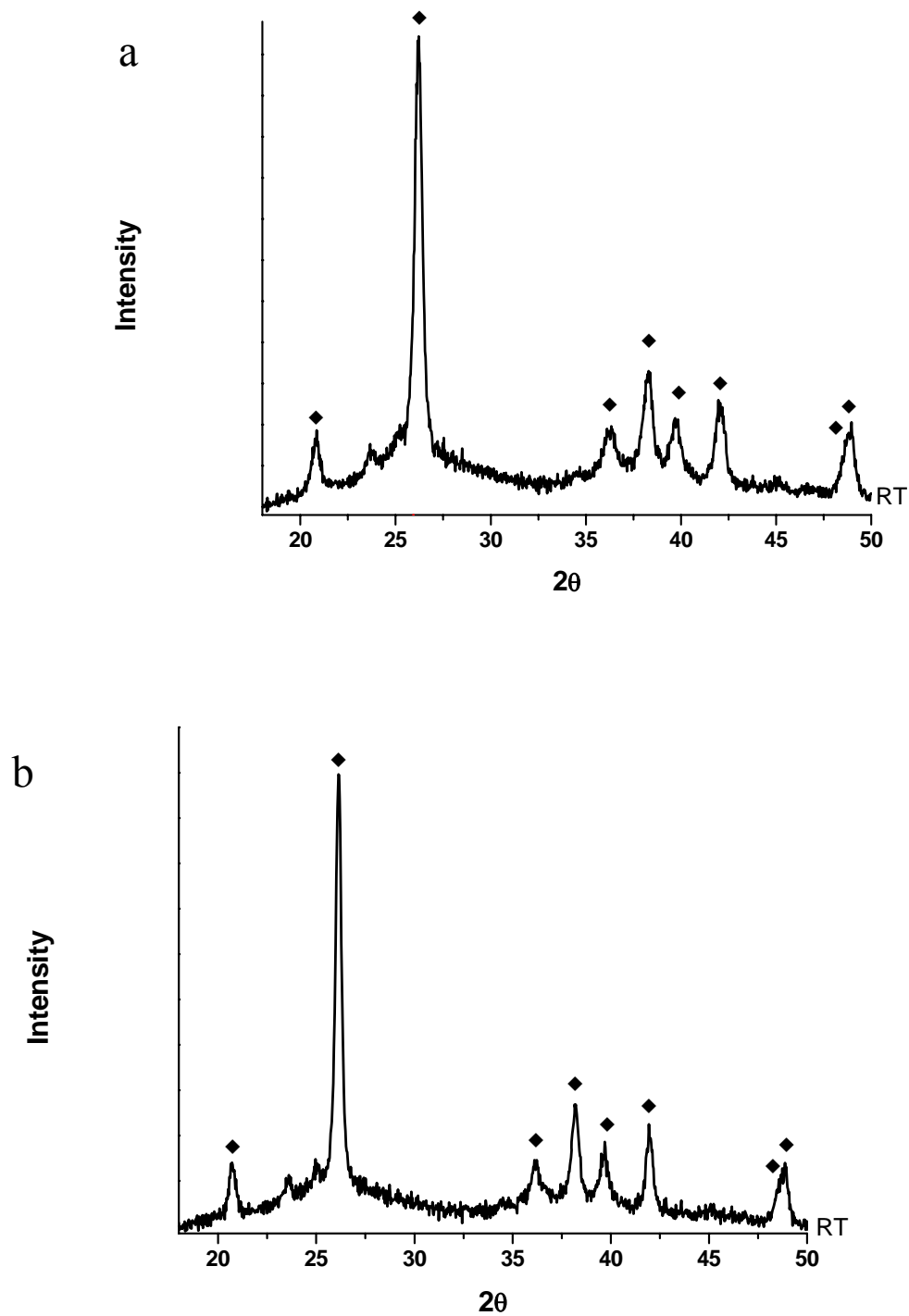


Figure 93: Variable temperature X-ray diffraction spectra of germanium dioxide precipitated in phosphate buffer from a) G-0 PAMAM, b) G-2 PAMAM, c) G-4 PAMAM, f) G-6 PAMAM, e) G4-PPI f) G-5 PPI (♦ α -phase)

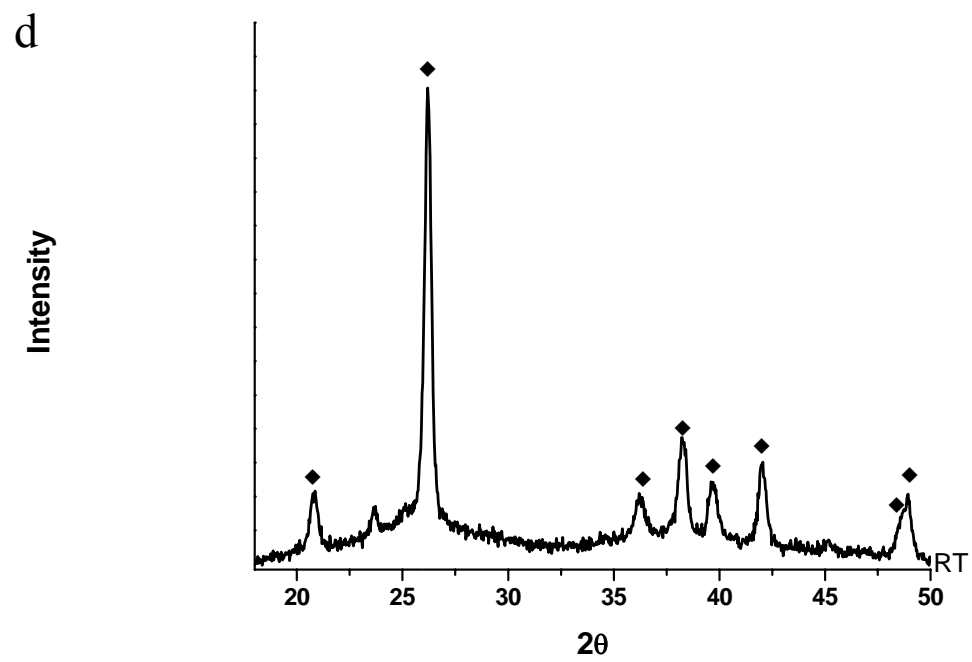
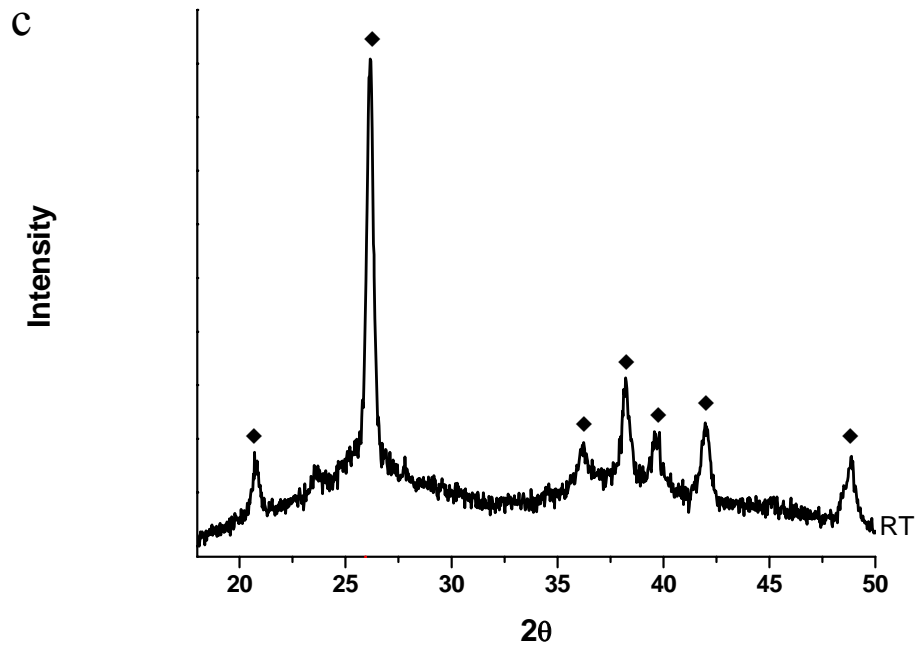


Figure 93. Continued.

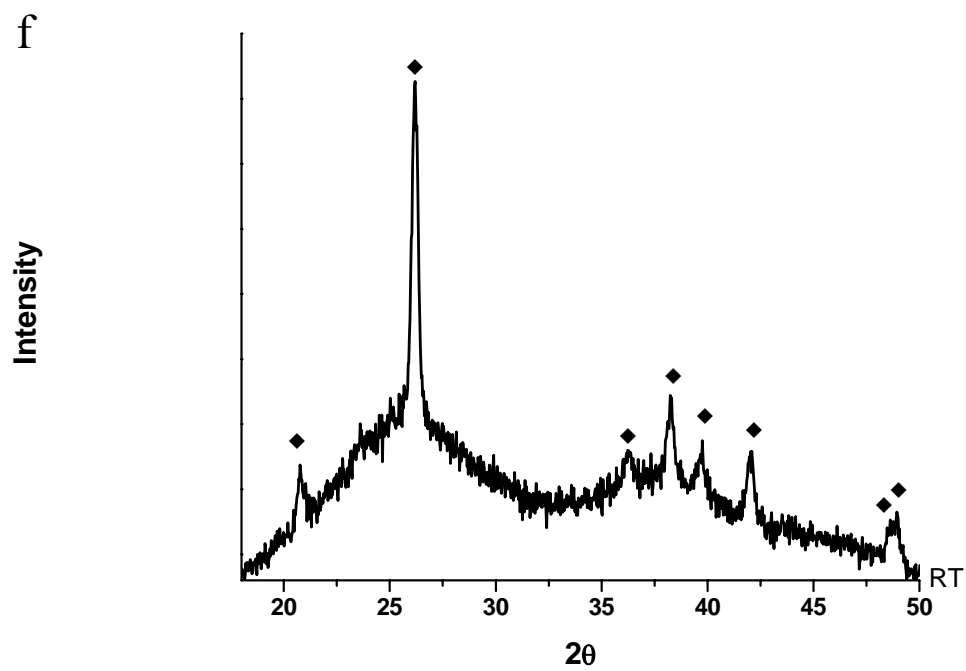
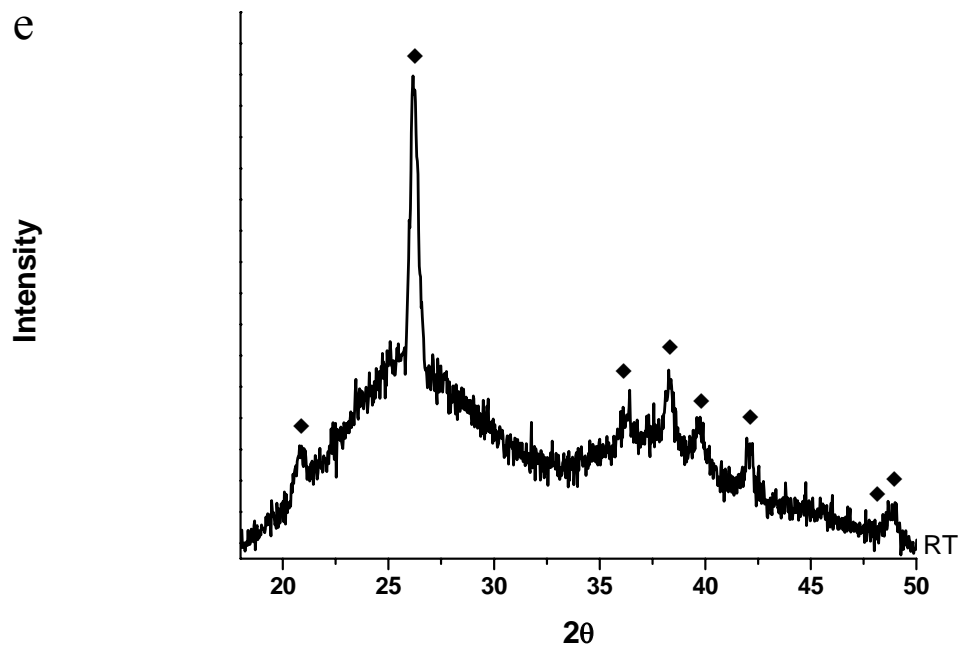


Figure 93. Continued.

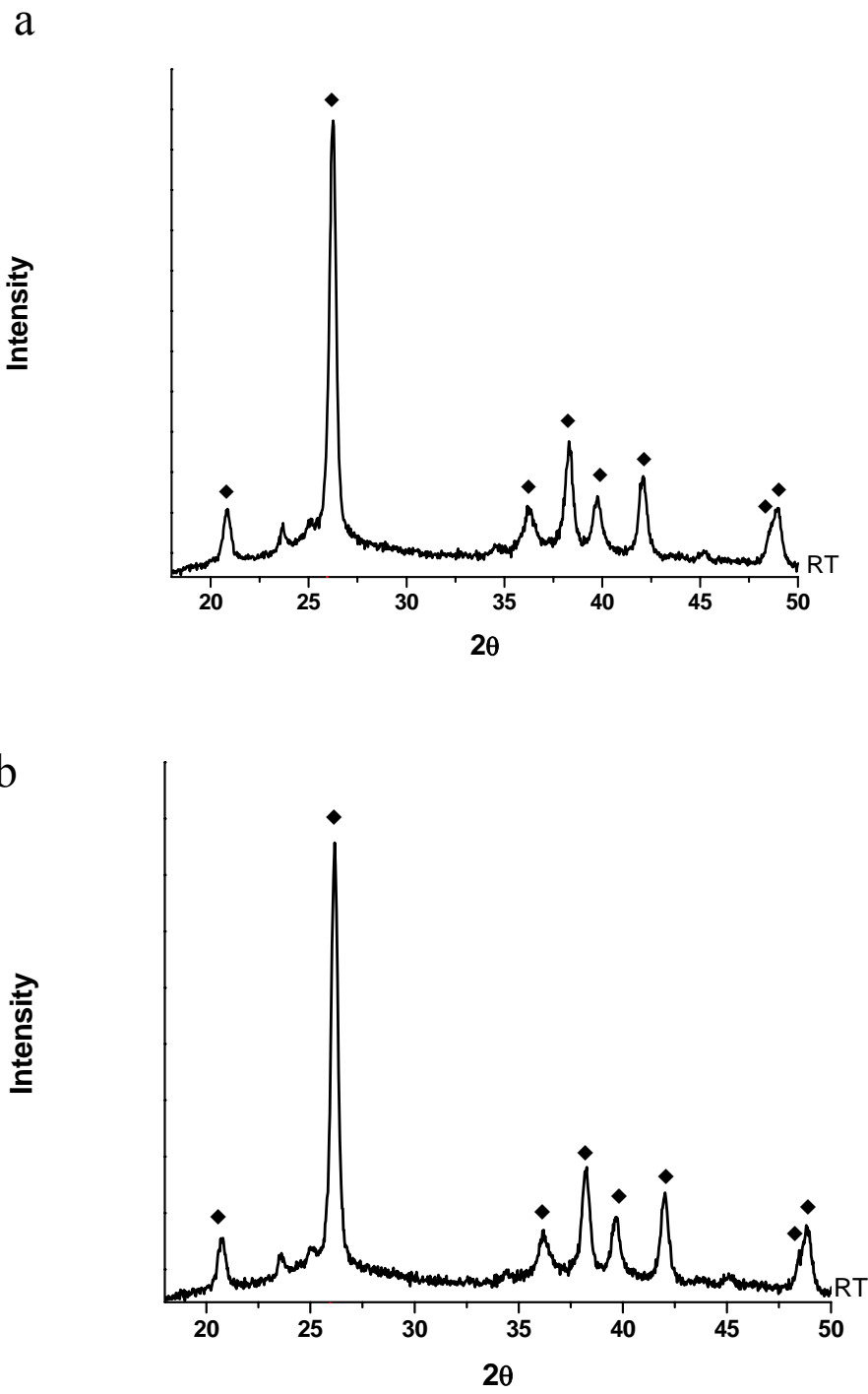


Figure 94: Variable temperature X-ray diffraction spectra of germanium dioxide precipitated in water from a) G-0 PAMAM, b) G-2 PAMAM, c) G-4 PAMAM, f) G-6 PAMAM, e) G4-PPI f) G-5 PPI (\blacklozenge α -phase)

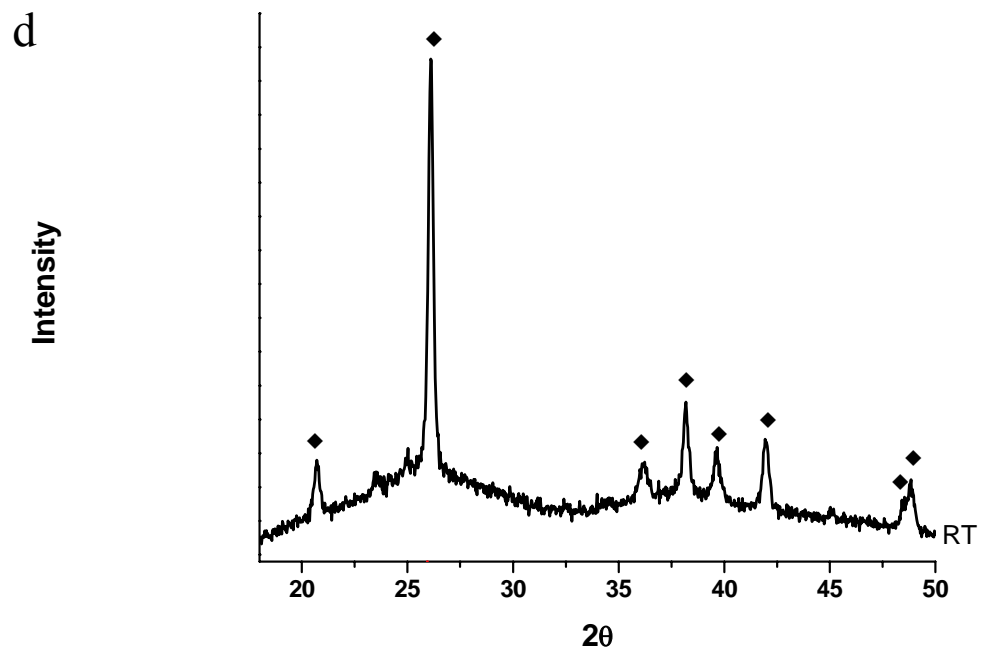
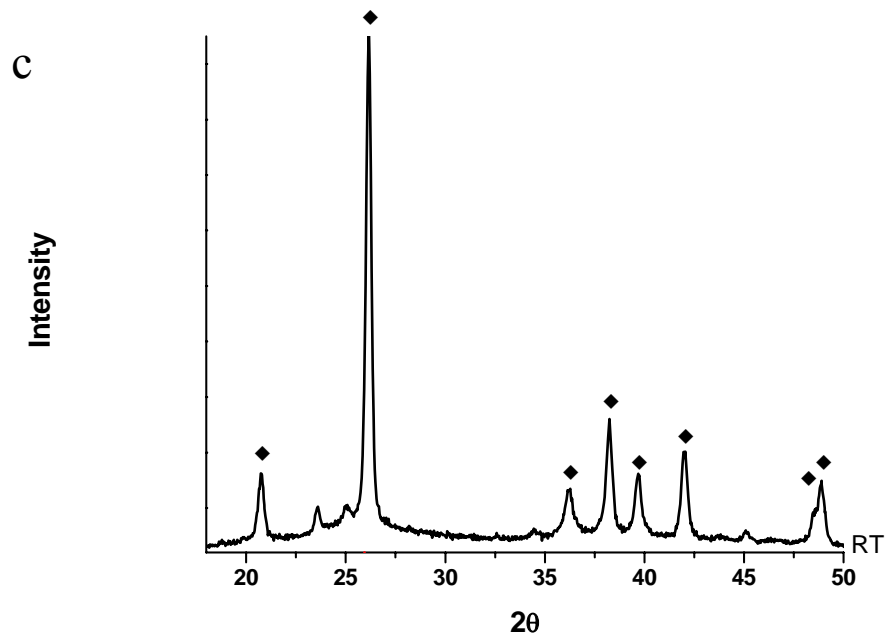


Figure 94. Continued.

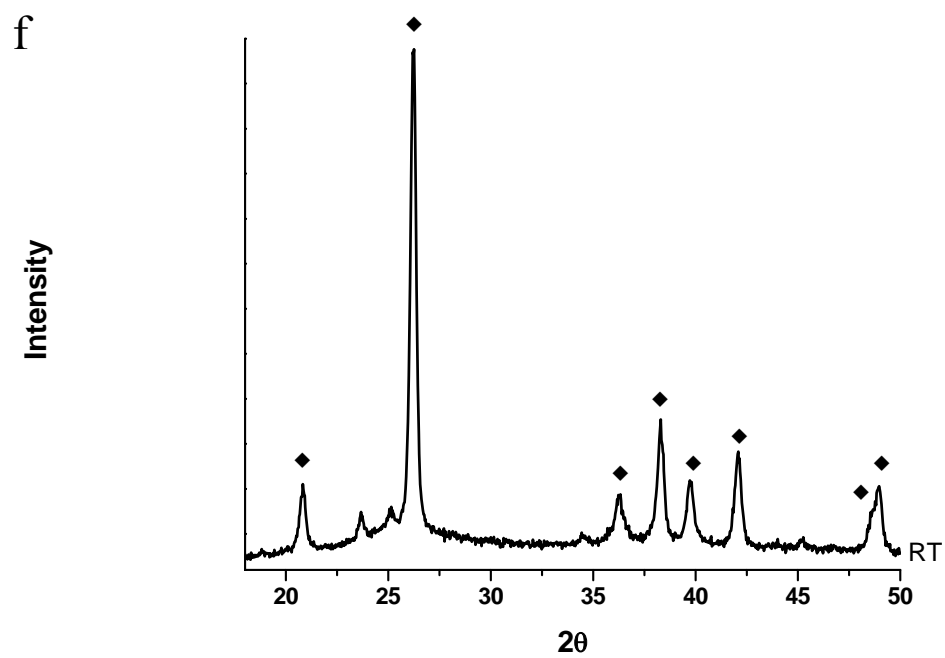
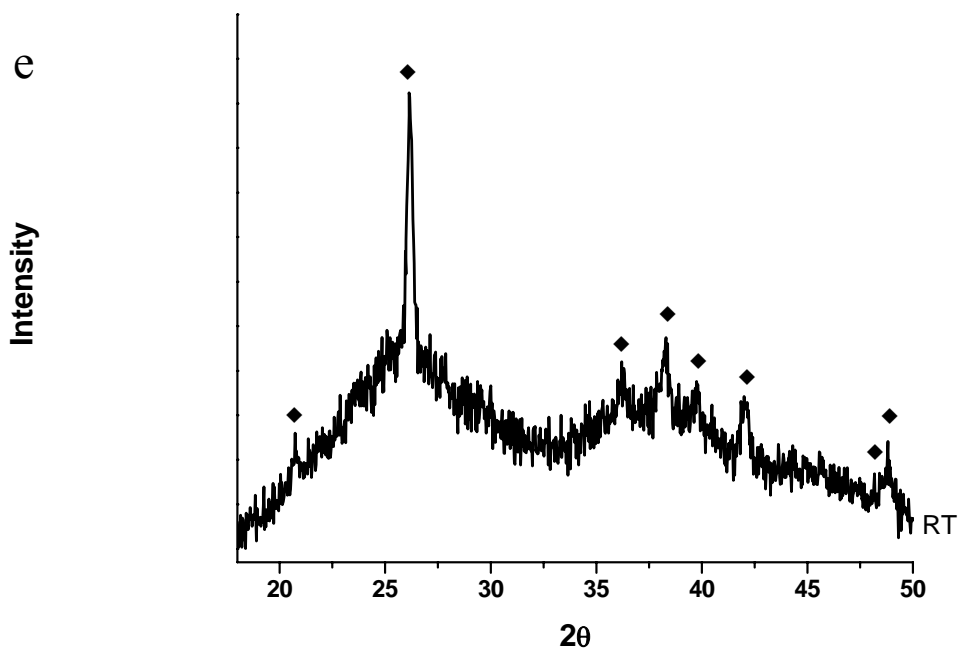


Figure 94. Continued.

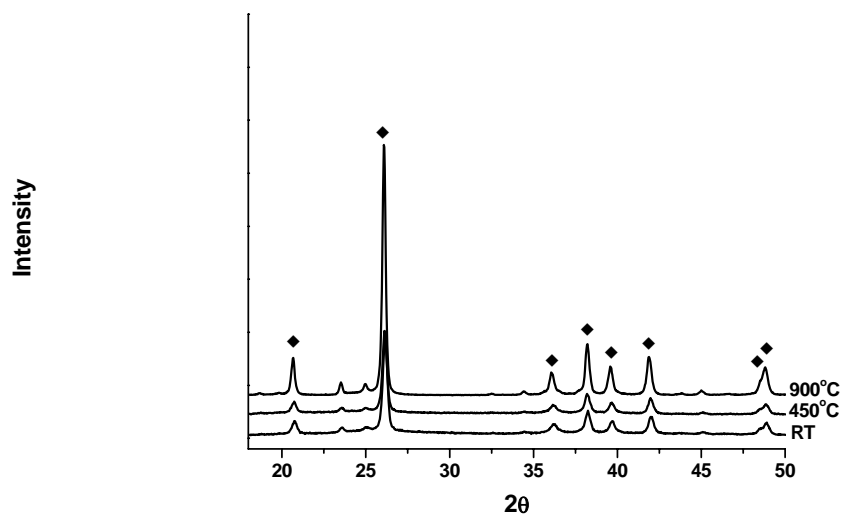


Figure 95: Variable temperature X-ray diffraction spectra of G4 PAMAM templated germanium dioxide in phosphate buffer

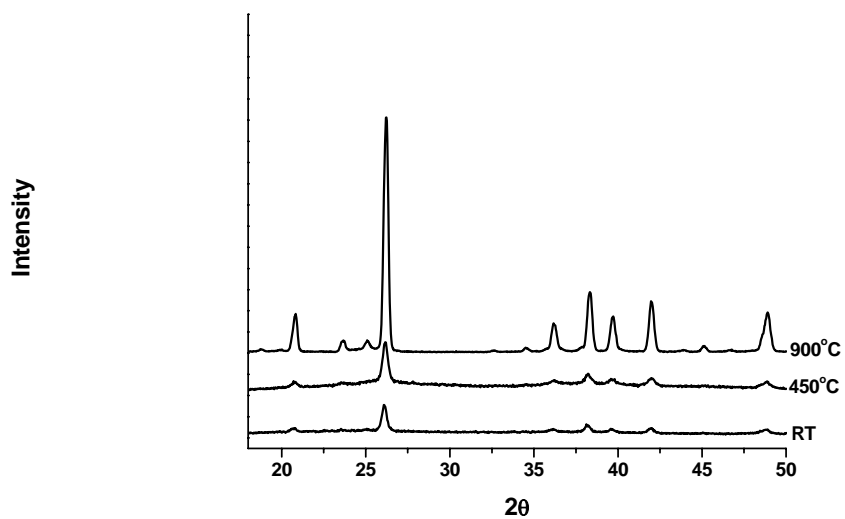


Figure 96: Variable temperature X-ray diffraction spectra of G4 PAMAM templated germanium dioxide in water

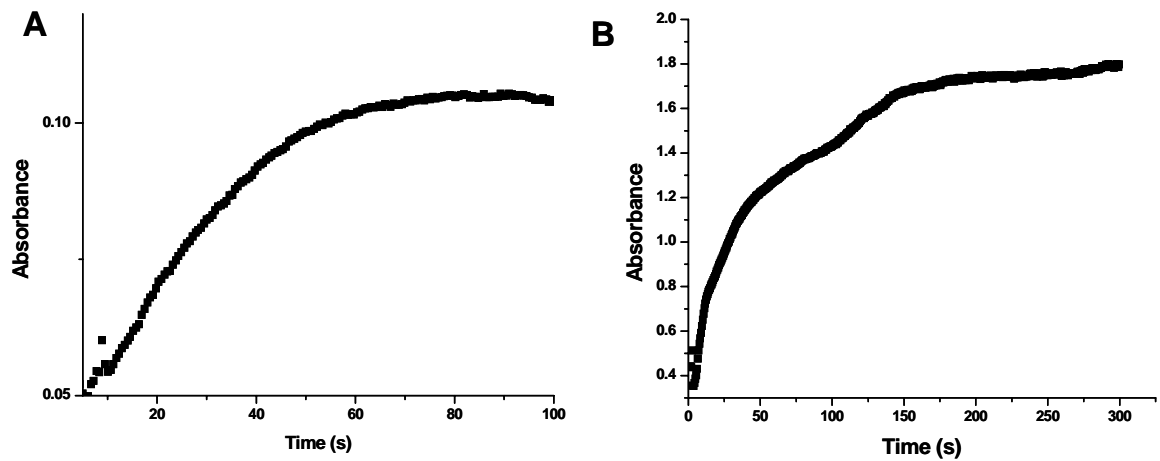


Figure 97: A) Light scattering profile of G4 dendrimer templated GeO_2 reaction in water. B) Light scattering profile of G4 dendrimer templated TiO_2 reaction in water. (absorbance at 480)

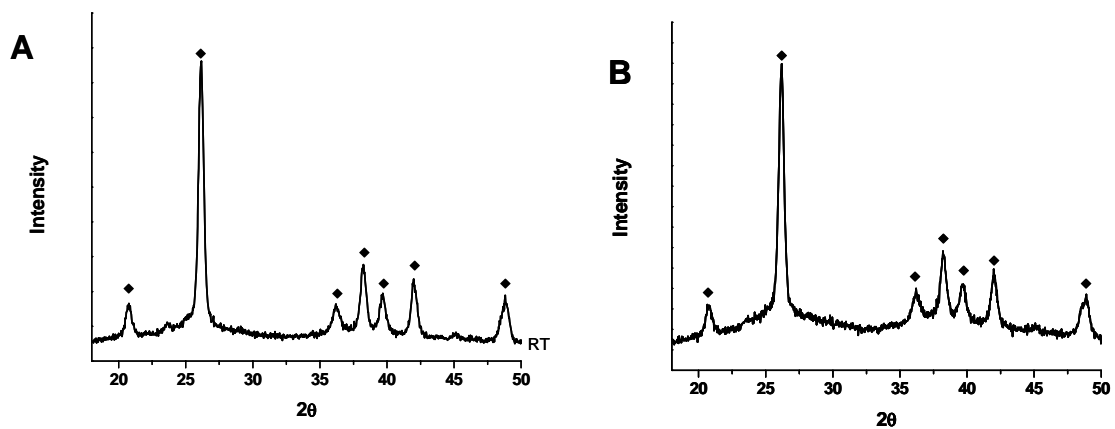


Figure 98: A) XRD of G4 PAMAM templated GeO_2 in water using TMOG as the precursor. B) XRD of G4 PAMAM templated GeO_2 in phosphate buffer, 100 mM, pH 7.5, using TMOG as the precursor (♦ α -phase).

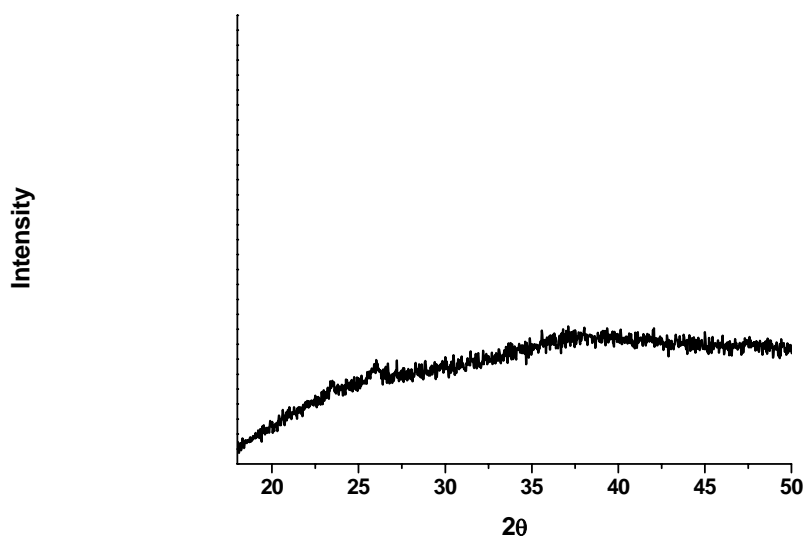


Figure 99: XRD of G4 PAMAM templated GeO_2 using TIPG as the precursor and phosphate buffer (100 mM, pH 7.5) as the solvent

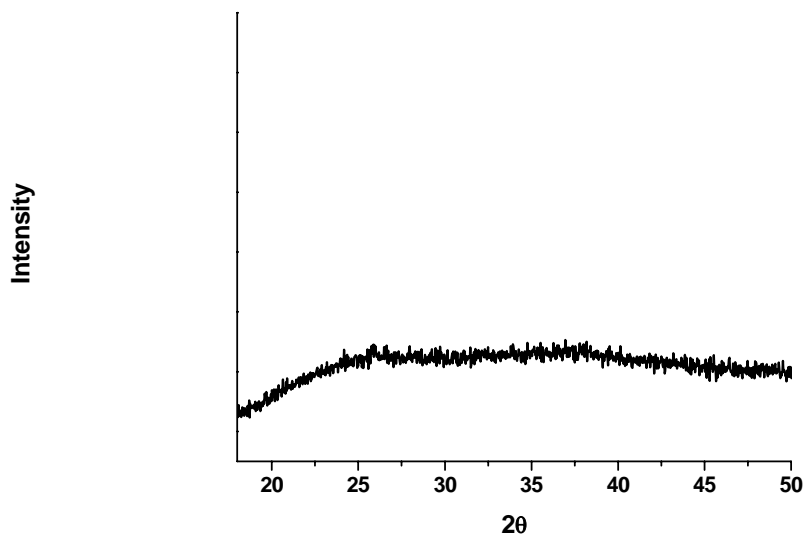


Figure 100: XRD of G4 PAMAM templated GeO_2 using TIPG as the precursor and water as the solvent

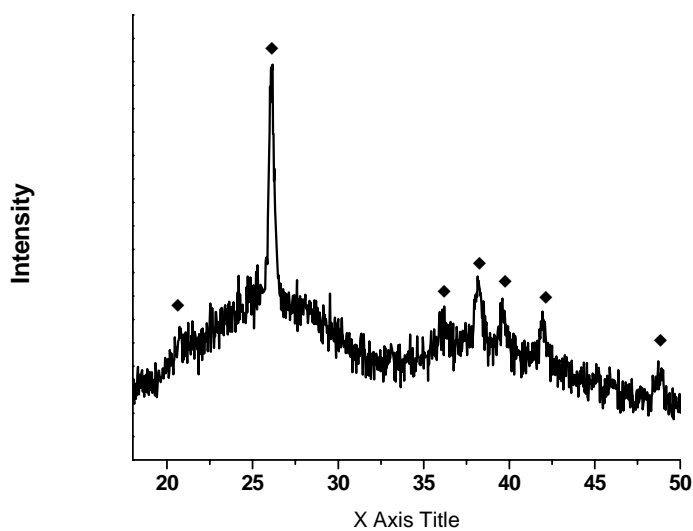


Figure 101: XRD of PLL templated GeO_2 using TMOG as the precursor and phosphate buffer (100 mM, pH 7.5) as the solvent (♦ α -phase)

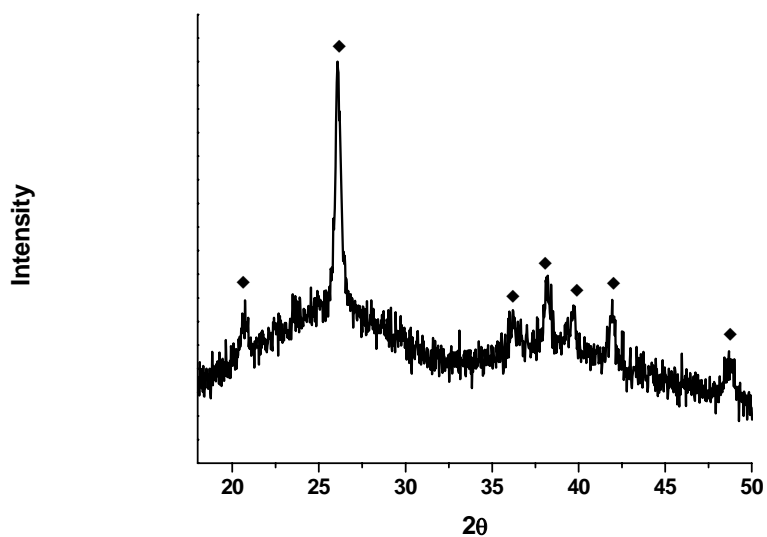


Figure 102: XRD of PLL templated GeO_2 using TEOG as the precursor and phosphate buffer (100 mM, pH 7.5) as the solvent (♦ α -phase)

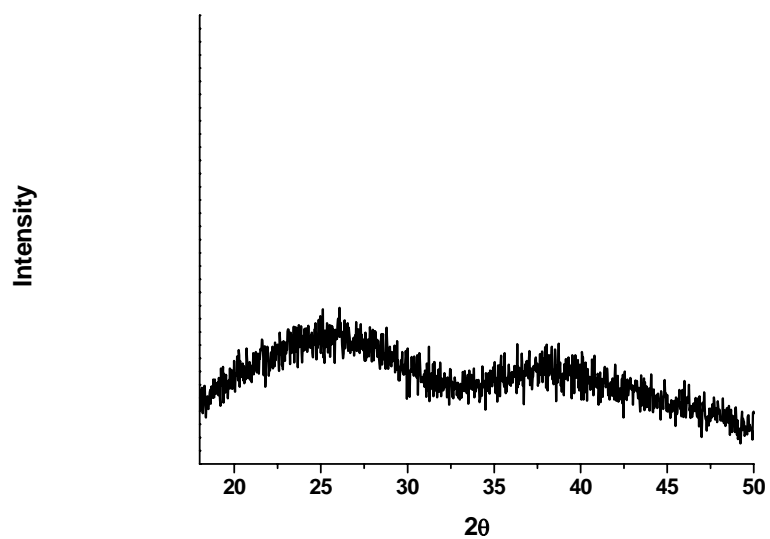


Figure 103: XRD of PLL templated GeO₂ using TIPG as the precursor and phosphate buffer (100 mM, pH 7.5) as the solvent

Sarah L. Sewell

Department of Chemistry, Vanderbilt University
7330 Stevenson Center, Station B 351822
Nashville, Tennessee 37235
Tel. (615) 403-2642; E-mail: sarah.l.sewell@vanderbilt.edu

Education:

- 2003-present Ph. D. Studies in Materials Chemistry, Vanderbilt University,
Nashville, Tennessee, 3.4 GPA
- 1999-2003 Bachelor of Science, Chemistry, *magna cum laude*, The University
of Tennessee at Chattanooga, Chattanooga, Tennessee, 3.9 GPA

Research Experience:

- 2003-present **Graduate Research with David W. Wright**
Vanderbilt University, Nashville, Tennessee
*Biomimetic Synthesis of Metal Oxide Nanoparticles Mediated by
Peptides and Polymers*
- 2001-2003 **Undergraduate Research with Kyle S. Knight**
The University of Tennessee at Chattanooga, Chattanooga,
Tennessee
A Mechanistic Study of Palladium Catalyzed Dehalogenation

Honors and Awards

- 2003 GAANN Fellowship (VU)
2003 American Institute of Chemist's Award (UTC)
2003 Outstanding Student Leadership Award (UTC)
1999-2003 Grote Scholarship (UTC)
1999-2003 Provost Scholarship (UTC)
1999-2003 Dean's List (UTC)

Affiliations

- 2003-present American Chemical Society, Nashville, Tennessee
2003 Mortar Board National Honor Society, The University of Tennessee at
Chattanooga
2000-2003 Golden Key National Honor Society, The University of Tennessee at
Chattanooga

Publications

“Detoxification Biominerals” Carney, C. K.; Harry, S. R.; Sewell, S.L.; Wright, D.W. *Curr. Top. Chem.*, K. Naka, Ed., Springer-Verlag: Amsterdam, **2006**, accepted.

“Piezoelectric Ink Jet Processing of Materials for Medical and Biological Applications” Sumerai, J.; Lewis, J.; Doraiswamy, A.; Deravi, L. F.; Sewell, S. L.; Gerden, A. E.; Wright, D. W.; Narayan, R. J. *Biotechnol. J.* **2006**, 1, 976-987.

“The Basis of Immunomodulatory Activity of Malaria Pigment (Hemozoin)” Carney, C. K.; Schrimpe, A. C.; Halfpenny, K.; Harry, S. R.; Miller, C. M.; Broncel, M.; Sewell, S.L.; Schaff, J. E. Deol, R.; Carter, M. D.; Wright, D. W. *J. Biol. Inorg. Chem.* **2006**, 11, 917-929.

“Biomimetic Synthesis of Titanium Dioxide Utilizing the R5 Peptide Derived from *Cylindrotheca fusiformis*” Sewell, S. L.; Wright, David W. *Chem. of Mater.* **2006**, 18, 3108-3113.

“Reduction of Secondary Alkyl Bromides by Palladium Catalysts Containing Chelating Diphosphine Ligands” Milczek, E. L.; Palmiero, L.; Sewell, S. L.; Knight, K. S. *Transition Metal Chemistry.* **2006**, 31, 27-29.

“Size Control of Dendrimer-Templated Silica” Knecht, M. R.; Sewell, S. L.; Wright, D. W. *Langmuir.* **2005**, 21, 2058-2061.

Presentations

“Biomimetic Synthesis of Metal Oxide Nanoparticles Utilizing PAMAM and PPI dendrimers”, Sarah L. Sewell, David W. Wright. Presented at the 231st National Meeting of the American Chemical Society, March 26-30, 2006 in Atlanta, Georgia.

“Dendrimer Mediated Synthesis of Metal Oxide Nanoparticles”, Sarah L. Sewell, David W. Wright. Presented at the 57th Southeast/61st Southwest Joint Regional Meeting of the American Chemical Society, November 1-4, 2005 in Memphis, Tennessee.

“Mechanistic Study of Palladium Catalyzed Dehalogenation”, Sarah L. Sewell, Kyle S. Knight. Poster Presentation at the 225th National Meeting of the American Chemical Society, March 23-27, 2003 in New Orleans, Louisiana.